

Copyright  
by  
Jonathan Charles Denyszyn  
2006

**The Dissertation Committee for Jonathan Charles Denyszyn certifies that this is the approved version of the following dissertation:**

**THE DIELECTRIC BEHAVIOR OF PEROVSKITE-RELATED  
MANGANESE OXIDES WITH STRETCHED BONDS OR  
MULTIFERROIC PROPERTIES**

**Committee:**

---

John B. Goodenough, Supervisor

---

Jianshi Zhou, Co-Supervisor

---

Sanjay K. Banerjee

---

Ananth Dodabalapur

---

Michael F. Becker

---

Chih-Kang Shih

**THE DIELECTRIC BEHAVIOR OF PEROVSKITE-RELATED  
MANGANESE OXIDES WITH STRETCHED BONDS OR  
MULTIFERROIC PROPERTIES**

**by**

**Jonathan Charles Denyszyn, B.S.; M.S.**

**Dissertation**

Presented to the Faculty of the Graduate School of

The University of Texas at Austin

in Partial Fulfillment

of the Requirements

for the Degree of

**Doctor of Philosophy**

**The University of Texas at Austin**

**December 2006**

## **Dedication**

This dissertation is dedicated to the memory of my father, Dr. Robert B. Denyszyn.

## **Acknowledgements**

I am indebted to many people who have helped me throughout my academic career. I will try to mention as many people as I can remember; however, my memory is not my strongest quality, so if you have helped me in any capacity, whether your name appears in this brief list of acknowledgements or not, thank you.

First, I would like to recognize my research supervisors Dr. John B. Goodenough and Dr. Jianshi Zhou; they welcomed me into their research group and shared their resources and expertise; I greatly appreciate the guidance they have offered me over the past 4 years.

I would also like to give thanks to the past and present members of our research group that have collaborated with me and contributed to my research and education: Jinguang Cheng, Roman Caudillo, Sangwon Kim, Dr. Yunhui Huang, Dr. Ronald Dass, Dr. Haidong Zhou, Dr. Jiaqang Yan, Dr. Steen Schougaard, and Dr. Fransisco Rivadulla. In addition to all the help they have given me, I would also like them to know that I greatly appreciate their friendship.

To my dissertation committee members: Dr. Sanjay Banerjee, Dr. Michael Becker, Dr. Ananth Dodabalapur, and Dr. Ken Shih, thank you for taking the time out of your schedules to review my work and offer your critique.

During my time as Master's student, I was fortunate enough to have Uttiya Chowdhury as a mentor. Dr. Chowdhury spent a great deal of time and energy guiding me, teaching me, and challenging me; I appreciate all of that effort very much. I would also like to recognize my Master's thesis advisor, Dr. Russell Dupuis, for encouraging me to pursue a doctoral degree and fostering me through the beginning of the journey.

I would like to thank Michelle Lejuene and Jamie Wentz for taking care of all the administrative details during my time as a Ph.D. student.

I am also indebted to the very helpful people that staff the physics store: David Elias and Jeffery Kent, the mechanical engineering machine shop: Don Artieschoufsky, Danny Jares, and Curtis Johnson, and the physics cryogenics lab: Lanny Sandefur and Ed Baez.

I have been very fortunate to have grown up in a loving and supportive family; to my brother, Matthew Denyszyn, mother, Patricia Denyszyn, and father, Robert Denyszyn, thank you for all your support and encouragement over the years.

Most importantly, I want to thank my wife, Jodi Harris-Denyszyn, who has supported me in every possible way throughout the entire doctoral process. She has sacrificed a lot during these years and experienced all the bumps in the road. I want her to know that I appreciate everything she has done for me and for our partnership over the past four years. Thank you.

# **The Dielectric Behavior of Perovskite-Related Manganese Oxides with Stretched Bonds or Multiferroic Properties**

Publication No. \_\_\_\_\_

Jonathan Charles Denyszyn, Ph.D.

The University of Texas at Austin, 2006

Supervisor: John B. Goodenough

Co-Supervisor: Jianshi Zhou

This dissertation presents two investigations into the dielectric behavior of non- $d^0$  perovskite-related manganese oxides: the first investigation probes the unique multiferroic properties of the hexagonal-perovskite series  $\text{RMn}_{1-x}\text{Ga}_x\text{O}_3$  ( $\text{R} = \text{Y}, \text{Ho}$ ) and the second explores the importance of lattice stress and the effect of the metal-cation  $d^n$ -character on the dielectric properties of the perovskite series  $\text{Sr}_y\text{Ca}_{1-y}\text{Mn}_{1-x}\text{B}_x\text{O}_{3-\delta}$  ( $\text{B} = \text{Ti}, \text{Zr}$ ).

In the hexagonal-perovskite series, doping the Mn-site with Ga increased the  $c$  lattice constant and diluted the magnetic interactions in the  $ab$  plane. The interplay of these two effects perturbed the ferrielectric, antiferromagnetic, and multiferroic interactions. The change in these interactions demonstrated chemical control of the multiferroic interactions in the hexagonal-perovskite system for the first time and highlighted the structural mechanism behind the multiferroic properties.

In the second investigation, the relationship between the tensile stress on the (Mn – O) bond and the ionic dielectric constant of  $\text{Sr}_y\text{Ca}_{1-y}\text{MnO}_{3-\delta}$  proved difficult to quantify because the small band gap and chemical activity of the  $\text{Mn}^{4+}$  cation made samples with  $y \geq 0.5$  too conducting to measure the dielectric relaxations. To explore the ionic contribution to the dielectric behavior by an alternate path, a doping scheme was devised to decrease the sample conductivity of  $\text{SrMnO}_{3-\delta}$  at the expense of some of the tensile stress on the (Mn – O) bond. Doping the Mn site with larger 4+ cations (Ti and Zr) reduced the dielectric constant; however, the reduction of the dielectric constant cannot be explained by the effect of the tensile stress on the (Mn – O) bond alone.



## Table of Contents

List of Tables .....	xiii
List of Figures .....	xiv
List of Figures .....	xiv
Chapter 1: Introduction .....	1
Chapter 2: Background .....	4
2.1 Crystallographic structure .....	4
2.1.1 Tolerance factor $< 1$ .....	5
2.1.2 Hexagonal 5-fold coordinated manganese pervoskites .....	9
2.1.3 Hexagonal polytypes .....	11
2.1.4 Oxygen-vacancy ordering .....	13
2.2 Electronic structure .....	14
2.2.1 Tight-binding model .....	19
2.2.2 Jahn-Teller effect .....	20
Chapter 3: Supporting Experiments .....	22
3.1 Iodimetric titration .....	22
3.1.1 Procedure .....	23
3.1.2 Endpoint .....	24
3.1.3 Example .....	25
3.1.4 Error .....	27
3.2 Thermoelectric power Seebeck effect measurements .....	28
3.2.1 Measurement hardware .....	28
3.2.2 Measurement technique .....	28
3.3 DC conductivity .....	30
3.3.1 Measurement hardware .....	30
3.3.2 Measurement techniques .....	31
3.3.3 Voltmeter loading .....	32

3.4 Magnetic measurements.....	32
3.5 Powder X-ray diffraction .....	33
Chapter 4: Impedance Measurements .....	35
4.1 Polarization in static fields.....	35
4.2 Polarization in time-dependent fields .....	36
4.2.1 The Debye equations.....	37
4.2.2 The Kramers-Kronig relations .....	39
4.3 Polarizing mechanisms .....	40
4.3.1 Space-charge polarization.....	42
4.3.2 Hopping polarization .....	42
4.3.3 Ionic polarization .....	45
4.3.4 Electronic polarization .....	47
4.4 Impedance .....	48
4.5 Circuit element modeling.....	49
4.5.1 Linear circuit-element dielectric-relaxation modeling.....	51
4.5.2 Constant-phase element .....	52
4.5.3 DC-conductivity.....	53
4.6 Grain boundaries.....	54
4.7 Measurement techniques.....	55
4.7.1 Measurement hardware.....	55
4.7.2 Measurement limitations.....	56
Chapter 5: $\text{RMn}_{1-x}\text{Ga}_x\text{O}_3$ (R = Ho and Y).....	61
5.1 Synthesis .....	65
5.2 Ferrielectric transistion .....	68
5.2.1 High-temperature X-ray diffraction.....	68
5.2.2 Thermomechanical analysis.....	70
5.3 Antiferromagnetic transition.....	71
5.4 Spin-rotation transition .....	77
5.5 Second spin rotation.....	80
5.6 Discussion .....	82

Chapter 6: $\text{Sr}_x\text{Ca}_{1-x}\text{MnO}_{3-\delta}$ .....	85
6.1 Synthesis .....	87
6.2 Dielectric behavior of $\text{CaMnO}_{3-\delta}$ .....	92
6.2.1 Effects of oxygen annealing.....	92
6.2.2 Surface capacitance effects .....	94
6.2.3 Sample density effects .....	96
6.3 Dielectric behavior of $\text{Sr}_x\text{Ca}_{1-x}\text{MnO}_3$ ( $0 < x < 0.5$ ).....	97
6.4 Dielectric behavior of $\text{Sr}_x\text{Ca}_{1-x}\text{MnO}_3$ ( $0.5 \leq x \leq 1$ ).....	98
6.5 Discussion .....	107
Chapter 7: $\text{SrMn}_{1-x}\text{B}_x\text{O}_{3-\delta}$ ( $\text{B} = \text{Mn}^{3+}, \text{Ni}^{2+}, \text{Ti}^{4+}, \text{Zr}^{4+}$ ).....	109
7.1 $\text{SrMn}^{4+}_{1-2\delta}\text{Mn}^{3+}_{2\delta}\text{O}_{3-\delta}$ .....	109
7.2 $\text{SrMn}^{4+}_{1-2\delta+2x}\text{Mn}^{3+}_{2\delta-2x}\text{Ni}^{2+}_x\text{O}_{3-\delta}$ .....	114
7.2.1 Synthesis .....	115
7.2.2 Discussion .....	116
7.3 $\text{SrMn}^{4+}_{1-2\delta-x}\text{Mn}^{3+}_{2\delta}\text{Ti}^{4+}_x\text{O}_{3-\delta}$ .....	118
7.3.1 Synthesis .....	119
7.3.2 Admittance .....	124
7.3.3 Discussion .....	129
7.4 $\text{SrMn}^{4+}_{1-2\delta-x}\text{Mn}^{3+}_{2\delta}\text{Zr}^{4+x}\text{O}_{3-\delta}$ .....	130
7.4.1 Synthesis .....	131
7.4.2 Admittance .....	137
7.5 Kramers-Kronig Analysis of $\text{SrMnO}_{3-\delta}$ .....	138
7.6 Discussion .....	141
Chapter 8: $\text{SrMn}_{1-x}\text{Ti}_x\text{O}_{3-\delta}$ .....	144
8.1 $\text{ATiO}_3$ ( $\text{A} = \text{Ca}, \text{Sr}, \text{and Ba}$ ).....	144
8.2 Synthesis .....	147
8.3 Admittance .....	149
8.4 Discussion .....	151

Chapter 9: Conclusion.....	155
9.1 Multiferroic Hexagonal Perovskites ( $\text{RMnO}_3$ ) .....	155
9.2 Manganese Perovskites with Stressed Bonds ( $\text{AMnO}_3$ ).....	157
References.....	162
Vita	169

## List of Tables

Table 3.1:	Example of the results of a standardization of $\text{Na}_2\text{S}_2\text{O}_3$ titer solution with $\text{K}_2\text{CrO}_7$ .	24
Table 3.2:	List of expressions needed to determine the number of oxygen vacancies in $\text{SrMnO}_{3-\delta}$ by iodimetric titration.	26
Table 3.3:	Number of oxygen vacancies ( $\delta$ ) in $\text{SrMnO}_{3-\delta}$ determined by iodimetric titration.	26
Table 4.1:	Transformation table for converting the impedance, admittance, and dielectric constant.	52
Table 6.1:	The annealing conditions and fraction of oxygen vacancies of $\text{Sr}_x\text{Ca}_{1-x}\text{MnO}_{3-\delta}$ samples measured by impedance spectroscopy.	99
Table 7.1:	Effective ionic radii for $\text{Mn}^{3+}$ , $\text{Mn}^{4+}$ and $\text{Ni}^{2+}$ (Shannon and Prewitt 1969).	114
Table 7.2:	Constraints on $\text{Ni}^{2+}$ (x) doping and mole fractions of $\text{Mn}^{4+}$ and $\text{Mn}^{3+}$ for various amounts of oxygen vacancies.	115
Table 7.3:	Effective ionic radii for $\text{Mn}^{3+}$ , $\text{Mn}^{4+}$ and $\text{Ti}^{4+}$ (Shannon and Prewitt 1969).	119
Table 7.4:	Effective ionic radii for $\text{Mn}^{3+}$ , $\text{Mn}^{4+}$ and $\text{Ti}^{4+}$ , $\text{Zr}^{4+}$ (Shannon and Prewitt 1969).	131

## List of Figures

Figure 2.1:	Three-dimensional ball-and-stick schematic of the cubic $Pm\bar{3}m$ manganese perovskite crystal structure along with two-dimensional cross-sectional schematics of close-packed ionic spheres of the Mn – O and A – O planes.....	5
Figure 2.2:	Three-dimensional ball and stick schematic of the tetragonal ( $I4/mcm$ ) manganese perovskite crystal structure along with a two-dimensional projection along the $c$ -axis. ....	6
Figure 2.3:	Three-dimensional ball and stick schematic of the orthorhombic ( $Pbnm$ ) manganese perovskite crystal structure along with two 2-dimensional projections along the $a$ -axis and $c$ -axis, respectively.	7
Figure 2.4:	General structural phase-diagram for transition-metal perovskite oxides ( $A^{2+}M^{4+}O_3$ ). ....	8
Figure 2.5:	Simulated X-ray diffraction patterns for the cubic, tetragonal, and orthorhombic perovskite structures shown in Figures 2.1, 2.2, and 2.3, respectively; the patterns were simulated using the <i>FindIt Visualizer</i> program.....	9
Figure 2.6:	Structural phase diagram for $R^{3+}Mn^{3+}O_3$ for decreasing $R^{3+}$ ionic radius ( $r_R$ ) (Brinks et al. 2001; Shannon and Prewitt 1969). ....	10
Figure 2.7:	Three-dimensional ball and stick schematic of the hexagonal ( $P6_3cm$ ) manganese perovskite crystal structure along with two-dimensional cross-sectional schematics of close-packed ionic spheres of the Mn – O and R ab-planes.....	11

Figure 2.8:	Ball-and-stick models for the 4H (a) and 2H (b) manganese oxides hexagonal polytypes.....	12
Figure 2.9:	Ball-and-stick model of the oxygen-deficient $\text{AMnO}_{2.5}$ orthorhombic ( $Pbam$ ) crystal structure and a comparison of the simulated X-ray diffraction patterns for the $Pbam$ and $Pm\bar{3}m$ perovskite structures. ....	14
Figure 2.10:	Schematic energy splittings and for a $\text{Mn}^{2+}$ in octahedral coordination. ....	15
Figure 2.11:	Crystal-field wavefunctions for manganese cation in octahedral coordination. ....	16
Figure 2.12:	Schematic energy comparison of adding an electron to a $d^3$ manifold where $J_{ex} < \Delta_C$ in the “low-spin” or $J_{ex} > \Delta_C$ in the “high-spin” configurations, respectively. ....	17
Figure 2.13:	Schematic energy splittings and for a $\text{Mn}^{3+}$ cation in square-pyramidal coordination. ....	17
Figure 2.14:	Energy splittings and crystal-field wavefunctions for a manganese cation in trigonal-bipyramidal coordination. ....	18
Figure 2.15:	Electronic band diagram for the $e_g$ states of $\text{LaMnO}_3$ with and without the Jahn-Teller distortion.....	21
Figure 3.1:	Iodimetric titration using an oxidation-reduction electrode to determine the endpoint.....	25
Figure 3.2:	Illustration of the temperature gradient across a sample; the gradient produces a potential that includes a contribution from the wires as well as the sample. ....	29

Figure 3.3:	Sketch of the cryogenic system, control hardware, and measurement instruments for measuring DC-resistivity as a function of temperature. ....	31
Figure 3.4:	Sketch illustrating current loading when $R_{\text{sample}} \approx R_{\text{in}}$ while measuring DC-resistivity. ....	32
Figure 4.1:	Relationship between the electric displacement, electric field, and polarization for a parallel-plate capacitor without and with a dielectric interior(Polnus 1978). ....	35
Figure 4.2:	Increase in the polarization due to an applied field. ....	36
Figure 4.3:	Bode plot (a) and Nyquist plot (b) exhibiting the dielectric relaxations of Debye equations. ....	38
Figure 4.4:	Various polarization contributions during the transient response (Kao 2004). ....	41
Figure 4.5:	Example of the effect of the “universal dielectric response” on the AC-conductivity ( $\sigma$ ), the imaginary-part of the relative dielectric constant ( $\epsilon''$ ), and the real-part of the relative dielectric constant ( $\epsilon'$ ) for a semiconducting sample. ....	44
Figure 4.6:	Schematic of a dipole in an oscillation Electric field. ....	45
Figure 4.7:	Simulated example of the real ( $\epsilon'$ ) and imaginary ( $\epsilon''$ ) components of the dielectric constant due to three ionic resonances. ....	47
Figure 4.8:	General sinusoidal voltage response to a forced sinusoidal current. ....	48
Figure 4.9:	Phasor diagram of the impedance. ....	49
Figure 4.10:	Simple circuit element models for describing an impedance or admittance. ....	50



Figure 4.11:	Scaling of the admittance $Y$ of a sample by its thickness and area to give the size-independent admittance $y$ . ....	50
Figure 4.12:	Admittance circuit with a frequency response equivalent to the Debye relaxation equations. ....	51
Figure 4.13:	Bode plot (a) and Nyquist plot (b) of the dielectric relaxations of the circuit in Figure 4.12, having replaced the resistor with a CPE. ....	53
Figure 4.14:	Bode plot (a) and Nyquist plot (b) of the dielectric relaxations of a circuit model with a DC-resistance; the arrow points to the direction of increasing $R_{DC}$ . ....	54
Figure 4.15:	Admittance measurement limitations and minimum capacitance for the HP4192A impedance analyzer. ....	57
Figure 4.16:	The admittance magnitude (a), phase (b), linear-fit residual (c), and dielectric constant (d) of a commercial piece of (1 0 0)-oriented $SrTiO_3$ measured at room temperature. ....	58
Figure 5.1:	Schematic of the lanthanide and manganese positions for orthorhombic $LaMnO_3$ and the hexagonal $YMnO_3$ ; the orthorhombic structure has corner-linked octahedra and the hexagonal structure has planes of corner-linked trigonal-bipyramids (for clarity, only a few oxygen polyhedra are shown). ....	61
Figure 5.2:	Schematic drawing of the locations of the R, Mn, and O ions in the centrosymmetric hexagonal ( $P6_3/mcm$ ) (a) and the ferroelectric hexagonal ( $P6_3cm$ ) phases of $RMnO_3$ (Van Aken et al. 2004). ...	62

Figure 5.3:	Projections of the six possible magnetic orderings for the manganese oxide planes in spin-frustrated hexagonal RMnO <sub>3</sub> ; the spins of the magnetic symmetries P6 <sub>3</sub> and P6 <sub>3</sub> ' are randomly oriented with respect to the major axes, groups P6 <sub>3</sub> cm and P6 <sub>3</sub> 'c'm are perpendicular, and groups P6 <sub>3</sub> 'cm' and P6 <sub>3</sub> c'm' are parallel (Lonkai et al. 2002). ....	63
Figure 5.4:	Examples of digitized Laue back-diffraction patterns simulated by the <i>OrientExpress</i> software for a randomly oriented (a) and c-axis oriented piece of HoMnO <sub>3</sub> (b). ....	66
Figure 5.5:	The lattice parameters and <i>c/a</i> ratio for RMn <sub>1-x</sub> Ga <sub>x</sub> O <sub>3</sub> (R = Y, Ho) (x = 0, 0.03, 0.1, 0.2) (Zhou et al. 2005); the symbols represent the actual data and the lines represent linear interpolations of the parameters of the parent compounds RMnO <sub>3</sub> and RGaO <sub>3</sub> (Geller et al. 1975). ....	67
Figure 5.6:	Temperature dependencies of the <i>a</i> (a) and <i>c</i> (b) lattice constants of RMn <sub>1-x</sub> Ga <sub>x</sub> O <sub>3</sub> (R = Y, Ho) (x = 0, 0.2) determined by high-temperature X-ray diffraction; the lines represent linear fits over the entire temperature range for the <i>a</i> lattice constant, and for the <i>c</i> lattice constant separate fits were made above and below T <sub>C</sub> (indicated by the arrows) (Zhou et al. 2005). ....	69
Figure 5.7:	Thermal expansion of the <i>c</i> -axis lattice parameter for RMn <sub>1-x</sub> Ga <sub>x</sub> O <sub>3</sub> (R = Y, Ho) (x = 0, 0.1, 0.2) as determined by TMA; the inset shows the increase of T <sub>C</sub> with Ga-doping (Zhou et al. 2005). ....	71

Figure 5.8:	Temperature dependence of the magnetic susceptibility of $\text{YMn}_{1-x}\text{Ga}_x\text{O}_3$ and the change in $T_N$ with Ga-doping (inset) (Zhou et al. 2005). ....	72
Figure 5.9:	Temperature dependence of the specific heat of $\text{HoMn}_{1-x}\text{Ga}_x\text{O}_3$ ( $x = 0, 0.03, 0.1, 0.2$ ) and the dependence of $T_N$ on Ga-doping (inset) (Zhou et al. 2006a). ....	73
Figure 5.10:	The change in $T_N$ verses the in-plane lattice constant $a$ for $\text{RMnO}_3$ (Munoz et al. 2000), Lu (Van Aken et al. 2001b; Van Aken and Palstra 2004), Yb (Sugie et al. 2002; Van Aken et al. 2001c), Er (Sugie et al. 2002; Van Aken et al. 2001a), Ho, and Y} and $\text{RMn}_{1-x}\text{Ga}_x\text{O}_3$ ( $R = \text{Y, Ho}$ ) ( $x = 0.03, 0.1, 0.2$ ).....	74
Figure 5.11:	Temperature dependence of the relative dielectric constant along the c-axis for $\text{HoMnO}_3$ samples grown by floating-zone image furnace (blue squares) and a sample grown with the flux method (red squares); the lines serve as eye-guides.....	76
Figure 5.12:	Evolution of the spin-rotation temperature ( $T_{\text{SR}}$ ) for $\text{HoMn}_{1-x}\text{Ga}_x\text{O}_3$ observed by differentiation of the inverse magnetic susceptibility (a), dielectric permittivity (b), and specific heat (c) (Zhou et al. 2005; Zhou et al. 2006a). ....	78
Figure 5.13:	Dependence of the spin-rotation temperature on Ga-doping, the $\times$ -symbols are averages of the $T_{\text{SR}}$ determined by the magnetic susceptibility, dielectric permittivity, and specific heat.....	79

Figure 5.14:	Evolution of the second spin-rotation temperature ( $T_2$ ) as peaks in the temperature dependences of the differentiated, inverse magnetic susceptibility (a) and specific heat (b); the inset shows the change in $T_2$ for increasing Ga-doping in $\text{HoMn}_{1-x}\text{Ga}_x\text{O}_3$ (Zhou et al. 2005; Zhou et al. 2006a). ....	81
Figure 5.15:	Phase diagram for $\text{HoMn}_{1-x}\text{Ga}_x\text{O}_3$ indicating the ferrielectric transition temperature ( $T_C$ ), the antiferromagnetic transition temperature ( $T_N$ ), the spin-rotation temperature ( $T_{SR}$ ), and the second spin-rotation temperature ( $T_2$ ). ....	84
Figure 6.1:	Thermo-structural phase diagram for the series $\text{Sr}_x\text{Ca}_{1-x}\text{MnO}_{3-\delta}$ (Dabrowski et al. 2003). ....	86
Figure 6.2:	Schematic representation of the 6-fold coordinated oxygen octahedra, the cubic static of octahedra, and the four layer hexagonal stacking. ....	88
Figure 6.3:	Oxygen vacancy phase diagram for $\text{SrMnO}_{3-\delta}$ illustrating the non-equilibrium path for obtaining the cubic perovskite phase (Negas and Roth 1970). ....	89
Figure 6.4:	The X-ray diffraction patterns for $\text{SrMnO}_{3-\delta}$ sample (JSC100-6) before and after oxygen annealing. ....	91
Figure 6.5:	The dielectric relaxations of $\text{CaMnO}_{3-\delta}$ as a function of temperature (a) and frequency (b). ....	93
Figure 6.6:	Thermoelectric power temperature dependencies for a $\text{CaMnO}_{3-\delta}$ sample (ZCMO-2) before and after annealing in oxygen. ....	94

Figure 6.7:	Comparison of the dielectric relaxations of a $\text{CaMnO}_{3-\delta}$ sample (JSC00-3) cut to two different thickness: 0.42 cm and 0.24 cm respectively. ....	95
Figure 6.8:	The dielectric relaxation of two $\text{CaMnO}_3$ samples of different densities.....	96
Figure 6.9:	Dielectric phase diagram of $\text{Sr}_x\text{Ca}_{1-x}\text{MnO}_3$ ( $0 \leq x \leq 0.75$ ); data taken from (Cohn et al. 2004). The shaded area ( $x > 0.5$ ) represents an oxygen-deficient region. ....	97
Figure 6.10:	AC-conductivity (a) and dielectric (b) temperature dependencies for $\text{Sr}_{0.6}\text{Ca}_{0.4}\text{MnO}_{3-\delta}$ samples with $\delta = 0.39$ and 0.2.....	100
Figure 6.11:	Thermoelectric power of $\text{Sr}_{0.75}\text{Ca}_{0.25}\text{MnO}_{3-\delta}$ samples having undergone a variety of annealing conditions. ....	101
Figure 6.12:	AC-conductivity (a) and dielectric (b) temperature dependencies for $\text{Sr}_{0.75}\text{Ca}_{0.25}\text{MnO}_{3-\delta}$ samples with $\delta = 0.37$ and 0.2. ....	102
Figure 6.13:	AC-conductivity (a) and dielectric (b) temperature dependencies for $\text{SrMnO}_{3-\delta}$ samples with $\delta = 0.44$ and 0.05. ....	104
Figure 6.14:	Fitting of the dielectric relaxation convergence of $\text{SrMnO}_{3-\delta}$ ( $\delta = 0.5$ ) with a non-linear curve fit (a) and a linear fit (b). ....	106
Figure 7.1:	Sketches of the half-spin density of states for a stoichiometric (a) and reduced sample(b).....	110
Figure 7.2:	Evolution of the thermoelectric power Seebeck coefficient of $\text{SrMnO}_{3-\delta}$ before and after sitting for several months in an ambient environment and then undergoing successive anneals in an oxygen atmosphere. ....	112

Figure 7.3:	X-ray diffraction patterns of $\text{SrNi}_x\text{Mn}_{1-x}\text{O}_3$ for $x = 0, 0.05$ , and $0.1$ ; the arrows indicate a Ni-related impurity phase. ....	116
Figure 7.4:	Illustration of the two 5-fold coordinated $\text{Mn}^{3+}$ site created next to an oxygen vacancy .....	117
Figure 7.5:	Comparison of the X-ray diffraction patterns taken before and after oxygen annealing for $\text{SrTi}_x\text{Mn}_{1-x}\text{O}_{3-\delta}$ samples with $x = 0.025$ (SMT0025), $0.05$ (SMT005), and $0.1$ (SMT010). ....	121
Figure 7.6:	The lattice constant of the series $\text{SrTi}_x\text{Mn}_{1-x}\text{O}_{3-\delta}$ ( $0 \leq x \leq 0.4$ ); the solid line represents the linearly interpolated values calculated from the parent compounds $\text{SrMnO}_3$ and $\text{SrTiO}_3$ . ....	122
Figure 7.7:	Fraction of oxygen vacancies ( $\delta$ ) determined by iodimetric titration for the series $\text{SrTi}_x\text{Mn}_{1-x}\text{O}_{3-\delta}$ ; the solid line serves as an eye guide. ....	123
Figure 7.8:	AC-conductivity for $\text{SrMnO}_{2.95}$ (JSC100-7-1) and $\text{SrMn}_{1-x}\text{Ti}_x\text{O}_{3-\delta}$ ( $x = 0.025, 0.05, 0.1, 0.2, 0.3, 0.4$ ); the closed symbols are for $\nu = 10^3$ Hz and the open symbols are for $\nu = 10^4$ Hz. ....	124
Figure 7.9:	The dielectric relaxations of the sample $\text{SrMn}_{0.8}\text{Ti}_{0.2}\text{O}_{2.98}$ (SMT020) with curve fitting from $10$ Hz to $10^6$ Hz (large plot) and $10^4$ Hz to $10^6$ Hz (inset); the open symbols represents the data and the solid lines are the fitted curves (a). The temperature bias of the fitted parameter $\epsilon_{\eta}$ ; the solid lines are eye guides (b).....	126

- Figure 7.10: The dielectric relaxations of the sample  $\text{SrMn}_{0.7}\text{Ti}_{0.3}\text{O}_{3-\delta}$  (SMT030) with curve fitting from 10 Hz to  $10^6$  Hz (large plot) and  $10^4$  Hz to  $10^6$  Hz (inset); the open symbols represents the data and the solid lines are the fitted curves (a). The temperature bias of the fitted parameter  $\epsilon_{\eta}$ ; the solid lines are eye guides (b).....127
- Figure 7.11: The dielectric relaxations of the sample  $\text{SrMn}_{0.6}\text{Ti}_{0.4}\text{O}_{3-\delta}$  (SMT040) with curve fitting from 10 Hz to  $10^6$  Hz (large plot) and  $10^4$  Hz to  $10^6$  Hz (inset); the open symbols represents the data and the solid lines are the fitted curves (a). The temperature bias of the fitted parameter  $\epsilon_{\eta}$ ; the solid lines are eye guides (b).....128
- Figure 7.12: X-ray diffraction patterns for  $\text{SrMn}_{1-x}\text{Zr}_x\text{O}_{3-\delta}$  ( $x = 0.025, 0.05$ , and  $0.1$ ) before and after annealing in oxygen. ....132
- Figure 7.13: Comparison of the diffractograms of  $\text{SrMn}_{0.975}\text{Zr}_{0.025}\text{O}_{3-\delta}$  before (black) and after (red) annealing in oxygen; the peak labels correspond to the  $Pm\bar{3}m$  phase (h k l), superstructure peaks of ordered oxygen vacancies ( $\text{V}_\text{O}$ ), tungsten- $\text{L}\alpha$  lines, and unaccounted peaks (\*). ....134
- Figure 7.14: Comparison of the diffractograms of  $\text{SrMn}_{0.95}\text{Zr}_{0.05}\text{O}_{3-\delta}$  before (black) and after (red) annealing in oxygen; the peak labels correspond to the  $Pm\bar{3}m$  phase (h k l), tungsten- $\text{L}\alpha$  lines, and unaccounted peak (\*). ....135
- Figure 7.15: Comparison of the diffractograms of  $\text{SrMn}_{0.90}\text{Zr}_{0.10}\text{O}_{3-\delta}$  before (black) and after (red) annealing in oxygen; the peak labels correspond to the  $Pm\bar{3}m$  phase (h k l), and tungsten- $\text{L}\alpha$  lines. ....136

Figure 7.16:	Comparison of the AC-conductivity of $\text{SrMnO}_{2.95}$ (JSC100-7-1), $\text{SrMn}_{0.95}\text{Zr}_{0.05}\text{O}_{3-\delta}$ (SMZ005), and $\text{SrMn}_{0.90}\text{Zr}_{0.10}\text{O}_{3-\delta}$ (SMZ010).	137
Figure 7.17:	Comparison between the dielectric behaviors of $\text{SrMn}_{0.95}\text{Zr}_{0.05}\text{O}_{3-\delta}$ (SMZ005) $\text{SrMn}_{0.90}\text{Zr}_{0.10}\text{O}_{3-\delta}$ (SMZ010).	138
Figure 7.18:	Infra-red imaginary part of the dielectric constant from Sacchetti <i>et al.</i> (Sacchetti <i>et al.</i> 2005) (open symbols), fitting of the imaginary dielectric constant with Equation 4.19b (dashed line), and corresponding plot of the real part of dielectric constant (solid line) from Equation 4.19a.	140
Figure 7.19:	The relationship between the tolerance factor and the relative dielectric constant for doped $\text{SrMn}_{1-x}\text{B}_x\text{O}_{3-\delta}$ for ( $\text{B}_x = \text{Ti}_{0.2}$ and $\text{Zr}_{0.1}$ ); the tolerance-factor error of $\text{SrMn}_{0.8}\text{Ti}_{0.2}\text{O}_{2.98}$ represents uncertainty in the distribution of $\text{Ti}^{4+}$ on 5-fold and 6-fold coordinated sites and the tolerance-factor error of $\text{SrMn}_{0.9}\text{Zr}_{0.1}\text{O}_{3-\delta}$ and $\text{SrMnO}_{3-\delta}$ represents the uncertainty in $\delta$ , assuming $\delta \approx 0.00 \pm 0.02$ .	142
Figure 8.1:	The Curie-Weiss temperature dependence of the dielectric constant of $\text{CaTiO}_3$ , $\text{SrTiO}_3$ , and $\text{BaTiO}_3$ (Rupprecht and Bell 1964).	145
Figure 8.2:	The change in the lattice constant with $x$ for the series $\text{SrTi}_x\text{Mn}_{1-x}\text{O}_{3-\delta}$ ; the solid line represents the linearly interpolated values calculated from the parent compounds $\text{SrMnO}_3$ and $\text{SrTiO}_3$ .	147
Figure 8.3:	Thermoelectric power temperature dependencies for $\text{SrMn}_{1-x}\text{Ti}_x\text{O}_{3-\delta}$ ( $0.025 \leq x \leq 0.6$ ).	148
Figure 8.4:	AC-conductivity temperature dependencies of $\text{SrMn}_{1-x}\text{Ti}_x\text{O}_{3-\delta}$ for $x = 0.1$ to $0.9$ ; open symbols are for $\nu = 10^3$ Hz and closed symbols for $\nu = 10^4$ Hz.	149



Figure 8.5:	Temperature-dependent dielectric relaxations for $\text{SrMn}_{1-x}\text{Ti}_x\text{O}_{3-\delta}$ ( $x = 0.6, 0.7, 0.8, 0.9$ ).....	150
Figure 8.6:	(a) Probability of a randomly distributed Ti cation having “n” number of randomly distributed Ti near neighbors; (b) the average (Mn – O) bond length vs. x in the $\text{SrMn}_{1-x}\text{Ti}_x\text{O}_{3-\delta}$ system calculated from the lattice constant determined from room-temperature X-ray diffraction and assuming a constant ratio of (Ti – O) to (Mn – O) bond lengths as determined from the tabulated room-temperature equilibrium values.....	152
Figure 8.7:	Dielectric phase diagram for the series $\text{SrMn}_{1-x}\text{Ti}_x\text{O}_{3-\delta}$ ; the shaded region represents samples where the soft-mode is actively increasing the dielectric constant as the temperature decreases.....	154

## Chapter 1: Introduction

Perovskite-related transition-metal oxides have been widely studied for their diverse set of physical properties created by the large number of chemical degrees of freedom available for synthesizing new materials. The discovery of ferroelectricity (von Hippel 1950), high-temperature superconductivity (Bednorz and Muller 1986; Bednorz and Muller 1988), and colossal magnetoresistance (Jin et al. 1994) in perovskite-related materials have been so revolutionary and technologically promising that they have spawned significant sectors of condensed-matter research.

The investigations of the perovskite-related transition-metal oxides can be organized into two main categories: in the first category, the perovskite oxides with transition-metal cations with  $d^0$  electronic configurations have been investigated largely for their dielectric, ferroelectric, pyroelectric, piezoelectric, and optical properties; the second category contains perovskite oxides with transition-metal cations with non- $d^0$  electronic configurations that have been investigated primarily for their transport and magnetic properties.

Recent research has begun to blur the distinction between the  $d^0$  and non- $d^0$  categories of perovskite oxides. From the  $d^0$  side, researchers are doping insulating oxides with non- $d^0$  cations to obtain spin-dependent properties for dilute magnetic semiconductors (DMS) (Pearson et al. 2004; Prellier et al. 2003). A second effort approaches the research gap between  $d^0$  and non- $d^0$  perovskite oxides by investigating the electric properties (electric polarization, dielectric behavior, *etc.*) of non- $d^0$  oxides. A large contingent of this second effort pertains to the investigation of materials exhibiting “multiferroic” properties. Multiferroicity refers to the presence of both electric-dipole and magnetic ordering; a fraction of multiferroic samples have a coupling between the

electric-dipole and magnetic order-parameters and are referred to as magnetoelectrics (Eerenstein et al. 2006); magnetoelectrics allow electric fields to effect the magnetic state or vice versa.

Along with the allure of studying the fundamental physical properties of complex magnetic and electric interactions, the interest in DMS and magnetoelectric-multiferroics is also being driven by hopes that these materials will contribute to the field of *Spintronics*, a new class of electronics where the spin degrees of freedom will be manipulated to create devices such as the SpinFET (Datta and Das 1990), the SpinLED and photomagnet (Pearson et al. 2004), and the magnetoelectric Spin-valve (Binek and Doudin 2005).

So far three different flavors of multiferroicity have been observed in the perovskite-related manganese oxides: the first flavor is found in  $\text{BiMnO}_3$  (Hill and Rabe 1999; Kimura et al. 2003b), where the lone-pair of the  $\text{Bi}^{3+}$  ion displaces it out of the center of symmetry and creates an electric moment; the second flavor is found in the hexagonal-perovskite manganites ( $\text{RMnO}_3$ ) where cooperative rotations of the Mn polyhedra lead to a ferroelectric displacement of the R – O chains (Van Aken et al. 2004); the third flavor is found in the orthorhombic perovskite  $\text{TbMnO}_3$  where a commensurate spin-density wave creates an electric polarization (Kimura et al. 2003a).

The work presented in this dissertation contains two investigations into the dielectric properties of non- $d^0$  perovskite-related manganese oxides: the first investigation probes the unique multiferroic properties of the hexagonal-perovskite series  $\text{RMn}_{1-x}\text{Ga}_x\text{O}_3$  ( $\text{R} = \text{Y}, \text{Ho}$ ) and the second explores the importance of lattice stress and the effect of the metal-cation  $d^n$ -character on the dielectric properties of the perovskite series  $\text{Sr}_y\text{Ca}_{1-y}\text{Mn}_{1-x}\text{B}_x\text{O}_{3-\delta}$  ( $\text{B} = \text{Ti}, \text{Zr}$ ).

There is a common thread in the experimental method used to investigate both the hexagonal-perovskite and  $\text{Mn}^{4+}$ -perovskite systems: the parent phase is systematically doped to observe systematic changes in the physical properties. Based on the systematic changes in the physical properties, qualitative arguments are made to explain the origin of the multiferroic or dielectric phenomena.

The organization of this dissertation is structured to give the interested reader the theoretical background necessary to follow the arguments made in the discussion sections as well as the experimental background required to reproduce the presented results. Chapter 2 contains background information on the perovskite-related materials' crystallographic and electronic structures. In Chapter 3, there are brief summaries of the supporting experiments used to supplement the dielectric measurements; Chapter 4 gives an in-depth summary of the theory and experimental details involved with measuring the dielectric constant with impedance spectroscopy. Chapter 5 begins the sequence of experimental sections with the investigation of the hexagonal-perovskite series. Chapters 6 and 7 focus on the dielectric properties of manganese perovskites with stretched ( $\text{Mn}^{4+}$  – O) bonds and Chapter 8 investigates the importance of the  $d^n$ -character in determining the dielectric behavior. The final chapter, Chapter 9, summarizes the conclusions that could be drawn from our investigations and offers some ideas for future work.

## Chapter 2: Background

This chapter reviews the crystallographic and electronic structures of the  $\text{AMnO}_3$  perovskite-related oxides investigated in this dissertation. The non-cubic alternative phases that develop are explained as deviations from an ideal cubic perovskite resulting from ionic size and lattice strain considerations or oxygen-vacancy ordering. The electronic structure is explained by starting from an ionic model but allowing for the crystal-field wavefunctions to have like-near-neighbor interactions to form tight-binding bands.

### 2.1 CRYSTALLOGRAPHIC STRUCTURE

The perovskite structure corresponds to the chemical formula  $\text{AMX}_3$ ; the structure consists of a network of corner-linked  $\text{MX}_6$  octahedra surrounding large A cations; the ideal cubic perovskite belongs to the space group  $Pm\bar{3}m$ . Figure 2.1 illustrates the three-dimensional network of octahedra as well as the two-dimensional planes of close-packed ionic spheres.

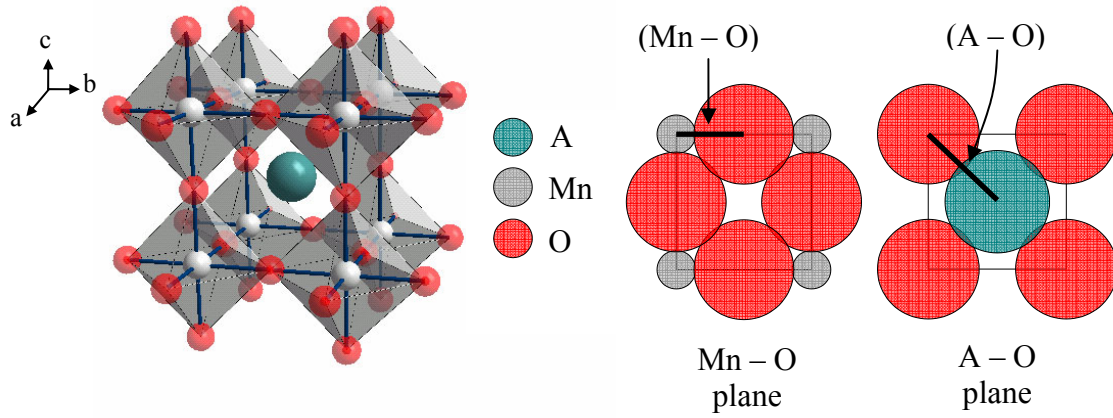


Figure 2.1: Three-dimensional ball-and-stick schematic of the cubic  $Pm\bar{3}m$  manganese perovskite crystal structure along with two-dimensional cross-sectional schematics of close-packed ionic spheres of the Mn – O and A – O planes

The packing of the ionic spheres illustrates the geometric relationship between the equilibrium (A – O) and (Mn – O) bond lengths; this relationship is referred to as the geometric tolerance factor  $t$ :

$$t \equiv \frac{(A - O)}{\sqrt{2}(M - O)} \quad (2.1)$$

Where  $t \approx 1$ , the crystal structure is cubic and there is little elastic strain on the (A – O) or (M – O) bonds. Where  $t < 1$ , the (A – O) bonds are under tensile stress and (M – O) bonds are under compressive stress. The bonds' stress character is reversed if  $t > 1$ : the (A – O) bonds are under compressive stress whereas the (M – O) bonds are under tensile stress.

### 2.1.1 Tolerance factor < 1

The perovskite crystal structure is able to minimize the elastic strain associated with having  $t < 1$  by cooperatively rotating the oxygen octahedra. A rotation about the (0

0 1) axis lowers the symmetry from cubic ( $Pm\bar{3}m$ ) to tetragonal ( $I4/mcm$ ); the rotation doubles the unit-cell height and  $ab$ -plane area. The cooperative rotations of the octahedra bend the  $ab$ -plane M – O – M bond angle to make it less than  $180^\circ$ ; the decrease in the bond angle is illustrated in the projection along the  $c$ -axis Figure 2.2.

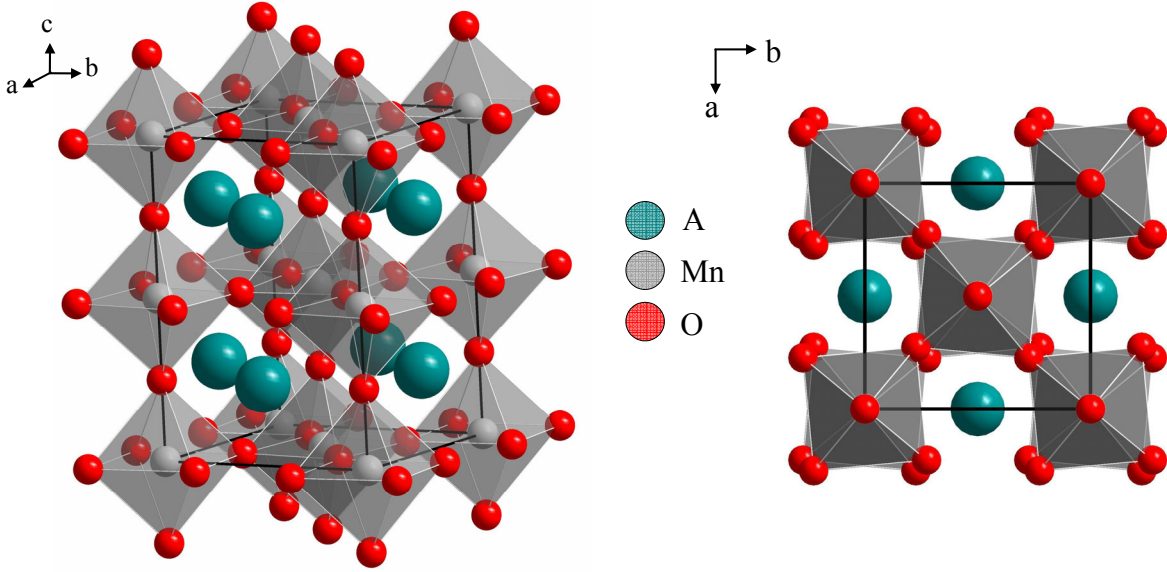


Figure 2.2: Three-dimensional ball and stick schematic of the tetragonal ( $I4/mcm$ ) manganese perovskite crystal structure along with a two-dimensional projection along the  $c$ -axis.

Comparing the tetragonal structure with the cubic structure, the bending of the M – O – M bond angle in the  $ab$ -plane changes the lattice parameter  $a$  to be less than the scaled cubic lattice constant ( $\sqrt{2} a_{cubic}$ ) and the out-of-phase rotations about the  $c$  axis reduce the  $O^{2-} - O^{2-}$  repulsions to allow  $c$  to be slightly less than the scaled cubic lattice constant ( $2 a_{cubic}$ ).

Another rotation of the oxygen octahedra about the (1 1 0) direction lowers the symmetry to orthorhombic ( $Pbnm$ ). The rotation decreases the  $ab$ -plane M – O – M

bending angle further and creates an out-of-plane M – O – M bending. The ball and stick model and close-packed planes for the  $AMX_3$   $Pbnm$  structure are drawn in Figure 2.3.

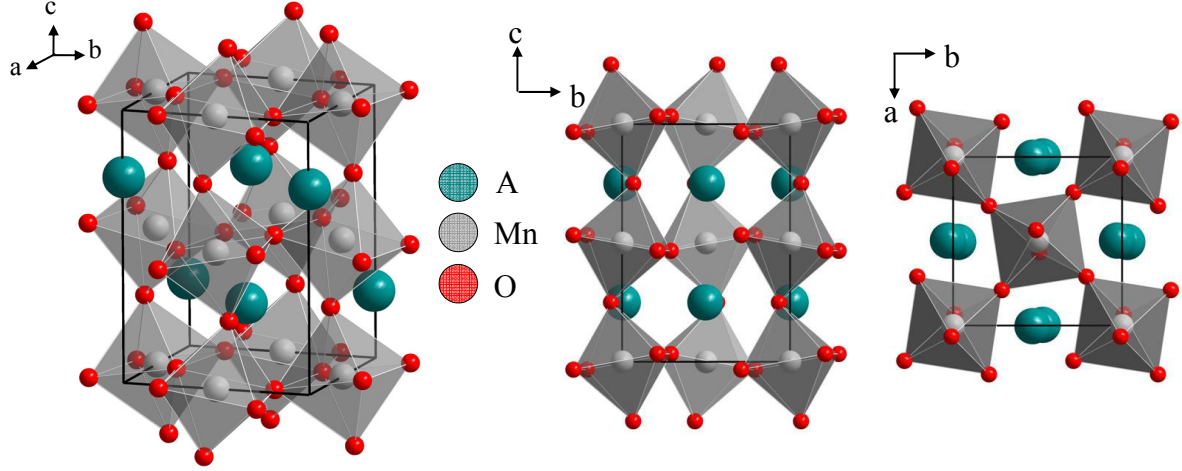


Figure 2.3: Three-dimensional ball and stick schematic of the orthorhombic ( $Pbnm$ ) manganese perovskite crystal structure along with two 2-dimensional projections along the  $a$ -axis and  $c$ -axis, respectively.

The change in the symmetry from cubic ( $Pm\bar{3}m$ ) to tetragonal ( $I4/mcm$ ) to orthorhombic ( $Pbnm$ ) with decreasing tolerance factor follows the same pattern for several series of transition-metal perovskite oxides:  $Sr_{1-x}Ca_xTiO_3$  (Ball et al. 1998; Qin et al. 2000),  $Sr_{1-x}Ca_xVO_3$  (Garcia-Jaca et al. 1999),  $Ba_{1-x}Sr_xZrO_3$  (Kennedy et al. 2001), and  $Ba_{1-x}Ca_xZrO_3$  (Levin et al. 2003).

It is also possible for a rotation of the oxygen octahedra about the  $(1\ 1\ 1)$  direction to give a rhombohedral symmetry; however, this symmetry is observed for  $R^{3+}Mn^{3+}O_3$  systems and the distorted-perovskite samples investigated in this dissertation are in the  $A^{2+}Mn^{4+}O_3$  system.

The (A – O) bond has a larger thermal expansion coefficient than the (M – O) bond, causing  $t$  to decrease as the temperature is decreased. Thus, the same series of structural phase-transitions that occur as a function of decreasing tolerance factor also



occur as a function of decreasing temperature. Figure 2.4 shows a general phase diagram for the transition-metal perovskite oxides that follow the  $Pm\bar{3}m$  to  $I4/mcm$  to  $Pbnm$  phase transitions in  $A^{2+}M^{4+}O_3$  systems.

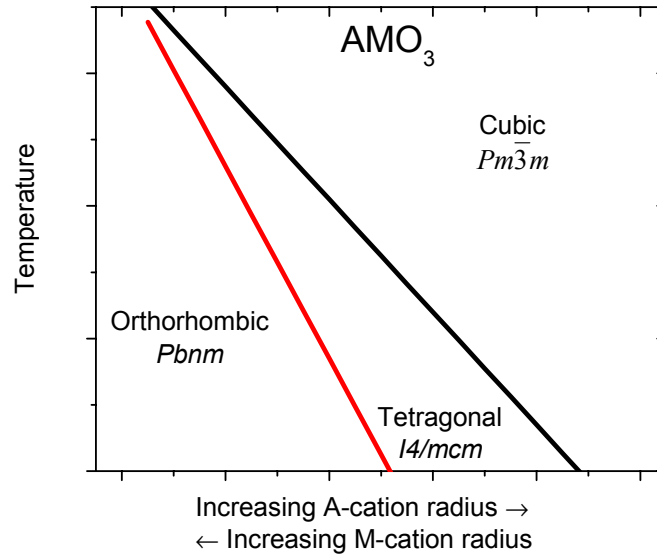


Figure 2.4: General structural phase-diagram for transition-metal perovskite oxides ( $A^{2+}M^{4+}O_3$ ).

The structural phase transitions can be observed directly with variable-temperature powder X-ray diffraction; as the octahedra rotate and the symmetry is lowered, the diffraction peaks split and increase in separation. Figure 2.5 shows simulated X-ray diffraction patterns for the cubic, tetragonal, and orthorhombic structures; the patterns were simulated with the *FindIt Visualizer* program.

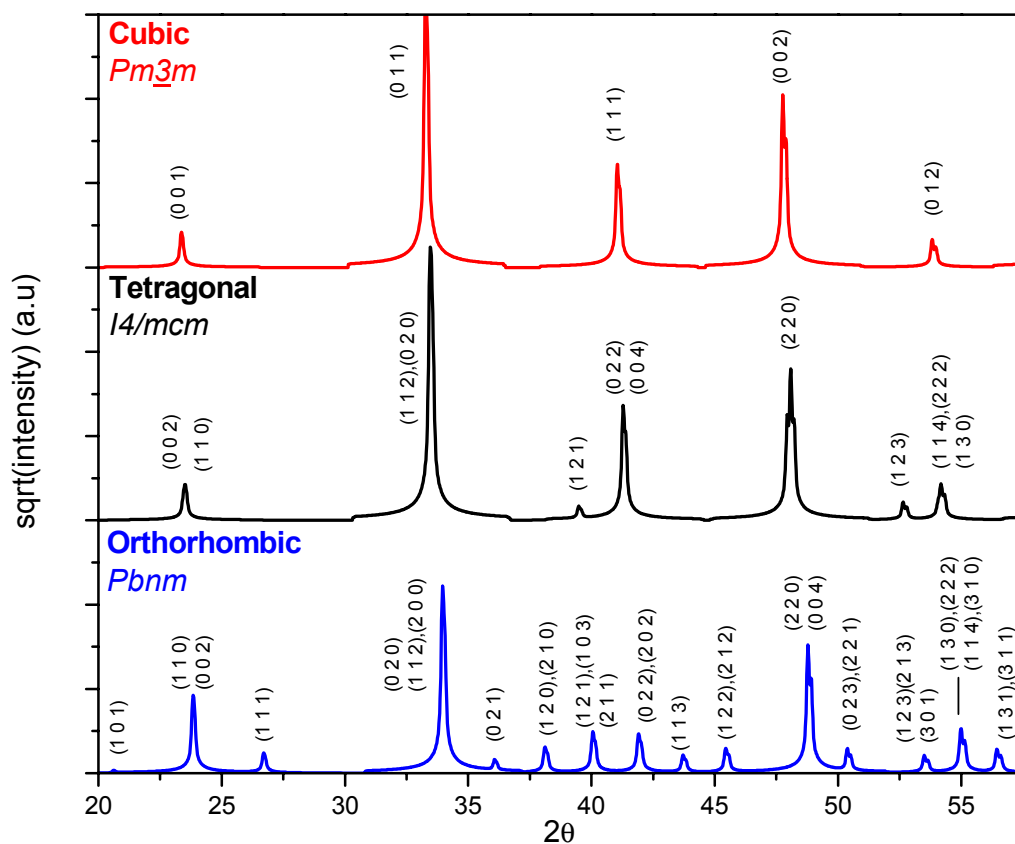


Figure 2.5: Simulated X-ray diffraction patterns for the cubic, tetragonal, and orthorhombic perovskite structures shown in Figures 2.1, 2.2, and 2.3, respectively; the patterns were simulated using the *FindIt Visualizer* program.

### 2.1.2 Hexagonal 5-fold coordinated manganese perovskites

For the  $\text{Mn}^{3+}$   $\text{RMnO}_3$  perovskites, where  $\text{R}^{3+}$  is either a column (III) transition-metal ion or lanthanide ion, the tolerance factor is always less than one. For  $\text{RMnO}_3$  synthesis under ambient conditions, the samples with  $\text{R}^{3+}$  cations with ionic radii smaller than the radius of Dy form a hexagonal phase with space group  $P6_3cm$  instead of the perovskite orthorhombic phase; this transition is illustrated in the phase diagram of Figure 2.6.

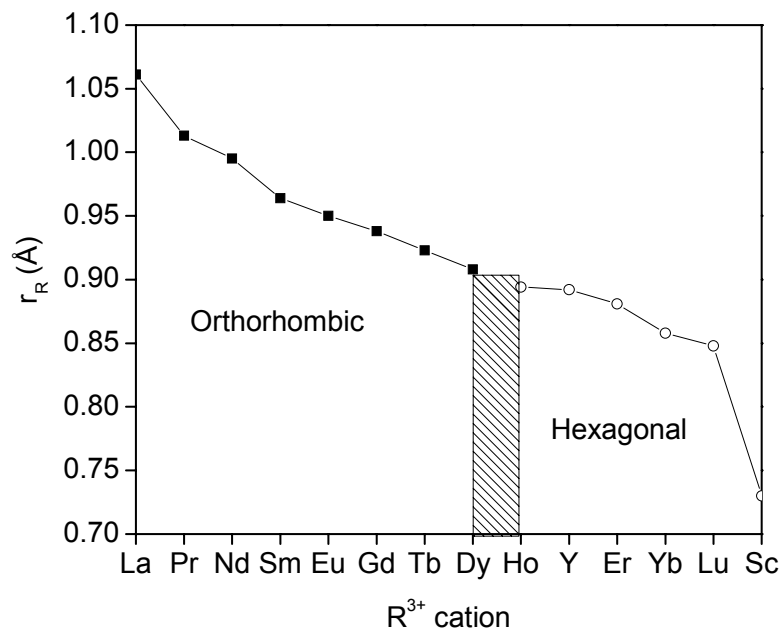


Figure 2.6: Structural phase diagram for  $R^{3+}Mn^{3+}O_3$  for decreasing  $R^{3+}$  ionic radius ( $r_R$ ) (Brinks et al. 2001; Shannon and Prewitt 1969).

In the hexagonal phase, the  $Mn^{3+}$  cations are five-fold coordinated by oxygen trigonal-bipyramids. The trigonal-bipyramids share corners and form a hexagonal network in the  $ab$ -plane but are not connected between the planes. The  $R^{3+}$  ions form their own plane with each ion six-fold coordinated by the apical oxygens of the trigonal-bipyramids. Figure 2.7 shows a three-dimensional ball-and-stick model and close-packed planes of the hexagonal  $RMnO_3$  structure.

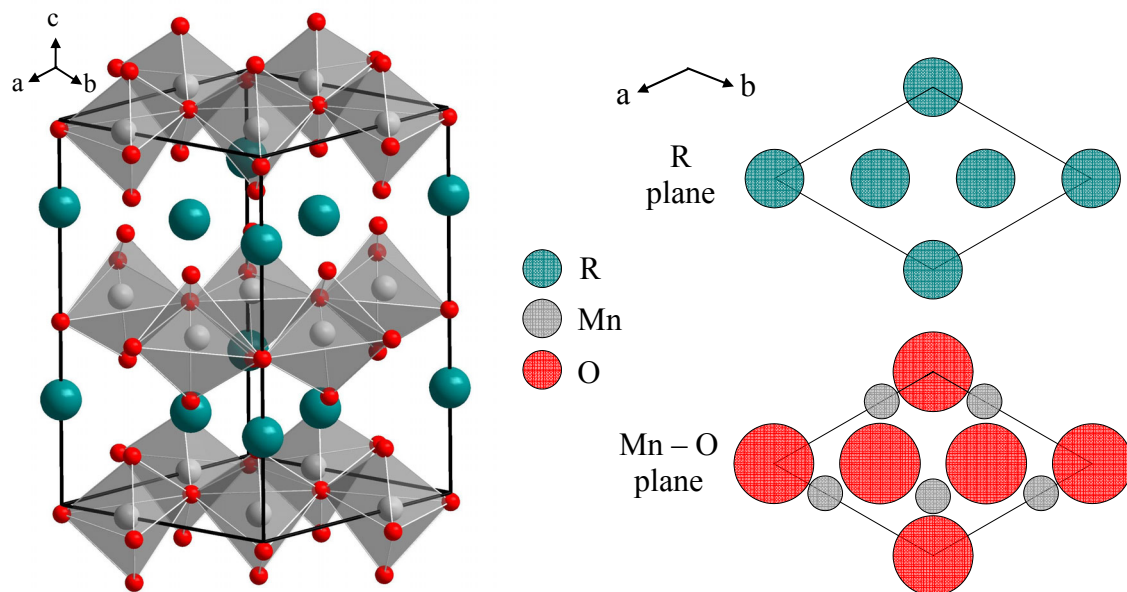


Figure 2.7: Three-dimensional ball and stick schematic of the hexagonal ( $P6_3cm$ ) manganese perovskite crystal structure along with two-dimensional cross-sectional schematics of close-packed ionic spheres of the  $Mn-O$  and  $R$  ab-planes.

In the  $P6_3cm$  space group, the  $R^{3+}$  cations have two different crystallographic settings and the  $O^{2-}$  anions have four different crystallographic settings; the physical implications of these multiple settings in the hexagonal structure are examined in detail in Chapter 5.

### 2.1.3 Hexagonal polytypes

Where  $t > 1$ , no cooperative rotations of the oxygen-octahedra can relieve the tensile stress on the ( $M-O$ ) bonds and compressive stress on the ( $A-O$ ) bonds. To relieve the increased strain, the material crystallizes in a hexagonal-polytype phase at the expense of some of the electrostatic energy associated with the ionic structure. The hexagonal polytypes are different than the hexagonal structure that develops where  $t < 1$ ; in the hexagonal polytypes, the  $Mn$ -cations remain 6-fold coordinated in oxygen

octahedra. The difference between the cubic perovskite phase and the hexagonal polytype phase is that in the cubic perovskite the  $\text{AO}_3$  close-packed (1 1 1) planes are stacked in a cubic arrangement; in the hexagonal polytypes, periodic hexagonal stackings of the  $\text{AO}_3$  (1 1 1) planes are introduced. The A-site cation size determines the periodicity of  $\text{AO}_3$  (1 1 1) plane stacking necessary to accommodate it. For example, in  $\text{SrMnO}_3$  a group of two face-shared octahedra share a corner with other groups of two face-shared octahedra; this structure is referred to as the 4H polytype. In  $\text{BaMnO}_3$ , (Ba has a larger ionic radius than Sr) the face-shared octahedra form columns that are not linked to each other; this structure is referred to as the 2H polytype. Figure 2.8 shows both the 4H and 2H hexagonal polytypes.

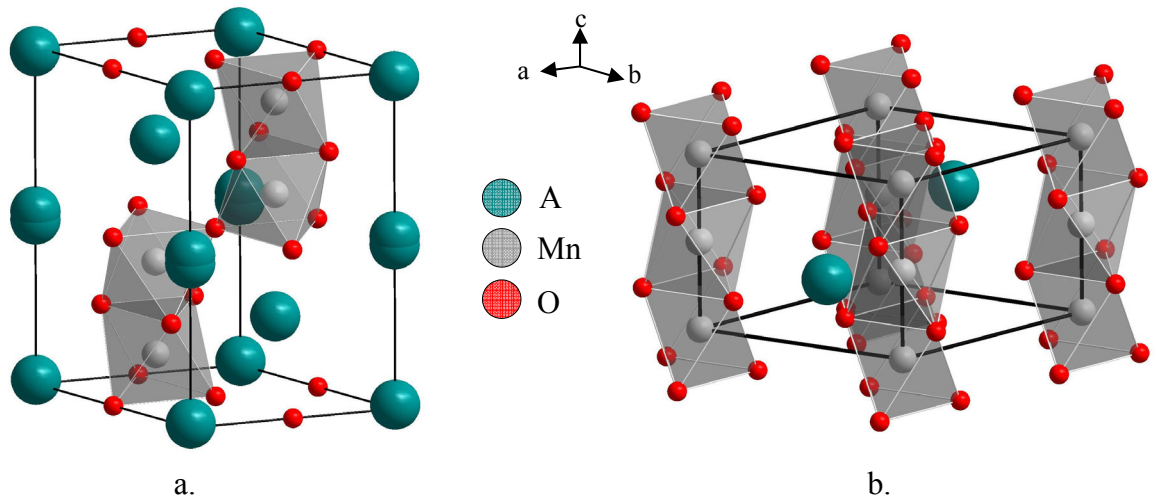


Figure 2.8: Ball-and-stick models for the 4H (a) and 2H (b) manganese oxides hexagonal polytypes.

#### 2.1.4 Oxygen-vacancy ordering

The  $\text{Mn}^{4+}$  perovskite oxides tend to lose oxygen during synthesis if the synthesis conditions require high temperatures or reducing environments. The loss of oxygen requires that two  $\text{Mn}^{4+}$  cations are reduced to  $\text{Mn}^{3+}$  cations to maintain charge balance in the structure. For specific mole fractions of oxygen vacancies, the Coulombic energy associated with the ionic crystal structure can be lowered if the oxide-ion vacancies order in regular patterns.

In the chemical formula  $\text{AMnO}_{3-\delta}$ , where  $\delta$  represents the number of oxide-ion vacancies per formula unit, all of the  $\text{Mn}^{4+}$  cations are reduced to  $\text{Mn}^{3+}$  cations for  $\delta = 0.5$ . Having 1/6 oxygen vacancies per formula unit places all of the  $\text{Mn}^{3+}$  cations in 5-fold coordinated square-pyramids. The ordering of the oxide-ion vacancies increases the unit cell so that  $a$  is equivalent to the cubic  $(1\ 0\ \bar{1})$  direction and  $b$  is equivalent to twice the cubic  $(1\ 0\ 1)$  direction; this ordering changes the X-ray diffraction pattern to include superstructure peaks consistent with the orthorhombic  $Pbam$  symmetry. The ball-and-stick model for  $\text{AMnO}_{2.5}$  is shown in Figure 2.9 along with a comparison of two simulated X-ray diffraction patterns of  $\text{AMnO}_{3-\delta}$ :  $\delta = 0.5$  and ordered oxide-ion vacancies and  $\delta = 0$  with no oxide-ion vacancies.

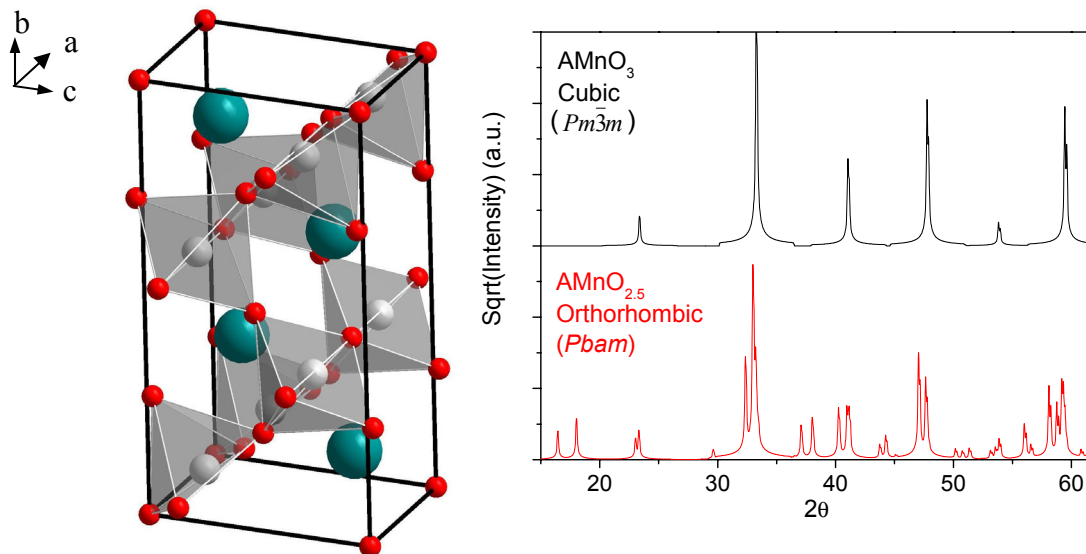


Figure 2.9: Ball-and-stick model of the oxygen-deficient  $AMnO_{2.5}$  orthorhombic ( $Pbam$ ) crystal structure and a comparison of the simulated X-ray diffraction patterns for the  $Pbam$  and  $Pm\bar{3}m$  perovskite structures.

## 2.2 ELECTRONIC STRUCTURE

The optimization of elastic strains on the bond lengths, long-range electrostatic interactions between the  $Mn^{(7-n)+}$  cations and  $O^{2-}$  anions, and short-range repulsive forces of the nuclei stabilizes the ionic crystal structures; the electronic energy levels of the oxide ions are lowered and those of the manganese cations are raised by the Madelung energy. The crystal field created by the neighboring ions perturbs the potential, lowering the degeneracy of the atomic wavefunctions.

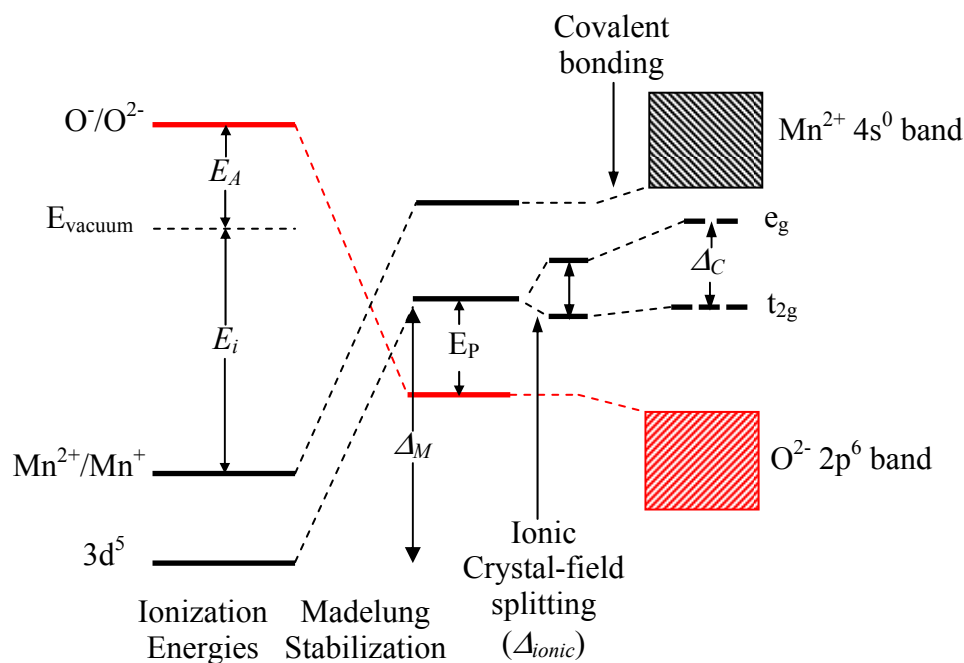


Figure 2.10: Schematic energy splittings and for a  $\text{Mn}^{2+}$  in octahedral coordination.

In addition to the ionic-bonding and ionic crystal-field splitting, there is significant covalent bonding between the manganese-4s states and the oxygen-2p states that creates broad bands. To a lesser extent, there is also covalent bonding between the manganese-3d states and the oxygen-2p states, so that the d-bands are much narrower. The covalent bonding pushes these antibonding states, primarily Mn 3d in character, up to higher energies; whereas the energy of the bonding states of O-2p character is lowered. The axial crystal field ( $\Delta_{\text{ionic}}$ ) and stronger covalent bonding along the axial directions separate the degeneracy between the two  $\sigma$ -bonding  $e_g$ -states ( $x^2-y^2$ ,  $3z^2-r^2$ ) and three  $\pi$ -bonding  $t_{2g}$ -states ( $xy$ ,  $yz$ ,  $zx$ ); the difference in energy between the  $e_g$  and  $t_{2g}$  states is



referred to as the cubic-field splitting  $\Delta_C$ . Figure 2.11 shows schematic drawings of the crystal wavefunctions in a basis that is convenient for cubic symmetries

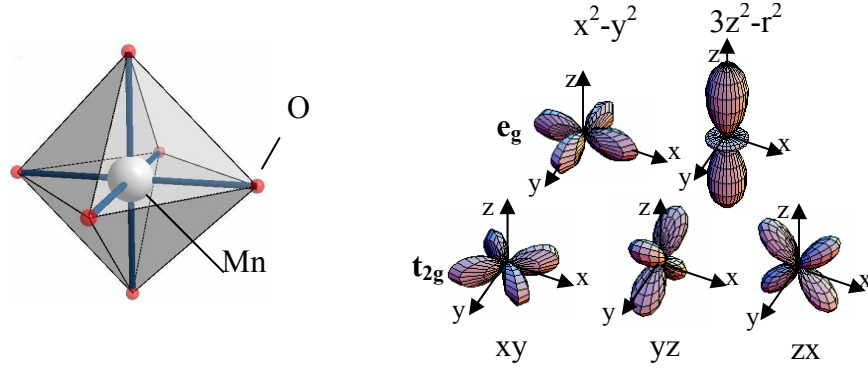


Figure 2.11: Crystal-field wavefunctions for manganese cation in octahedral coordination.

Due to the strong intra atomic electronic interactions on the transition-metal cations, there is a large energy  $U_H$  associated with adding an electron to the  $d^n$  manifold; the energy of the added electron is minimized by the exchange coupling (Hund's coupling)  $J_{ex}$  if the total electron spin of the manifold is maximized. In the manganese-perovskite oxides, the energy  $J_{ex}$  is typically larger than the cubic-field splitting  $\Delta_C$ . As a result of  $J_{ex} > \Delta_C$ , the electron added to a  $Mn^{4+}$   $d^3$ -manifold or  $Mn^{3+}$   $d^4$ -manifold goes in parallel to the parallel spins of the other electrons to give a “high-spin” state.

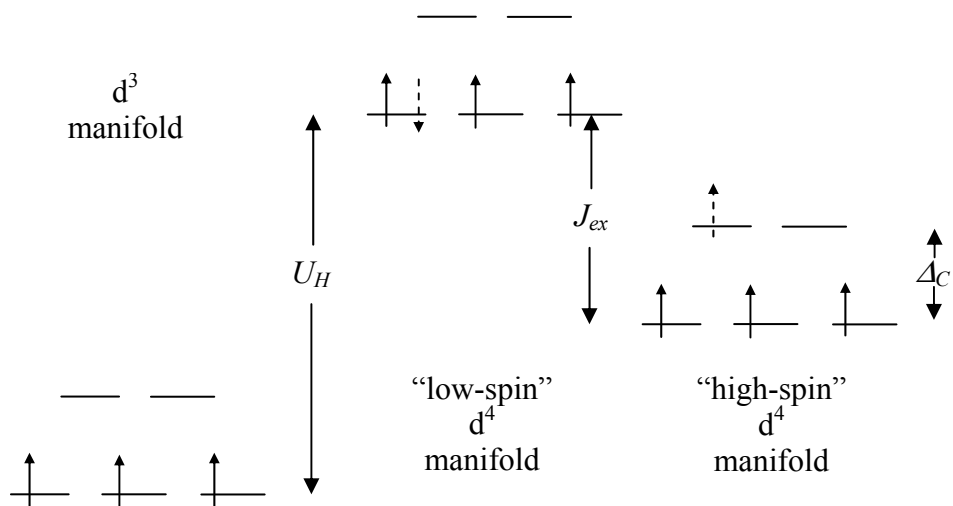


Figure 2.12: Schematic energy comparison of adding an electron to a  $d^3$  manifold where  $J_{ex} < \Delta_C$  in the “low-spin” or  $J_{ex} > \Delta_C$  in the “high-spin” configurations, respectively.

If the manganese cation is coordinated in a square-pyramid, as is the case for the  $Mn^{3+}$  cation in oxygen-deficient  $AMnO_{3-\delta}$ , the lower symmetry breaks the degeneracy of the 3d states even further.

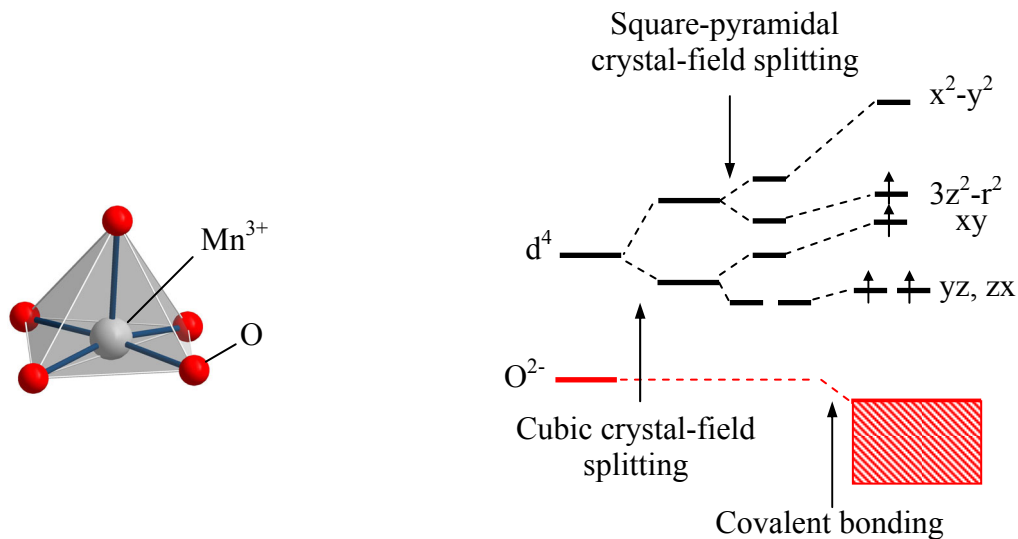


Figure 2.13: Schematic energy splittings and for a  $Mn^{3+}$  cation in square-pyramidal coordination.

The crystal-field wavefunctions of the square-pyramidal coordination have the same orbital symmetry as the octahedral coordination. The difference between the two is that the absence of one of the apical oxygen in the square-pyramidal coordination changes the crystal field and reduces the covalent bonding for the  $3z^2-r^2$ ,  $yz$ , and  $zx$  orbitals.

For the hexagonal perovskite manganites, a different basis is used for the crystal-field wavefunctions of  $\text{Mn}^{3+}$  cations coordinated in trigonal-bipyramids.

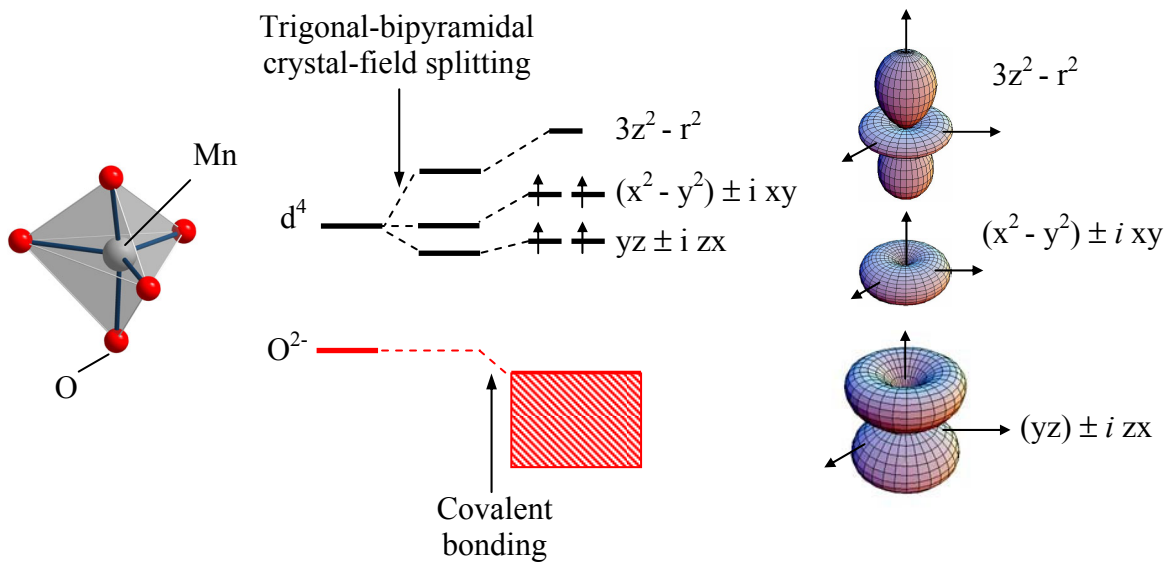


Figure 2.14: Energy splittings and crystal-field wavefunctions for a manganese cation in trigonal-bipyramidal coordination.

For the case of octahedral coordination, the total-cubic field splitting is equivalent to:

$$\Delta_C = \Delta_{ionic} + \Delta\epsilon_\sigma - \Delta\epsilon_\pi \quad (2.1)$$

Here,  $\Delta_{ionic}$  is the small electrostatic splitting and the  $\Delta\epsilon_\sigma$  and  $\Delta\epsilon_\pi$  terms are the  $3d - 2p$  hybridization energies for  $\sigma$ -bonding and  $\pi$ -bonding, respectively.

The hybridization energies are given by second-order perturbation theory:

$$\Delta\mathcal{E}_{ij} = \frac{b_{ij}^2}{E_p} = \frac{\langle\psi_i|H|\psi_j\rangle^2}{E_p} \quad (2.2)$$

$E_p$  is the difference in energy between the Mn-3d state ( $\psi_i$ ) and O-2p state ( $\psi_j$ ). The resonance integral is abbreviated as  $b_{ij}$  and is also referred to as the spin-independent hopping parameter. The spin-dependent resonance integral  $t_{ij}$  takes into account the angle between the spins on sites  $i$  and  $j$   $\theta_{ij}$ :

$$t_{ij} = b_{ij} \left[ \cos\left(\frac{\theta_{ij}}{2}\right) + \sin\left(\frac{\theta_{ij}}{2}\right) \right] \quad (2.3)$$

The hopping parameter is proportional to the orbital overlap of the wavefunctions, so that in the distorted perovskites, a bending angle  $\phi$  between the two wavefunctions will decrease the sigma-bonding resonance integral by a factor of  $\cos(\phi)$  (Harrison 2004).

### 2.2.1 Tight-binding model

The tight-binding Hamiltonian assumes that a charge carrier spends most of its time on the atom at position  $\vec{R}$  and tunnels to neighboring atoms located at  $\vec{R} + \vec{\delta}$ ; the resonance integral  $t_{ij}$  is the expectation value of the tunneling between the neighbors. In Dirac notation the Hamiltonian is given by:

$$H_{TB} = \sum_{\vec{R}, \vec{\delta}} \frac{t_{ij}}{2} \left( |\vec{R}\rangle\langle\vec{R} + \vec{\delta}| + |\vec{R} + \vec{\delta}\rangle\langle\vec{R}| \right) + \sum_{\vec{R}} V |\vec{R}\rangle\langle\vec{R}| = E |\vec{R}\rangle\langle\vec{R}| \quad (2.4)$$

Here, the first term is the kinetic energy and the second term is the potential energy;  $\vec{R}$  is the cation position and  $\vec{\delta}$  is the displacement vector from  $\vec{R}$  to a nearest neighbor. Exact solutions of the tight-binding Hamiltonian can be found by applying Bloch's theorem to diagonalize the Hamiltonian.

$$|\vec{R} + \vec{\delta}\rangle = e^{i\vec{k} \cdot \vec{\delta}} |\vec{R}\rangle \quad (2.5a)$$

$$H_{TB} = \sum_{\vec{R}, \vec{\delta}} \left[ t_{ij} \cos(\vec{k} \cdot \vec{\delta}) + V \right] |\vec{R}\rangle \langle \vec{R}| \quad (2.5b)$$

Taking the sum over  $z$  nearest neighbors gives the width of the band  $W_b$  created by near-neighbor hopping.

$$W_b = 2 z t_{ij} \quad (2.6)$$

### 2.2.2 Jahn-Teller effect

In orthorhombic  $\text{RMnO}_3$  with an  $\text{R}^{3+}$  lanthanide-ion, the manganese cation is in the high-spin 3+ valence state and its single  $e_g$  electron can occupy either the  $|x^2-y^2, \uparrow\rangle$  or  $|3z^2-r^2, \uparrow\rangle$  orbitals. This orbital degeneracy creates a structural instability because the electron energy is lowered by cooperative displacements of the  $\text{O}^{2-}$  anions. The cooperative displacements soften as the temperature is decreased; below a critical temperature ( $T_{JT}$ ), the displacements become static and distort all of the octahedra in a cooperative manner. The cooperative displacements order the occupied  $e_g$  orbitals of neighboring sites into the  $|3x^2-r^2, \uparrow\rangle$  and  $|3y^2-r^2, \uparrow\rangle$ , respectively. The ordering gives rise to ferromagnetic interactions within the (0 0 1) planes and the  $t_{2g}$  interactions couple the (0 0 1) planes antiferromagnetically.

To illustrate the importance of the Jahn-Teller distortion on the electronic band structure, the  $e_g$ -bands of  $\text{LaMnO}_3$  were calculated with and without the Jahn-Teller distortion according to the tight-binding formalism of Ahn and Millis (Ahn and Millis 2000); the results are plotted in Figure 2.15.

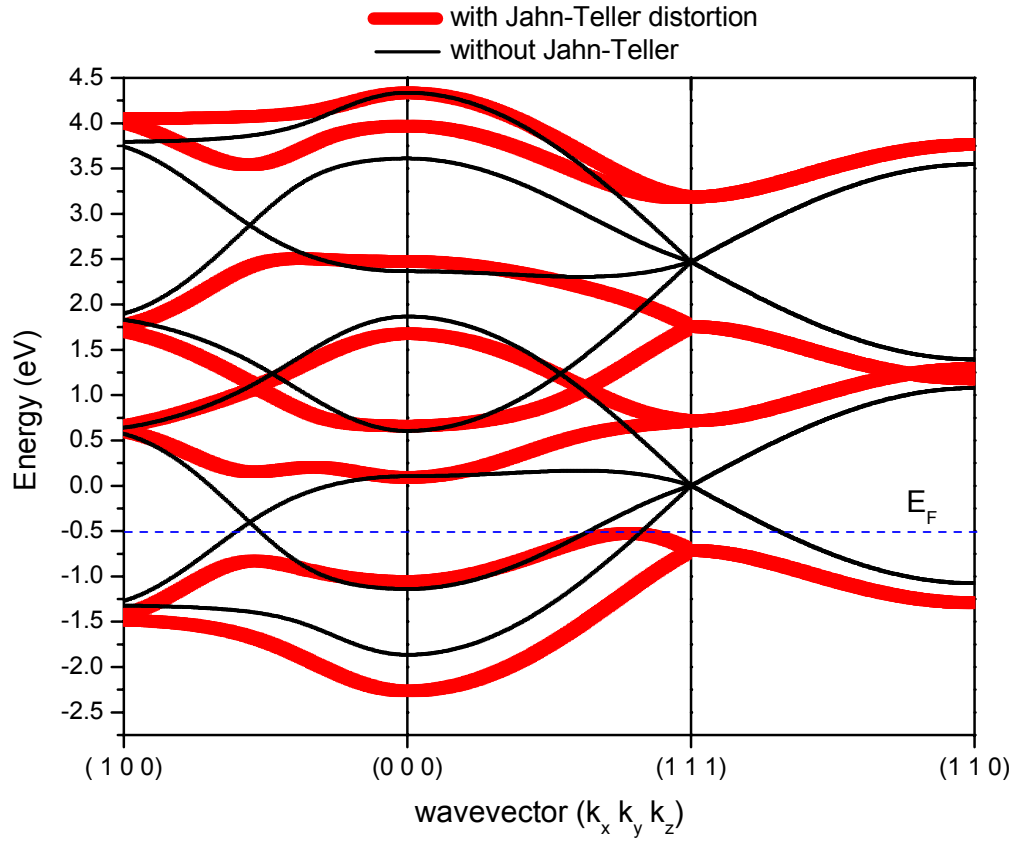


Figure 2.15: Electronic band diagram for the  $e_g$  states of  $\text{LaMnO}_3$  with and without the Jahn-Teller distortion.

If the Jahn-Teller distortion is excluded, there is significant overlap between the  $\text{Mn}^{4+}/\text{Mn}^{3+}$  and  $\text{Mn}^{3+}/\text{Mn}^{2+}$  redox couples ( $U_H \approx W_b$ ), where  $W_b$  is the bandwidth of the redox couples; if the Jahn-Teller distortion is included, a gap between the couples opens up. The opening of the bandgap makes the Jahn-Teller transition in  $\text{RMnO}_3$  ( $\text{R}^{3+}$ ) a metal-insulator transition. In addition to changing the electronic properties, the orbital-ordering changes the magnetic exchange interactions from 3D-ferromagnetic to 2D-ferromagnetic (0 0 1) planes coupled antiferromagnetically.

## **Chapter 3: Supporting Experiments**

This chapter reviews the experiments that are used to complement the impedance measurements in our investigation of the dielectric behavior of the manganese-perovskite oxides: iodimetric titration, thermoelectric power, DC-conductivity, magnetometry, and powder X-ray diffraction.

### **3.1 IODIMETRIC TITRATION**

The physical properties of manganese oxides are critically dependent on their oxygen stoichiometry. Obtaining reliable information about the oxygen stoichiometry by X-ray diffraction is not practical due to the small scattering factor of oxide ions. For large oxygen deviations, it is possible to use thermal gravimetric analysis to measure the mass difference during an oxidation/reduction; however, this method requires a very stable, high-precision balance as well as knowledge of the stoichiometry either before or after the experiment.

Iodimetric titration, on the other hand, only requires known information of the chemical formula and mole ratio of the metal ions. With this information, the valence state of the metal ions and also the oxygen content can be determined by performing a controlled oxidation/reduction reaction. As a matter of vocabulary, the unknown in the reaction is referred to as the titrant and the known reactant as the titer.

Designing a good titration is straightforward, but not trivial. The accuracy and precision are limited by the chemistry of the materials being used, the available amount of sample, as well as the chemist's control of adding titer to titrant.

For the manganese oxides, iodimetric titration is often used for the following reasons: a) iodine's intense color makes determining the endpoint easier and b) the

oxidation of iodide anions by  $Mn^{3+}/Mn^{4+}$ , to form iodine, is energetically favorable in an acidic aqueous solution according to the reaction:



### 3.1.1 Procedure

First a titer of known concentration is prepared. For iodimetric titration, the reducing agent sodium thiosulfate ( $Na_2(S_2O_3)$ ) is typically used. To determine the needed concentration, it was necessary to take into account the amount of sample available and the volume of titer desired to complete the reaction. For example, titrating 40 mg of  $CaMnO_3$  with 20 ml of titer required the following:



$$\frac{40mg \text{ } CaMnO_3}{143g/mol} \times \frac{2 \text{ mol } (S_2O_3)^{2-}}{20ml} \approx 0.028 \text{ M } Na_2(S_2O_3) \quad (5.2c)$$

$Na_2(S_2O_3)$  is hygroscopic and needs to be standardized to determine its concentration in solution; in other words, a weighed amount of solid has an unknown amount of absorbed water. The effective molarity of the titer was established by titrating into a titrant with known quantity of  $I_2$ . The known quantity of  $I_2$  was created by oxidizing  $I^-$  solution with a stable compound of known oxidation state, typically  $K_2Cr_2O_7$  ( $Cr^{6+}$ ) or  $KMnO_4$  ( $Mn^{7+}$ ). A starch indicator was used to maximize the contrast of solution color slightly before and slightly after the endpoint has been reached. Table 3.1 below is an example of a  $Na_2S_2O_3$  titer standardization with 25 ml of 0.002 M  $K_2Cr_2O_7$  solution.



Table 3.1: Example of the results of a standardization of  $\text{Na}_2\text{S}_2\text{O}_3$  titer solution with  $\text{K}_2\text{CrO}_7$ .

	<b>Volume</b>	<b>Molarity</b>
1	14.78	0.02037
2	14.67	0.02052
3	14.65	0.02055
4	14.76	0.02040
5	14.72	0.02045
	average	<b>0.02047</b>
	std dev	0.0008
	student-t error (95%)	0.0010

After standardizing the titer, accurate weights of the sample mass were added to an excess of KI. Water was added so that the titer was not greater than 50% of the final volume. Then acid was added and the solution was swished until the sample was fully dissolved; the solution was titrated immediately. The solubility of the sample in acidic iodide solution is incredibly important; if the sample cannot readily dissolve, performing an accurate titration is not possible. The presence of iodide ions in solution aided the dissolution. Also, the volatility of  $\text{I}_2$  increased with the acidity of the solution; the normality of the sample solution was kept less than 0.5 N to minimize the  $\text{I}_2$  volatility. I have had success making 100 ml solutions with approximately 40 mg of sample, 1g of KI, and 3 ml of HCl.

### 3.1.2 Endpoint

As mentioned in the previous section, the endpoint is defined as the volume at which the indicator color is completely absent from the solution. After some practice, it

is generally straightforward to observe the endpoint and the results should be repeatable if all has been performed correctly. Since the iodimetric titration is a reduction-oxidation reaction, it is possible to observe the endpoint by monitoring the solution potential. Using an *Oakton* ORP platinum-band electrode, the endpoint was determined for a titer standardization with  $\text{K}_2\text{Cr}_2\text{O}_7$  and  $\text{MnO}_2$ .

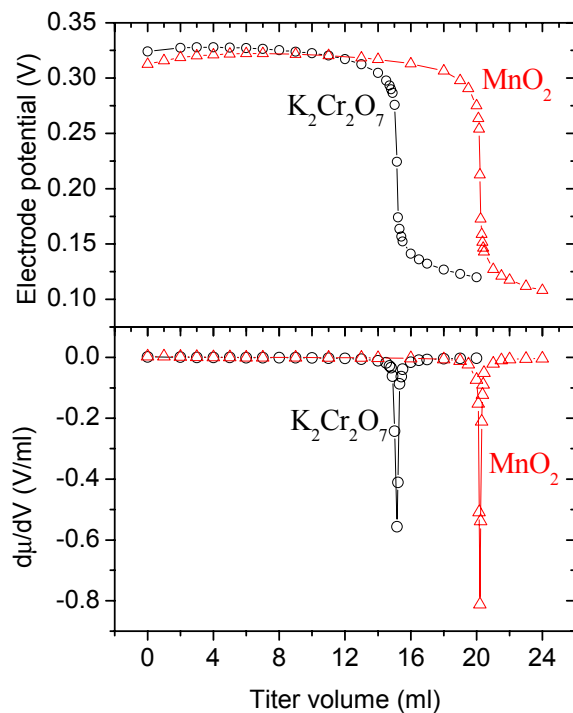


Figure 3.1: Iodimetric titration using an oxidation-reduction electrode to determine the endpoint.

### 3.1.3 Example

For a sample of  $\text{SrMnO}_{3-\delta}$  with mass ( $m$ ), a volume ( $V$ ) of a titer with molarity ( $M$ ) is required to reach the endpoint of the iodine reduction. If  $P$  is the molar mass of  $\text{SrMnO}_3$  and  $P_O$  is the molar mass of oxygen, the number of oxide-ion vacancies can be solved for by writing the charge balance and mass balance equation in terms of  $\delta$ . Table 3.2 lists the relevant formulas, reactions, and equations needed to solve for  $\delta$ .

Table 3.2: List of expressions needed to determine the number of oxygen vacancies in  $\text{SrMnO}_{3-\delta}$  by iodimetric titration.

Chemical Formula	$\text{SrMn}_{1-x}^{4+}\text{Mn}_x^{3+}\text{O}_{3-\delta}$
Charge Balance	$x = 2\delta$
Iodide oxidation reaction	$(1-x)\text{Mn}^{4+} + x\text{Mn}^{3+} + (2-x)\text{I}^- \rightarrow \text{Mn}^{2+} + \frac{(2-x)}{2}\text{I}_2$
Iodine reduction reaction	$2(\text{S}_2\text{O}_3)^{2-} + \text{I}_2 \rightarrow (\text{S}_4\text{O}_6)^{2-} + 2\text{I}^-$
Mass Balance	$m = \frac{MV(P - P_o)\delta}{2(1-\delta)}$

As with most experiments, it is important to perform multiple trials to be able to determine the magnitude of the experimental error. Table 3.3 lists the results of a titration of five trials performed on the same  $\text{SrMnO}_{3-\delta}$  sample with  $\delta = 0.05 \pm 0.004$ .

Table 3.3: Number of oxygen vacancies ( $\delta$ ) in  $\text{SrMnO}_{3-\delta}$  determined by iodimetric titration.

$M(\text{Na}_2\text{S}_2\text{O}_4) = 0.0198 \text{ [mol/l]}$		$P(\text{SrMnO}_3) = 190.5562 \text{ [g/mol]}$	
trial	$m(\text{SrMnO}_3) \text{ [mg]}$	$V(\text{Na}_2\text{S}_2\text{O}_3) \text{ [ml]}$	$\delta$
1	41.4	20.85	0.0564
2	41.8	21.21	0.0487
3	40.3	20.42	0.0502
4	41.1	20.87	0.0480
5	41.3	20.9	0.0515
average			<b>0.051</b>
stdev			0.003
student-t error 95%			0.004

### 3.1.4 Error

For both the titer standardization and the sample titration, five trials were performed to ensure statistically accurate answers. The random error of the experiment leads to relative errors less than 10%. However, there are other sources of error (the sample mass, the titer volume reading, and the measured titer molarity) that propagate into the measurement and should be considered before quoting an error bar. The following estimation takes into account the error from these three sources with the Taylor expansion method used to calculate the error.

$$\delta = 2 - \frac{MVP}{m}, \delta \ll 1 \quad (5.3a)$$

$$\Delta\delta = \left| \frac{VP}{m} \right| \Delta M + \left| \frac{MP}{m} \right| \Delta V + \left| \frac{MVP}{m^2} \right| \Delta m \quad (5.3b)$$

$$\begin{aligned} \Delta\delta \approx & \left| \frac{(20 \text{ ml})(200 \text{ g/mol})}{(40 \text{ mg})} \right| (0.0002 \text{ mol/l}) + \\ & \left| \frac{(0.02 \text{ mol/l})(200 \text{ g/mol})}{(40 \text{ mg})} \right| (0.05 \text{ ml}) + \\ & \left| \frac{(0.02 \text{ mol/l})(20 \text{ ml})(200 \text{ g/mol})}{(40 \text{ mg})^2} \right| (0.1 \text{ mg}) \end{aligned}$$

$$\Delta\delta \approx 0.02 + 0.005 + 0.005$$

This rough estimation shows that the error could possibly be as large as 0.03 or 60% relative error; this calculation shows how critical the titration standardization is to the overall error. My opinion is that this calculation is an overestimation of the error and a good estimation of the error  $\Delta\delta$  is 0.01.

### **3.2 THERMOELECTRIC POWER SEEBECK EFFECT MEASUREMENTS**

The Seebeck effect produces an equilibrium potential in response to a thermal gradient.

#### **3.2.1 Measurement hardware**

Measuring the Seebeck effect requires temperature control on both sides of the temperature gradient as well as the ability to measure the potential between the sample contacts. Two Lakeshore 805 temperature controllers control the temperature and monitor the 4-point resistance of two calibrated, semiconducting diodes; the diodes were mounted to the brass sample contacts on the high-temperature side and low-temperature side, respectively. The Seebeck voltage was measured by a Hewlett Packard 3478A multimeter. The Lakeshore 805s supplied current to two wire-wrapped boron-nitride heaters to increase the temperature of each side of the sample independently. The electronic hardware (temperature controllers and multimeter) were controlled with an IBM PS/2 model 30 PC running a program sequence written in the BASICA software language.

#### **3.2.2 Measurement technique**

The Seebeck-effect measurement always includes the thermoelectric voltage of the wires connecting in addition to the sample. Figure 3.2 illustrates the temperature gradient across sample that leads to a gradient across the wires.

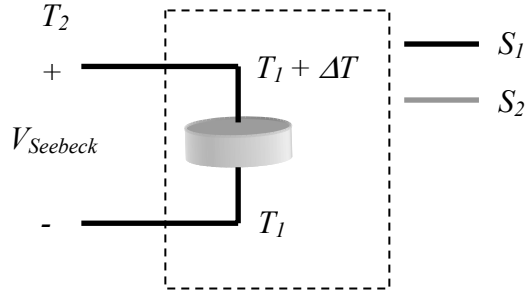


Figure 3.2: Illustration of the temperature gradient across a sample; the gradient produces a potential that includes a contribution from the wires as well as the sample.

The absolute thermoelectric potentials from the wires and the sample, respectively, can be determined by integrating the Seebeck coefficient over the temperature gradient:

$$\begin{aligned} \int S dT &= \int_{T_2}^{T_1+\Delta T} S_1 dT + \int_{T_1+\Delta T}^{T_1} S_2 dT + \int_{T_1}^{T_2} S_1 dT \\ &= \int_{T_1+\Delta T}^{T_1} S_2 dT - \int_{T_1+\Delta T}^{T_1} S_1 dT \end{aligned} \quad (3.4)$$

With this relationship, the wire contribution to the thermoelectric potential can be subtracted to give the absolute thermoelectric power of the sample. The contribution of the copper wires to the total Seebeck voltage was removed by using the absolute thermoelectric power for copper determined by Cusack and Kendall (Cusack and Kendall 1958). Their data were fit to a linear model and added to the total measured value to obtain the absolute thermoelectric power for the unknown sample  $S_2$ .

$$\begin{aligned}
S_2 &= S + S_1 \\
&= S + 0.30884 + 0.0050606 \cdot T
\end{aligned}
\tag{3.5}$$

The linear fit is sufficient for modeling the absolute thermoelectric power for temperatures above 150 K. Below 150 K, the phonon drag contribution to the thermoelectric power of the copper wires results in a deviation from the linear model. However, all the samples measured in this work were insulating and had large thermoelectric-power voltages; the contribution of the copper wires to the total thermoelectric-power voltage is less than 1.5  $\mu\text{V/K}$ , which is less than 1%. If greater accuracy were needed, the thermoelectric contribution of the copper wires in the low-temperature Seebeck-coefficient measurement system could be determined experimentally by measuring superconducting  $\text{YB}_2\text{Cu}_3\text{O}_7$  (YBCO). The thermoelectric power of a superconductor is zero; therefore, the measured voltage is the product of the contacting wires exclusively. YBCO is superconducting below 92 K; so the absolute thermoelectric power of the wires could be determined explicitly for all temperatures below 92 K.

### 3.3 DC CONDUCTIVITY

#### 3.3.1 Measurement hardware

The DC conductivity was obtained by forcing a current with a *Keithley* 224 programmable current source and measuring the voltage drop across the sample with either a *Keithley* 181 nanovoltmeter or *Keithley* 617 programmable electrometer. The temperature was controlled by a *Lakeshore* 340 temperature controller that monitors the voltage of a calibrated Si-diode excited by a current of 10  $\mu\text{A}$ . Cryogenic temperatures were achieved by using a *Daikin* closed-cycle helium compressor and expander. The

sample was placed in a Cu holder that was mounted to a 2-stage *Daikin* expander. The 2<sup>nd</sup> stage was covered with a Cu radiant heat shield and both stages are enclosed in a vacuum shroud sealed with two O-rings. The shroud was evacuated with an *Edwards* turbo pump backed by a *VRC* rotary-vane pump, and the pressure was monitored with a thermocouple gauge, ion-gauge, and *Lesker* IG4400 ionization gauge controller. The entire setup was computer controlled via a  *GPIB* interface with a PC running *Labview* software.

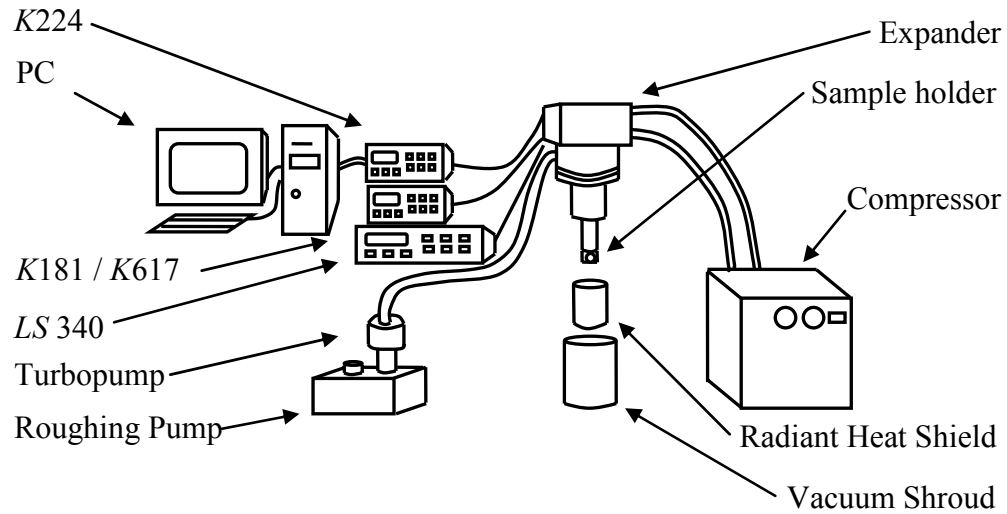


Figure 3.3: Sketch of the cryogenic system, control hardware, and measurement instruments for measuring DC-resistivity as a function of temperature.

### 3.3.2 Measurement techniques

The measurement was typically performed with the 4-point contact sample geometry to eliminate the contribution of the contact resistance. The sample is measured with current flowing in the forward and then reverse direction to eliminate the contribution of a contact potential offset.



### 3.3.3 Voltmeter loading

The primary assumption of either a two-point or four-point resistance measurement is that all the forced current flows through the sample. This assumption breaks down as the sample resistance becomes comparable to the input resistance of the voltmeter. For high-resistance samples, the *Keithley* 617 programmable electrometer was preferred over the more precise *Keithley* 181 nanovoltmeter for its larger input resistance; The K617 has an input resistance greater than 200 T $\Omega$  (K617 manual) whereas the input of the K181 is greater than 1 G $\Omega$  (K181 manual).

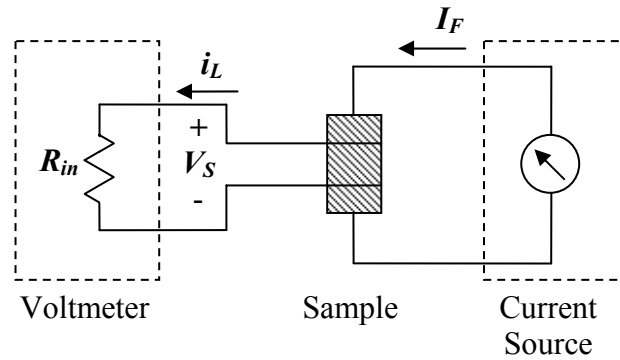


Figure 3.4: Sketch illustrating current loading when  $R_{\text{sample}} \approx R_{\text{in}}$  while measuring DC-resistivity.

## 3.4 MAGNETIC MEASUREMENTS

Magnetic measurements were made in a *Quantum Design* magnetic-property measuring system (MPMS) DC magnetometer. The MPMS uses a superconducting quantum interference device (SQUID) to measure the magnetization of small pieces of single crystal or small pellets of polycrystalline powder over a temperature range of 2 K to 400 K and in magnetic fields from 0 to 5.5 Tesla.

The primary system components of the SQUID are contained in a large liquid-He dewar to cool the superconducting solenoid and sample space. The superconducting

solenoid-magnet surrounds the evacuated measurement space and the sensing-coils of the SQUID circuit. At the base of the measurement space, a germanium thermometer measures the temperature from 1.9 K to 40 K and a platinum thermometer measures from 40 K to 400 K; the output of the thermometers are fed-back into a temperature control system that controls the volume and temperature of He gas released from the reservoir to maintain a temperature setpoint. A PC with MPMS software is used to set temperature and magnetic setpoints, write programs for temperature and field scans, and record the data.

During a measurement, the sample was scanned through the measurement space, inducing a voltage in the sensing-coil that is proportional to the flux created by the sample magnetization. The result of the scan was a voltage versus position data-set that was fit to the dipole equation to calculate the magnetic induction of the sample and the fitting error. The temperature, magnetic field, and magnetization fitting data were all output to an ASCII text file.

### **3.5 POWDER X-RAY DIFFRACTION**

Sample preparation for the powder X-ray diffraction measurements consisted of grinding about 25 mg – 50 mg of sample into fine powder and mixing the powder with pentyl acetate on a glass slide; after the pentyl acetate dries, the powder adheres to the slide.

Two different diffractometers were used to make the X-ray diffraction measurements presented in this dissertation. The first instrument was a *Philips* PW1720 X-ray generator with two  $\theta$ - $2\theta$  goniometers that allow for two samples to be measured simultaneously. The goniometers are equipped with metal clips to hold the glass slides in the center of the diffraction circle and a scintillation detector converted the diffracted radiation to a voltage signal. The  $2\theta$  scan-range, step-width, and step duration were input

on a PC running the *Philips Datascan* software. The PW1720 powers a Cu anode for X-ray generation and diffraction patterns revealed that there is some tungsten poisoning of the Cu-tube from the tungsten filament cathode. The sputtered tungsten generates W-L $\alpha$  radiation in addition to the Cu-K $\alpha$  radiation; this radiation shows up in the diffraction pattern as low-intensity peaks to the low-angle side of a high-intensity Cu-K $\alpha$  peaks.

The second diffractometer was a *Philips Xpert* equipped with a Cu X-ray tube, a  $\theta$ -2 $\theta$  goniometer, and a Xe-gas “proportional detector.” The *Xpert* showed no evidence of tungsten-poisoning of the Cu X-ray tube.

The intensity versus 2 $\theta$  angle data was analyzed using the *JADE-7 XRD Pattern Processing* software. The *JADE-7* software enabled the X-ray pattern to be compared to other patterns stored in the powder-diffraction file (PDF) database. The software is also equipped with numerous analysis functions that can remove the background, fit the pattern’s peaks, and calculate the cell parameters for a given space group.

## Chapter 4: Impedance Measurements

This chapter surveys the basic physics of electric polarization. The derivations of several important relations are sketched out because they are referred to frequently throughout this work. The various polarizing mechanisms are reviewed as is the phenomenology of modeling dielectric relaxations with circuit elements. Finally, the chapter concludes with a discussion of the techniques used to measure the impedance and the measurement limitations.

### 4.1 POLARIZATION IN STATIC FIELDS

In vacuum, the charge between two parallel plates creates an electric field perpendicular to the plates. Placing a polarizing material in between the plates reduces the magnitude of the electric field.

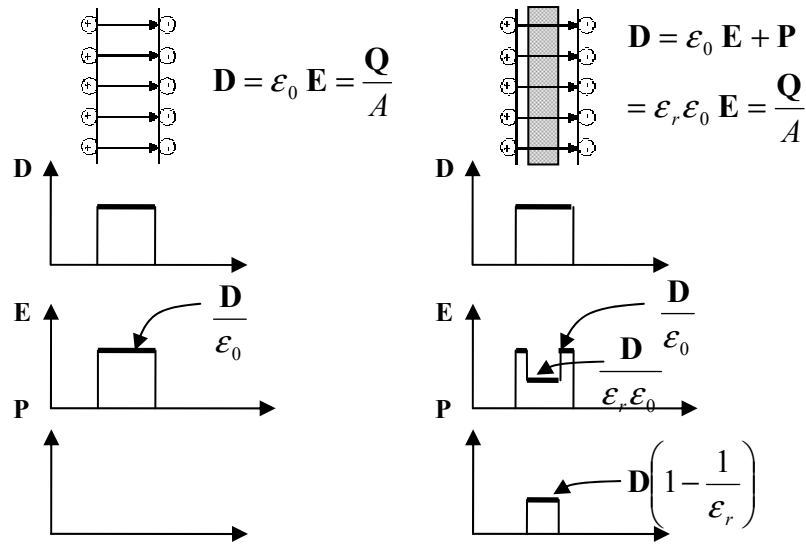


Figure 4.1: Relationship between the electric displacement, electric field, and polarization for a parallel-plate capacitor without and with a dielectric interior (Polnus 1978).

## 4.2 POLARIZATION IN TIME-DEPENDENT FIELDS

The transient response of a polarizing material subjected to an external field is typically an instantaneous jump in the polarization followed by an increasing monotonic rise toward the static value.

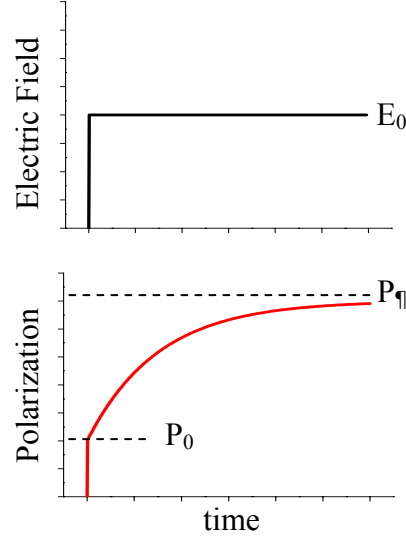


Figure 4.2: Increase in the polarization due to an applied field.

To first order, the time-dependent response can be considered an exponential function. After turning on the field, the polarization response is characterized by:

$$\mathbf{P} = \mathbf{P}_\infty + (\mathbf{P}_0 - \mathbf{P}_\infty) \left[ 1 - \exp\left(\frac{-t}{\tau}\right) \right] \quad (4.1a)$$

$$= (\epsilon_\infty - 1)\epsilon_0 \mathbf{E} + (\epsilon_s - \epsilon_\infty)\epsilon_0 \mathbf{E} \left[ 1 - \exp\left(\frac{-t}{\tau}\right) \right] \quad (4.1b)$$

Here  $\epsilon_\infty$  and  $\epsilon_s$  are the dielectric constant at high-frequency conditions and static conditions, respectively.

### 4.2.1 The Debye equations

The exponential increase in polarization introduces a lag time into the steady-state response to an oscillating field. The response lag time corresponds to a polarization component that is  $\pi/2$  radians out of phase with the applied field and coefficients that are dependent on the characteristic relaxation time  $\tau$  and the applied-field frequency ( $\omega$ ). The time-dependent response of the polarization is derived by integrating the product of the exponentially increasing function and the sinusoidal field.

$$\mathbf{E} = \mathbf{E}_0 \cos(\omega t) = \text{Re}(\exp(j \omega t)) \quad (4.2)$$

$$d\mathbf{P}(t-x) = (\epsilon_\infty - 1)\epsilon_0 d\mathbf{E}(t-x) + (\epsilon_s - \epsilon_\infty)\epsilon_0 \left[ 1 - \exp\left(-\frac{(t-x)}{\tau}\right) \right] d\mathbf{E}(x) \quad (4.3a)$$

$$\mathbf{P}(t) = (\epsilon_\infty - 1)\epsilon_0 \mathbf{E}_0 \cos(\omega t) + \frac{(\epsilon_s - \epsilon_\infty)\epsilon_0 \mathbf{E}_0}{\tau} \text{Re} \left[ \int_{-\infty}^t \exp(j \omega t) \exp\left(-\frac{(t-x)}{\tau}\right) dx \right] \quad (4.3b)$$

$$\mathbf{P}(t) = (\epsilon_\infty - 1)\epsilon_0 \mathbf{E}_0 \cos(\omega t) + \frac{(\epsilon_s - \epsilon_\infty)\epsilon_0 \mathbf{E}_0}{1 + \omega^2 \tau^2} [\cos(\omega t) + \omega \tau \sin(\omega t)] \quad (4.3c)$$

If the relationship between the electric polarization, electric field and the electric displacement is used and a complex dielectric constant is assumed, then Equation 4.3c can be rewritten in terms of the real and imaginary part of the dielectric constant.

$$\mathbf{D} = \epsilon_0 \mathbf{E} + \mathbf{P} \quad (4.4a)$$

$$= \text{Re}[(\epsilon' - j\epsilon'')\mathbf{E}_0 \exp(j\omega t)] \quad (4.4b)$$

$$= \epsilon_0 \mathbf{E}_0 [\epsilon' \cos(\omega t) + \epsilon'' \sin(\omega t)] \quad (4.4c)$$

Comparing Equation 4.4c with 4.3c, it follows that:

$$\epsilon'(\omega) = \epsilon_\infty + \frac{(\epsilon_s - \epsilon_\infty)}{1 + \omega^2 \tau^2} \quad (4.5a)$$

$$\epsilon''(\omega) = \frac{(\epsilon_s - \epsilon_\infty) \omega \tau}{1 + \omega^2 \tau^2} \quad (4.5b)$$

These relationships are referred to as the Debye equations; they are frequently used to characterize dielectric relaxations. The relaxations are illustrated graphically in Bode plots to show the frequency relationship and in Nyquist plots to show the relationship between the real and imaginary components.

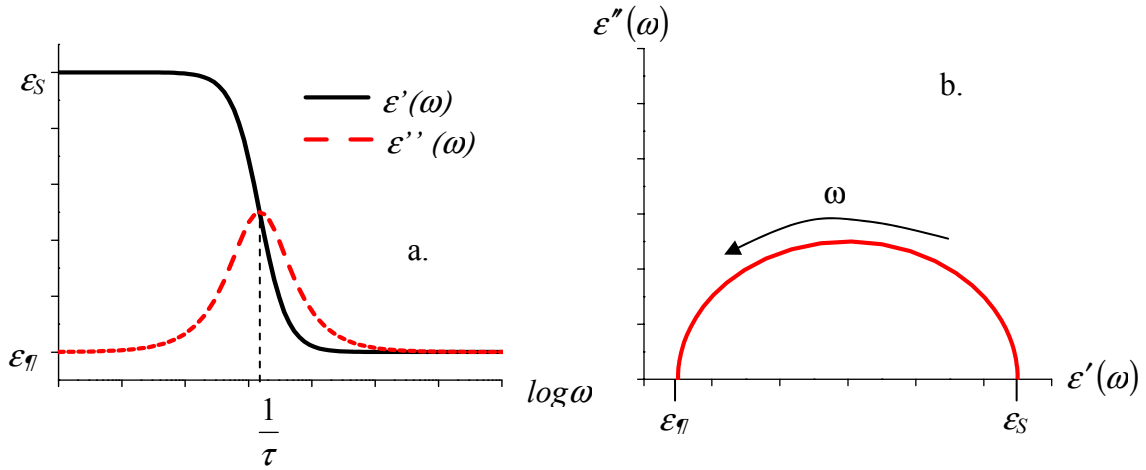


Figure 4.3: Bode plot (a) and Nyquist plot (b) exhibiting the dielectric relaxations of Debye equations.

#### 4.2.2 The Kramers-Kronig relations

The Debye equations are the steady-state solutions for a polarizing material with an exponential response to an electric field. Although many materials have been characterized by the Debye equations, most materials have more complicated response functions that do not have a simple analytical formula. However, re-deriving the dielectric response equations with the assumption of a general response function  $\alpha(t)$  and using the Fourier theorem to invert the result yields an important relationship: the real and imaginary parts of the dielectric constant are connected and one can be determined by measuring the other. The derivation begins by using an oscillating electric field  $\mathbf{E}$  and calculating the electric displacement  $\mathbf{D}$  of a material with an electric response function  $\alpha(t)$ .

$$\begin{aligned} \mathbf{D}(t) = & \epsilon_{\infty} \epsilon_0 \mathbf{E}_0 \cos(\omega t) + \\ & \epsilon_0 (\epsilon_s - \epsilon_{\infty}) \mathbf{E}_0 \int_0^{\infty} \alpha(x) \cos(\omega(t-x)) dx \end{aligned} \quad (4.6a)$$

$$\begin{aligned} = & \epsilon_{\infty} \epsilon_0 \mathbf{E}_0 \cos(\omega t) + \\ & \epsilon_0 (\epsilon_s - \epsilon_{\infty}) \mathbf{E}_0 \cos(\omega t) \int_0^{\infty} \alpha(x) \cos(\omega x) dx + \\ & \epsilon_0 (\epsilon_s - \epsilon_{\infty}) \mathbf{E}_0 \sin(\omega t) \int_0^{\infty} \alpha(x) \sin(\omega x) dx \end{aligned} \quad (4.6b)$$

Then, by using equation 4.4c the expression can be simplified to yield the real and imaginary components of the dielectric constant.

$$\epsilon'(\omega) = \epsilon_{\infty} + (\epsilon_s - \epsilon_{\infty}) \int_0^{\infty} \alpha(x) \cos(\omega x) dx \quad (4.7a)$$

$$\epsilon''(\omega) = (\epsilon_s - \epsilon_{\infty}) \int_0^{\infty} \alpha(x) \sin(\omega x) dx \quad (4.7b)$$



The real and imaginary components of the dielectric constant can be inverted by using Fourier's theorem to produce expressions for the response function  $\alpha(x)$ .

$$\alpha(x) = \frac{2}{\pi} \int_0^{\infty} \frac{(\epsilon'(\mu) - \epsilon_{\infty})}{(\epsilon_s - \epsilon_{\infty})} \cos(\mu x) d\mu \quad (4.8a)$$

$$\alpha(x) = \frac{2}{\pi} \int_0^{\infty} \frac{\epsilon''(\mu)}{(\epsilon_s - \epsilon_{\infty})} \sin(\mu x) d\mu \quad (4.9a)$$

Substituting  $\alpha(x)$  back into the expressions for  $\epsilon'(\omega)$  and  $\epsilon''(\omega)$  and integrating with respect to  $x$  gives the real and imaginary components in terms of one another.

$$\epsilon'(\omega) = \epsilon_{\infty} + \frac{2}{\pi} \lim_{R \rightarrow \infty} \int_0^{\infty} \epsilon''(\mu) \frac{1}{2} \left( \frac{1 - \cos((\mu + \omega)R)}{\mu + \omega} + \frac{1 - \cos((\mu - \omega)R)}{\mu - \omega} \right) d\mu \quad (4.10a)$$

$$\epsilon'(\omega) = \epsilon_{\infty} + \frac{2}{\pi} \int_0^{\infty} \epsilon''(\mu) \frac{\mu}{\mu^2 - \omega^2} d\mu \quad (4.10b)$$

$$\epsilon''(\omega) = \frac{2}{\pi} \int_0^{\infty} (\epsilon'(\mu) - \epsilon_{\infty}) \frac{\omega}{\omega^2 - \mu^2} d\mu \quad (4.11)$$

These integrals connecting the real part of the dielectric constant to the imaginary part are called the Kramers-Kronig relations. They are important relationships in Physics; their application can be generalized to include the real and imaginary frequency components of all linear responses to an oscillatory forcing function.

### 4.3 POLARIZING MECHANISMS

The seemingly instantaneous rise in the polarization is attributed to fast polarizing mechanisms whereas the exponential increase is due to the slowest polarization mechanism. Plotting the same response on a broad logarithmic time scale reveals the multiple polarization mechanisms that occur in solids.

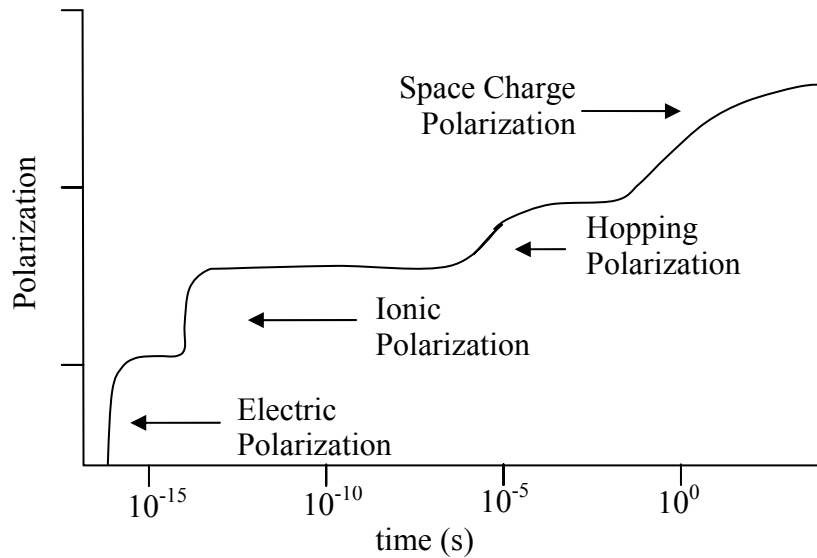


Figure 4.4: Various polarization contributions during the transient response (Kao 2004).

The types of polarization mechanisms can be grouped into two categories: relaxation polarizations and resonant polarizations. For solids, the relaxation polarizations consist of space-charge polarization and hopping polarization. The resonant polarizations are ionic and electric. The polarizations are active over a broad range of the frequency spectrum, and a variety of experimental techniques are required to characterize their behavior. Often the type of experimental technique used to measure the polarization or dielectric behavior operates over a narrow frequency range and thus can only measure one type of polarization mechanism. Thus the polarization mechanism is often associated with the measurement technique or frequency range.

#### **4.3.1 Space-charge polarization**

Space-charge polarization occurs at the interface of materials. The chemical potential difference at the boundary leads to charge transfer that depletes or accumulates charge at the interface. Charge transfer is common across semiconductor-metal junctions and electrochemical interfaces; interfacial defects and traps also lead to the formation of a space-charge layer. In Figure 4.4, the space-charge polarization has a broad range of response times that come from the variety of charge carriers; ions and ion vacancies are charge carriers with large masses and therefore much longer response times than much lighter electron and hole charge carriers. In fact, the space-charge regions in semiconductors can be quite fast and are used in high-speed electronic bipolar transistors and diodes.

When investigating the dielectric effects of materials with a capacitor configuration, it is important to be aware of the contribution of the space-charge region at the interfaces; as Lunkenheimer *et al.* have pointed out, in most cases the observation of a very large dielectric response is of extrinsic origin (Lunkenheimer et al. 2002).

#### **4.3.2 Hopping polarization**

Hopping polarization, like space-charge polarization, is also a relaxation mechanism created by defects. However, hopping polarization originates from charge carriers that are localized at defects in the bulk. The charge carriers are thermally excited to neighboring localized states; in the presence of an electric field, the distribution of carriers in neighboring states is altered to give a net polarization.

The first hopping-polarization studies were aimed at explaining the low-temperature conduction in compensation-doped elemental semiconductors Si and Ge; the experiments and theory of Pollak and Geballe and later Golin showed that the hopping

conduction produced an AC-conductivity with an exponential frequency dependence (Golin 1963; Pollak and Geballe 1961). As these authors pointed out, the dispersion in the conductivity also implies dispersion in the dielectric behavior according to the Kramers-Kronig relations.

In addition to compensation-doped elemental semiconductors, hopping conductivity/polarization has been observed and characterized in oxygen-deficient and in Li-doped NiO where the hopping takes place between mixed valent Ni-sites (Aiken and Jordan 1968; Kabashima and Kawakubo 1968; Snowden and Saltsburg 1965). Later, Jonscher showed that the hopping conductivity/polarization in a wide variety of organic and inorganic solids and liquids followed a simple exponential frequency dependence he referred to as the “universal dielectric response” (UDR) (Jonscher 1977).

The exponent of the AC-conductivity frequency dependence for the UDR is less than one; the total conductivity is the sum of the DC and AC-conductivities, and the imaginary-part of the dielectric constant is the conductivity divided by the frequency.

$$\sigma = \sigma_{DC} + A\omega^s \quad s < 1 \quad (4.12)$$

$$\varepsilon'' = \frac{\sigma}{\omega\varepsilon_0} = \frac{\sigma_{DC}}{\omega\varepsilon_0} + \frac{A\omega^{s-1}}{\varepsilon_0} \quad (4.13)$$

According to the Kramer-Kronig relations, the real part of the dielectric constant due to the UDR must be:

$$\varepsilon' = \tan\left(\frac{s\pi}{2}\right) \frac{A\omega^{s-1}}{\varepsilon_0} + \varepsilon_\infty \quad (4.14)$$

Figure 4.5 illustrates the universal dielectric response's effect on the AC-conductivity, imaginary dielectric constant, and real dielectric constant of a semiconducting sample.

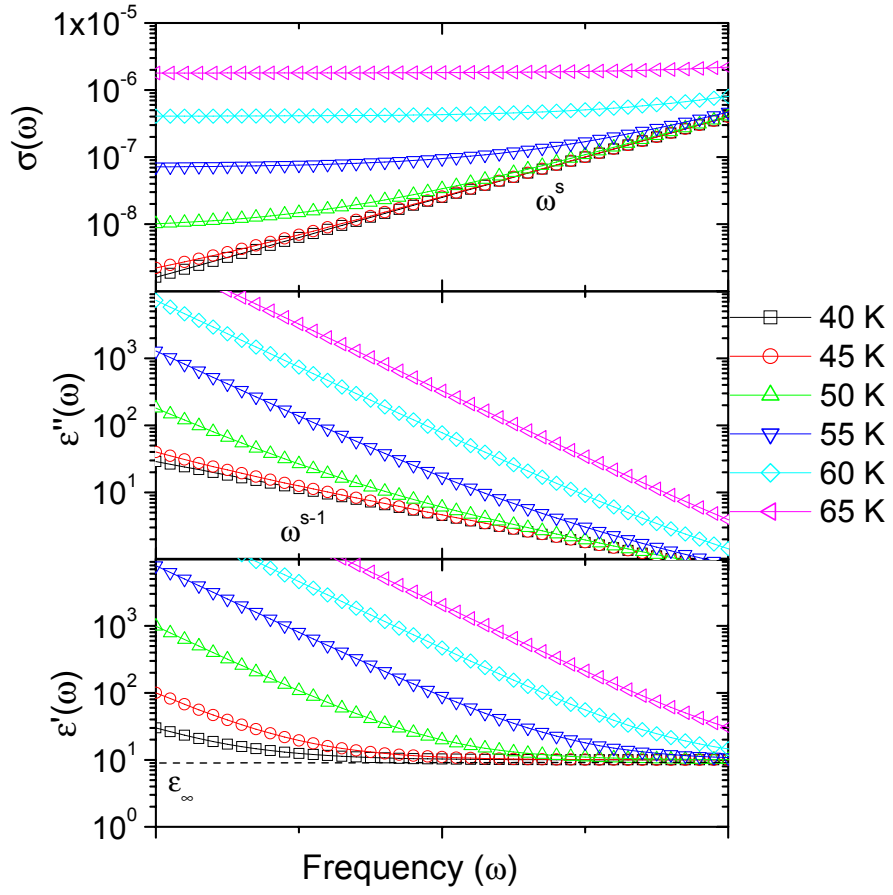


Figure 4.5: Example of the effect of the “universal dielectric response” on the AC-conductivity ( $\sigma$ ), the imaginary-part of the relative dielectric constant ( $\epsilon''$ ), and the real-part of the relative dielectric constant ( $\epsilon'$ ) for a semiconducting sample.

### 4.3.3 Ionic polarization

In ionic crystals, the equilibrium position of the ions can be displaced by the presence of a field; this displacement results in a polarization. In an ionic structure, the short-range coulombic forces provide a restoring force that increases the vibrational frequencies; furthermore, the damping associated with the ionic displacements is small in comparison to the damping for hopping polarization. These characteristics make ionic polarization a resonance polarization with resonances in the microwave, near-infra-red to infra-red frequency ranges.

The total ionic polarization of a solid is the vector sum of all the dipole polarizations. Calculating the dielectric constant from first principles is theoretically and analytically complex; it requires a detailed knowledge of the vibrational structure and crystal symmetry to analyze the quantum-mechanical equations governing vibrational transitions (e.g. Kubo-Greenwood formula) (Marder 2000). Although a quantum-mechanical model would provide all the details, a classic model is sufficient for calculating the frequency dependence of the complex dielectric-constant and is more useful for developing a qualitative understanding of the ionic polarization resonances. Classically, the polarization of a dipole shown in Figure 4.5 is written as:

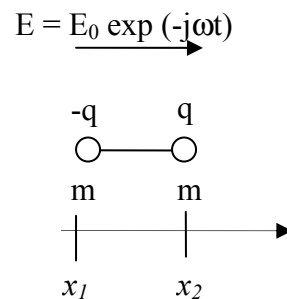


Figure 4.6: Schematic of a dipole in an oscillating Electric field.

$$\vec{F}_1 = -q\vec{E} + k(\vec{x}_2 - \vec{x}_1 - \vec{x}_0) + \frac{m}{\tau}(\vec{x}'_2 - \vec{x}'_1) = \vec{x}''_1 m \quad (4.15a)$$

$$\vec{F}_2 = q\vec{E} - k(\vec{x}_2 - \vec{x}_1 - \vec{x}_0) + \frac{m}{\tau}(\vec{x}'_1 - \vec{x}'_2) = \vec{x}''_2 m \quad (4.15b)$$

$$\vec{x} = \vec{x}_2 - \vec{x}_1 - \vec{x}_0 \quad (4.16)$$

$$\vec{F}_2 - \vec{F}_1 = 2q\vec{E} - 2k\vec{x} + 2\frac{m}{\tau}\vec{x}' = \vec{x}''m$$

$$x'' - \gamma x' + \beta^2 x = \alpha \exp(-j\omega t) \quad (4.17)$$

$$\beta = \sqrt{\frac{2k}{m}} \quad \alpha = \frac{2qE_0}{m} \quad \gamma = \frac{2}{\tau}$$

$$\bar{p} = q\bar{x} = \frac{-q\alpha \exp(-j\omega t)}{(\beta^2 - \omega^2) - j\omega\gamma} \quad (4.18)$$

Summing the polarization from all the vibrational modes that contribute to the polarization and converting the polarization to the real and imaginary components of the dielectric constant yields (Kao 2004; Marder 2000):

$$\varepsilon'(\omega) = \varepsilon_0 \left[ 1 + \sum_l \frac{n_l q^2 (\beta_l^2 - \omega^2)}{(\beta_l^2 - \omega^2)^2 + \omega^2 \gamma_l^2} \right] \quad (4.19a)$$

$$\varepsilon''(\omega) = \varepsilon_0 \sum_l \frac{n_l q^2 \gamma_l \omega}{(\beta_l^2 - \omega^2)^2 + \omega^2 \gamma_l^2} \quad (4.19b)$$

A graphical example of the real and imaginary components of the dielectric constant created by the ionic-polarization are shown in Figure 4.7.

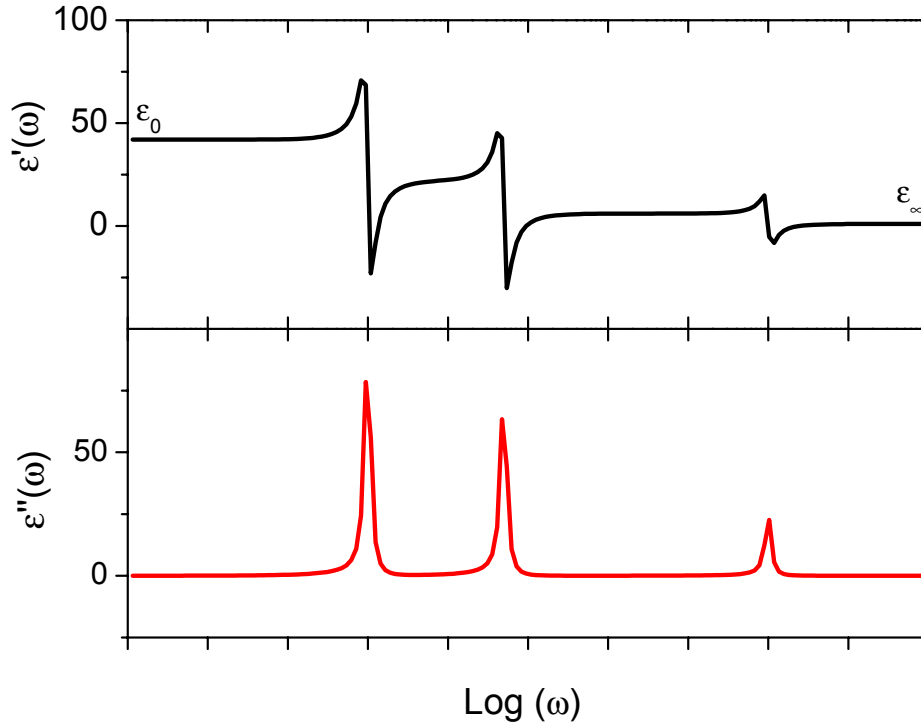


Figure 4.7: Simulated example of the real ( $\epsilon'$ ) and imaginary ( $\epsilon''$ ) components of the dielectric constant due to three ionic resonances.

#### 4.3.4 Electronic polarization

At frequencies beyond the near-infra-red (infra-red, visible, and ultraviolet, X-ray) photons provide enough energy to excite the electron clouds surrounding the atoms to higher energy states.

As was the case for the ionic contribution to the dielectric constant, the electronic contribution is quite complex to calculate from first principles; it requires a detailed



knowledge of the electronic band structure whereas the classical dipole model provides sufficient insight to understand the underlying physics.

An illustrative qualitative comparison of the effect of electronic transitions on the complex dielectric constant is the series of column-IV elemental semiconductors C (diamond), Si, and Ge. The band gap of the column-IV semiconductors decreases from 5.2 eV, to 1.1 eV, to 0.7 eV for C, Si, and Ge, respectively; in addition, the respective high-frequency dielectric constants increases from 5.68, to 12, to 16. Qualitatively, this is similar to the ionic dipoles; an inverse relationship exists between the resonant frequency and dielectric constant.

#### 4.4 IMPEDANCE

Stimulating a linear sample or circuit element with a sinusoidal current produces a sinusoidal potential drop across the sample. The steady-state response is characteristic of the sample.

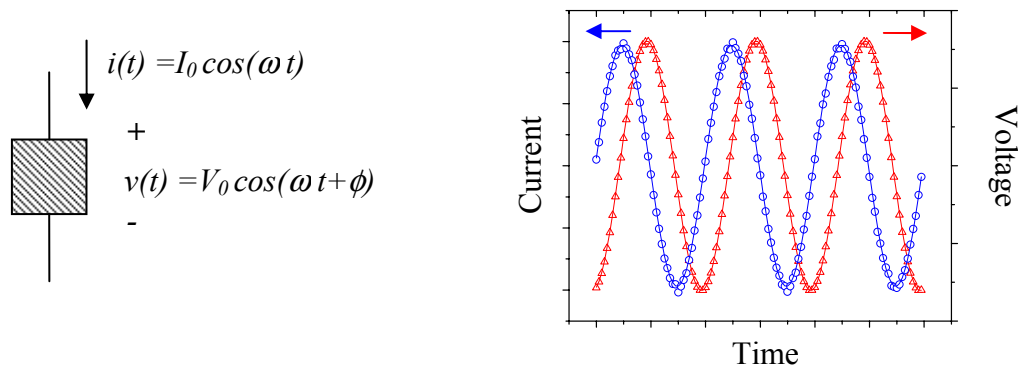


Figure 4.8: General sinusoidal voltage response to a forced sinusoidal current.

A convenient form to describe the characteristic response of the linear element is the impedance. The impedance is a complex quantity defined as the ratio of the Fourier

transform of the voltage to the Fourier transform of the current (Barsoukov and Macdonald 2005).

$$\mathbf{Z}(\omega) = \frac{F[v(t)]}{F[i(t)]} = \frac{V_0}{I_0} \exp(j\phi) \quad (4.20)$$

The complex impedance can be expressed graphically, in a phasor diagram, to show the polar magnitude and phase angle or the Cartesian real and imaginary components. The real component  $Z'$  is also called the resistance  $R$  and the imaginary component  $Z''$  is referred to as the reactance  $X$  and all have units of  $\Omega$ s.

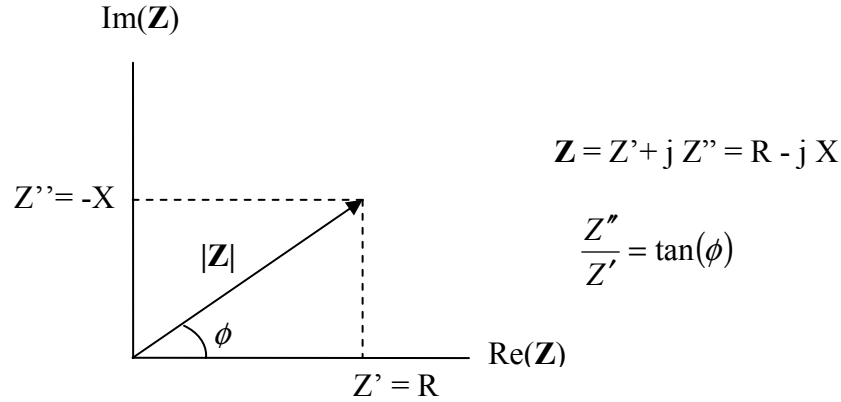


Figure 4.9: Phasor diagram of the impedance.

Another useful quantity for analyzing the frequency response of a linear system is the complex admittance  $\mathbf{Y} = \mathbf{Z}^{-1}$ . The complex admittance is composed of a real conductance  $G$  and an imaginary susceptance  $B$ , so that  $\mathbf{Y} = G + j B$  with units of  $\Omega^{-1}$ .

#### 4.5 CIRCUIT ELEMENT MODELING

The impedance and admittance of a linear system can be represented by linear circuit elements: resistors, capacitors, and inductors connected in series or parallel.

Impedances are represented by two elements in series whereas admittances are represented by elements in parallel.

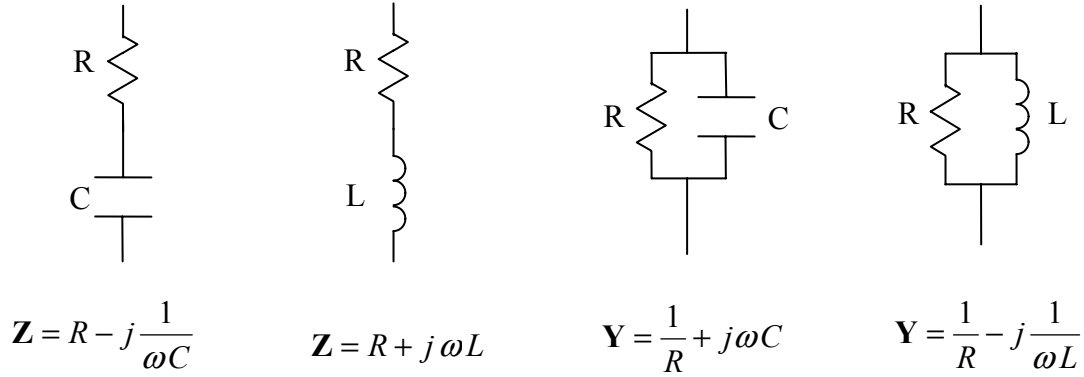


Figure 4.10: Simple circuit element models for describing an impedance or admittance.

For a given frequency, the impedance or admittance of a material can be scaled by the shape's geometric dimensions to give a size-independent property. For instance, if the material has a positive susceptance, then it has a capacitive behavior. This means that the sample is most easily modeled by a simple linear circuit containing a resistor and a capacitor in parallel. If the sample's shape is a rectangular prism or cylinder, the conductance and capacitance can be scaled to give the conductivity  $\sigma$  and permittivity  $\epsilon$ .

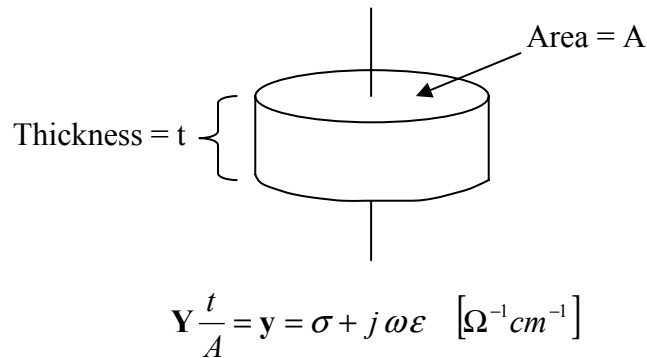


Figure 4.11: Scaling of the admittance  $\mathbf{Y}$  of a sample by its thickness and area to give the size-independent admittance  $\mathbf{y}$ .

#### 4.5.1 Linear circuit-element dielectric-relaxation modeling

The procedure of connecting a sample's behavior to a linear circuit can be taken a step further by using more complex circuits to model the frequency behavior of a material property. For example, the series combination of a resistor (R) and capacitor (C<sub>2</sub>) in parallel with a capacitor (C<sub>1</sub>) gives the same frequency behavior as the Debye model for a single dielectric relaxation.

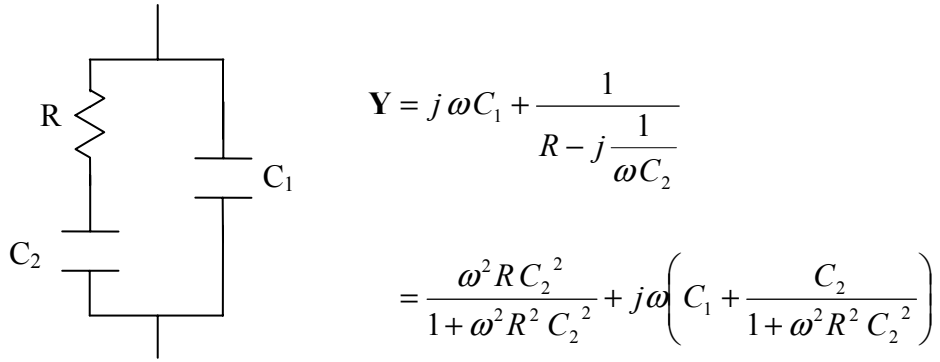


Figure 4.12: Admittance circuit with a frequency response equivalent to the Debye relaxation equations.

The Debye equations (given as Equations 4.5a, b) are matched to the frequency response of the circuit above by setting  $\tau = RC_2$ ,  $C_2 = (\epsilon_s - \epsilon_\infty)$ , and  $C_1 = \epsilon_\infty$ . This example shows the convenience of modeling a dielectric phenomenon with a linear circuit because a polarizing or conduction mechanism can be symbolized with the schematic representations of circuit elements that obey the same differential equations.

The linear circuit representation is usually exploited in the reverse direction: first the impedance measurement is made on the sample and then a circuit model is developed to fit both the real and imaginary parts of the frequency spectrum. If the fitting is good, then a physical model can be developed to explain the impedance behavior. Developing a good circuit model that adequately and accurately represents the behavior of the

material is an art-form; depending on the results of the impedance/admittance measurement, it is often advantageous to plot the data in both Bode and Nyquist plots for the  $\mathbf{z}$ ,  $\mathbf{y}$ , and  $\boldsymbol{\varepsilon}$ . The following table is a reference for transforming the data between these three functions.

Table 4.1: Transformation table for converting the impedance, admittance, and dielectric constant.

	$\mathbf{z}$	$\mathbf{y}$	$\boldsymbol{\varepsilon}$
$\mathbf{z} =$	1	$y^{-1}$	$\frac{-j}{\omega \varepsilon_0 \varepsilon}$
$\mathbf{y} =$	$z^{-1}$	1	$j \omega \varepsilon_0 \varepsilon$
$\boldsymbol{\varepsilon} =$	$\frac{-j}{\omega \varepsilon_0 z}$	$\frac{-j y}{\omega \varepsilon_0}$	1

#### 4.5.2 Constant-phase element

Measuring the impedance of real materials often reveals a dielectric behavior that looks qualitatively similar to the Debye equations but cannot be modeled by ideal circuit elements; in these cases a non-ideal circuit element is used to obtain good empirical agreement with the data. The most commonly used non-ideal circuit element is the constant-phase element (CPE). The CPE has an impedance of:

$$\mathbf{Z} = A(j\omega)^{-s} \quad (4.21)$$

The CPE can be thought of as a complex generalization of the “universal dielectric response” proposed by Jonscher. The CPE acts like a pure resistor for  $s = 0$  and a pure capacitor for  $s = 1$ ; this sets the limits for  $s$ . Macdonald has pointed out that although the CPE behavior is used for empirical curve fitting, it does have a physical interpretation – if, instead of a single response time there is an energy-activated exponential distribution of response times (Barsoukov and Macdonald 2005). Figure

4.13a illustrates the frequency dispersion and complex behavior of the admittance circuit shown in Figure 4.12 after replacing the resistor with a CPE and allowing  $s$  to vary from resistor-like  $s = 0$  towards a more capacitor-like  $s = 1$ .

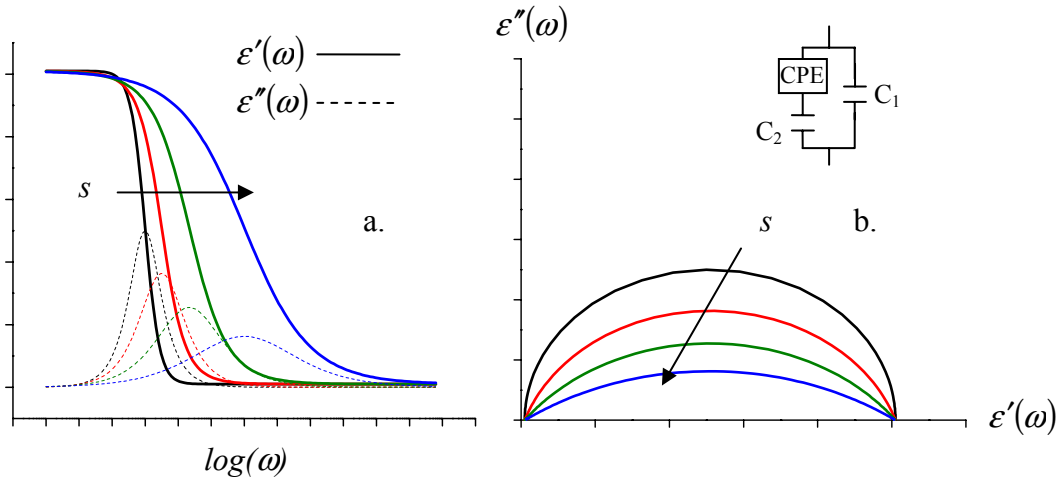


Figure 4.13: Bode plot (a) and Nyquist plot (b) of the dielectric relaxations of the circuit in Figure 4.12, having replaced the resistor with a CPE.

### 4.5.3 DC-conductivity

For many materials, there is appreciable DC-conductivity in addition to dielectric relaxations. The DC-conductivity is modeled as a simple resistor in parallel with a relaxation circuit, as shown in Figure 4.14.

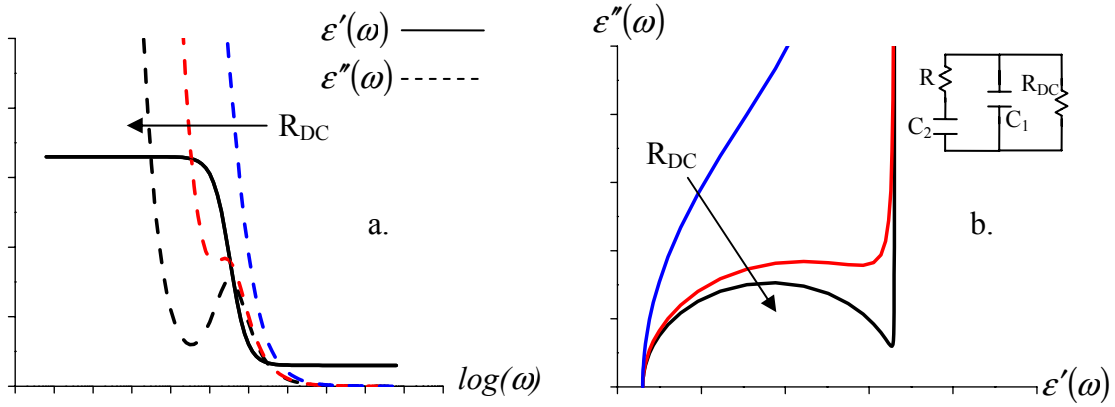


Figure 4.14: Bode plot (a) and Nyquist plot (b) of the dielectric relaxations of a circuit model with a DC-resistance; the arrow points to the direction of increasing  $R_{DC}$ .

Increasing the DC-conductivity has the effect of washing out the dielectric-loss relaxation peak in the imaginary part of the dielectric spectrum. In theory, the real part of the dielectric response is unaffected by the presence of appreciable DC-conductivity; however, in practice this condition is limited by the resolution of the impedance analyzer. It is also important to note that the DC conductivity must be subtracted from the impedance spectrum for the Kramers-Kronig relations to be consistent.

#### 4.6 GRAIN BOUNDARIES

In polycrystalline materials, grain boundaries are another source of dielectric behavior that may superimpose and cloud the intrinsic dielectric response of the material in the radio-frequency range. The boundaries effect transport behavior differently in different materials depending on what effect is dominant. The boundaries act as scattering sites for charge carriers, increasing the total impedance. The intergrain impedance also depends on the contact between the grains; loosely packed grains will have a smaller intergrain contact area, resulting in an impedance associated with the

constriction of the conduction path. The boundaries can also act to lower the impedance by providing a separate conduction path via carrier hopping along surfaces states. The intergrain contact area correlates with the macroscopic density of the polycrystalline pellet; thus the sample density is an important parameter for understanding the impedance behavior of polycrystalline samples.

## **4.7 MEASUREMENT TECHNIQUES**

### **4.7.1 Measurement hardware**

The impedance setup makes use of much of the same hardware as the DC-conductivity setup described in Chapter 3. The impedance was measured with a *Hewlett-Packard* 4192A Impedance Analyzer (HP4192A). The HP4192A is connected, via four coaxial cables, to BNC bulkhead connections that are mounted to an aluminum box. Inside the box, four *Lakeshore* type-SC coaxial cables are fed into the vent port of the cryogenic-expander cooling head. The *Lakeshore* cables wrap around the first and second cooling head stages and terminate at the sample stage where the shielding is pulled back from the inner conductor and grounded to the body of the cooling head. The inner conductors are left free to solder to the sample holder.

Two different sample holders have been used to measure the impedance of samples presented in this thesis. The body of both sample holders is constructed out of machined copper. To electrically insulate the connection from the copper body, a piece of single-crystal sapphire is adhered to the inner base of the body with silver epoxy. The advantage of single-crystal sapphire is that it is electrically insulating but thermally conducting; the good thermal conductivity minimizes temperature gradients between the sample and temperature sensor that would lead to inaccuracies in the impedance versus temperature data.



The first sample holder employs four small copper posts to connect the wires bonded to the sample surface to the inner conductors of the *Lakeshore* coaxial cables. One drawback of the first sample holder is that the sample size must fit in between the four copper posts; this limits the sample size to an approximate area of  $5\text{ mm} \times 5\text{ mm}$ . Sample preparation for the first sample holder requires cutting the polycrystalline pellets to this area, polishing the surfaces to remove loose powder, and sputtering Au or Pt on the top and bottom surfaces to make the parallel plate capacitors.

To allow for larger sample areas, a second sample holder was fabricated without the four Cu posts. Instead, large wires were attached to each side of the capacitor with Ag epoxy. After the epoxy had dried, the sample was placed into the holder; a Teflon disk placed in between the lid and the sample ensures electrical isolation of the sample. Using the second sample holder, samples with areas of  $10\text{ mm} \times 10\text{ mm}$  could be measured.

#### **4.7.2 Measurement limitations**

The HP4192A is capable of measuring the vector voltage/current ratio (impedance or admittance) at frequencies of 5 Hz to 13 MHz; however, there are limitations on the magnitude of the vector  $V/I$  ratio and the measurement frequency at which an accurate measurement can be made. Although the HP4192A has a minimum admittance magnitude resolution of  $1\text{ n}\Omega^{-1}$ , it cannot measure the phase unless the admittance is greater than  $500\text{ n}\Omega^{-1}$ . For dielectric measurements, the capacitance of the sample must be large enough so that the susceptance (product of the frequency and capacitance) is greater than the admittance minimum; these limitations are displayed graphically for reference in Figure 4.15.

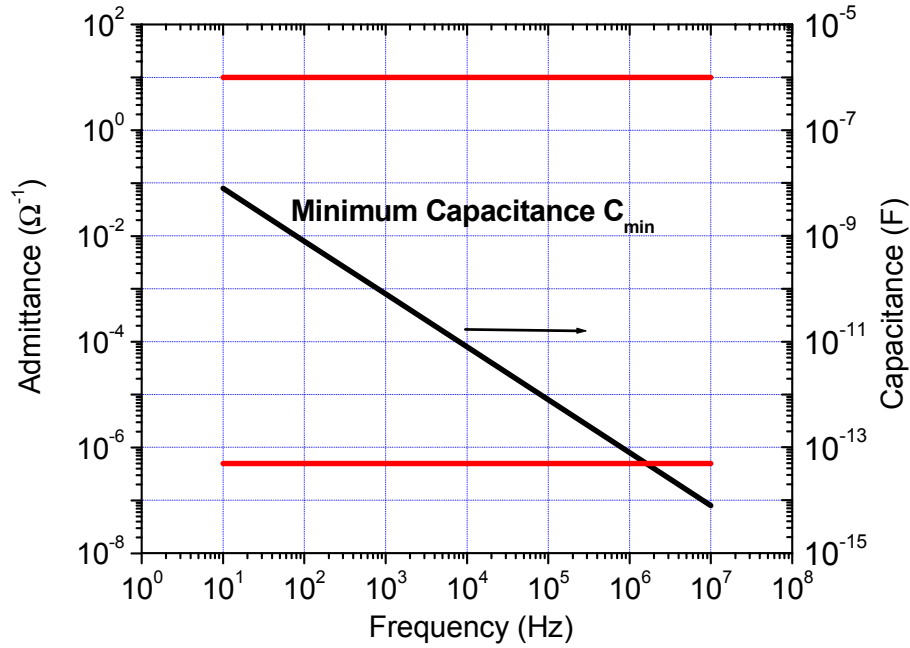


Figure 4.15: Admittance measurement limitations and minimum capacitance for the HP4192A impedance analyzer.

The combination of the capacitance minimum and the available sample space in the sample holders puts further limitations on the dielectric constants that can be measured and the resolution with which they can be measured. To fit the sample into the current sample holder, a practical sample must be less than 1 cm in diameter and less than 5mm thick. If the dielectric constant is too small and the capacitance is below the minimum capacitance at a given frequency, then a higher frequency is needed to measure accurately the corresponding capacitance; it is typical for this constraint to set the low-frequency limit of measuring the dielectric properties of a sample.

The high-frequency measurement limitations were originally thought to be constrained by the parasitic capacitive and inductive couplings in the electrical connections. However, careful measurement of the setup under shorted and opened

conditions revealed that the error in the measurement was not due to any linear-type parasitic elements in the measurement circuit. To confirm this, a commercial piece (*SCI Engineered Materials*) of (1 0 0) oriented SrTiO<sub>3</sub> single-crystal was measured and the results were compared to the dielectric data in the scientific literature. The benefit of measuring SrTiO<sub>3</sub> as a dielectric standard is that it has a relatively high dielectric constant ( $\epsilon_r = 330$  (Neville et al. 1972)), negligible dielectric loss, and no dispersion below 10<sup>12</sup> Hz at room temperature (Servoin et al. 1980). Figure 4.16 shows the results of the admittance measurement on SrTiO<sub>3</sub>.

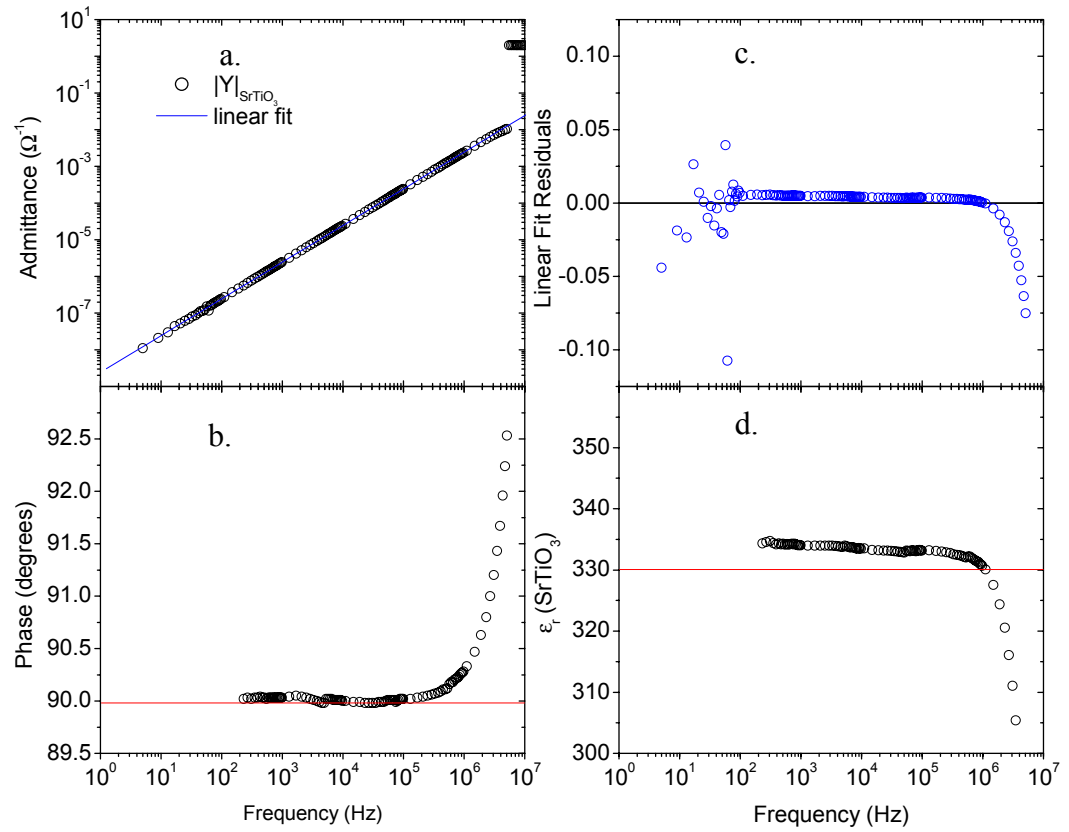


Figure 4.16: The admittance magnitude (a), phase (b), linear-fit residual (c), and dielectric constant (d) of a commercial piece of (1 0 0)-oriented SrTiO<sub>3</sub> measured at room temperature.

The magnitude of the admittance of the  $\text{SrTiO}_3$  sample was fit to a line with a slope of 1, as would be expected for a dielectric with no dispersion and negligible loss; the residual of the fit is plotted in Figure 4.15c. The residual plot shows large random variations below 100 Hz and a systematic decrease in the fit-residual above  $10^6$  Hz. The admittance phase plot also shows a systematic divergence from the expected value of  $\phi = 90^\circ$ ; the increase is evident above  $10^5$  Hz. In Figure 4.15d, the capacitance was scaled by the sample dimensions to give the dielectric constant. For frequencies between  $10^2$  Hz to  $10^6$  Hz, the measured value is very close to the value measured by Neville; however, above  $10^6$  Hz the value diverges even though it is expected to be dispersionless for another 6 decades.

The  $\tan(\phi)$  function that represents the ratio of the imaginary part of the admittance to the real part goes from negative infinity to infinity, which implies that  $\phi$  is bound to be between  $-90^\circ$  and  $90^\circ$ . Therefore, an increase in the phase above  $90^\circ$  is inconsistent with any combination of linear circuit elements. Therefore, the unexpected decrease in the dielectric constant is not due to some parasitic effect. It is likely that the extrinsic increase in the phase is due to a detuning of the HP4192A high-frequency measurement circuit. An effort was made to re-tune the circuit; however, it was unsuccessful.

The divergence from the expected behavior of the magnitude of the admittance suggests that an adequate high-frequency limit for obtaining accurate admittances is  $10^6$  Hz. On the other hand, the divergence in the expected behavior at  $10^5$  Hz suggests that constraining the limit to  $10^5$  Hz would be a more prudent choice. Since the high-frequency range is so important for observing dielectric relaxations and the dielectric measurement does not show a significant divergence until  $10^6$  Hz, the work presented in this dissertation uses  $10^6$  Hz as the high-frequency limit for obtaining accurate values.

However, it is important to remember that the measured dielectric constant above  $10^5$  Hz will slightly underestimate the actual value due to the divergence of the phase.

## Chapter 5: $\text{RMn}_{1-x}\text{Ga}_x\text{O}_3$ ( $\text{R} = \text{Ho}$ and $\text{Y}$ )

For the series  $\text{RMnO}_3$ , where  $\text{R}$  is a lanthanide ion, the rotations of the oxygen octahedra which give  $\text{RMnO}_3$  orthorhombic ( $Pbnm$ ) symmetry, increase as the size of the lanthanide ion is decreased. As the rotation angle of the octahedra increases, the angle of the  $\text{M} - \text{O} - \text{M}$  bond decreases. The decreasing bond angle increases the elastic energy; and for lanthanide ions with smaller ionic radii than dysprosium ( $\text{Dy}$ ), the  $\text{Mn}^{3+}$  cation moves into a 5-fold coordinated site, creating a hexagonal phase ( $P6_3cm$ ) that is more stable than the orthorhombic phase under ambient synthesis conditions (Goodenough 2003).

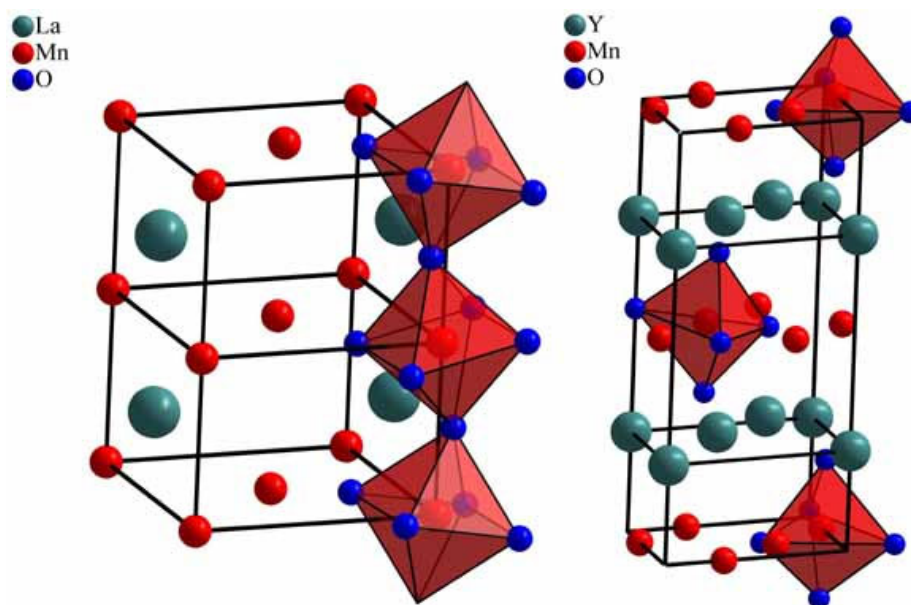


Figure 5.1: Schematic of the lanthanide and manganese positions for orthorhombic  $\text{LaMnO}_3$  and the hexagonal  $\text{YMnO}_3$ ; the orthorhombic structure has corner-linked octahedra and the hexagonal structure has planes of corner-linked trigonal-bipyramids (for clarity, only a few oxygen polyhedra are shown).

At high temperatures the hexagonal phases have symmetry ( $P6_3/mcm$ ); below a critical temperature ( $T_t$ ), the larger  $R^{3+}$  cations place a compressive stress on the apical O – Mn – O bond and trigger rotations of the  $MnO_5$  bipyramids, removing the mirror plane perpendicular to the  $c$ -axis and lowering the symmetry to ( $P6_3cm$ ). The bipyramid-rotation angle increases as the temperature is lowered; and below the Curie temperature ( $T_C < T_t$ ), the bipyramid rotations lead to a buckling of the R-plane. Figure 5.2 shows a triangular cell with two R-site positions of different symmetries that have dipole polarizations that do not cancel.

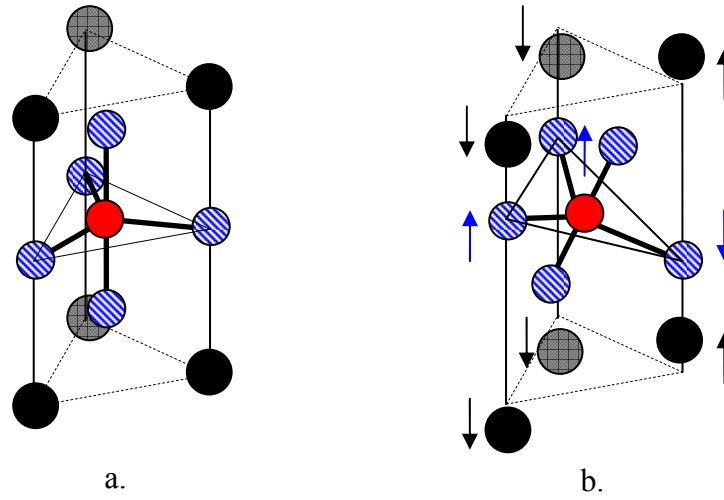


Figure 5.2: Schematic drawing of the locations of the R, Mn, and O ions in the centrosymmetric hexagonal ( $P6_3/mcm$ ) (a) and the ferrielectric hexagonal ( $P6_3cm$ ) phases of  $RMnO_3$  (Van Aken et al. 2004).

In addition to being ferrielectric, the antiferromagnetic spin-spin interactions of the 5-fold coordinated  $Mn^{3+}$ -cations are frustrated by the close-packed Mn array of the basal planes. The spin frustration in the plane suppresses long-range magnetic interactions to make  $T_N$  much lower than the extrapolated Weiss constant ( $\theta$ ) obtained from fitting the Curie-Weiss-like susceptibility for all the hexagonal  $RMnO_3$  samples (Zhou et al. 2006b). Below  $T_N$ , the spins on the  $Mn^{3+}$  cations order in triangular patterns

with each spin rotated  $120^\circ$  from its nearest neighbors. In comparison to the intraplane interactions, the magnetic interactions between the planes are weak. The weak interplane interactions lead to a variety of magnetic phases with different orientations of  $120^\circ$  spin-triangles with respect to the major axis. There are three possibilities of  $120^\circ$  spin-triangle orientations: the spins can have an arbitrary angle with respect to the major axes, be perpendicular to the major axes, or be parallel to the major axes. The total number of spin phases possible is six since the planes at  $z = 0$  and  $z = 1/2$  can be in a parallel or antiparallel configuration; the six possible magnetic phases are shown in Figure 5.3.

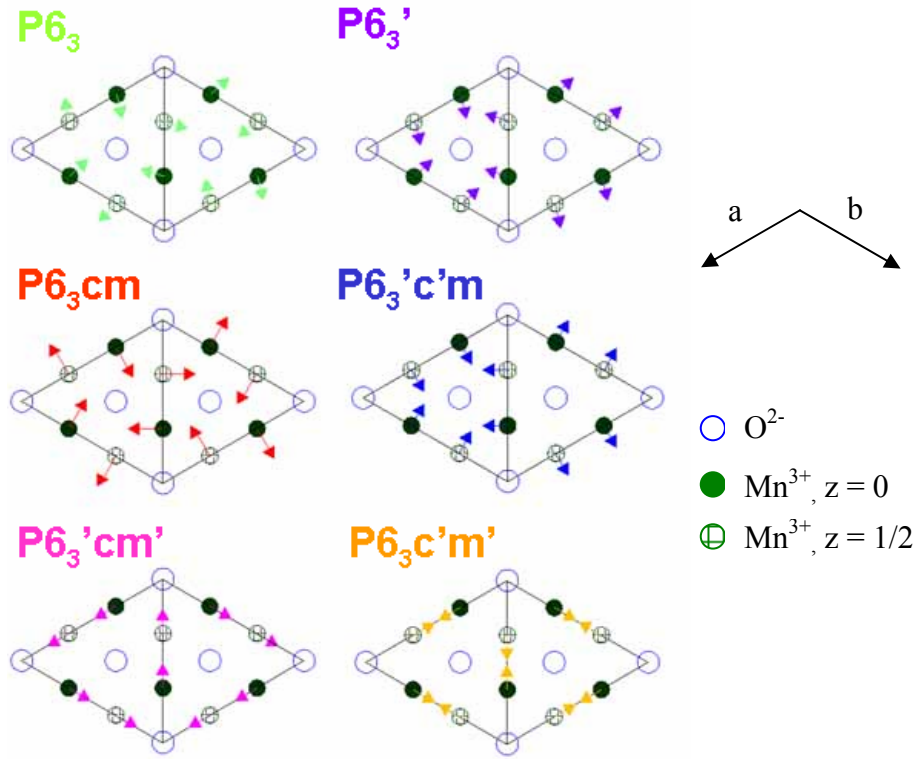


Figure 5.3: Projections of the six possible magnetic orderings for the manganese oxide planes in spin-frustrated hexagonal  $\text{RMnO}_3$ ; the spins of the magnetic symmetries  $\text{P6}_3$  and  $\text{P6}_3'$  are randomly oriented with respect to the major axes, groups  $\text{P6}_3\text{cm}$  and  $\text{P6}_3'\text{c'm}$  are perpendicular, and groups  $\text{P6}_3'\text{cm'}$  and  $\text{P6}_3\text{c'm'}$  are parallel (Lonkai et al. 2002).



The different magnetic phases are very close to each other in energy; as a consequence, the magnetic phase is dependent on which lanthanide  $R^{3+}$  ion is used, the magnetic ordering of the  $R^{3+}$  ions, as well as the thermodynamic variables: temperature, magnetic field, and pressure (dela Cruz et al. 2005; Fiebig et al. 2000; Fiebig et al. 2003; Lonkai et al. 2002; Lorenz et al. 2004; Munoz et al. 2000; Munoz et al. 2001; Yen et al. 2005).

The differences between the magnetic transitions of  $YMnO_3$  and  $HoMnO_3$  show just how sensitive the spin-frustrated system is to perturbations. The  $Y^{3+}$  and  $Ho^{3+}$  cations are 6-fold coordinated in the hexagonal structure and have nearly equivalent ionic radii (0.892 Å and 0.894 Å, respectively (Shannon and Prewitt 1969));  $Y^{3+}$  has a  $4f^0$  electronic configuration and therefore is nonmagnetic whereas  $Ho^{3+}$  has a  $4f^{10}$  electronic configuration with two unpaired spins to contribute to the magnetism. Both  $YMnO_3$  and  $HoMnO_3$  have Néel temperatures ( $T_N$ ) of  $\sim 70K$ ; however,  $YMnO_3$  adopts the  $P6_3'cm'$  magnetic phase below  $T_N$  whereas  $HoMnO_3$  adopts the  $P6_3'c'm$  structure (Fiebig et al. 2003).  $YMnO_3$  maintains its magnetic phase to 0 K but  $HoMnO_3$  goes through several other magnetic transitions as the temperature is lowered. At  $T < T_{SR}$  ( $\sim 40$  K) the spins in the plane rotate through an intermediate  $P6_3'$  configuration and settle in the  $P6_3'cm'$  configuration. Another spin rotation takes place at  $T = T_2$  ( $\sim 5$  K) resulting in the  $P6_3cm$  magnetic structure; this spin rotation coincides with the magnetic ordering of one of the Ho-sites.

There are also transitions in the magnetic phase that take place under the application of a magnetic field (Lorenz et al. 2004; Vajk et al. 2005); however the complexity of the temperature vs. magnetic field diagram is beyond the scope of this work.

What is unique about the spin-rotation transitions is that they can be observed as peaks or plateaus in the dielectric constant (Lorenz et al. 2004; Sharma et al. 2004; Yen et al. 2005). The experimental work of this chapter investigates the effect of Ga-doping on the multiferroic properties of  $\text{RMnO}_3$  ( $\text{R} = \text{Ho}, \text{Y}$ ) near the ferrielectric transition temperature  $T_C$ , the antiferromagnetic ordering temperature  $T_N$ , the spin-rotation temperature  $T_{\text{SR}}$ , and the second spin-rotation temperature  $T_2$ . Ga-doping provides two perturbations to the hexagonal  $\text{RMnO}_3$  samples: the first perturbation is a larger  $c$ -axis lattice constant as is expected since  $\text{YGaO}_3$  and  $\text{HoGaO}_3$  are isostructural with  $\text{YMnO}_3$  and  $\text{HoMnO}_3$  but have slightly larger  $c$  lattice parameters (Geller et al. 1975). The second perturbation is the dilution of the spin-frustrated antiferromagnetic Mn - O - Mn interactions with nonmagnetic  $\text{Ga}^{3+}$  cations; the effect of diluting the antiferromagnetic interactions has already been successfully demonstrated for the orthorhombic-perovskite manganese oxides (Goodenough 2003) but not for the hexagonal spin-frustrated manganites.

## 5.1 SYNTHESIS

Polycrystalline samples of  $\text{RMn}_{1-x}\text{Ga}_x\text{O}_3$  ( $\text{R} = \text{Y}, \text{Ho}$ ) ( $x = 0, 0.03, 0.1, 0.2$ ) were synthesized with standard solid-state techniques from stoichiometric mixtures of  $\text{Y}_2\text{O}_3$ ,  $\text{Ho}_2\text{O}_3$ ,  $\text{Mn}_2\text{O}_3$  and  $\text{Ga}_2\text{O}_3$ . The samples were fired in air at  $950^\circ\text{C}$  for 24 hours, ground into powder, and then fired again at  $1100^\circ\text{C}$ . The samples were reground and then pressed into 6-mm-diameter, 60-mm-long rods with 400 atm of hydrostatic pressure. The rods were fired in air at  $1200^\circ\text{C}$  for 20 hours. After the rods were prepared, single crystals were grown in an *NEC* IR-heated image furnace; the details of the growth are described elsewhere (Zhou et al. 2005).

The single-crystal rods were oriented by Laue back diffraction; an image plate captured the diffraction pattern, which was digitally scanned, and the pattern was

imported onto a PC. The image was analyzed with the *OrientExpress* software, which performs a least squares fit of the pattern for the current orientation and calculates the necessary rotation angles for reorientation along a specific axis.

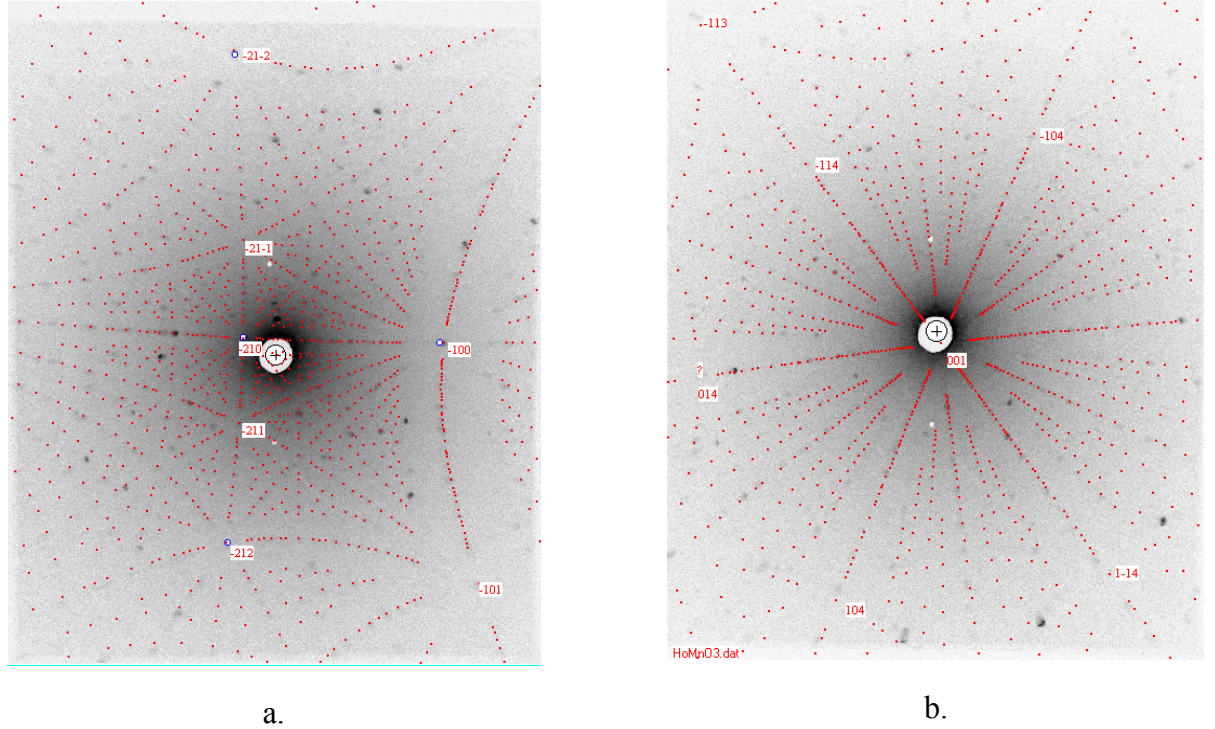


Figure 5.4: Examples of digitized Laue back-diffraction patterns simulated by the *OrientExpress* software for a randomly oriented (a) and c-axis oriented piece of  $\text{HoMnO}_3$  (b).

In addition to checking the orientation, small pieces of the single crystal were ground into powder and analyzed by room temperature X-ray diffraction; the phase was checked against the powder-diffraction-file database and the unit-cell parameters were determined by fitting the peak positions to the hexagonal  $P6_3cm$  space group. All of the crystals were single-phase; the change in the lattice parameters and the  $c/a$  ratio with Ga-doping is shown in Figure 5.5.

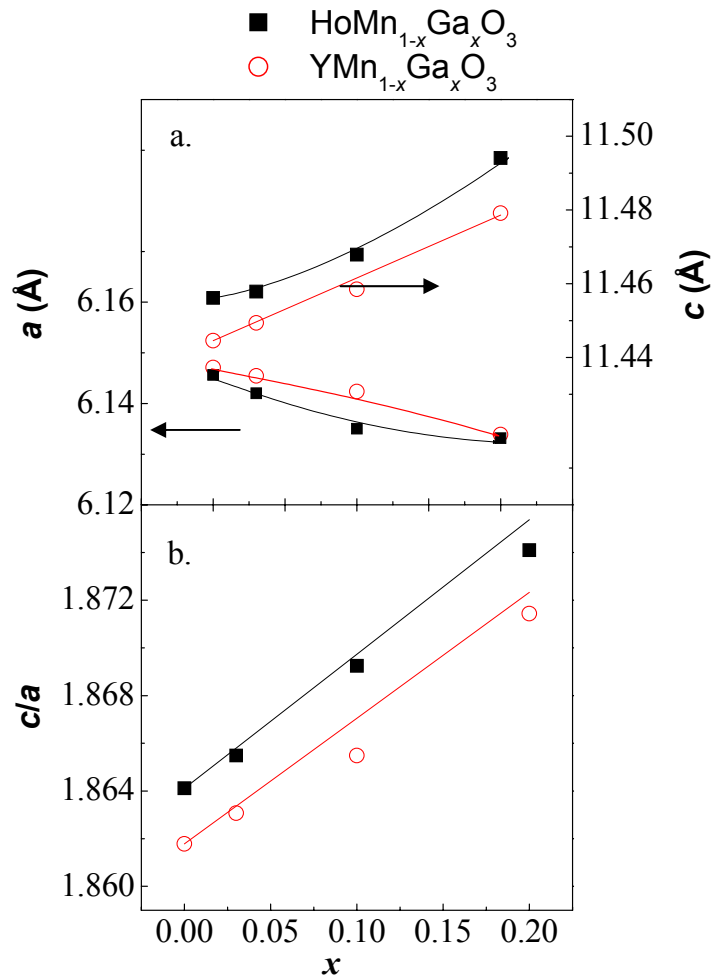


Figure 5.5: The lattice parameters and  $c/a$  ratio for  $\text{RMn}_{1-x}\text{Ga}_x\text{O}_3$  ( $R = \text{Y}, \text{Ho}$ ) ( $x = 0, 0.03, 0.1, 0.2$ ) (Zhou et al. 2005); the symbols represent the actual data and the lines represent linear interpolations of the parameters of the parent compounds  $\text{RMnO}_3$  and  $\text{RGaO}_3$  (Geller et al. 1975).

There are small deviations of the lattice parameters from the interpolated values of the parent compounds  $\text{RMnO}_3$  and  $\text{RGaO}_3$ ; however, it is clear that the  $c$  lattice parameter of  $\text{HoMnO}_3$  is larger than that of  $\text{YMnO}_3$ ; for both compounds, the  $c$  lattice parameter increases with Ga doping. On the other hand, the  $a$  lattice parameter is about

the same for  $\text{HoMnO}_3$  and  $\text{YMnO}_3$  and it decreases with increasing Ga doping. The net result is a  $c/a$  ratio that increases linearly with Ga doping.

## 5.2 FERRIELECTRIC TRANSITION

Ismailzade and Kizhaev observed a peak in the pyroelectric current at the ferrielectric transition in  $\text{YMnO}_3$  at  $T = 933 \text{ K}$ ; they also observed a positive thermal expansion and a discontinuous jump in both the  $a$ -axis and  $c$ -axis lattice parameters by high-temperature X-ray diffraction HTXRD (Ismailzade and Kizhaev 1965). A later report of the temperature dependence of the lattice parameters of  $\text{YMnO}_3$  by HTXRD show that the  $c$ -axis lattice parameter actually had a negative thermal expansion and a change in symmetry from  $P6_3cm$  to  $P6_3/mcm$  at  $1273 \text{ K}$  (Lukaszewicz and Karut-Kalicinska 1974). The ferrielectric  $T_C$  of other members of the hexagonal  $\text{RMnO}_3$  family, including  $\text{HoMnO}_3$  ( $T_C = 875 \text{ K}$ ), are summarized by Abrahams (Abrahams 2001).

### 5.2.1 High-temperature X-ray diffraction

To investigate the changes in the  $a$  and  $c$  lattice parameters near the ferrielectric transition temperature ( $T_C$ ) of the series  $\text{RMn}_{1-x}\text{Ga}_x\text{O}_3$ , HTXRD measurements as well as thermomechanical (TMA) measurements were performed. The HTXRD measurements were performed on a Schintag theta-theta diffractometer equipped with a Pt-Rh strip to heat the sample. Figure 5.6 shows the changes of both the  $a$  and  $c$  lattice parameters with temperature from the high-temperature X-ray diffraction measurements.

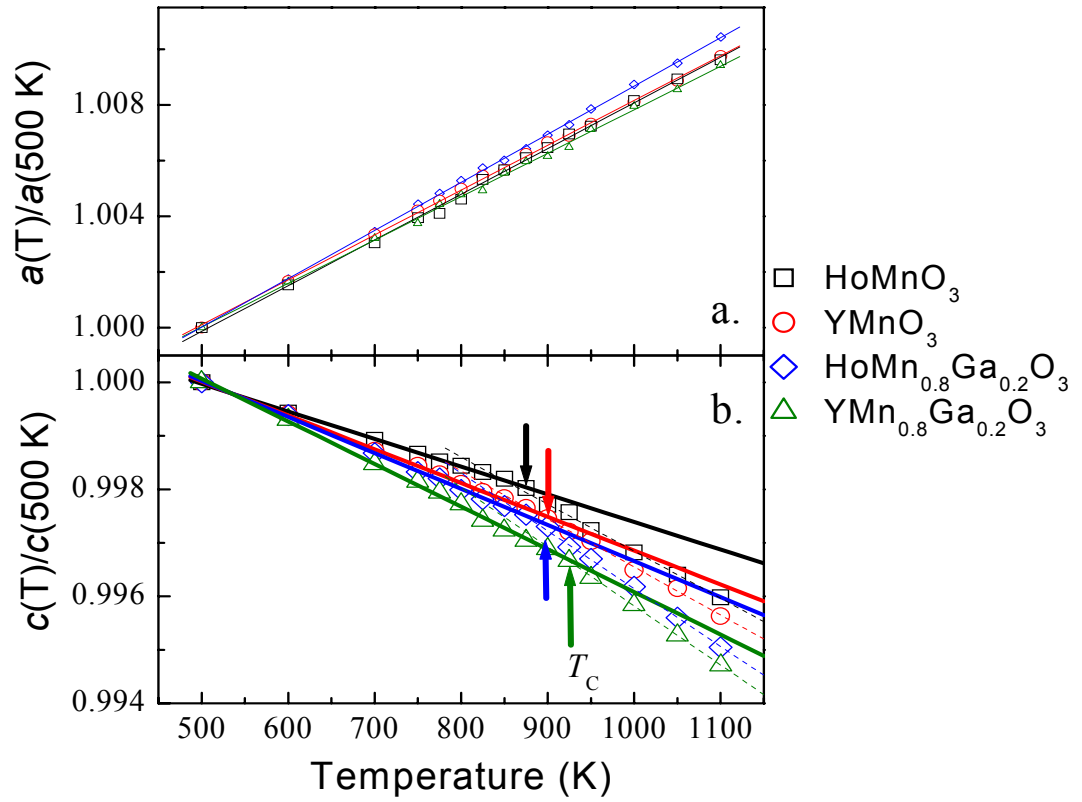


Figure 5.6: Temperature dependencies of the  $a$  (a) and  $c$  (b) lattice constants of  $\text{RMn}_{1-x}\text{Ga}_x\text{O}_3$  ( $R = \text{Y}, \text{Ho}$ ) ( $x = 0, 0.2$ ) determined by high-temperature X-ray diffraction; the lines represent linear fits over the entire temperature range for the  $a$  lattice constant, and for the  $c$  lattice constant separate fits were made above and below  $T_C$  (indicated by the arrows) (Zhou et al. 2005).

The high-temperature X-ray results show that the thermal expansion of the  $a$ -axis lattice constant is positive and linear and has about the same magnitude for all the samples measured. The  $c$ -axis lattice-constant data show that the expansion is negative and linear up to  $T_C$  and then diverges to a linear thermal contraction with a more negative slope above  $T_C$ . The thermal expansion of  $a$  and the thermal contraction of  $c$  are consistent with the results of Lukaszewicz and Karut-Kalicinska; however, these authors

did not make the measurement at enough temperature points to compare any change of slope at  $\sim 900$  K.

Both  $\text{HoMn}_{1-x}\text{Ga}_x\text{O}_3$  and  $\text{YMn}_{1-x}\text{Ga}_x\text{O}_3$  show increases in the value of  $T_C$  as  $x$  increases from 0 to 0.2; Ga doping increases both the ferrielectric transition temperature and the  $c$ -axis lattice constant, which suggests a correlation between the two.

### **5.2.2 Thermomechanical analysis**

The HTXRD results of the thermal contraction of  $c$  for the  $\text{RMn}_{1-x}\text{Ga}_x\text{O}_3$  samples were verified by thermomechanical measurements; TMA has the advantage of needing less analysis time and therefore permitting more temperature points to be taken. The disadvantage is that there is less spatial resolution and sensitivity than an X-ray diffraction experiment. The thermal-expansion measurements were carried out on a Perkin-Elmer Series 7 Thermomechanical Analyzer (TMA); the results are shown in Figure 5.7

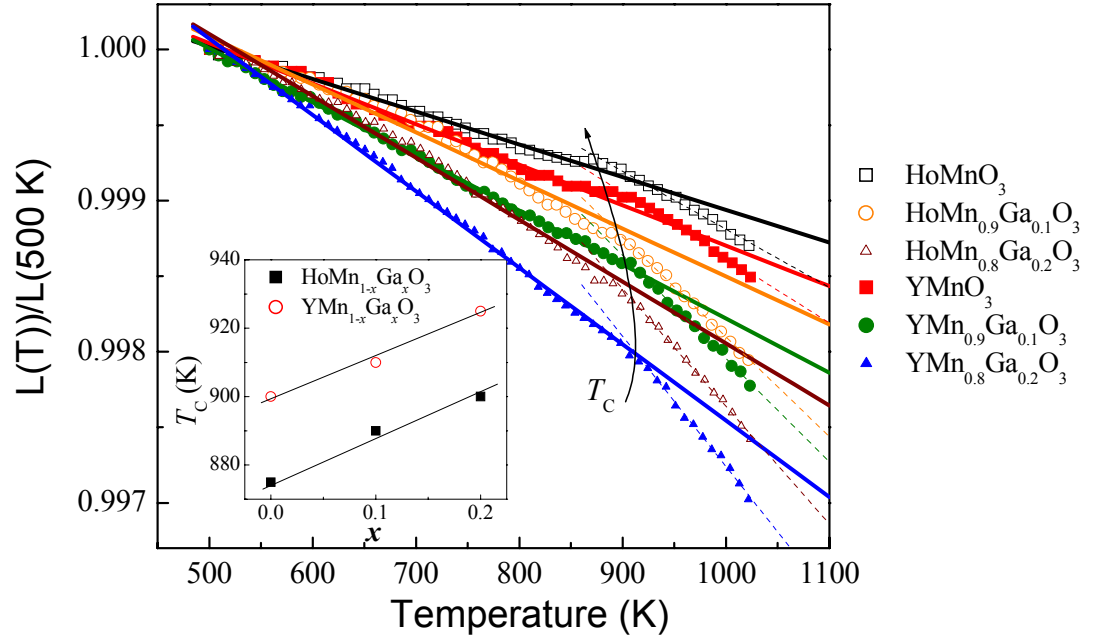


Figure 5.7: Thermal expansion of the  $c$ -axis lattice parameter for  $\text{RMn}_{1-x}\text{Ga}_x\text{O}_3$  ( $R = \text{Y}, \text{Ho}$ ) ( $x = 0, 0.1, 0.2$ ) as determined by TMA; the inset shows the increase of  $T_C$  with Ga-doping (Zhou et al. 2005).

The TMA results and the HTXRD results are in good agreement. Furthermore, the  $T_C = 900\text{ K}$  for  $\text{YMnO}_3$  and  $T_C = 875\text{ K}$  for  $\text{HoMnO}_3$  observed by HTXRD and TMA compare well with the respective  $T_C = 935\text{ K}$  (Ismailzade and Kizhaev 1965) and  $T_C = 875\text{ K}$  (Abrahams 2001) reported in other works. Also, the  $T_C$  of the  $\text{RMn}_{1-x}\text{Ga}_x\text{O}_3$  samples increased as  $x$  was increased as was also seen in the XRD experiments.

### 5.3 ANTIFERROMAGNETIC TRANSITION

The spin-frustrated hexagonal  $\text{RMnO}_3$  samples undergo an antiferromagnetic transition at  $T_N$ ; for samples with an  $\text{R}^{3+}$  cation that is non-magnetic ( $R = \text{Sc}, \text{Y}$ ) it is possible to observe the transition as a peak in the magnetic susceptibility at  $T_N$ . However, for samples with  $\text{R}^{3+}$  cations with unpaired  $f$ -electrons, the paramagnetic



susceptibility of the f-electrons washes out the contribution from the Mn ions, and  $T_N$  has to be determined by another method (e.g. thermal conductivity or specific heat). Figure 5.8 shows the magnetic susceptibility of  $\text{YMn}_{1-x}\text{Ga}_x\text{O}_3$  measured with a field of  $H = 100$  Oe after cooling in zero field.

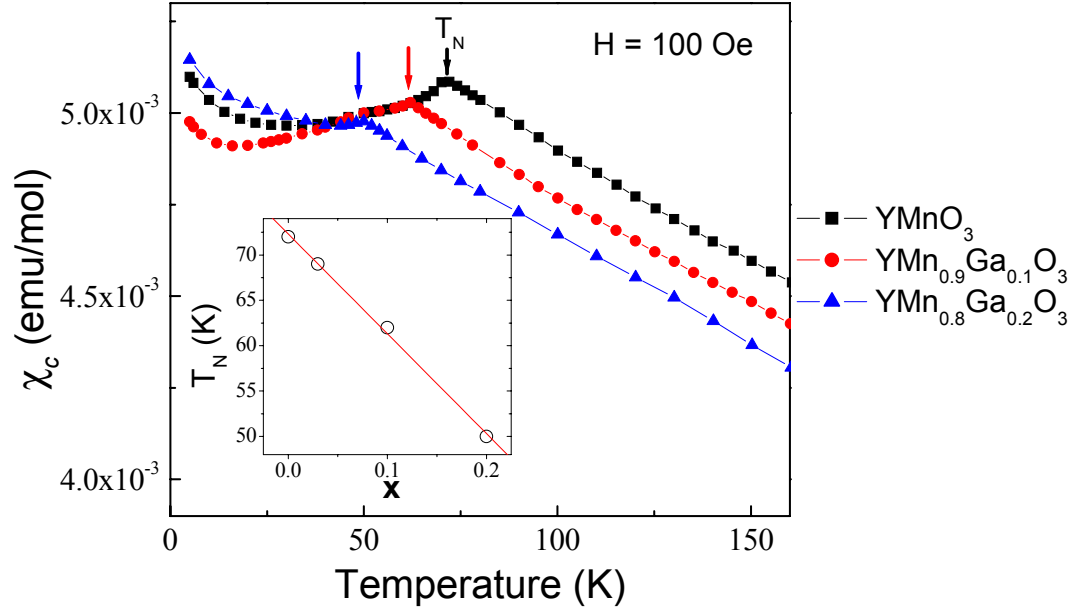


Figure 5.8: Temperature dependence of the magnetic susceptibility of  $\text{YMn}_{1-x}\text{Ga}_x\text{O}_3$  and the change in  $T_N$  with Ga-doping (inset) (Zhou et al. 2005).

The magnetic susceptibility shows that as the hexagonal Mn planes are diluted with Ga, the  $T_N$  decreases. It is expected that the change in  $T_N$  with Ga doping would be the same for  $\text{HoMn}_{1-x}\text{Ga}_x\text{O}_3$  as for  $\text{YMn}_{1-x}\text{Ga}_x\text{O}_3$  since the antiferromagnetic transition is determined by the Mn interactions and the parent compounds have about the same  $T_N$  to begin with. To verify that the  $T_N$  trend with  $x$  is the same for  $\text{HoMn}_{1-x}\text{Ga}_x\text{O}_3$ , Zhou *et al.* measured the specific heat; the data are displayed in Figure 5.9.

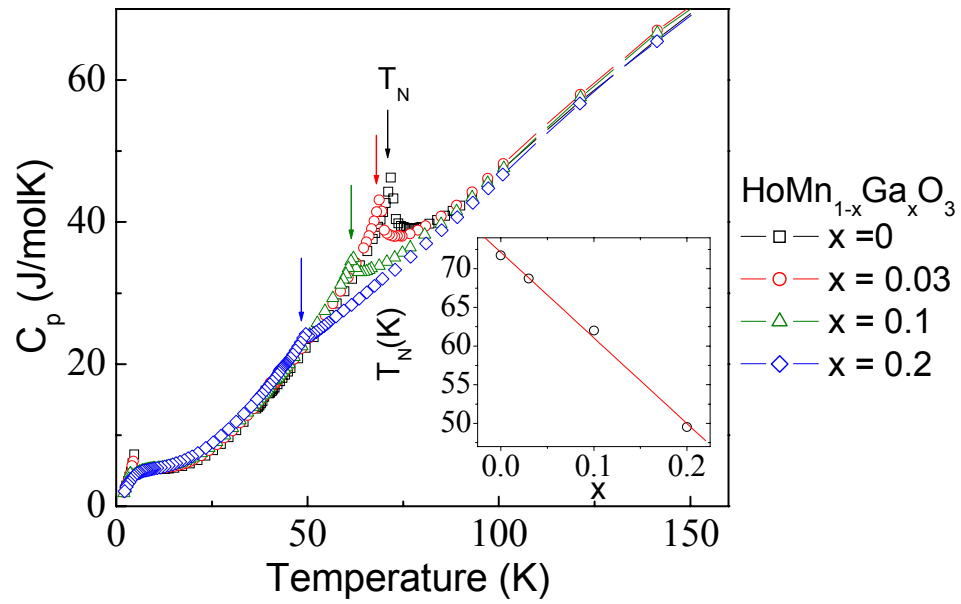


Figure 5.9: Temperature dependence of the specific heat of  $\text{HoMn}_{1-x}\text{Ga}_x\text{O}_3$  ( $x = 0, 0.03, 0.1, 0.2$ ) and the dependence of  $T_N$  on Ga-doping (inset) (Zhou et al. 2006a).

The specific-heat measurements of  $\text{HoMn}_{1-x}\text{Ga}_x\text{O}_3$  and the magnetic susceptibility of  $\text{YMn}_{1-x}\text{Ga}_x\text{O}_3$  confirm that  $T_N$  is not dependent on the magnetic properties of the lanthanide ion. Although  $T_N$  is not dependent on the magnetic properties of the lanthanide ion, it is dependent on the size of the lanthanide and its effect on the in-plane lattice constant; Figure 5.10 shows the strong dependence of  $T_N$  on the  $a$ -axis lattice constant of the hexagonal  $\text{RMnO}_3$  samples with different  $\text{R}^{3+}$  cations.

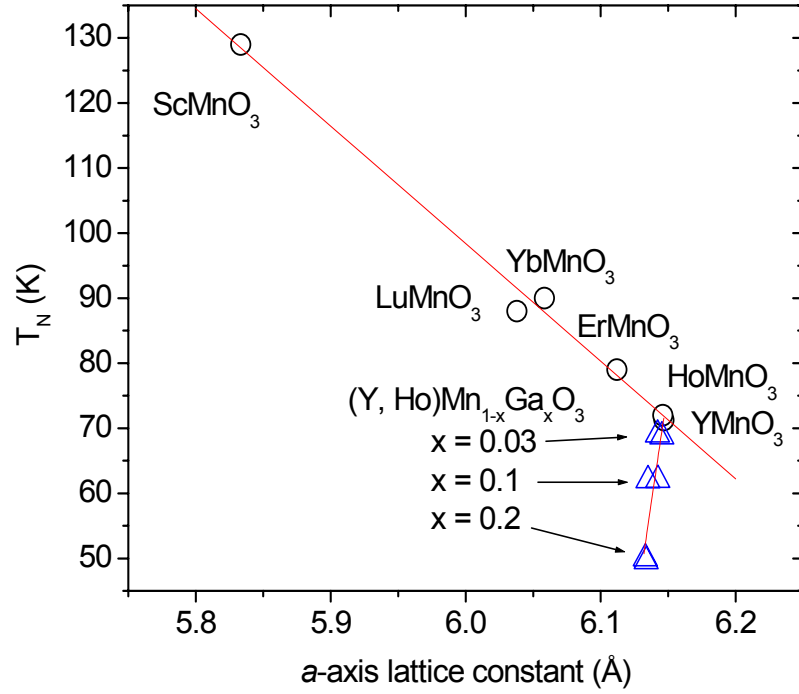


Figure 5.10: The change in  $T_N$  versus the in-plane lattice constant  $a$  for  $\text{RMnO}_3$  (Munoz et al. 2000), Lu (Van Aken et al. 2001b; Van Aken and Palstra 2004), Yb (Sugie et al. 2002; Van Aken et al. 2001c), Er (Sugie et al. 2002; Van Aken et al. 2001a), Ho, and Y} and  $\text{RMn}_{1-x}\text{Ga}_x\text{O}_3$  ( $R = \text{Y, Ho}$ ) ( $x = 0.03, 0.1, 0.2$ ).

The negative dependence of  $T_N$  on the  $a$ -axis lattice constant shows the importance of the  $\text{R}^{3+}$  cation in setting the size of the hexagonal lattice. As the  $\text{R}^{3+}$ -cation size is increased from Sc to Y, the in plane  $a$ -axis lattice constant increases and reduces the Mn-O-Mn superexchange within the plane, decreasing  $T_N$ . On the other hand, increasing the amount of Ga doping slightly decreases the  $a$ -axis lattice constant, but  $T_N$  decreases because the antiferromagnetic interactions are being diluted by the non-magnetic  $\text{Ga}^{3+}$  ions.

Another important feature of the antiferromagnetic transition is the exchange striction of the lattice at temperatures below  $T_N$ ; the increased covalent bonding of the antiferromagnetic superexchange contracts the hexagonal lattice within the plane. The exchange striction of the hexagonal manganites has been observed directly with low-temperature X-ray diffraction (Lee et al. 2005) and low-temperature TMA measurements (dela Cruz et al. 2005). The ferroelectric polarization and the contraction of the hexagonal network are not independent; by bringing the Mn-ions closer together, the exchange striction increases the cooperative rotations of the trigonal bipyramids, which increases the  $R^{3+}$  ion displacement. Increased tilting of the bipyramids leads to an increase in the  $c$ -axis lattice constant that mirrors the decrease in the  $a$ -axis lattice constant. The increase in strain associated with the magnetically driven Mn-site rotation adds rigidity to the lattice, which suppresses the dielectric constant within the plane and along the  $c$ -axis (dela Cruz et al. 2005); Figure 5.11 shows the suppression of the relative dielectric constant along the  $c$ -axis at  $T_N$  for  $\text{HoMnO}_3$ .

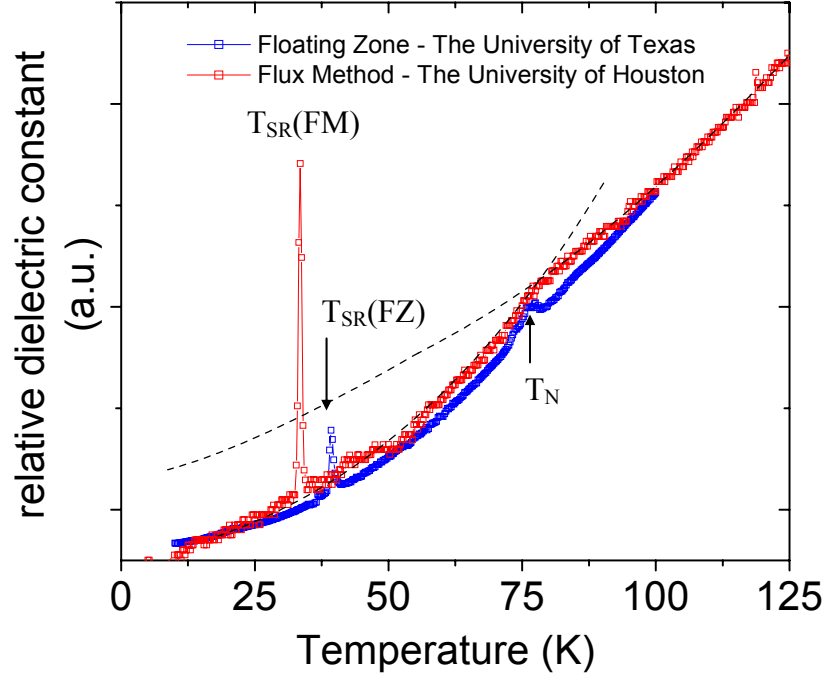


Figure 5.11: Temperature dependence of the relative dielectric constant along the  $c$ -axis for  $\text{HoMnO}_3$  samples grown by floating-zone image furnace (blue squares) and a sample grown with the flux method (red squares); the lines serve as eye-guides.

The increased suppression of the dielectric constant below  $T_N$  has been observed for all of the hexagonal  $\text{RMnO}_3$  family (Katsufuji et al. 2001; Sharma et al. 2004; Sugie et al. 2002). The exchange-strictive suppression of the dielectric constant at  $T_N$  has been observed for a variety of inorganic fluorides and oxides, which Seehra and Helmich briefly review in their investigation of the dielectric anomaly at  $T_N$  for  $\text{MnO}$  (Seehra and Helmick 1981).

#### 5.4 SPIN-ROTATION TRANSITION

In addition to the suppression of the dielectric constant at  $T_N$ , Figure 5.11 shows a sharp peak in  $\epsilon_r$  at  $T_{SR} \approx 40$  K for the floating-zone grown sample and at  $T_{SR} \approx 35$  K for the flux-grown sample. Neutron diffraction data reveal that below  $T_{SR}$  the spins rotate  $90^\circ$  in the plane to go from  $P6_3'c'm$  to  $P6_3'cm'$  symmetry. It is possible that the Pb-flux (Litvinchuk et al. 2004) used in the flux method allowed for Pb substitution into the  $\text{HoMnO}_3$  structure and this affected the spin-rotation peak temperature and intensity.

Ga-doping has an interactive effect on the electric and magnetic properties of the hexagonal manganites. Structurally, Ga-doping increases the  $c$ -axis lattice constant and with it the ferrielectric displacements. Magnetically, Ga-doping weakens the magnetic interactions by dilution. Given these electric and magnetic perturbations, investigating the effect of Ga-doping on the spin-rotation should reveal a lot about the multiferroic nature of  $\text{HoMnO}_3$ . Three separate techniques have been used to measure the change in  $T_{SR}$  of  $\text{HoMn}_{1-x}\text{Ga}_x\text{O}_3$ : magnetic susceptibility, dielectric permittivity, and specific heat; the results are displayed in Figure 5.12.

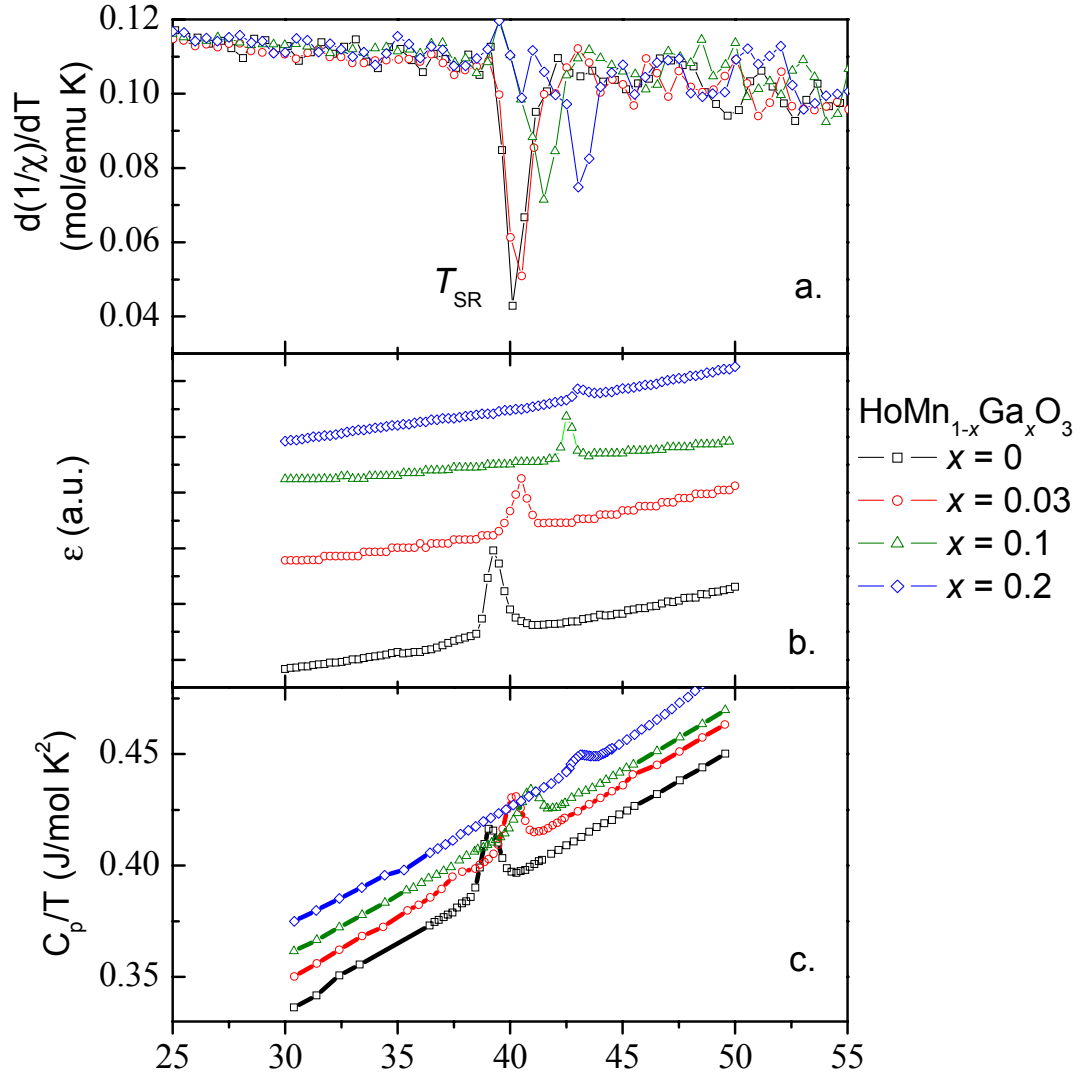


Figure 5.12: Evolution of the spin-rotation temperature ( $T_{\text{SR}}$ ) for  $\text{HoMn}_{1-x}\text{Ga}_x\text{O}_3$  observed by differentiation of the inverse magnetic susceptibility (a), dielectric permittivity (b), and specific heat (c) (Zhou et al. 2005; Zhou et al. 2006a).

For all three measurements (magnetic susceptibility, dielectric permittivity, and specific heat) there are clear peaks indicating the position of  $T_{\text{SR}}$ . It is also evident that there is a monotonic increase in  $T_{\text{SR}}$  as the Ga-doping is increased and the intensity of the

peaks at  $T_{SR}$  decreases with increasing Ga-doping. A closer investigation of the  $T_{SR}$  dependence on Ga-doping reveals there are slight disagreements between the  $T_{SR}$  determined by the different methods; the  $T_{SR}$  dependence on Ga-doping is shown in Figure 5.13.

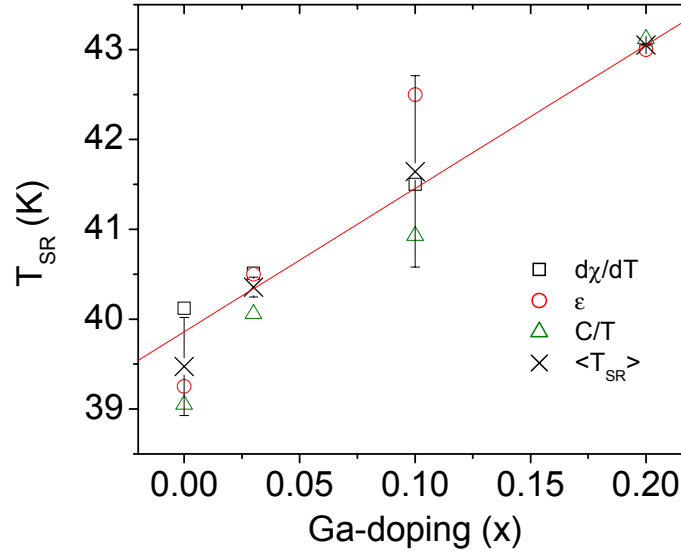


Figure 5.13: Dependence of the spin-rotation temperature on Ga-doping, the  $\times$ -symbols are averages of the  $T_{SR}$  determined by the magnetic susceptibility, dielectric permittivity, and specific heat.

The error in  $T_{SR}$  is likely experimental error due to the different experimental setups used to make the three measurements; however, the experimental error does not detract from the monotonic increase in  $T_{SR}$  with Ga-doping. Since  $T_{SR}$  is the boundary between two different magnetic phases, the increase in  $T_{SR}$  represents a relative energetic stabilization of the intermediate-temperature phase relative to the high-temperature phase. The decrease in the peak intensity with increasing Ga doping is an indication that the change in entropy at the phase transition is decreasing.



## 5.5 SECOND SPIN ROTATION

Neutron-diffraction studies show that below  $T_2 \approx 5$  K the Mn-spins of  $\text{HoMnO}_3$  rotate again to order in the  $P6_3cm$  magnetic phase; the rotation is coupled to a magnetic ordering of one of the two Ho-sites (Lonkai et al. 2002). Lorenz *et al.* have shown that a dielectric peak does occur at  $T_2$ ; however, 5 K is the limit of our dielectric-measurement setup. Although the evolution of  $T_2$  with increasing  $x$  in the series  $\text{HoMn}_{1-x}\text{Ga}_x\text{O}_3$  cannot be observed by my dielectric measurements, it was possible to observe  $T_2$  with magnetic susceptibility measurements and specific-heat measurements.

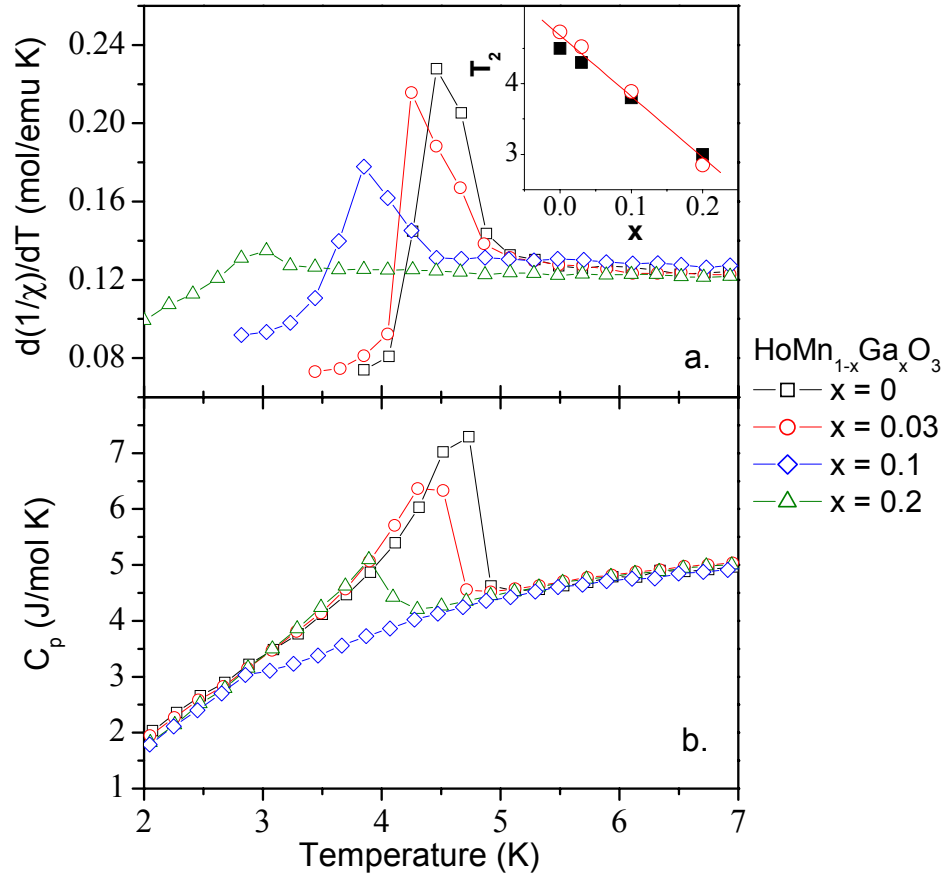


Figure 5.14: Evolution of the second spin-rotation temperature ( $T_2$ ) as peaks in the temperature dependences of the differentiated, inverse magnetic susceptibility (a) and specific heat (b); the inset shows the change in  $T_2$  for increasing Ga-doping in  $\text{HoMn}_{1-x}\text{Ga}_x\text{O}_3$  (Zhou et al. 2005; Zhou et al. 2006a).

Although Ga-doping increased the temperature of the first spin-rotation ( $T_{\text{SR}}$ ), the temperature ( $T_2$ ) and the intensity of the specific-heat peak decrease with increasing Ga doping. The decrease of  $T_2$  parallels that of  $T_N$ , which indicates that the low-temperature magnetic ordering on the Mn sub-array drives the long-range magnetic order of the  $\text{Ho}^{3+}$  ions.

## 5.6 DISCUSSION

The HTXRD data of Lukaszewicz and Karut-Kalicinska show that the symmetry of hexagonal  $\text{YMnO}_3$  goes from centrosymmetric  $P6_3/mcm$  to non-centrosymmetric  $P6_3cm$  as the sample is cooled below 1273 K (Lukaszewicz and Karut-Kalicinska 1974); however, the peak in the pyroelectric current caused by the ferrielectric transition does not occur until 935 K according to Ismailzade and Kizhaev (Ismailzade and Kizhaev 1965). Density-functional calculations by van Aken *et al.* show that the loss of mirror-plane symmetry is associated with the cooperative tilting of the bipyramids (Van Aken *et al.* 2004); the tilting allows for a cooperative ferrielectric displacement of the R – O chains to occur without changing the hexagonal symmetry. Our observations of a larger thermal contraction above  $T_C$  and an increase in  $T_C$  for  $\text{RMn}_{1-x}\text{Ga}_x\text{O}_3$  with increasing  $x$  support the idea that the ferrielectricity is triggered at a critical rotation angle of the bipyramids, which is consistent with the two-step ferrielectric model, *i.e.*  $T_C < T_t$ .

The temperature of the antiferromagnetic transition ( $T_N$ ) of  $\text{RMn}_{1-x}\text{Ga}_x\text{O}_3$  for (R = Y, Ho) was not dependent on the magnetic properties of the  $\text{R}^{3+}$  cation but was dependent on the amount of Ga doping, which decreased  $T_N$  by diluting the magnetic interactions. Although  $\text{YMnO}_3$  and  $\text{HoMnO}_3$  have the same  $T_N$ , neutron diffraction (Lonkai *et al.* 2002; Munoz *et al.* 2001; Van Aken *et al.* 2001b) and second-harmonic generation (Fiebig *et al.* 2002; Fiebig *et al.* 2000; Fiebig *et al.* 2003) studies have shown that the magnetic phase in the compounds is different; the Mn-spins of  $\text{YMnO}_3$  order into the  $P6_3'cm'$  structure whereas they order into the  $P6_3'c'm$  structure in  $\text{HoMnO}_3$ . This subtle difference in the magnetic structure appears to be the result of a difference in the interplanar magnetic interactions through the magnetic  $\text{Ho}^{3+}$  cations versus the non-magnetic  $\text{Y}^{3+}$  cations.

The transition at  $T_{SR}$  in  $\text{HoMnO}_3$  is not present in  $\text{YMnO}_3$ . Since the sizes of the  $\text{Y}^{3+}$  and  $\text{Ho}^{3+}$  cations are nearly the same and  $T_N$  is the same for both compounds, the appearance of a  $P6_3'c'm$  phase in the interval  $T_{SR} < T < T_N$  in  $\text{HoMnO}_3$  must be due to interactions between the  $4f^{10}$  electrons on the  $\text{Ho}^{3+}$  cation and the  $\text{Mn}^{3+}$  cations – even in the absence of magnetic order on the  $\text{Ho}^{3+}$  cations. With magnetic ordering of the  $\text{Ho}^{3+}$  cations below  $T_2$ , the magnetic symmetry of the  $\text{Mn}^{3+}$  ions changes again to  $P6_3cm$ . In the interval  $T_2 < T < T_{SR}$ , the  $P6_3'cm'$  symmetry is the same as that for  $\text{YMnO}_3$  at all temps below  $T_N$ .

Since Ga-doping increases the trigonal-bipyramid cooperative rotations and ferrielectric displacements, the increase of  $T_{SR}$  with increasing Ga doping is an indication that the magnetic phase transition at  $T_{SR}$  occurs at some critical  $c$ -axis lattice constant or bipyramid rotation. A peak in the dielectric constant occurs at  $T_{SR}$  because the polarizability of the structure is increased when the exchange-striction is unlocked during the transition.

Below  $T_2 \approx 5$  K, the spins rotate again and another peak is observed in the dielectric constant, magnetic susceptibility, and specific heat. Increasing the Ga doping of  $\text{HoMn}_{1-x}\text{Ga}_x\text{O}_3$  decreases  $T_2$ . Ga doping dilutes the Ho-O-Mn magnetic interactions that drive the magnetic phase transition at  $T_2$  that is associated with ordering of one of the Ho sites. The increase in  $T_{SR}$  and the decrease in  $T_2$  show that the intermediate phase is stabilized by Ga-doping.

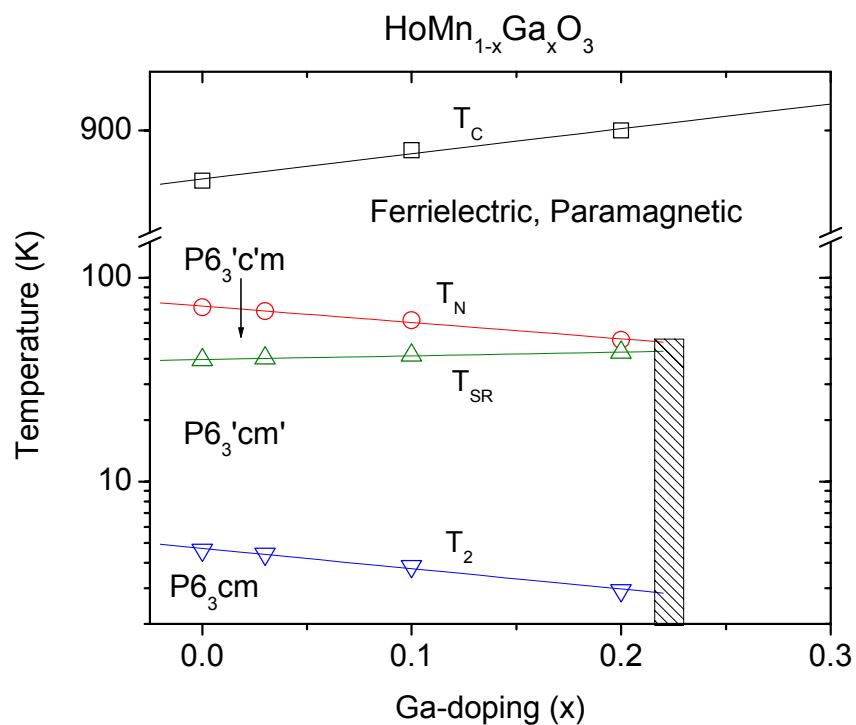


Figure 5.15: Phase diagram for  $\text{HoMn}_{1-x}\text{Ga}_x\text{O}_3$  indicating the ferrielectric transition temperature ( $T_C$ ), the antiferromagnetic transition temperature ( $T_N$ ), the spin-rotation temperature ( $T_{SR}$ ), and the second spin-rotation temperature ( $T_2$ ).

## Chapter 6: $\text{Sr}_x\text{Ca}_{1-x}\text{MnO}_{3-\delta}$

The series  $\text{Sr}_x\text{Ca}_{1-x}\text{MnO}_{3-\delta}$  has been investigated for the relationship between its magnetic and structural properties (Chmaissem et al. 2001) as well as the relationship between its phase stability and structural properties (Dabrowski et al. 2003). The structural phase diagram for the series presented in Figure 6.1 shows the progression of the perovskite crystal symmetry from orthorhombic to tetragonal to cubic as the Sr content is increased from 0 to 1. It also shows the temperature limit above which the phase begins to lose oxygen and form oxide-ion vacancies. The shaded area of the graph represents the compounds that form an alternative phase under ambient conditions; these samples require a non-equilibrium two-step synthesis to stabilize the perovskite phase because the larger  $\text{Sr}^{2+}$  ion stretches the Mn – O bonds beyond their equilibrium value.

For a given temperature, the equilibrium bond length is equivalent to the Mn – O bond length on the cubic side of the cubic to tetragonal transition. Compositions that are to the right of the cubic to tetragonal transition have a Mn – O bond length that is under tensile strain and an A – O bond length that is under compressive strain; compositions that are to the left of the cubic to tetragonal transition have the opposite bond strain relationship: the Mn – O bond is under compressive strain and the A – O bond is under tensile strain. At room temperature the equilibrium Mn – O bond length determined from the lattice constant of  $\text{Sr}_{0.8}\text{Ca}_{0.2}\text{MnO}_3$  (Chmaissem et al. 2001) is 1.986 Å.

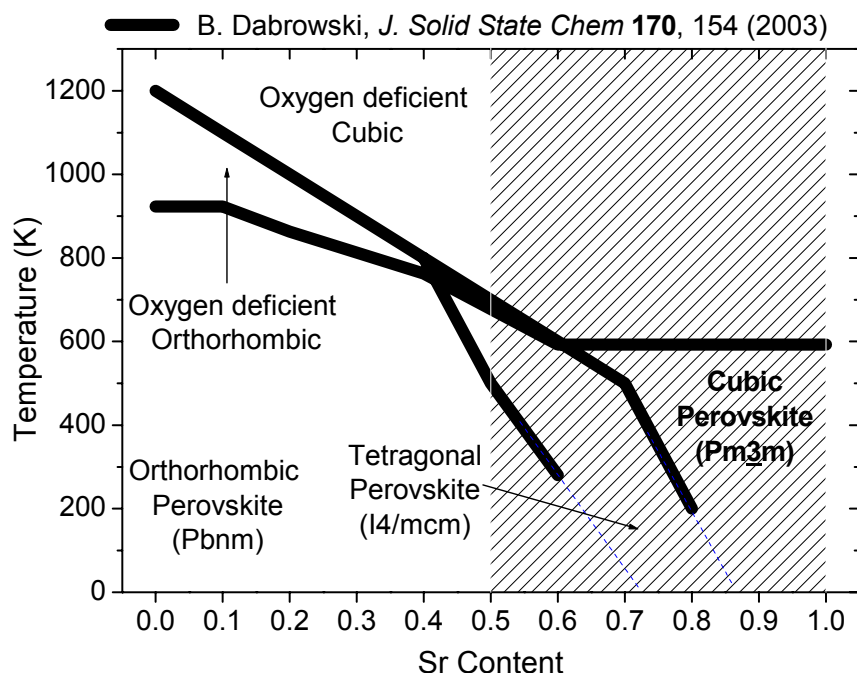


Figure 6.1: Thermo-structural phase diagram for the series  $\text{Sr}_x\text{Ca}_{1-x}\text{MnO}_{3-\delta}$  (Dabrowski et al. 2003).

The series  $\text{Sr}_x\text{Ca}_{1-x}\text{MnO}_3$  is isostructural with  $(\text{Sr,Ca})\text{TiO}_3$ , which exhibits technologically important dielectric phenomena as well as a physically interesting competition between ferroelectric and paraelectric behavior. Measuring the dielectric behavior of  $\text{Sr}_x\text{Ca}_{1-x}\text{MnO}_3$  with its  $d^3 \text{Mn}^{4+}$  cations allows a comparison with  $\text{Sr}_x\text{Ca}_{1-x}\text{TiO}_3$  and its  $d^0 \text{Ti}^{4+}$  cations.

The dielectric behavior for  $\text{Sr}_x\text{Ca}_{1-x}\text{MnO}_{3-\delta}$  for  $0 \leq x \leq 0.75$  has already been measured (Cohn et al. 2004); however, samples with  $x > 0.5$  were oxygen deficient (Neumeier 2005) and the effect of oxygen vacancies on the dielectric behavior is unknown in that study. The temperature dependence of the dielectric constant and loss tangent has been measured in the cubic perovskite phase of  $\text{SrMnO}_3$  down to 100 K (Lee

and Iguchi 1995); however, this was not a low enough temperature to observe a dielectric relaxation and reveal the intrinsic contribution of the ionic polarization. Thus, questions about the dielectric behavior of Sr rich  $\text{Sr}_x\text{Ca}_{1-x}\text{MnO}_3$  still remain open.

The goal of this investigation was to measure the intrinsic dielectric constant of the increasingly stretched  $\text{Mn}^{4+} - \text{O} - \text{Mn}^{4+}$  bond as  $x$  increases from 0.5 to 1 in the series  $\text{Sr}_x\text{Ca}_{1-x}\text{MnO}_{3-\delta}$ ; consideration is given to the value of  $\delta$  to investigate the effect of oxygen vacancies on the dielectric behavior.

## 6.1 SYNTHESIS

Polycrystalline samples in the series  $\text{Sr}_x\text{Ca}_{1-x}\text{MnO}_{3-\delta}$  were synthesized by mixing stoichiometric ratios of  $\text{SrCO}_3$ ,  $\text{CaCO}_3$ , and  $\text{MnO}_2$ . For  $x < 0.5$ , samples were fired in an ambient environment at 1250 - 1300°C for 20-30 hours with intermediate grindings. The X-ray diffraction patterns revealed no impurity phases.

For  $\text{Sr}_x\text{Ca}_{1-x}\text{MnO}_{3-\delta}$  samples with  $x \geq 0.5$ , a two-step method was necessary to obtain the perovskite phase over the more stable hexagonal-polytype phase. The hexagonal polytype forms as the geometric tolerance factor exceeds one.

$$t = \frac{(A - O)}{\sqrt{2}(M - O)} \quad (6.1)$$

Here,  $(A - O)$  and  $(M - O)$  are the mean equilibrium cation – oxide-ion bond lengths for the Alkaline Earth and manganese cations, respectively.

Figure 6.2 shows the different stacking of the cubic perovskite phase versus the hexagonal-4H polytype by using 2-dimensional representations of the oxygen-octahedra; the cubic phase has corner-linked octahedra, whereas the hexagonal-4H phase has two face-shared octahedra corner-linked to another unit of face-shared octahedra.



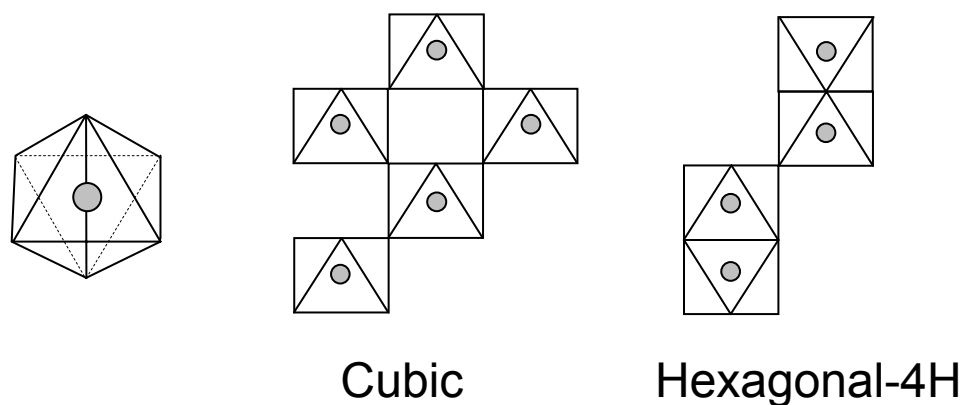


Figure 6.2: Schematic representation of the 6-fold coordinated oxygen octahedra, the cubic static of octahedra, and the four layer hexagonal stacking.

Generally there is a larger thermal expansion of the (A – O) bond than the (Mn – O) bond, so the tolerance factor increases with temperature. Thus, samples with a Sr molar content as low as 0.5 have a tolerance factor greater than 1 at the temperatures necessary for solid-state reactions to occur. There is no way for the perovskite structure to relieve the strain caused by a tolerance factor greater than one at ambient pressure; the introduction of alternating cubic and hexagonal stacking of the  $\text{AO}_3$  planes relieves this strain, but at the expense of a larger Coulomb repulsion between  $\text{Mn}^{4+}$  cations across a shared face. Samples with Sr content between 0.5 and 0.8 tend to form a mixture of both phases, and samples with Sr content greater than 0.8 tend to form the hexagonal phase under ambient conditions.

Stabilizing the perovskite phase requires lowering the tolerance factor. This can be accomplished by increasing the temperature high enough to form oxide-ion vacancies that reduce two  $\text{Mn}^{4+}$  cations into two  $\text{Mn}^{3+}$  cations for each oxide-ion vacancy. The  $\text{Mn}^{3+}$  cation has a larger ionic radius than  $\text{Mn}^{4+}$ ; thus, having more  $\text{Mn}^{3+}$  reduces the

tolerance factor. In this first synthesis step, the samples were heated to 1250 - 1400°C in an ambient environment to exhaust the carbonate precursors and form the oxygen-deficient perovskite phase (Negas and Roth 1970); the environment was changed to an argon atmosphere without cooling and fired for an additional 10 hours before the sample was cooled at a rate of 3°C/min in argon. Cooling in argon prevents the sample from transforming into the low-temperature hexagonal-polytype phase (Chmaissem et al. 2001; Dabrowski et al. 2003). Figure 6.3 illustrates how cooling in an inert atmosphere permits access to the oxygen-deficient perovskite phase. The phase boundaries are delineated by the experiments of Negas and Roth; their X-ray and oxidation analysis data were taken after quenching samples from different temperatures.

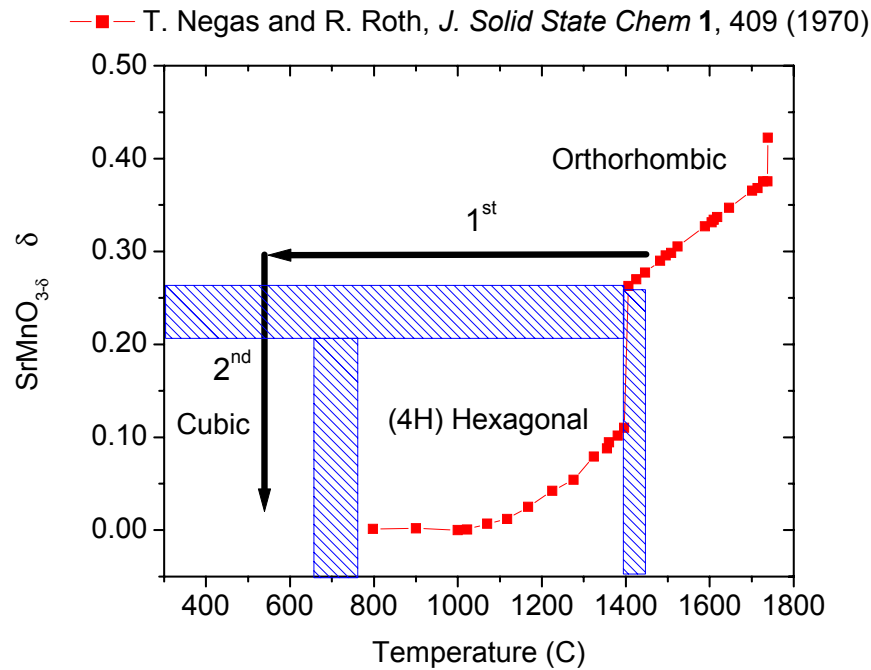


Figure 6.3: Oxygen vacancy phase diagram for  $\text{SrMnO}_{3-\delta}$  illustrating the non-equilibrium path for obtaining the cubic perovskite phase (Negas and Roth 1970).

The first arrow in Figure 6.3 indicates the cooling process that takes place as the sample is quenched, or preferably slow-cooled in an inert atmosphere. The second arrow indicates the second step: the sample is transferred to a low-temperature tube furnace and annealed at 300 - 600°C in an O<sub>2</sub> atmosphere to oxidize the samples.

The method of cooling in an inert atmosphere makes a difference in the nature of the oxygen-vacancy ordering in the oxygen-deficient perovskite phase. If the sample is quenched, the oxygen vacancies are randomly located at oxygen sites in the perovskite structure. If the sample is slow-cooled in Argon, the oxygen vacancies order into regular long-range patterns, altering the size of the unit cell. The extreme case is SrMnO<sub>2.5</sub> where all the Mn-cations have a 3+ valence state. SrMnO<sub>2.5</sub> has an orthorhombic cell with the lattice parameters  $a \approx \sqrt{2} a_c$ ,  $b \approx 2\sqrt{2} a_c$ ,  $c \approx a_c$  (Caignaert et al. 1985), where  $a_c$  is the cubic lattice parameter of SrMnO<sub>2.5</sub> with random oxide-ion vacancies. The change in the unit cell means there will be additional peaks in the X-ray diffraction pattern; the diffractograms shown in Figure 6.4 illustrate this point.

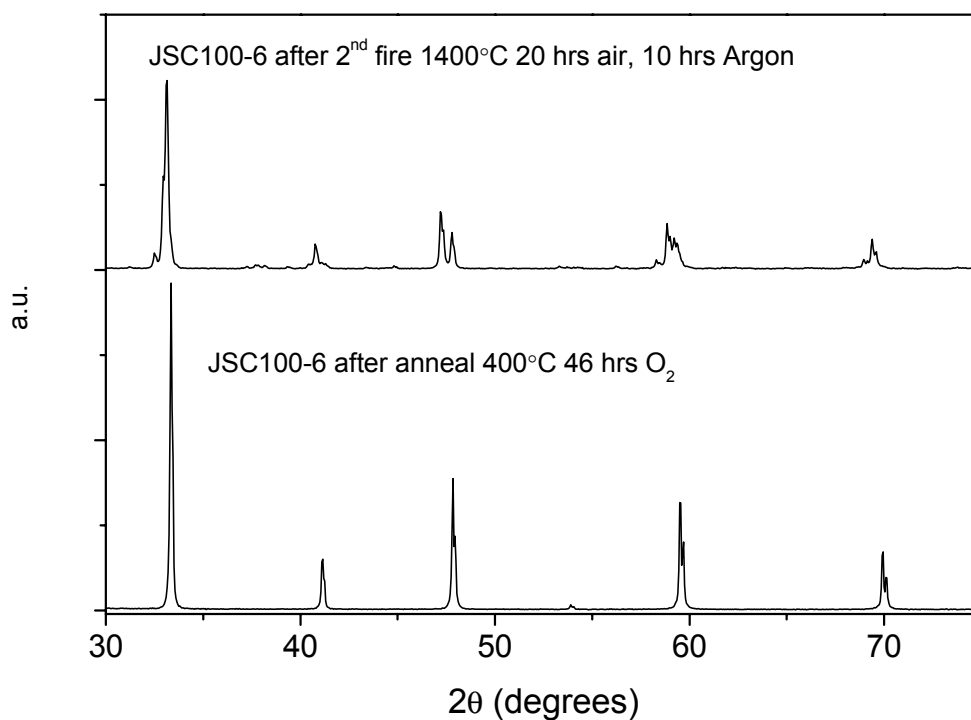


Figure 6.4: The X-ray diffraction patterns for  $\text{SrMnO}_{3-\delta}$  sample (JSC100-6) before and after oxygen annealing.

The top diffractogram from the oxygen deficient  $\text{SrMnO}_{3-\delta}$  has many peak splittings whereas after the oxygen anneal there are only single peaks at positions consistent with the cubic  $Pm\bar{3}m$  space group.

Most oxygen-deficient  $\text{SrMnO}_{3-\delta}$  samples are not reduced to the extreme  $\text{SrMnO}_{2.5}$ ; a close comparison of the diffractograms reveals peak splittings not accounted for by the peak list of  $\text{SrMnO}_{2.5}$  in the powder diffraction file database. The peaks unaccounted for originate from other orderings of smaller oxide-ion vacancy fractions. These orderings have been investigated in  $\text{CaMnO}_{3-\delta}$  where long-range ordering of the oxide-ion vacancies occurs at  $\delta = 0.2$  (Reller et al. 1983), 0.25 (Chiang

and Poeppelmeier 1991), and 0.5 (Poeppelmeier et al. 1982). As with  $\text{CaMnO}_{3-\delta}$ ,  $\text{SrMnO}_{3-\delta}$  samples with oxide-ion fractions that do not correspond to ordered fractions segregate into regions of ordered fractions. This leads to diffraction patterns that look as though several impurities phases have formed; however, after oxygen annealing the diffraction patterns look to be representative of a single phase.

## **6.2 DIELECTRIC BEHAVIOR OF $\text{CaMnO}_{3-\delta}$**

After investigation of the impedance behavior of a group of  $\text{Sr}_x\text{Ca}_{1-x}\text{MnO}_{3-\delta}$  samples, it became clear that there were several extrinsic effects that interfere with the intrinsic dielectric phenomena. It then became necessary to investigate the dielectric behavior of these extrinsic effects in the parent phase  $\text{CaMnO}_3$ , which has a more extensive record of theoretical and experimental investigations to support the data.

### **6.2.1 Effects of oxygen annealing**

In Figures 6.5a and 6.5b the temperature and frequency dependences of the dielectric relaxations are plotted for a  $\text{CaMnO}_3$  sample before and after an oxygen anneal. In the data taken before annealing, the relative dielectric constant relaxes from a value of about 125 whereas the annealed sample relaxes from a value above the range of the graph at 75 K and below  $10^4$  Hz.

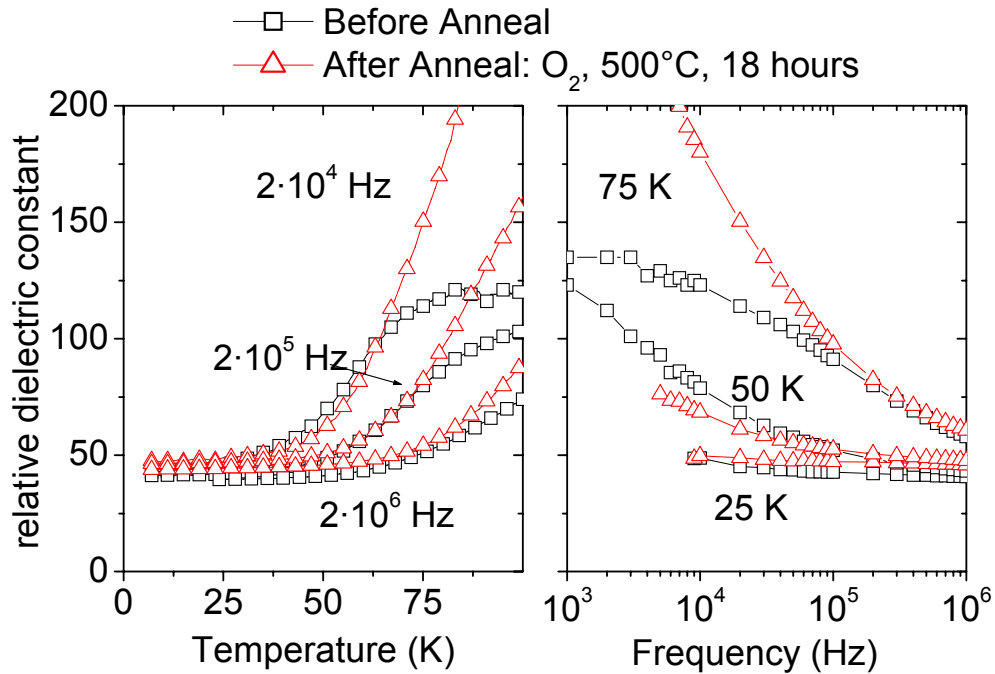


Figure 6.5: The dielectric relaxations of  $\text{CaMnO}_{3-\delta}$  as a function of temperature (a) and frequency (b).

At temperatures around 25 K, where there is a convergence in the dielectric constant of the annealed and unannealed samples, the charge carriers of both samples are frozen out and the dielectric response converges to the bulk value determined by the ionic polarization of the structure.

The stoichiometry differences between the samples are highlighted in the thermoelectric power versus temperature,  $\alpha(T)$ , behavior of the annealed and unannealed  $\text{CaMnO}_3$  sample shown in Figure 6.6; the  $\alpha(T)$  behavior reveals a difference in the number of oxide-ion vacancies. The unannealed sample has a small absolute value with a metallic-like temperature dependence whereas the annealed sample has a very large

absolute value, as anticipated for fewer activated charge carriers and less oxide-ion vacancies.

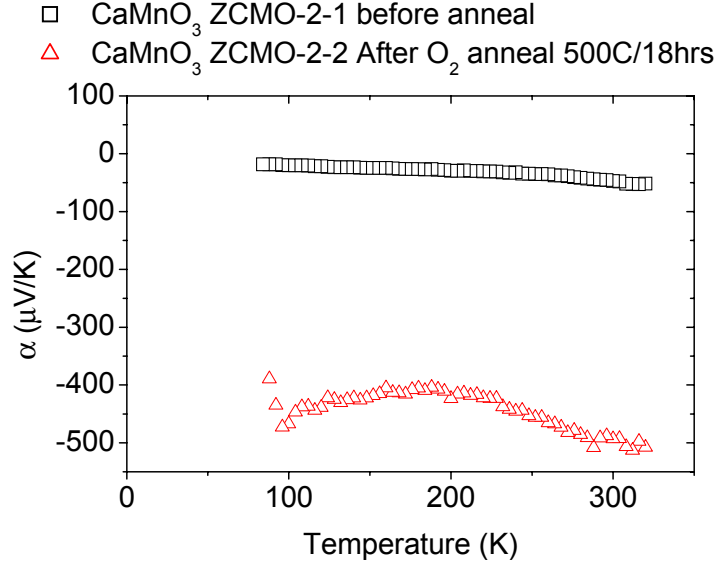


Figure 6.6: Thermoelectric power temperature dependencies for a  $\text{CaMnO}_{3.8}$  sample (ZCMO-2) before and after annealing in oxygen.

### 6.2.2 Surface capacitance effects

Discrepancies in the dielectric behavior are a common occurrence for samples with slight geometric variations as well as oxidative variations. For instance, in figure 6.7 a  $\text{CaMnO}_3$  sample was measured before and after cutting the sample down to a smaller thickness. The relaxations for the different thicknesses cross at increasingly lower frequencies for data taken at lower temperatures. At 40 K, the dielectric constants of the thicker and thinner samples do not cross in the frequency range displayed; although the dielectric constant has not relaxed to the intrinsic ionic value  $\epsilon_r \sim 50$ , the dielectric constant of both samples converge and approach the same limit together.

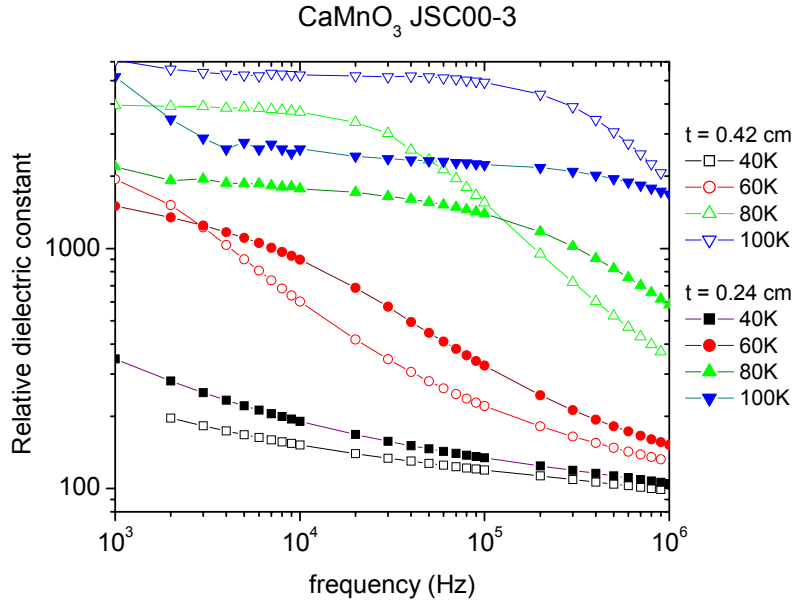


Figure 6.7: Comparison of the dielectric relaxations of a  $\text{CaMnO}_{3.8}$  sample (JSC00-3) cut to two different thickness: 0.42 cm and 0.24 cm respectively.

The variation in the dielectric relaxations of the  $\text{CaMnO}_3$  sample cut to different thicknesses reveals that the dielectric relaxation mechanism does not scale with the thickness of the sample. Space-charge polarization at the surface of the sample is a likely candidate to explain this phenomenon. Since the space charge occurs near the surface, changing the thickness does not change its contribution to the measured capacitance; so when the measured capacitance is scaled to determine the dielectric constant, the thicker sample exhibits a larger dielectric constant at frequencies where the space-charge polarization dominates.



### 6.2.3 Sample density effects

In addition to variations in the dielectric relaxation caused by differences in the oxidative state and the space-charge polarization contribution, the dielectric relaxations also depend on the grain structure of the polycrystalline samples (Barsoukov and Macdonald 2005). The dielectric relaxations of a sample with loosely packed grains are more sensitive to the size, shape, and orientation of the grains in comparison to densely packed samples. Figure 6.8 illustrates this effect by comparing two samples: the first sample was sintered after pressing into a pellet with a piston-press and less than 1 MPa of pressure, which yielded a density  $\rho = 3.1 \text{ g/cm}^3$ ; the second sample was sintered after pressing a rod of polycrystalline powder with  $\sim 10 \text{ MPa}$  of hydrostatic pressure and had a  $\rho = 4.6 \text{ g/cm}^3$ .

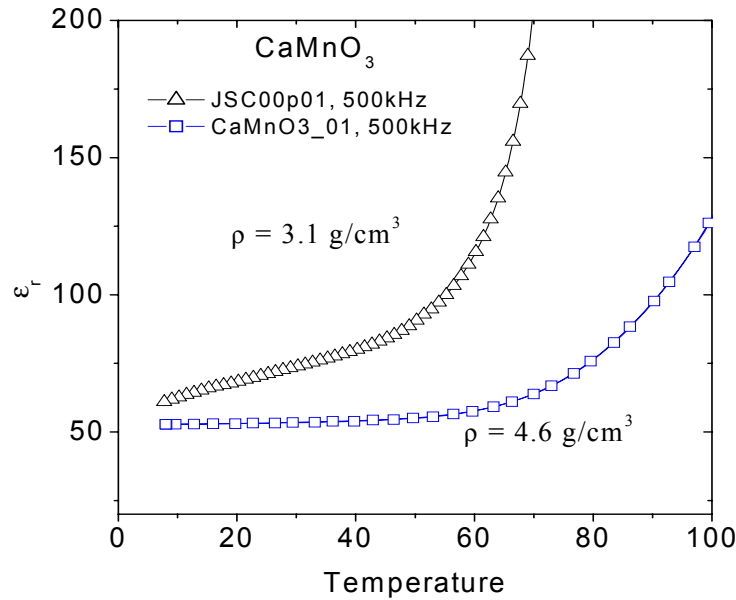


Figure 6.8: The dielectric relaxation of two  $\text{CaMnO}_3$  samples of different densities.

The changes in the dielectric relaxation behavior upon annealing in oxygen, changing the sample dimensions, or changing the sample density reveal extrinsic factors that influence the dielectric behavior. On the other hand, the convergence of the dielectric constant at low temperatures and high frequencies is indicative of an intrinsic bulk property of the material:  $\epsilon_r \cong 50$ . This value is in agreement with the value of  $\epsilon_r = 55 \pm 6$  measured by Cohn (Cohn et al. 2004).

### 6.3 DIELECTRIC BEHAVIOR OF $\text{Sr}_x\text{Ca}_{1-x}\text{MnO}_3$ ( $0 < x < 0.5$ )

Cohn's group measured the  $\text{Sr}_x\text{Ca}_{1-x}\text{MnO}_3$  series for  $x = 0, 0.1, 0.2, 0.3, 0.5, 0.75$ . For samples with  $x < 0.5$ , the synthesis was performed in an ambient environment; for samples with  $x \geq 0.5$  the samples were synthesized in an Argon environment and are oxygen deficient (Neumeier 2005). The intrinsic ionic polarization dielectric constant was determined by inspection of the low-temperature limit of the dielectric constant.

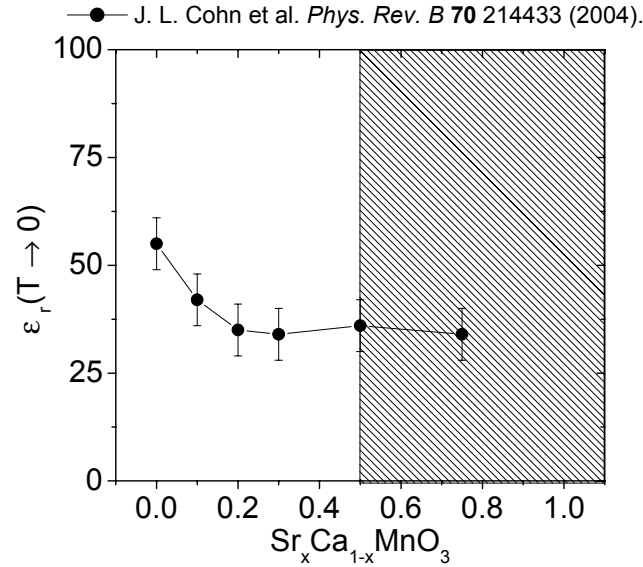


Figure 6.9: Dielectric phase diagram of  $\text{Sr}_x\text{Ca}_{1-x}\text{MnO}_3$  ( $0 \leq x \leq 0.75$ ); data taken from (Cohn et al. 2004). The shaded area ( $x > 0.5$ ) represents an oxygen-deficient region.

The dielectric phase diagram of Cohn *et al.* shows the dielectric constant monotonically decreases from a value of 55 for  $\text{CaMnO}_3$  to a value of 35 for  $\text{Sr}_{0.2}\text{Ca}_{0.8}\text{MnO}_3$ . The shaded area covers the portion of the phase diagram where the samples are oxygen deficient.

#### **6.4 DIELECTRIC BEHAVIOR OF $\text{Sr}_x\text{Ca}_{1-x}\text{MnO}_3$ ( $0.5 \leq x \leq 1$ )**

A closer investigation of samples with Sr mole fractions greater than 0.5 revealed dramatically different admittance behavior between samples that had a large amount of oxygen vacancies and those that were slightly oxygen deficient.

Samples with  $x = 0.60, 0.75$ , and 1 were prepared from  $\text{CaCO}_3$ ,  $\text{SrCO}_3$ , and  $\text{MnO}_2$  precursors with the solid state technique. The polycrystalline pellets were sintered in Argon to obtain the oxygen-deficient perovskite phase and then sliced into thin disks. Half of the disks were annealed in an oxygen environment for 18 to 46 hours at temperatures of  $400^\circ\text{C} - 500^\circ\text{C}$ . The admittance was measured on the unannealed and annealed disks. Iodimetric titration was performed on five samples of unannealed and annealed disks, respectively, to determine the oxidative state of the manganese and the number of oxygen vacancies in each sample.

Table 6.1: The annealing conditions and fraction of oxygen vacancies of  $\text{Sr}_x\text{Ca}_{1-x}\text{MnO}_{3-\delta}$  samples measured by impedance spectroscopy.

	Sample Name	Anneal Conditions	$\delta$
$\text{Sr}_{0.6}\text{Ca}_{0.4}\text{MnO}_{3-\delta}$	JSC060-3A-3	-	$0.39 \pm 0.01$
	JSC060-3A-1	$\text{O}_2$ , 400°C, 41 hrs	$0.02 \pm 0.01$
$\text{Sr}_{0.75}\text{Ca}_{0.25}\text{MnO}_{3-\delta}$	JSC075-3C-4	-	$0.37 \pm 0.01$
	JSC075-3C-2	$\text{O}_2$ , 500°C, 18 hrs	$0.02 \pm 0.01$
$\text{SrMnO}_{3-\delta}$	JSC100-7-6	-	$0.44 \pm 0.01$
	JSC100-7-1	$\text{O}_2$ , 400°C, 40 hrs	$0.05 \pm 0.01$

Figures 6.10a, 6.10b show the AC-conductivity and dielectric behavior for the unannealed and annealed pieces of the  $\text{Sr}_{0.6}\text{Ca}_{0.4}\text{MnO}_{3-\delta}$  pellet. The unannealed sample with  $\delta = 0.39$  has a significantly lower conductivity than the annealed sample with  $\delta = 0.02$ . In addition, the temperature dependence of the dielectric constant of the unannealed sample shows a relaxation to a value of  $\epsilon_r = 20$ . The dielectric constant of the annealed sample looks to be relaxing from a value of  $\epsilon_r = 3 \times 10^5$  at high temperatures to a lower value, but it has not relaxed enough to reveal the frequency and temperature independent dielectric behavior indicative of the dielectric contribution due to the ionic polarization.

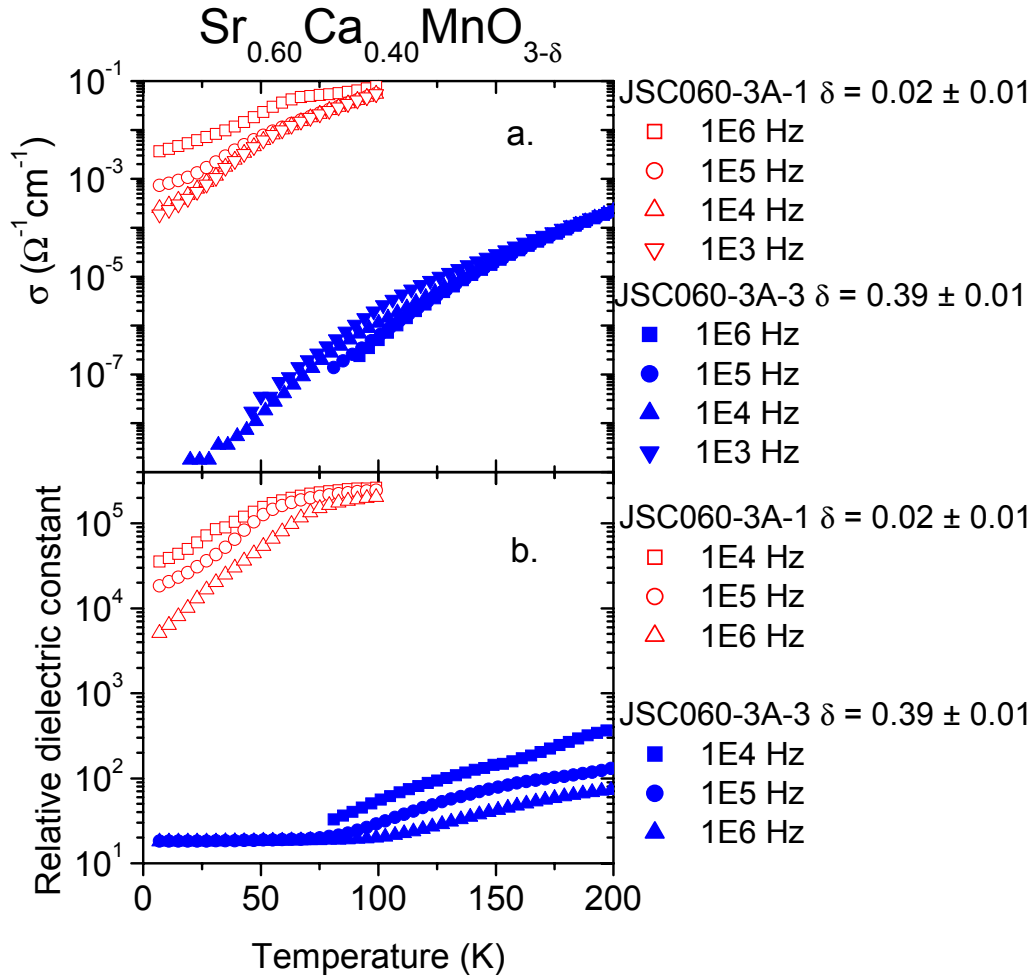


Figure 6.10: AC-conductivity (a) and dielectric (b) temperature dependencies for  $\text{Sr}_{0.6}\text{Ca}_{0.4}\text{MnO}_{3-\delta}$  samples with  $\delta = 0.39$  and  $0.2$ .

The thermoelectric properties of  $\text{Sr}_{0.75}\text{Ca}_{0.25}\text{MnO}_{3-\delta}$  were measured in addition to the dielectric properties to provide additional information as to the electronic character. The thermoelectric power of the all samples had roughly similar temperature dependencies for the range investigated, which means that the oxide-ion vacancies are responsible for the change in the statistical offset of the thermoelectric power. The samples also all had a negative thermoelectric power, which means they were all n-type.

The unannealed sample (JSC075-3C-5) had a high temperature limit of  $-200 \mu\text{V/K}$ , the sample annealed in oxygen for 18 hours had a limit of  $-300 \mu\text{V/K}$ , and the samples annealed for 60 hours both in ozone (JSC075-3B) and oxygen (JSC075-3A) had a limit of  $-330 \mu\text{V/K}$ .

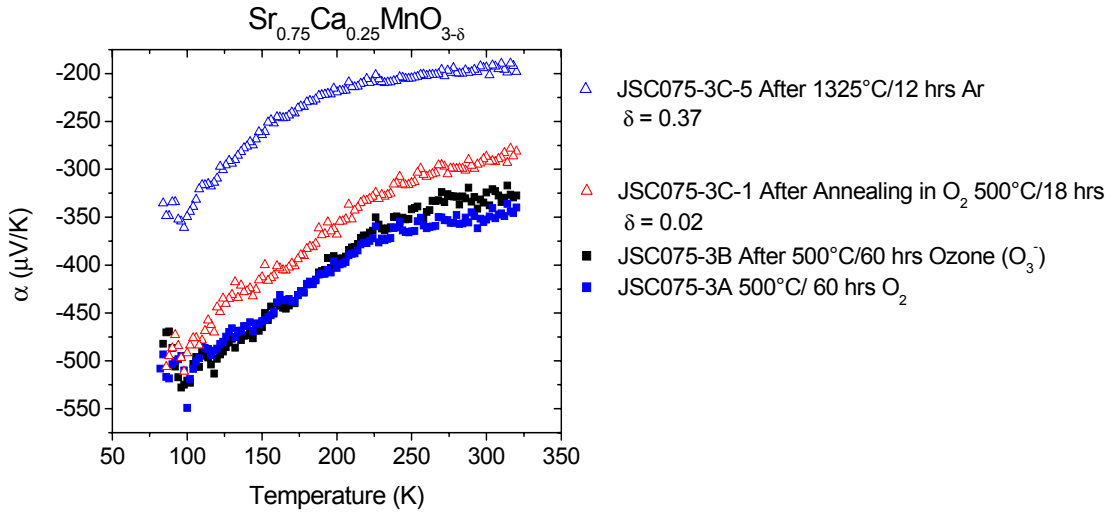


Figure 6.11: Thermoelectric power of  $\text{Sr}_{0.75}\text{Ca}_{0.25}\text{MnO}_{3-\delta}$  samples having undergone a variety of annealing conditions.

The comparisons of conductivity and dielectric constant between the unannealed and annealed pieces of  $\text{Sr}_{0.75}\text{Ca}_{0.25}\text{MnO}_{3-\delta}$  are similar to those for  $\text{Sr}_{0.6}\text{Ca}_{0.4}\text{MnO}_{3-\delta}$ . The unannealed sample, with  $\delta = 0.37$ , has a lower conductivity and exhibits a dielectric relaxation to an  $\epsilon_r = 25$  at low temperatures and high frequencies; the annealed sample, with  $\delta = 0.02$ , is more conductive; even at 10 K,  $\epsilon_r$  has not begun to decrease toward a value representing the dielectric contribution of the ionic polarization.

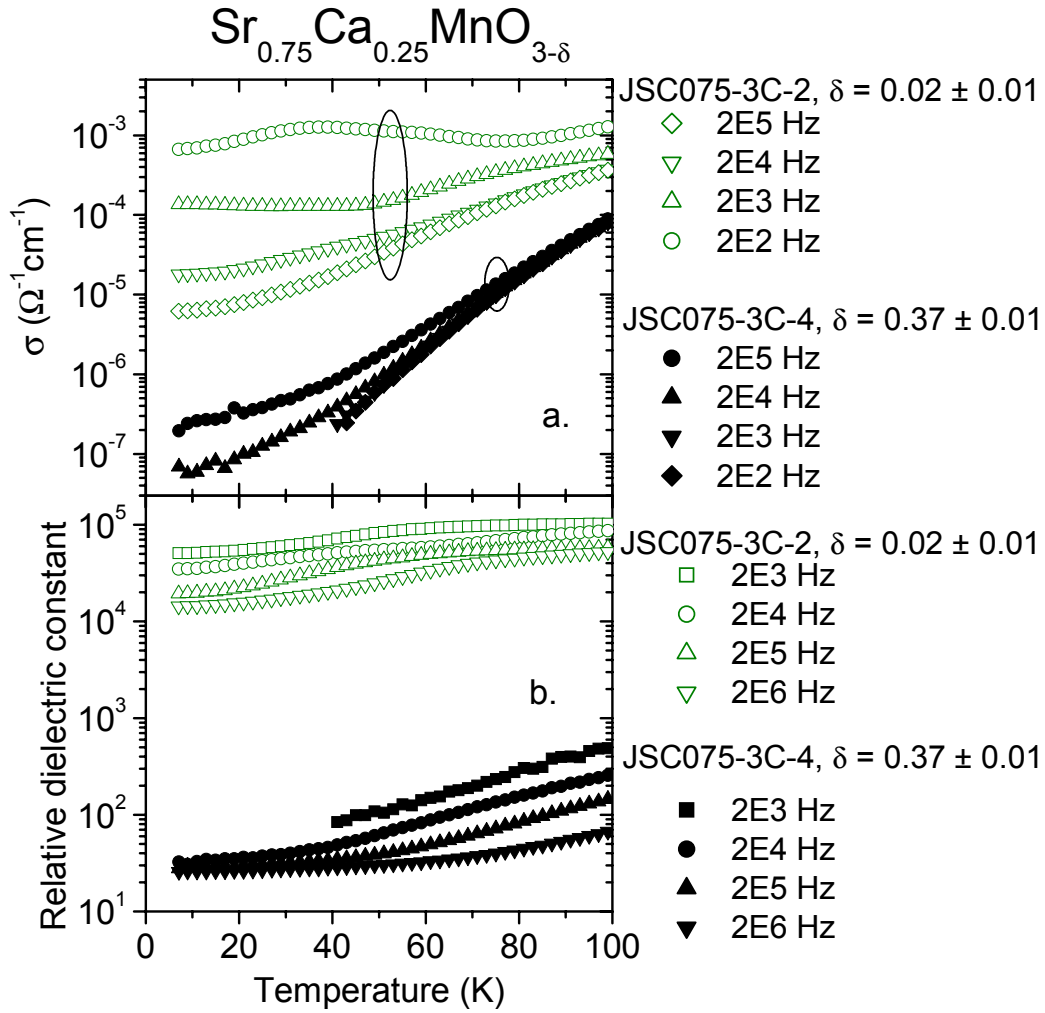


Figure 6.12: AC-conductivity (a) and dielectric (b) temperature dependencies for  $\text{Sr}_{0.75}\text{Ca}_{0.25}\text{MnO}_{3-\delta}$  samples with  $\delta = 0.37$  and  $0.2$ .

The admittance of the  $\text{SrMnO}_{3-\delta}$  unannealed samples shows similar conductivity and dielectric constant temperature dependences as the  $\text{Sr}_{0.6}\text{Ca}_{0.4}\text{MnO}_{3-\delta}$  and  $\text{Sr}_{0.75}\text{Ca}_{0.25}\text{MnO}_{3-\delta}$  samples: the conductivity is significantly lower for the unannealed sample, with  $\delta = 0.44$ , and the dielectric constant relaxes to an  $\epsilon_r = 24$ . The annealed  $\text{SrMnO}_{3-\delta}$  sample with  $\delta = 0.05$  differs from the other annealed samples in that the

conductivity shows a stronger temperature dependence at low temperatures; the strong temperature dependence leads to a low-frequency conductivity of  $10^{-7} \Omega^{-1}\text{cm}^{-1}$  at 10 K whereas  $\text{Sr}_{0.6}\text{Ca}_{0.4}\text{MnO}_{3-\delta}$  and  $\text{Sr}_{0.75}\text{Ca}_{0.25}\text{MnO}_{3-\delta}$  have low-frequency conductivities of  $10^{-4} \Omega^{-1}\text{cm}^{-1}$  and  $10^{-5} \Omega^{-1}\text{cm}^{-1}$ , respectively. In addition, the dielectric constant of the annealed  $\text{SrMnO}_{3-\delta}$  sample does appear to be converging on a number near  $\epsilon_r \approx 100$  whereas the other samples have not approached a frequency and temperature-independent value.



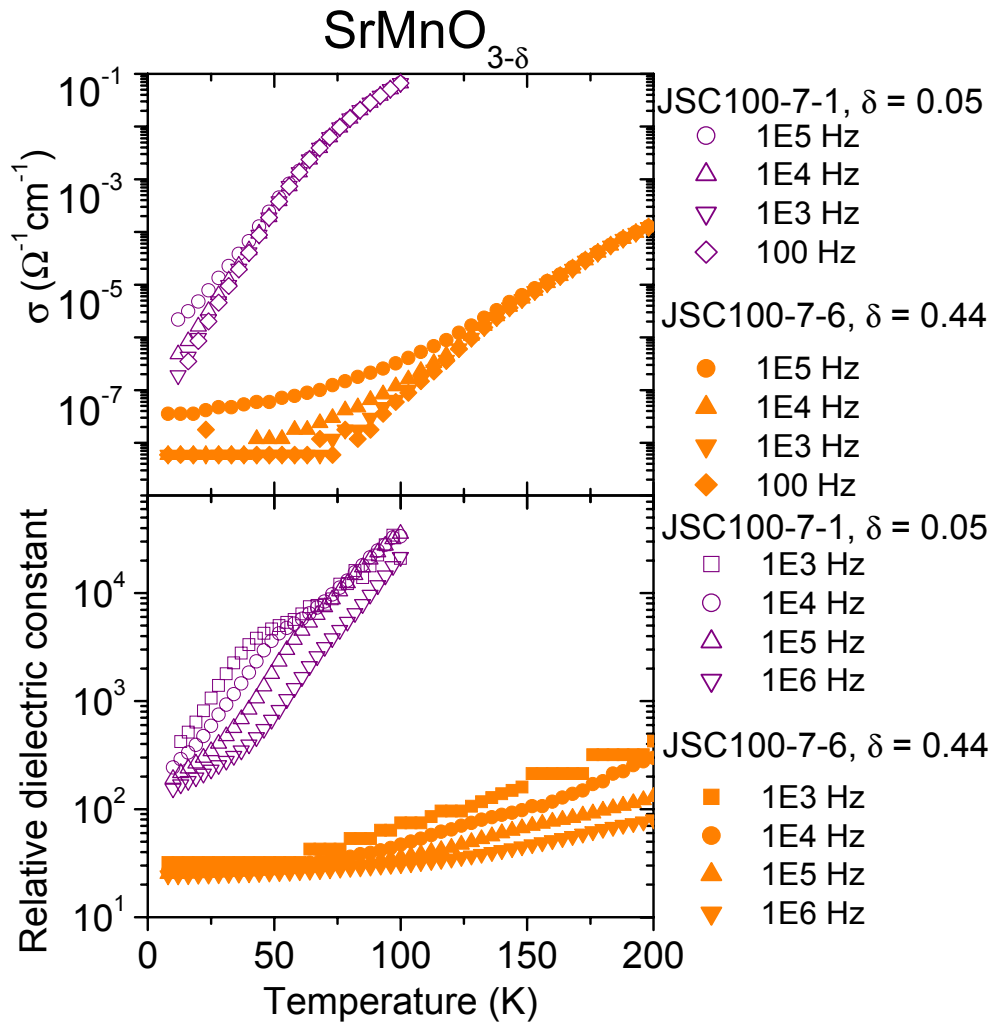


Figure 6.13: AC-conductivity (a) and dielectric (b) temperature dependencies for  $\text{SrMnO}_{3-\delta}$  samples with  $\delta = 0.44$  and  $0.05$ .

Extrapolating the dielectric constant by eye for the unannealed samples is straight-forward in that there is very little temperature and frequency dependence to suggest that a relaxation process is still occurring. Although the temperature-dependent curves for different frequencies appear to be converging, extrapolating the dielectric constant from the temperature dependence of the annealed  $\text{SrMnO}_{3-\delta}$  sample is more a

leap of faith; a more rigorous analysis is needed. To perform an accurate extrapolation, the exponential frequency dependence, or UDR (Chapter 4), of the dielectric relaxation was exploited to fit the data and to determine the value of the dielectric constant in the high-frequency limit ( $\epsilon_\infty$ ).

$$\epsilon_r = A\omega^{s-1} + \epsilon_\infty \quad (6.2)$$

Figure 6.14a shows the data and exponential fitting curves for temperatures from 10 K to 30 K. The curves appear to converge at high frequency and the fitting parameter  $\epsilon_\infty$  ranged from 90 – 120 for frequency curves taken at temperatures from 10 K to 24 K. Above 24 K the fitting gets progressively less dependent on the parameter  $\epsilon_\infty$  and thus less accurate for extrapolation. The weighted ensemble average of the parameter  $\epsilon_\infty$  from the fits of data from 10 K to 30 K gives a value of  $\epsilon_r = 111$ . Figure 6.14b shows this convergence in a linear fashion by plotting the dielectric constant vs. the independent variable  $\omega^{s-1}$ .

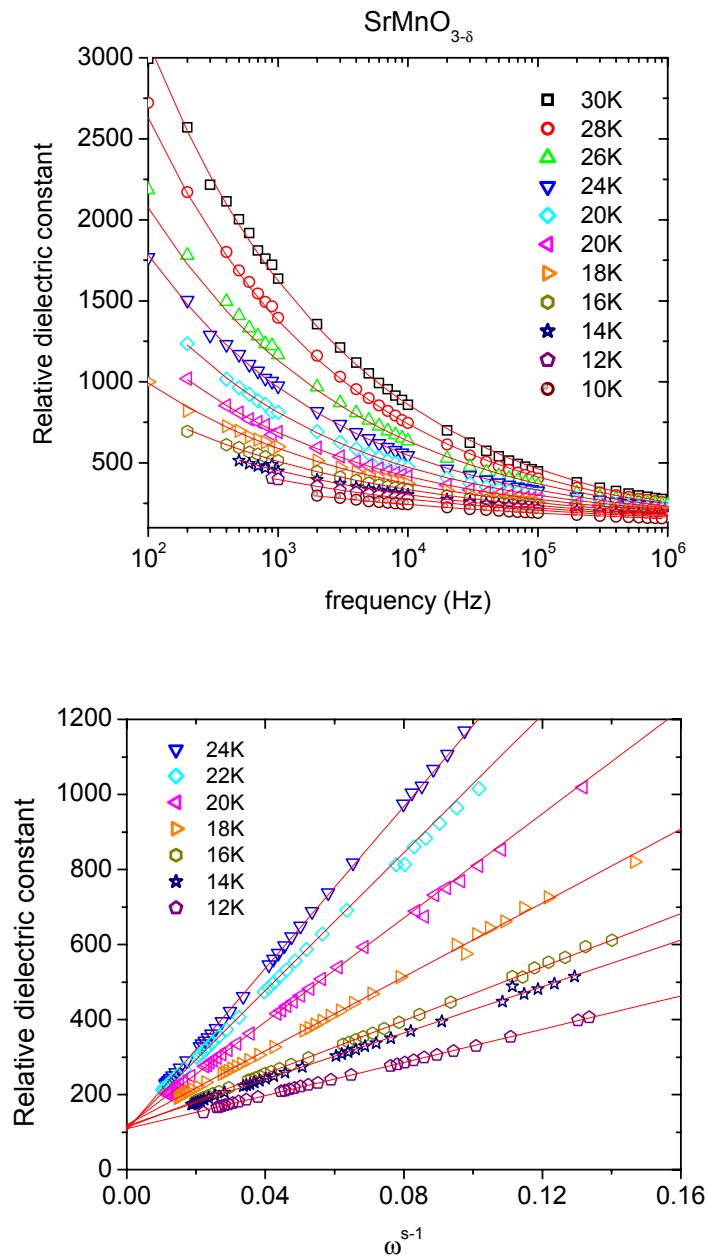


Figure 6.14: Fitting of the dielectric relaxation convergence of  $\text{SrMnO}_{3-\delta}$  ( $\delta = 0.5$ ) with a non-linear curve fit (a) and a linear fit (b).

## 6.5 DISCUSSION

From the impedance investigations on  $\text{CaMnO}_{3-\delta}$ , it is clear that the dielectric relaxations are dependent on the sample stoichiometry, surface, and density. This emphasizes the importance of the low-temperature and high-frequency convergence of the dielectric constant to give confidence that the extrapolated value is intrinsic to the material and is the high-frequency dielectric constant ( $\epsilon_\infty$ ) representative of the dielectric contributions of the ionic and electronic polarizations.

The phase diagram of the dielectric behavior of  $\text{Sr}_x\text{Ca}_{1-x}\text{MnO}_3$  for  $x = 0 - 0.75$  given by Cohn *et al.* shows a decrease of the dielectric constant from  $\epsilon_r = 55$  for  $\text{CaMnO}_3$  to  $\epsilon_r \sim 35$  for  $\text{Sr}_{0.2}\text{Ca}_{0.8}\text{MnO}_3$  to  $\text{Sr}_{0.75}\text{Ca}_{0.25}\text{MnO}_{3-\delta}$ . Cohn supposes that this larger value for  $\text{CaMnO}_3$  is due to a larger number of carriers; however, Figure 6.5 shows that the relaxations approach the same temperature-independent value of  $\epsilon_r \sim 50$  for a sample before and after oxygen annealing. The thermoelectric power of this sample, shown in Figure 6.6, is evidence that the carrier density of this sample is different before and after annealing. Thus the larger dielectric behavior cannot be accounted for by a larger carrier density. Since the dielectric constant that is shown in the phase diagram is intrinsic and is  $\epsilon_\infty$ , an alternative explanation is that the increasing Sr content leads to the smooth, monotonic decrease of the dielectric constant. There are two polarizable networks: the Mn – O bonds and the A – O bonds. Since the tolerance factor is less than one in this region of the phase diagram, it is the polarizability of the A – O bond that dominates the dielectric behavior. The increase in the tolerance factor lowers the tensile strain on A – O array and that lowers the restoring force of the ionic oscillator and leads to a decrease in the polarizability.

The dielectric behavior of Sr-rich samples of  $\text{Sr}_x\text{Ca}_{1-x}\text{MnO}_{3-\delta}$  ( $x = 0.6, 0.75, 1$ ) was measured for samples that had a large  $\delta$  ( $\delta = 0.39, 0.37, 0.44$ ), and oxygen-annealed samples that have a small  $\delta$  ( $\delta = 0.02, 0.02, 0.05$ ). All of the samples with large  $\delta$  had dielectric relaxations that converged on a low-temperature and high-frequency temperature-independent value of  $\epsilon_r \sim 20 - 25$ . X-ray diffraction studies revealed that the oxygen-deficient samples contain phases with ordered oxygen vacancies as well as disordered vacancies. Thermoelectric power indicates that the large- $\delta$  samples are n-type and the smaller magnitude of the thermoelectric power shows that either the number of electron charge carriers has increased or the number of sites available for hopping has decreased. Since the conductivity of the large- $\delta$  samples is significantly lower than that of the small- $\delta$  samples, a larger number of charge carriers would mean they have a much lower mobility.

The slightly oxygen-deficient samples  $x = 0.6$  and  $x = 0.75$  did not exhibit dielectric relaxations to a temperature-independent value within the frequency bandwidth of  $10 \text{ Hz} - 10^6 \text{ Hz}$  and temperature range  $10 \text{ K} - 300 \text{ K}$ . The number of oxygen vacancies ( $\delta = 0.02$ ) was significant enough to increase the carrier concentration without decreasing the mobility. For  $\text{SrMnO}_{2.95}$ , the larger concentration of oxygen vacancies did give a lower conductivity than that of the annealed  $x = 0.6$  and  $0.75$  samples. The conductivity was low enough that the relaxation curves could be extrapolated to give  $\epsilon_\infty = 111$ . If this extrapolated value is the intrinsic dielectric constant due to the ionic polarization, then this result supports the idea that it is the increased equilibrium Mn – O bond length that leads to an increase in the dielectric response from  $\text{CaMnO}_3$  to  $\text{SrMnO}_3$ .

## Chapter 7: $\text{SrMn}_{1-x}\text{B}_x\text{O}_{3-\delta}$ ( $\text{B} = \text{Mn}^{3+}, \text{Ni}^{2+}, \text{Ti}^{4+}, \text{Zr}^{4+}$ )

One of the results of the work presented in Chapter 6 was that the conductivity and dielectric behavior of  $\text{SrMnO}_{3-\delta}$  is strongly dependent on the stoichiometry, or mole-fraction of oxygen vacancies  $\delta$ .  $\text{Sr}_{1-x}\text{Ca}_x\text{MnO}_{3-\delta}$  samples with large values of  $\delta$  had dielectric relaxations to a temperature-independent and frequency independent value of  $\epsilon_r \sim 20 - 30$ . Conversely, samples with a small  $\delta$  had significantly larger conductivities, and even at temperatures below 10 K and frequencies of  $10^6$  Hz, their dielectric constants have not relaxed to a value representative of the ionic polarization.

This chapter explores the electronic effects of a nonzero  $\delta$  and presents the results for the doping scheme investigated to overcome the challenges of measuring the dielectric behavior of  $\text{SrMnO}_{3-\delta}$  for  $\delta < 0.05$ .

### 7.1 $\text{SrMn}^{4+}_{1-2\delta}\text{Mn}^{3+}_{2\delta}\text{O}_{3-\delta}$

Synthesizing  $\text{SrMnO}_{3-\delta}$  and obtaining the perovskite phase requires the formation of a significant amount of oxygen vacancies to create enough  $\text{Mn}^{3+}$  to relieve the strain associated with having a tolerance factor greater  $t > 1$ . After forming the perovskite phase, it is possible to oxidize  $\text{SrMnO}_{3-\delta}$  in Air or oxygen at low temperatures ( $300^\circ\text{C} - 600^\circ\text{C}$ ) where there is still good oxide-ion reactivity but no transformation of the cubic phase.

Several researchers claim to have reached  $\text{SrMnO}_3$  (Negas and Roth 1970) or  $\text{SrMnO}_{3.00 \pm 0.01}$  (Chmaissem et al. 2001; Dabrowski et al. 2003) after oxidation in air whereas another group reported  $\text{SrMnO}_{2.97}$  (Tichy and Goodenough 2002) after the same procedure. This seemingly slight discrepancy is actually quite important to the electronic character of the material since each oxygen vacancy is a double donor, creating two  $\text{Mn}^{3+}$  neighbors. If the samples are nearly stoichiometric, the energy gap  $\Delta_0$  between the

oxygen-2p valence band and the  $\text{Mn}^{3+}/\text{Mn}^{4+}$  redox couple would be expected to be several 100 meV, as illustrated in Figure 7.1a. However, if there are trapped electrons near oxygen vacancies, the trapping energy of the electrons near a vacancy would be on the order of several tens of meVs.

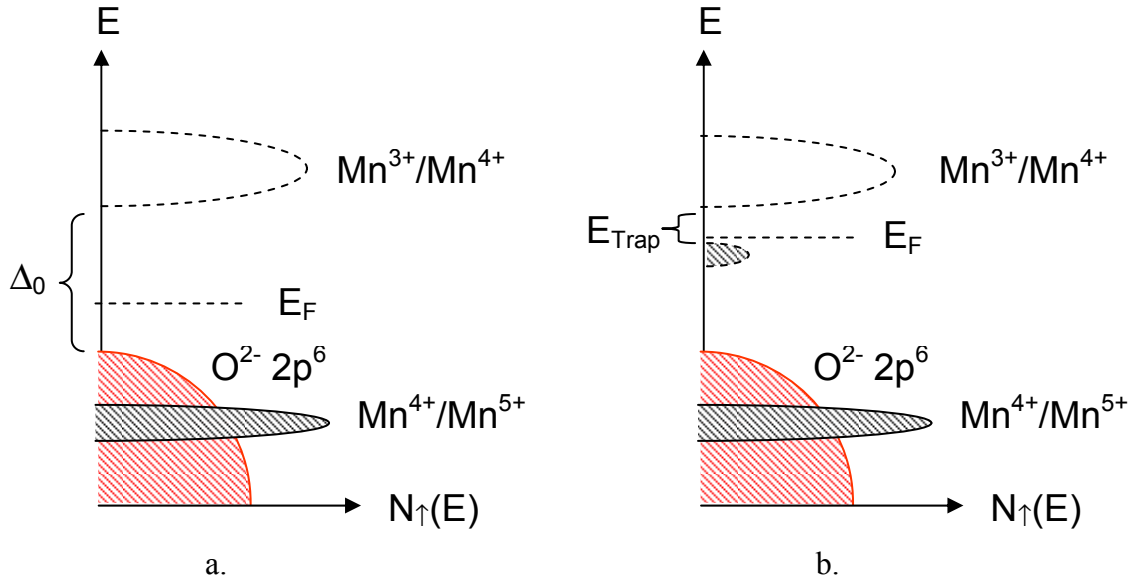


Figure 7.1: Sketches of the half-spin density of states for a stoichiometric (a) and reduced sample(b).

The oxygen content of the samples made by Negas and Roth and Chmaissem and Dabrowski were determined by thermogravimetric analysis (TGA), which is capable of measuring the relative weight changes of a sample upon heating or cooling in different atmospheres. Negas and Roth (Negas and Roth 1970) do not discuss the precision of their result or how the relative measurement can be used to determine the absolute oxidation content. Chmaissem and Dabrowski (Chmaissem et al. 2001; Dabrowski et al. 2003) normalize their TGA data by assuming the starting oxygen content is 3.00; perhaps not a good assumption. This leaves the question open as to whether  $\text{SrMnO}_{3-\delta}$  can be oxidized up to  $\delta = 3.00 \pm 0.01$ .

Even if  $\text{SrMnO}_{3-\delta}$  can be oxidized up to  $\delta = 3.00 \pm 0.01$  in a TGA instrument, the oxidation of polycrystalline pellets is less complete than the small volume of fine powder used in TGA experiments. Fine powder has the advantage of a large surface area and small particle volume for the oxygen to penetrate and oxidize the sample. For pellets, the interior grains are less likely to be oxidized. In addition, the denser the pellet, the more difficult it is for oxygen to penetrate. This creates competing requirements for measuring the dielectric behavior of the  $\text{Mn}^{4+}$  compounds: loosely packed samples would be ideal for oxygen penetration during oxidation; on the other hand, observing intrinsic dielectric properties requires densely-packed samples to limit grain boundary effects in the dielectric response.

Although there is some disagreement in the literature as to how efficiently the  $\text{SrMnO}_{3-\delta}$  can be oxidized in air, thermoelectric power measurements performed at The University of Texas at Austin and elsewhere (Maignan et al. 2002) show  $\text{SrMnO}_{3-\delta}$  to be n-type; this means that there are always some oxygen vacancies, even after annealing. Figure 7.2 illustrates the evolution of the thermoelectric power as the number of oxygen vacancies is reduced with successive anneals; the sample was synthesized using the two-step method (Dabrowski et al. 2003), left to sit in an ambient environment for several months, and then it was measured before and after it was annealed twice.



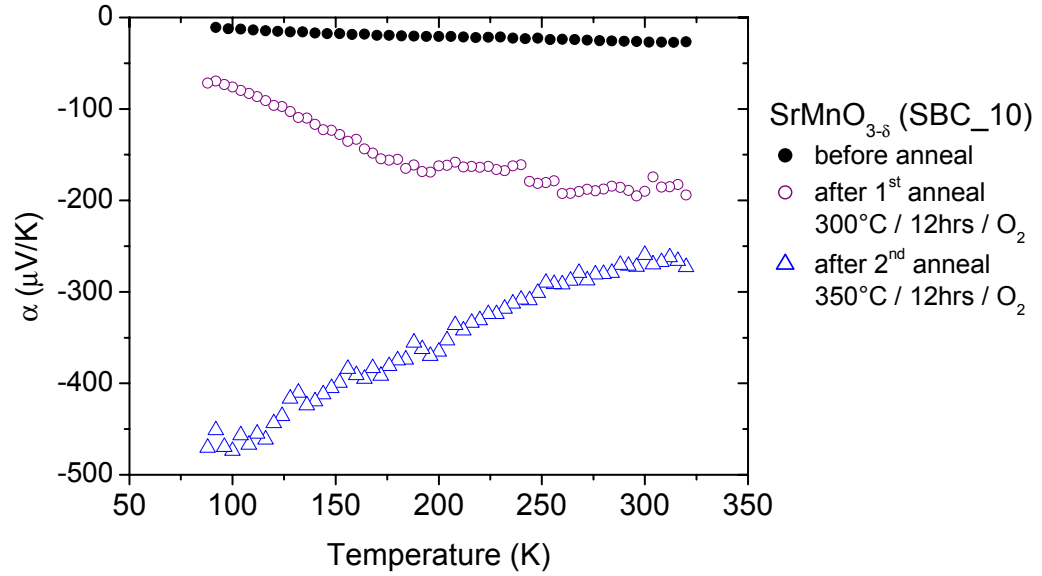


Figure 7.2: Evolution of the thermoelectric power Seebeck coefficient of  $\text{SrMnO}_{3-\delta}$  before and after sitting for several months in an ambient environment and then undergoing successive anneals in an oxygen atmosphere.

The high temperature limit of the  $\alpha(T)$  curves appear to be approaching a temperature-independent value. The temperature-independent value represents the entropy associated with small polaron hopping; the strong electronic correlations in manganese oxides remove the need for a spin degeneracy factor and this entropy term has a simple expression:

$$S = \frac{k}{q} \ln \left( \frac{1-x}{x} \right) \quad (7.1)$$

In this expression for the entropy term,  $k$  is Boltzmann's constant,  $q$  is the electronic charge, and  $x$  is the fraction of charge carriers to hopping sites. With this formula, the number of carriers can be estimated from the high-temperature limit to the  $\alpha(T)$  curves. For every two electrons there is one oxygen vacancy; however, when one of electrons is

excited from the trap, the second electron is bound by a larger trapping energy and can be assumed to be inactive at room temperature. Given these assumptions, the number of oxygen vacancies for sample SBC100 is  $\delta = 0.4$  before the first anneal,  $\delta = 0.1$  after the first anneal, and  $\delta = 0.04$  after the second anneal. These values of  $\delta$  seem consistent with expectations after successive anneals. However, the AC-conductivity of samples  $\text{SrMnO}_{2.95}$  (JSC100-7-1) and  $\text{SrMnO}_{2.56}$  (JSC100-7-6) presented in Chapter 6 show that the more oxygen deficient sample is actually less conducting. The difference between the annealed  $\text{SrMnO}_{3-\delta}$  sample (SBC100) and the unannealed (JSC100-7-6) and annealed (JSC100-7-1) is that the oxygen vacancies in SBC100 were created at room temperature and lacked the energy required to order whereas the unannealed sample (JSC100-7-6) was fired at  $1400^\circ\text{C}$  and slow-cooled, allowing for the vacancies to order. The oxygen-ordered phases are significantly more insulating than the disordered phases, and if the ordered phase makes up the majority of the mixture, the sample will be insulating.

It is difficult to measure the intrinsic dielectric behavior of the  $\text{Mn}^{4+} - \text{O} - \text{Mn}^{4+}$  bond as it is increasingly stretched as  $x$  increases from 0.5 to 1 in the series  $\text{Sr}_x\text{Ca}_{1-x}\text{MnO}_{3-\delta}$ . The high conductivity of oxidized samples with small  $\delta$  prohibits the observation of the dielectric relaxations within the experimental space. However, one oxidized Sr-rich sample,  $\text{SrMnO}_{2.95}$  (JSC100-7-1), was resistive enough to allow for the extrapolation of the dielectric behavior. This sample demonstrated that oxide-ion vacancies act as donor centers at a dilute level; however, if the number of ordered vacancies is increased, the periodic potential is changed to produce a greater charge-carrier trapping energy. This brought up an interesting question: could  $\text{SrMnO}_{3-\delta}$  be doped in other ways to increase localization enough to observe the dielectric relaxations of the stretched  $\text{Mn}^{4+} - \text{O} - \text{Mn}^{4+}$  bond?

## 7.2 $\text{SrMn}^{4+}_{1-2\delta+2x}\text{Mn}^{3+}_{2\delta-2x}\text{Ni}^{2+}_x\text{O}_{3-\delta}$

The first effort to make  $\text{SrMnO}_{3-\delta}$  samples less conducting involved Ni doping of the B-site. In the presence of  $\text{Mn}^{3+}$ , Ni cations reduce to  $\text{Ni}^{2+}$  and oxidize  $\text{Mn}^{3+}$  to  $\text{Mn}^{4+}$  (Sanchez et al. 2002); this has already been demonstrated experimentally for a couple of manganese perovskites series:  $\text{LaNi}_{1-x}\text{Mn}_x\text{O}_{3+\delta}$  (Blasco et al. 2002; Sanchez et al. 2002) and  $\text{La}_{0.8}\text{Sr}_{0.2}\text{Mn}_{1-x}\text{Ni}_x\text{O}_{3+\delta}$  (Mori 2004). In addition to oxidizing the  $\text{Mn}^{3+}$  to  $\text{Mn}^{4+}$ , the presence of  $\text{Ni}^{2+}$  would perturb the periodic potential, localizing the electrons further and decreasing the conductivity to make it possible to observe the dielectric relaxation.

There are other potential effects of Ni doping that could influence the results. As shown in Table 7.1, the effective ionic radius of  $\text{Ni}^{2+}$  is larger than the effective ionic radius of  $\text{Mn}^{4+}$  or  $\text{Mn}^{3+}$  (Shannon and Prewitt 1969). The smaller ionic radius would have the effect of reducing the tolerance factor with increasing Ni-doping and lowering the strain of the (Mn – O) bond that prevents  $\text{SrMnO}_{3-\delta}$  from being stoichiometric ( $\delta = 0$ ). However, if the dielectric behavior of the ionic lattice is also dependent on this strain, increasing the Ni doping would also lower the dielectric response.

Table 7.1: Effective ionic radii for  $\text{Mn}^{3+}$ ,  $\text{Mn}^{4+}$  and  $\text{Ni}^{2+}$  (Shannon and Prewitt 1969)

	6-fold (Å)	5-fold (Å)
$\text{Mn}^{3+}$	0.65	0.58
$\text{Mn}^{4+}$	0.54	-
$\text{Ni}^{2+}$	0.70	-

Comparing the effective ionic radii is a good starting point to predict whether the cations have a chance to substitute into a structure based on size. The  $\text{Ni}^{2+}$  cation is slightly larger than either  $\text{Mn}^{3+}$  or  $\text{Mn}^{4+}$ -cation, but not prohibitively larger. In addition to ionic size, another important requirement is that the final compound be charge balanced. The chemical formula for  $\text{Ni}^{2+}$  is  $\text{SrMn}_{1-2\delta+2x}^{4+}\text{Mn}_{2\delta-2x}^{3+}\text{Ni}_x^{2+}\text{O}_{3-\delta}$  with  $x \leq \delta$ . Table 7.2 lists the constraints on the Ni-doping fraction ( $x$ ) along with the fraction of  $\text{Mn}^{4+}$  and  $\text{Mn}^{3+}$  for a given fraction of oxide-ion vacancies.

Table 7.2: Constraints on  $\text{Ni}^{2+}$  ( $x$ ) doping and mole fractions of  $\text{Mn}^{4+}$  and  $\text{Mn}^{3+}$  for various amounts of oxygen vacancies.

$\delta$	$x$	$\text{Mn}^{4+}$	$\text{Mn}^{3+}$
0	$x = 0$	1	0
0.125	$0 \leq x \leq 0.125$	$0.75+2x$	$0.25-2x$
0.25	$0 \leq x \leq 0.25$	$0.5+2x$	$0.5-2x$
0.5	$0 \leq x \leq 0.5$	$2x$	$1-2x$

### 7.2.1 Synthesis

The synthesis of polycrystalline pellets of  $\text{SrMn}_{1-x}\text{Ni}_x\text{O}_{3-\delta}$  was attempted with the same two-step solid-state method that was used for synthesizing  $\text{Sr}_x\text{Ca}_{1-x}\text{MnO}_{3-\delta}$ . Powder precursors of  $\text{SrCO}_3$ ,  $\text{MnO}_2$ , and  $\text{NiO}$ , were mixed in stoichiometric ratios for  $x = 0.02$ , 0.05, and 0.1. After mixing the precursors, the powder was pressed into pellets and fired for 20 hours at 1375°C in air and then 10 hours in argon before cooling in argon. The samples were ground and refired under the same conditions. Finally, the samples were annealed in oxygen for 20 hours at 400°C. Figure 7.3 shows the X-ray diffraction patterns after oxygen annealing for the  $\text{SrMn}_{1-x}\text{Ni}_x\text{O}_{3-\delta}$  for  $x = 0.05$ , and 0.1 as well as  $x = 0$  for a reference.

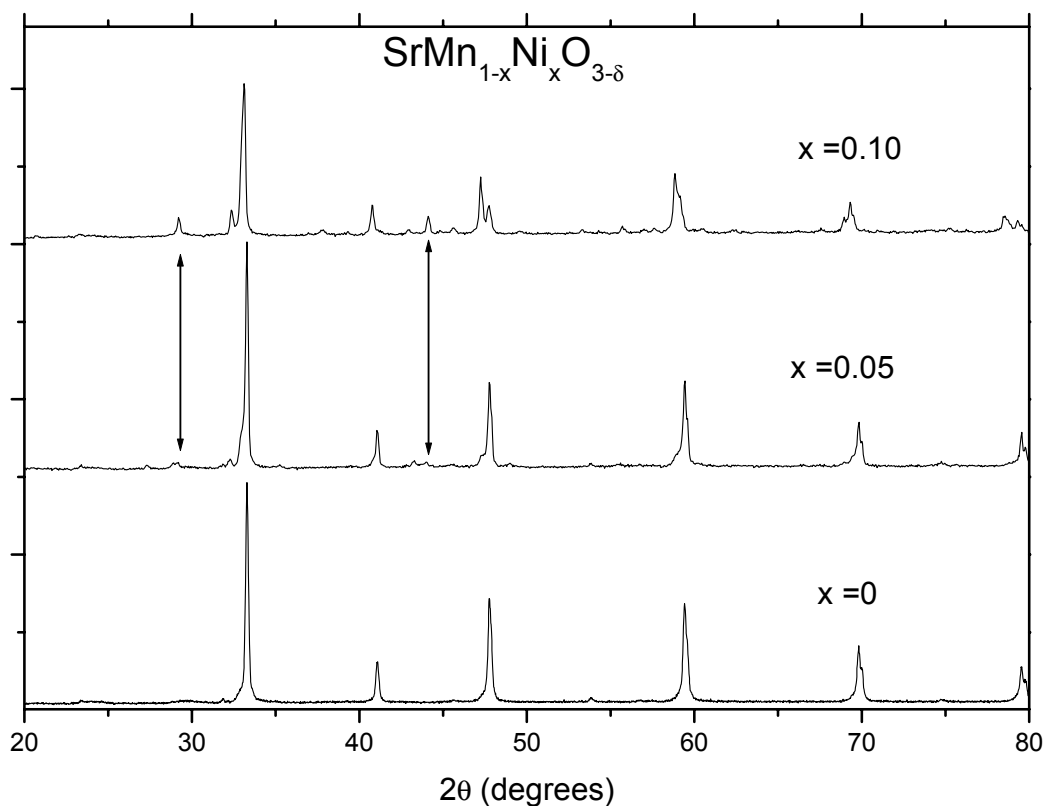


Figure 7.3: X-ray diffraction patterns of  $\text{SrNi}_x\text{Mn}_{1-x}\text{O}_3$  for  $x = 0, 0.05$ , and  $0.1$ ; the arrows indicate a Ni-related impurity phase.

The X-ray diffraction patterns taken after the oxygen anneal reveal that the samples are not single phase. Furthermore, the alumina crucibles used for the high-temperature synthesis step had green outlines of the sample after firing, an indication that the Ni-ions were not incorporating into the structure.

### 7.2.2 Discussion

Although the Ni doping failed to produce single-phase samples, lessons were learned to improve the chances for other doping schemes to succeed. What was missing from the preliminary estimations was a structural model of how the  $\text{Ni}^{2+}$  would substitute

onto either the 5-fold coordinated  $\text{Mn}^{3+}$ -site next to an oxygen vacancy or the 6-fold coordinated  $\text{Mn}^{4+}$ -site, both coordinations are shown in the sketch of the perovskite structure in Figure 7.4.

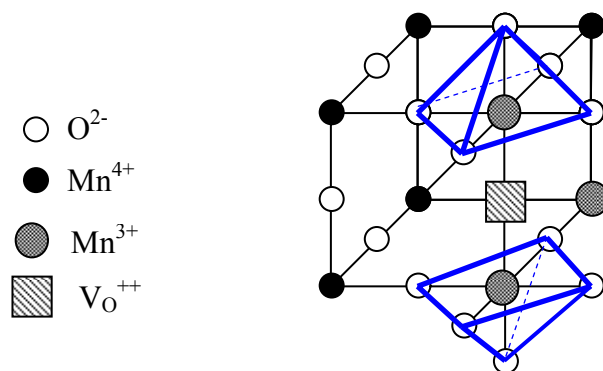


Figure 7.4: Illustration of the two 5-fold coordinated  $\text{Mn}^{3+}$  site created next to an oxygen vacancy

There are two factors that prevent Ni-incorporation on either the 5-fold or 6-fold coordinated sites of the oxygen-deficient perovskite structure of  $\text{SrMnO}_{3-\delta}$ . The first factor is that all the  $\text{Mn}^{3+}$  are trapped at the oxygen vacancies in 5-fold coordination and the  $\text{Ni}^{2+}$  cations, which have a strong octahedral-site preference, do not substitute into 5-fold coordinated sites; this is evident by the absence of data for a 5-fold-coordinated effective ionic radius in Table 7.1. The second factor is that the substitution of  $\text{Ni}^{2+}$  for  $\text{Mn}^{4+}$  on a 6-fold site would require a  $\text{Mn}^{3+}$  trapped at an oxygen vacancy to be oxidized to a  $\text{Mn}^{4+}$  to maintain charge balance; however,  $\text{Mn}^{4+}$  also does not tolerate 5-fold coordination. Thus, the  $\text{Ni}^{2+}$  has no site on which to substitute.

The second factor prohibiting  $\text{Ni}^{2+}$  incorporation onto a 6-fold site is general and has important implications for future doping schemes: the  $\text{Mn}^{3+}$  trapped next to an oxide-ion vacancy can only be oxidized to  $\text{Mn}^{4+}$  by filling the vacancy. This requirement

means that cation doping must be compensated to achieve charge balance if the valence is less than 4+.

### 7.3 $\text{SrMn}^{4+}_{1-2\delta-x}\text{Mn}^{3+}_{2\delta}\text{Ti}^{4+}_x\text{O}_{3-\delta}$

One of the conclusions of the Ni-doping experiment was that it would be easier to achieve charge balance by substituting a 4+ cation on the B-site. Although the presence of a 4+ cation would not change the fraction of  $\text{Mn}^{3+}$ , it is still a perturbation to the periodic potential created by the Mn – O array and should create states that help to localize charge carriers. Like  $\text{SrMnO}_{3-\delta}$ ,  $\text{SrTiO}_3$  is also a cubic perovskite with space group  $Pm\bar{3}m$ , so  $\text{Ti}^{4+}$  is a logical first choice for using a 4+ dopant.

There is a wealth of literature investigating the effect of Mn doping on the dielectric behavior of  $\text{SrTiO}_3$  (Azzoni et al. 2000; Lemanov et al. 2005; Norton et al. 2003; Tkach et al. 2005; Tkach et al. 2006). However, in all these articles, the maximum fraction of Mn in  $\text{SrTiO}_3$  mentioned is 15%, still very much on the Ti-rich side of the phase diagram. For this investigation, it is the Mn-rich side that is of interest. Therefore samples had to be synthesized without precedent in the literature.

The goal of this doping scheme is for the  $\text{Ti}^{4+}$  to perturb the periodic potential enough to lower the mobility and create Anderson localized states so that the dielectric relaxations can be observed within the measurement space. In the presence of  $\text{Mn}^{3+/4+}$ , Ti will have a 4+ valence and preserve charge balance without affecting the ratio of  $\text{Mn}^{3+}$  to  $\text{Mn}^{4+}$ . Furthermore,  $\text{Ti}^{4+}$  cations can tolerate 5-fold coordination, so that it is possible for  $\text{Ti}^{4+}$  to reside next to an oxygen vacancy in a 5-fold-coordinated site as well as in a 6-fold coordinated site.

Table 7.3: Effective ionic radii for  $\text{Mn}^{3+}$ ,  $\text{Mn}^{4+}$  and  $\text{Ti}^{4+}$  (Shannon and Prewitt 1969)

	6-fold (Å)	5-fold (Å)
$\text{Mn}^{3+}$	0.65	0.58
$\text{Mn}^{4+}$	0.54	-
$\text{Ti}^{4+}$	0.60	0.53

In addition to being able to handle either 5 or 6-fold coordinated sites,  $\text{Ti}^{4+}$  has a larger ionic radius than  $\text{Mn}^{4+}$ ; the larger ionic radius increases the average (M – O) bond length and thus decreases the tolerance factor. Again, substituting a larger B-site cation should reduce the strain that is associated with having a tolerance factor larger than one, making it easier to oxidize the sample. However, if the strain associated with having a tolerance factor greater than 1 contributes to an increased dielectric constant, then the dielectric constant could decrease with increasing Ti-doping.

### 7.3.1 Synthesis

The two-step solid-state synthesis was used again to obtain polycrystalline pellets of  $\text{SrMn}_{1-x}\text{Ti}_x\text{O}_{3-\delta}$  (SMT). Powder precursors of  $\text{SrCO}_3$ ,  $\text{MnO}_2$ , and  $\text{TiO}_2$ , were mixed in stoichiometric ratios for  $x = 0.025, 0.05, 0.1, 0.15, 0.2, 0.3, 0.4$ . After mixing the precursors, the powder was pressed into pellets and fired for 20 hours at  $1375^\circ\text{C}$  in air and then 10 hours in argon before cooling in argon. The samples were ground and refired under the same conditions. Finally, the samples were annealed in oxygen for 20 hours at  $400^\circ\text{C}$ .



The X-ray diffraction patterns of the SMT samples before and after the oxygen anneal are shown in Figure 7.5. The patterns taken before the anneal show peak splittings that diminish with increasing Ti content and are not visible for  $x = 0.1$ . In the patterns taken after the oxygen anneal, there are no peak splittings and the peaks fit the line markers for the expected  $Pm\bar{3}m$  space group.

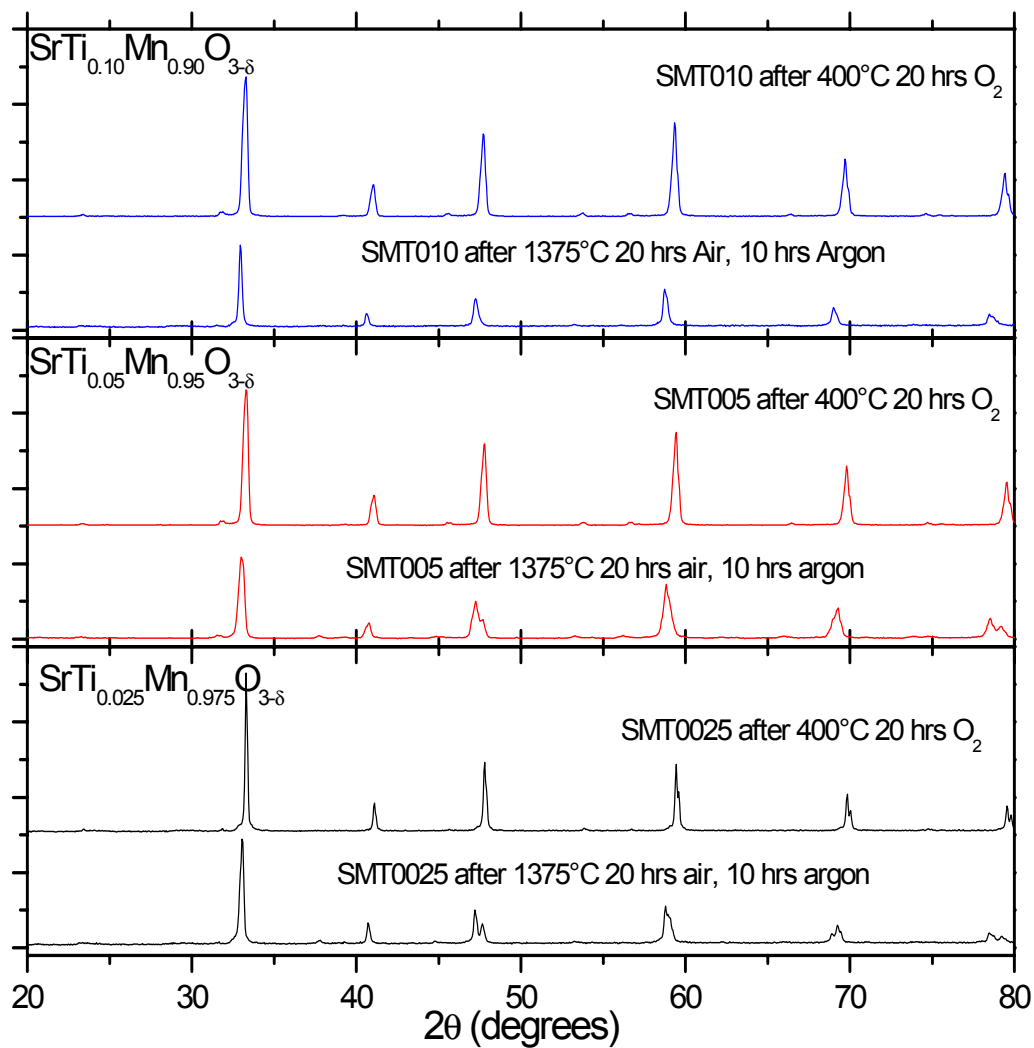


Figure 7.5: Comparison of the X-ray diffraction patterns taken before and after oxygen annealing for  $\text{SrTi}_x\text{Mn}_{1-x}\text{O}_{3-\delta}$  samples with  $x = 0.025$  (SMT0025),  $0.05$  (SMT005), and  $0.1$  (SMT010).

In the patterns taken before the oxygen anneal, the peaks that do not correspond to the  $Pm\bar{3}m$  space group must originate from phases with ordered-oxygen vacancies because they disappear after oxygen annealing and disordered vacancies would not lead to any superstructure diffraction. Since these peaks diminish with increasing Ti-content, the Ti doping randomizes the oxygen vacancies. The peak-shifting to higher angles in the pattern taken before the oxygen anneal to the pattern taken after is another confirmation that the samples have oxidized and the fraction of the smaller ionic radius  $Mn^{4+}$  has increased relative to the larger ionic radius  $Mn^{3+}$ .

The samples with larger Ti content had similar X-ray diffractions patterns as for the  $x = 0.1$  sample; no peak-splittings or unaccounted-for peaks were visible before or after oxygen annealing. All of the samples' patterns fit the  $Pm\bar{3}m$  space group and there is a monotonic increase in the lattice parameter with increasing Ti-doping, as can be seen in Figure 7.6.

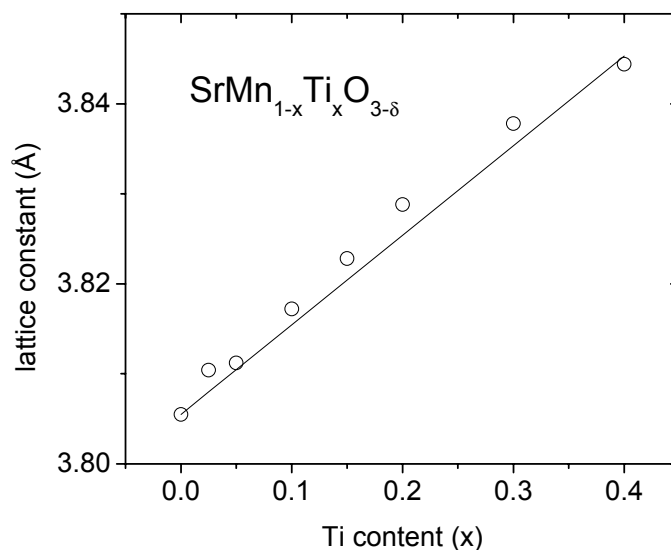


Figure 7.6: The lattice constant of the series  $SrTi_xMn_{1-x}O_{3-\delta}$  ( $0 \leq x \leq 0.4$ ); the solid line represents the linearly interpolated values calculated from the parent compounds  $SrMnO_3$  and  $SrTiO_3$ .

Although there is some error in the amount of Ti-doping, the most likely reason that the data points for  $0 < x < 0.4$  fall above the interpolated value is because the samples have some amount of  $\text{Mn}^{3+}$  and the larger ionic radius increases the measured lattice parameter.

The fraction of  $\text{Mn}^{3+}$  is equivalent to twice the number of oxygen vacancies; this fraction can be measured by iodimetric titration, and the results are shown in Figure 7.7.

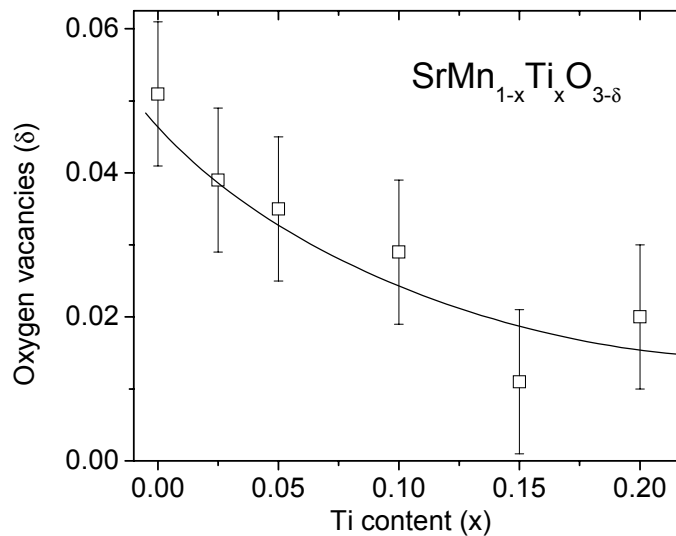


Figure 7.7: Fraction of oxygen vacancies ( $\delta$ ) determined by iodimetric titration for the series  $\text{SrTi}_x\text{Mn}_{1-x}\text{O}_{3-\delta}$ ; the solid line serves as an eye guide.

There is a systemic decrease in the number of oxygen vacancies as the Ti-doping increases. The  $\text{Ti}^{4+}$  cation is not soluble in acid and cannot be reduced in the presence of iodine, so that the samples with Ti content greater than 20% could not be dissolved efficiently to produce meaningful results.

### 7.3.2 Admittance

The original reason for Ti doping of  $\text{SrMnO}_{3-\delta}$  was to disorder the electronic potential and create trapping states that would lower the conductivity of the sample and allow for the dielectric relaxations to be observed within the measurement space. In practice, however, the conductivity of samples with small amounts of Ti-doping actually increased in comparison to the  $\text{SrMnO}_{2.95}$  sample investigated in Chapter 6.

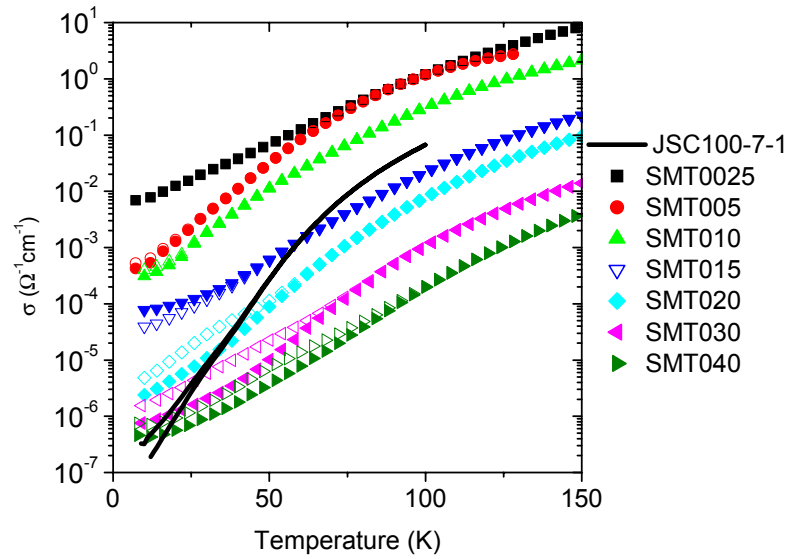


Figure 7.8: AC-conductivity for  $\text{SrMnO}_{2.95}$  (JSC100-7-1) and  $\text{SrMn}_{1-x}\text{Ti}_x\text{O}_{3-\delta}$  ( $x = 0.025, 0.05, 0.1, 0.2, 0.3, 0.4$ ); the closed symbols are for  $\nu = 10^3$  Hz and the open symbols are for  $\nu = 10^4$  Hz.

The conductivity of the SMT samples decreases with increasing Ti content. However, for  $x < 0.4$  the conductivity is larger than  $\text{SrMnO}_{2.95}$  (JSC100-7-1) and the samples with Ti-doping  $x < 0.2$  have conductivities that are too large to observe the dielectric relaxations. Samples with  $x = 0.2, 0.3, 0.4$  have not fully relaxed by  $10^6$  Hz, but it is possible to extrapolate a value by curve-fitting the data to relevant relaxation equations.

To account for fitting biases, two relaxation equations were used to fit the data. The first equation is a complicated formula arrived at by deriving an expression for the admittance of a capacitor in parallel with the series combination of a constant-phase-element (CPE) and capacitor; the imaginary part divided by the frequency yields the real part of the dielectric behavior.

$$Z_{CPE} = A(j\omega)^{-s} = A\omega^{-s} \left[ \cos\left(\frac{s\pi}{2}\right) - j \sin\left(\frac{s\pi}{2}\right) \right] \quad (7.2a)$$

$$Y_{Total} = j\omega C_1 + \frac{j\omega C_2}{1 + j\omega C_2 A\omega^{-s} \left[ \cos\left(\frac{s\pi}{2}\right) - j \sin\left(\frac{s\pi}{2}\right) \right]} \quad (7.2b)$$

$$C_2 = (\epsilon_0 - \epsilon_\infty)$$

$$C_1 = \epsilon_\infty$$

$$\epsilon' = \epsilon_\infty + \frac{(\epsilon_0 - \epsilon_\infty) \left( 1 + \omega(\epsilon_0 - \epsilon_\infty) A\omega^{-s} \sin\left(\frac{s\pi}{2}\right) \right)}{\left( 1 + \omega(\epsilon_0 - \epsilon_\infty) A\omega^{-s} \sin\left(\frac{s\pi}{2}\right) \right)^2 + \left( \omega(\epsilon_0 - \epsilon_\infty) A\omega^{-s} \cos\left(\frac{s\pi}{2}\right) \right)^2} \quad (7.2c)$$

The CPE relaxation equation was used to fit the data over the entire measurement frequency range from 10 Hz to  $10^6$  Hz. The second equation is the simple exponential relation (6.1) that was exploited to fit sample JSC100-7-1 in Chapter 6; it was used to fit the high-frequency region from  $10^4$  Hz to  $10^6$  Hz. For both the CPE equation and the exponential equation, the fitting was performed on the lowest temperature scans where the dielectric constant approaches the temperature-independent value attributed to the ionic polarization of the structure. The results for these two fittings are shown in Figure 7.9, Figure 7.10, and Figure 7.11 for  $\text{SrMn}_{0.8}\text{Ti}_{0.2}\text{O}_{2.98}$  (SMT020),  $\text{SrMn}_{0.7}\text{Ti}_{0.3}\text{O}_{3-\delta}$  (SMT030), and  $\text{SrMn}_{0.6}\text{Ti}_{0.4}\text{O}_{3-\delta}$  (SMT040), respectively.

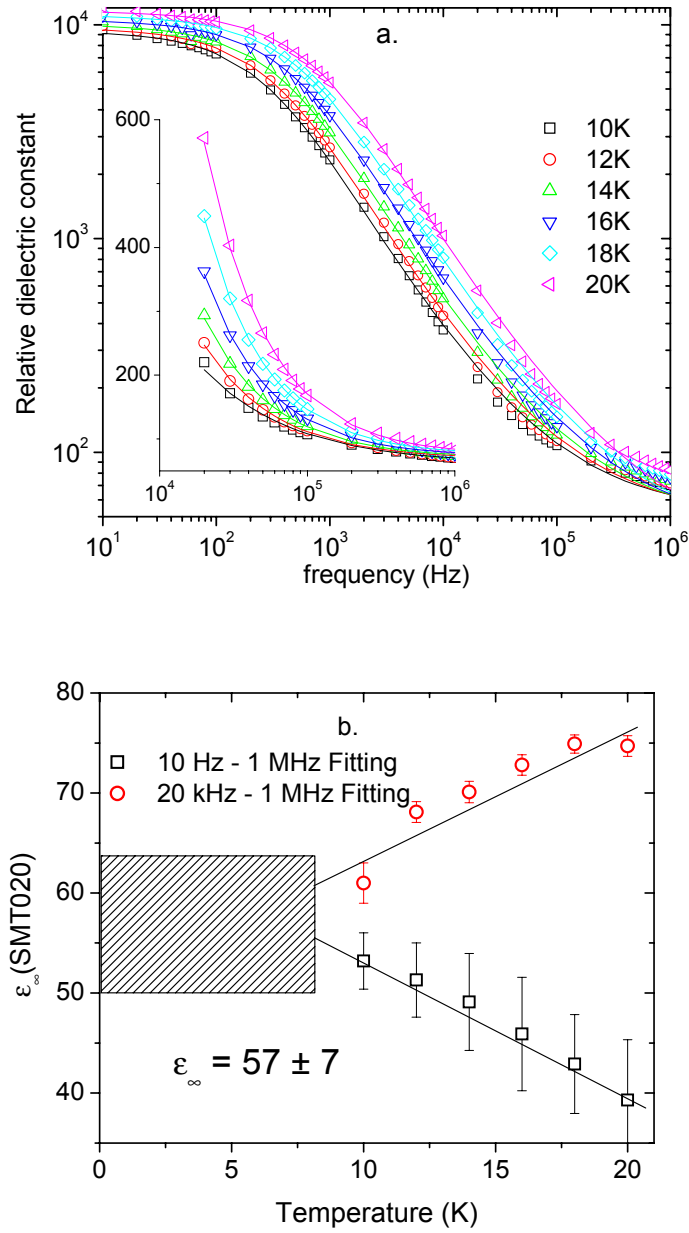


Figure 7.9: The dielectric relaxations of the sample  $\text{SrMn}_{0.8}\text{Ti}_{0.2}\text{O}_{2.98}$  (SMT020) with curve fitting from 10 Hz to  $10^6$  Hz (large plot) and  $10^4$  Hz to  $10^6$  Hz (inset); the open symbols represents the data and the solid lines are the fitted curves (a). The temperature bias of the fitted parameter  $\epsilon_{\infty}$ ; the solid lines are eye guides (b).

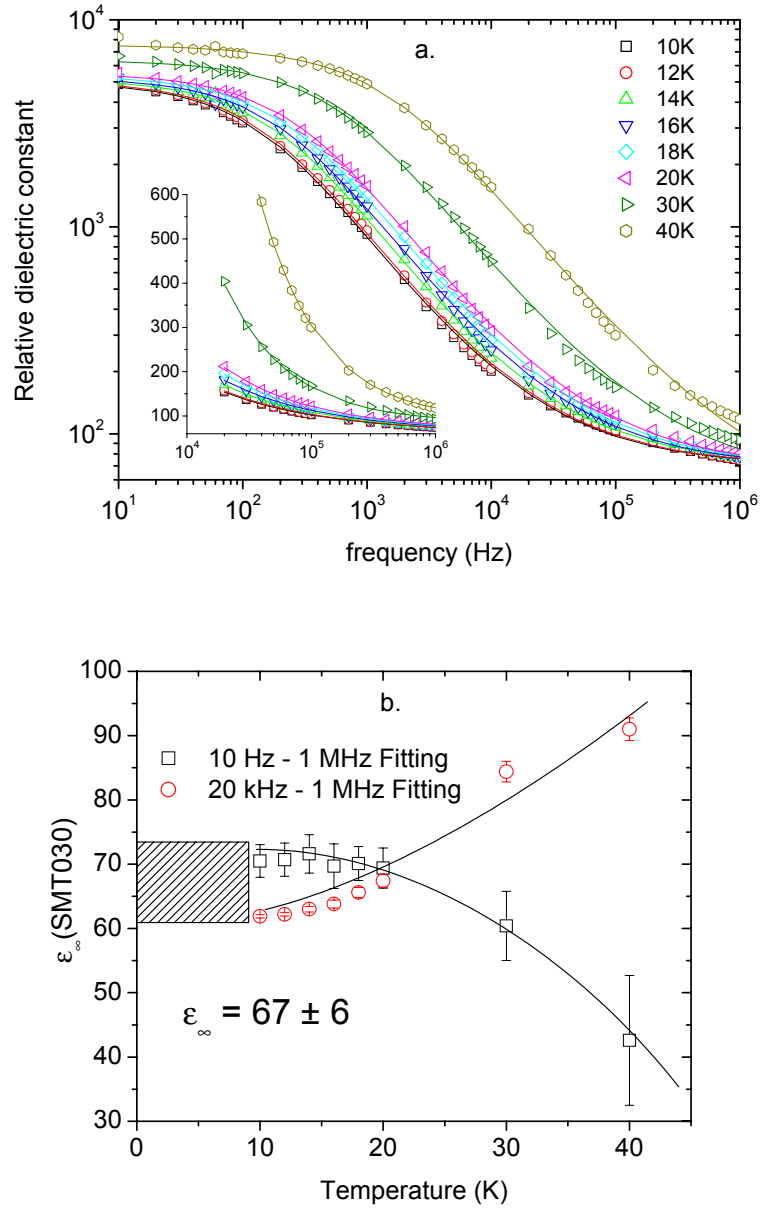


Figure 7.10: The dielectric relaxations of the sample  $\text{SrMn}_{0.7}\text{Ti}_{0.3}\text{O}_{3-\delta}$  (SMT030) with curve fitting from 10 Hz to  $10^6$  Hz (large plot) and  $10^4$  Hz to  $10^6$  Hz (inset); the open symbols represents the data and the solid lines are the fitted curves (a). The temperature bias of the fitted parameter  $\epsilon_\infty$ ; the solid lines are eye guides (b).



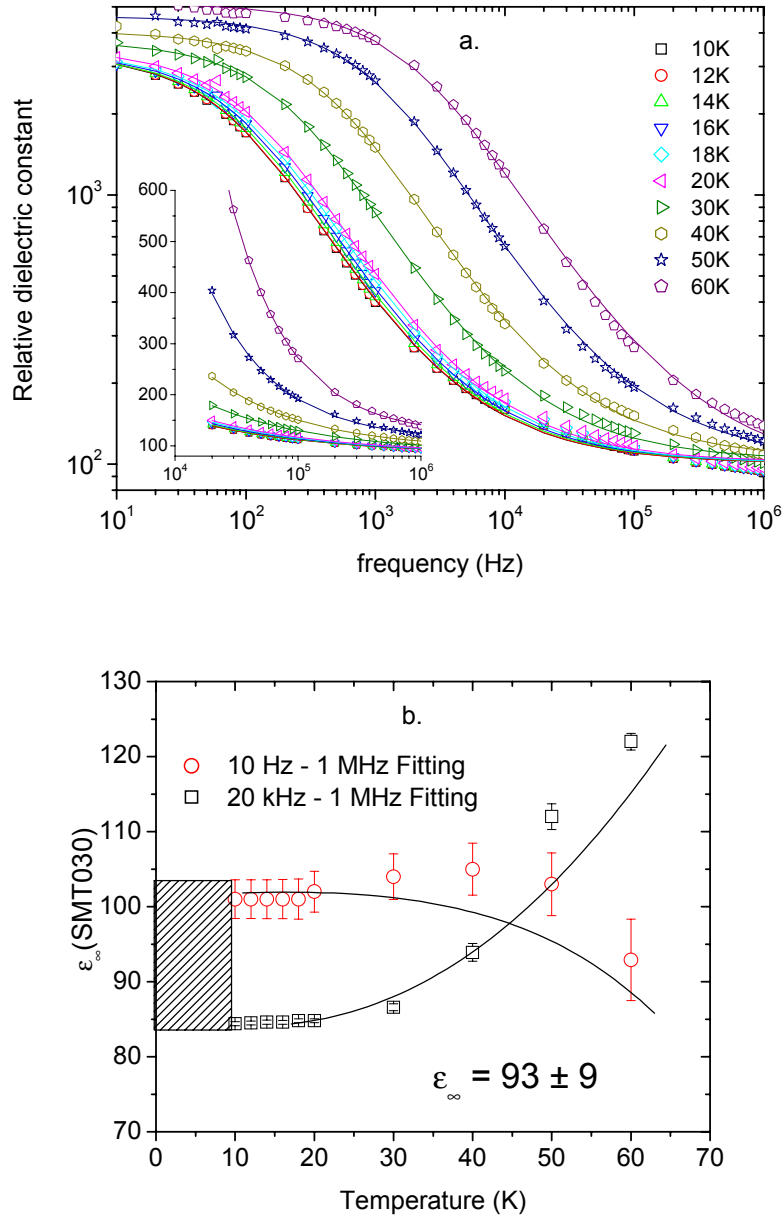


Figure 7.11: The dielectric relaxations of the sample  $\text{SrMn}_{0.6}\text{Ti}_{0.4}\text{O}_{3-\delta}$  (SMT040) with curve fitting from 10 Hz to  $10^6$  Hz (large plot) and  $10^4$  Hz to  $10^6$  Hz (inset); the open symbols represents the data and the solid lines are the fitted curves (a). The temperature bias of the fitted parameter  $\epsilon_\infty$ ; the solid lines are eye guides (b).

For all three samples, the CPE relaxation equation (7.2c) fits the data well over the low-frequency and mid-range frequency regions of the plot, but it diverges from the data in the high-frequency region. The exponential equation (6.1) only fits the data in the high frequency region and therefore gives a better fit over that region. Both fits have a temperature bias: the CPE equation increasingly underestimates the parameter  $\epsilon_{\infty}$  with increasing temperature and the exponential relationship overestimates  $\epsilon_{\infty}$  with increasing temperature.

As the Ti-content in the sample is increased from 0.2 to 0.3 to 0.4, the fitting results in Figure 7.9b, Figure 7.10b, and Figure 7.11b show the parameter  $\epsilon_{\infty}$  becomes temperature-independent over a larger and larger temperature region. However, the results of the two curve-fitting equations do not converge within the statistical error bars of the fit. It is likely that the systemic error discussed in Chapter 4 is skewing the high-frequency results. The final representative  $\epsilon_{\infty}$  value is the average of the lowest temperature fits from both equations, and the error is associated with the window of uncertainty created by both of the curve fitting results.

### 7.3.3 Discussion

Ti doping in  $\text{SrMn}_{1-x}\text{Ti}_x\text{O}_{3-\delta}$  for  $x < 0.4$  led to increased conductivity in comparison to  $\text{SrMnO}_{2.95}$ , contrary to the intent of the doping experiment. The Ti cation's ability to substitute for a 5-fold coordinated  $\text{Mn}^{3+}$ , next to an oxygen vacancy, created  $\text{Mn}^{3+}$  cations that were not trapped by oxygen vacancies and thus the electrons associated with the  $\text{Mn}^{3+}$  cations had a smaller motional enthalpy. Although Ti doping decreased the oxygen-vacancy concentration, it randomized the location of the vacancies which led to more conducting samples. However, the conductivity did decrease with increasing Ti doping, and for  $x \geq 0.2$  the conductivity was low enough to observe the dielectric relaxations within the measurement space.

The high-frequency dielectric constant due to the ionic polarization ( $\epsilon_\infty$ ) increased from  $57 \pm 6$  for  $\text{SrMn}_{0.8}\text{Ti}_{0.2}\text{O}_{2.98}$ , to  $67 \pm 7$  for  $\text{SrMn}_{0.7}\text{Ti}_{0.3}\text{O}_{3-\delta}$ , to  $93 \pm 9$  for  $\text{SrMn}_{0.6}\text{Ti}_{0.4}\text{O}_{3-\delta}$ . There remains doubt about the dielectric behavior in the area of dilute Ti doping ( $x < 0.2$ ) since the samples were too conducting to measure the dielectric relaxation. However, the portion of the  $\text{SrMn}_{1-x}\text{Ti}_x\text{O}_{3-\delta}$  dielectric phase diagram that has been measured does help limit the possibilities of the dielectric behavior of the stretched  $\text{Mn}^{4+} - \text{O} - \text{M}^{4+}$  of  $\text{SrMnO}_3$ . One possibility is that the previous measurement on  $\text{SrMnO}_{2.95}$  with  $\epsilon_\infty = 111$  was an extrinsic result and that the trend of decreasing  $\epsilon_\infty$  with decreasing Ti-content can be extrapolated back to  $x = 0$ ; this trend would require  $\text{SrMnO}_3$  to have an  $\epsilon_\infty < 57$ . The other possibility is that the value of  $\epsilon_\infty = 111$  is close to the actual value for  $\text{SrMnO}_3$  and the region  $0 \leq x \leq 0.2$  has a local minimum in the dielectric constant.

#### 7.4 $\text{SrMn}^{4+}_{1-2\delta-x}\text{Mn}^{3+}_{2\delta}\text{Zr}^{4+x}\text{O}_{3-\delta}$

Another doping alternative is to substitute  $\text{Zr}^{4+}$  for  $\text{Mn}^{4+}$ . The  $\text{Zr}^{4+}$  cation is larger than  $\text{Ti}^{4+}$  and does not tolerate 5-fold coordination; also, like  $\text{Ti}^{4+}$  it does not reduce easily to the 3+ valence state. If the  $\text{Zr}^{4+}$  is able to substitute onto the Mn sites, it will not be located next to an oxygen vacancy, which means that both of the  $\text{Mn}^{3+}$  created will be trapped next to the vacancy. This should allow  $\text{Zr}^{4+}$  to localize charge carriers more effectively than Ti-doped samples, allowing the dielectric relaxation to be observed within the measurement space with a smaller concentration of dopant. The  $\text{Zr}^{4+}$  cation is larger than  $\text{Ti}^{4+}$  and will reduce the tolerance factor with less doping than  $\text{Ti}^{4+}$ ; it sacrifices the bond strain and gives a larger  $\text{M} - \text{O} - \text{M}$  bond length variance.

Table 7.4: Effective ionic radii for  $\text{Mn}^{3+}$ ,  $\text{Mn}^{4+}$  and  $\text{Ti}^{4+}$ ,  $\text{Zr}^{4+}$  (Shannon and Prewitt 1969)

	6-fold (Å)	5-fold (Å)
$\text{Mn}^{3+}$	0.65	0.58
$\text{Mn}^{4+}$	0.54	-
$\text{Ti}^{4+}$	0.60	0.53
$\text{Zr}^{4+}$	0.72	-

#### 7.4.1 Synthesis

For synthesizing  $\text{SrMn}_{1-x}\text{Ti}_x\text{O}_{3-\delta}$  (SMT),  $\text{TiO}_2$  was used as the Ti precursor; the refractory nature of  $\text{ZrO}_2$  prohibits synthesizing  $\text{SrMn}_{1-x}\text{Zr}_x\text{O}_3$  (SMZ) by the solid-state method. Instead, a sol-gel method was used to prepare samples of  $\text{SrMn}_{1-x}\text{Zr}_x\text{O}_{3-\delta}$  for  $x = 0.025, 0.05$ , and  $0.1$ . As an alternative for  $\text{ZrO}_2$ ,  $\text{ZrO}(\text{NO}_3)_2 \cdot \alpha\text{H}_2\text{O}$  was used; the fraction of hydration ( $\alpha$ ) was determined by thermogravimetric analysis (TGA) so that an accurate amount of the precursor could be weighed.

Stoichiometric ratios of  $\text{SrCO}_3$ ,  $\text{MnO}_2$ , and  $\text{ZrO}(\text{NO}_3)_2 \cdot \alpha\text{H}_2\text{O}$  were dissolved in a 1 N nitric-acid solution. After the metal precursors have fully dissolved, ethylenediaminetetraacetic acid (EDTA) dissolved in a basic solution of ammonium hydroxide ( $\text{NH}_4\text{OH}$ ) was added. Additional ammonium hydroxide was added to increase the pH to 8 – 9 and then the water in the solution was evaporated on a hot plate with constant stirring from a magnetic stir-bar. After dehydration, the gel substance was fired at  $400^\circ\text{C}$  for 5 hours in air to break down the organics; the resulting sponge-like formation was lightly scraped from the Pyrex beaker to yield fine particles. The fine

particles were poured into an alumina crucible and fired at 800°C for 10 hours in air to break down the carbonates. The resulting precursor powder was then ground in a mortar, pressed into a pellet, and fired at 1400°C for 20 hours in air and then 10 hours in argon. Finally, the samples were annealed at 400°C for 40 hours in oxygen.

Powder X-ray diffraction was performed on the three SMZ samples before and after the oxygen anneal. The diffractograms are shown in Figure 7.12.

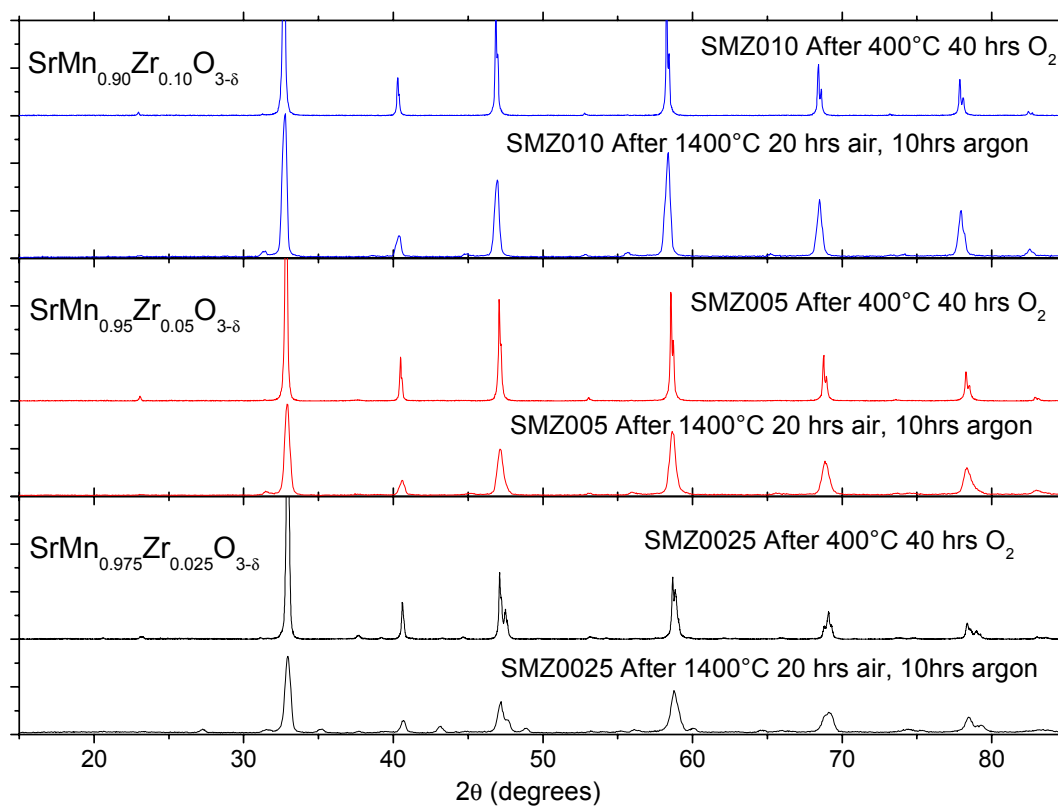


Figure 7.12: X-ray diffraction patterns for  $\text{SrMn}_{1-x}\text{Zr}_x\text{O}_{3-\delta}$  ( $x = 0.025, 0.05, \text{ and } 0.1$ ) before and after annealing in oxygen.

Similar to the X-ray pattern of the unannealed SMT0025 sample, the unannealed SMZ0025 pattern had extra peaks and peak-splittings that did not correspond to the  $Pm\bar{3}m$  space group. For the SMT0025 sample, peaks that did not correspond to the phase disappeared after annealing in oxygen. For SMZ0025, there are also peaks that clearly vanish or diminish after anneal, but some of the additional peaks that remain do not correspond to the phase. Figure 7.13 shows a close-up of these low-intensity peaks; the peaks are labeled to indicate those that correspond to the phase (h k l), the superstructure peaks that must be due to oxygen ordering ( $V_O$ ), and the peaks that do not correspond to the phase (\*). Additionally, the unannealed samples' X-ray diffraction patterns were taken on a diffractometer with a copper source that has been contaminated with tungsten and thus has low-intensity  $W_{L\alpha}$  diffraction peaks; these peaks are indicated as well.

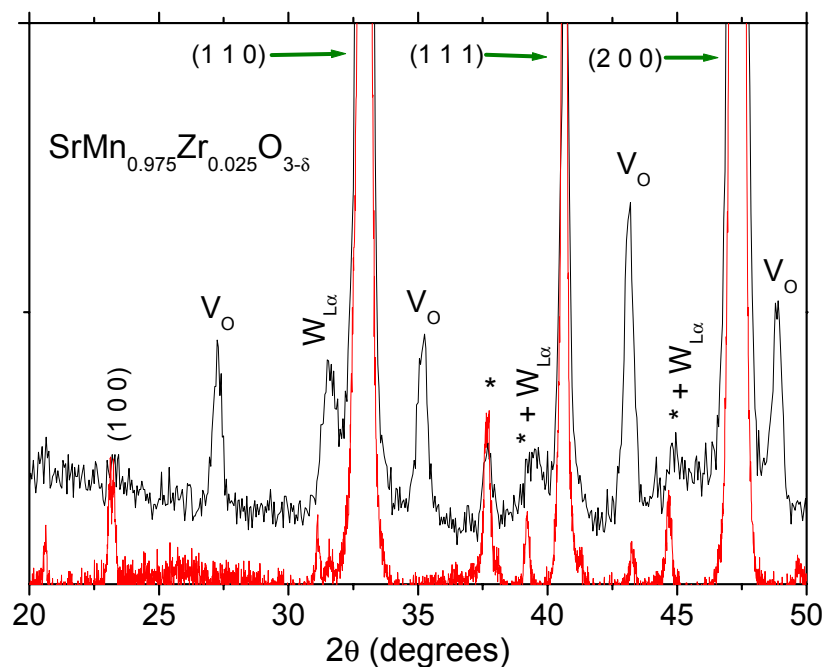


Figure 7.13: Comparison of the diffractograms of  $\text{SrMn}_{0.975}\text{Zr}_{0.025}\text{O}_{3-\delta}$  before (black) and after (red) annealing in oxygen; the peak labels correspond to the  $Pm\bar{3}m$  phase (h k l), superstructure peaks of ordered oxygen vacancies ( $V_O$ ), tungsten-L $\alpha$  lines, and unaccounted peaks (\*).

The unaccounted peaks in the annealed SMZ0025 X-ray pattern did not correspond to any phase with a combination of the chemical constituents Sr, Mn, Zr, or O listed in the PDF database. The peaks were also checked to see whether they corresponded with ordering of the  $\text{Zr}^{4+}$  and  $\text{Mn}^{4+}$ ; however there was poor agreement with expected peak locations and the unaccounted peaks.

In contrast to SMZ0025, the X-ray diffraction pattern of SMZ005, shown in Figure 7.14, has no peaks associated with the ordering of oxygen vacancies before the anneal. However, there is one peak, at  $2\theta = 37.6^\circ$  that does not belong to the  $Pm\bar{3}m$  phase and is present in both the unannealed and annealed patterns. This peak has about the

same  $2\theta$  value as the most intense unaccounted peak in the SMZ0025 patterns ( $2\theta = 37.7^\circ$ ).

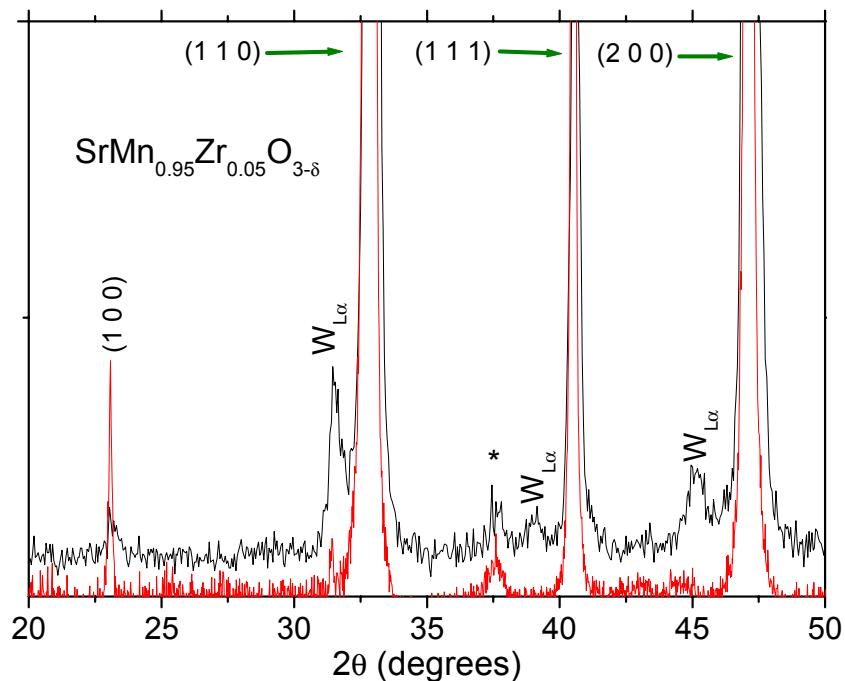


Figure 7.14: Comparison of the diffractograms of  $\text{SrMn}_{0.95}\text{Zr}_{0.05}\text{O}_{3-\delta}$  before (black) and after (red) annealing in oxygen; the peak labels correspond to the  $Pm\bar{3}m$  phase (h k l), tungsten-L $\alpha$  lines, and unaccounted peak (\*).

The X-ray diffraction pattern of the SMZ010 sample, shown in Figure 7.15, has no unaccounted-for peaks corresponding to ordered oxygen vacancies or unknown impurities.



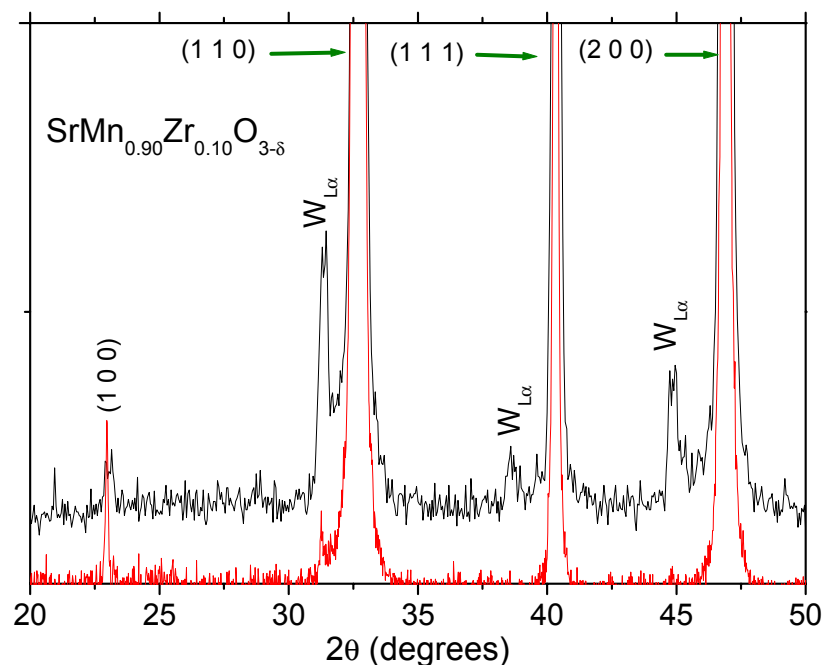


Figure 7.15: Comparison of the diffractograms of  $\text{SrMn}_{0.90}\text{Zr}_{0.10}\text{O}_{3-\delta}$  before (black) and after (red) annealing in oxygen; the peak labels correspond to the  $Pm\bar{3}m$  phase (h k l), and tungsten- $L\alpha$  lines.

The unaccounted peaks in SMZ0025 and SMZ005 must correspond to some impurity phase. The fraction of impurity phase present in SMZ005 is less than that in SMZ0025, which is why only a weak peak is visible at the position of the strongest impurity peak of SMZ0025. The trend continues to SMZ010, which has no detectable impurity peaks. Although the impurity phase could not be identified, the decreasing impurity mole fraction with increasing Zr content suggests there is error in the amount of Zr precursor added to form single phase samples; this is a reasonable explanation when considering the Zr precursor was hygroscopic and only a small amount (70 mg) was required for the dilute Zr doping in SMZ0025. It is likely that the impurity phase can be avoided by preparing larger masses of samples.

### 7.4.2 Admittance

To investigate the dielectric behavior, the charge carriers need to be sufficiently localized so that the dielectric relaxations occur within the measurement range. The conductivities for  $\text{SrMn}_{0.95}\text{Zr}_{0.05}\text{O}_{3-\delta}$  (SMZ005) and  $\text{SrMn}_{0.90}\text{Zr}_{0.10}\text{O}_{3-\delta}$  (SMZ010) are displayed in Figure 7.16.

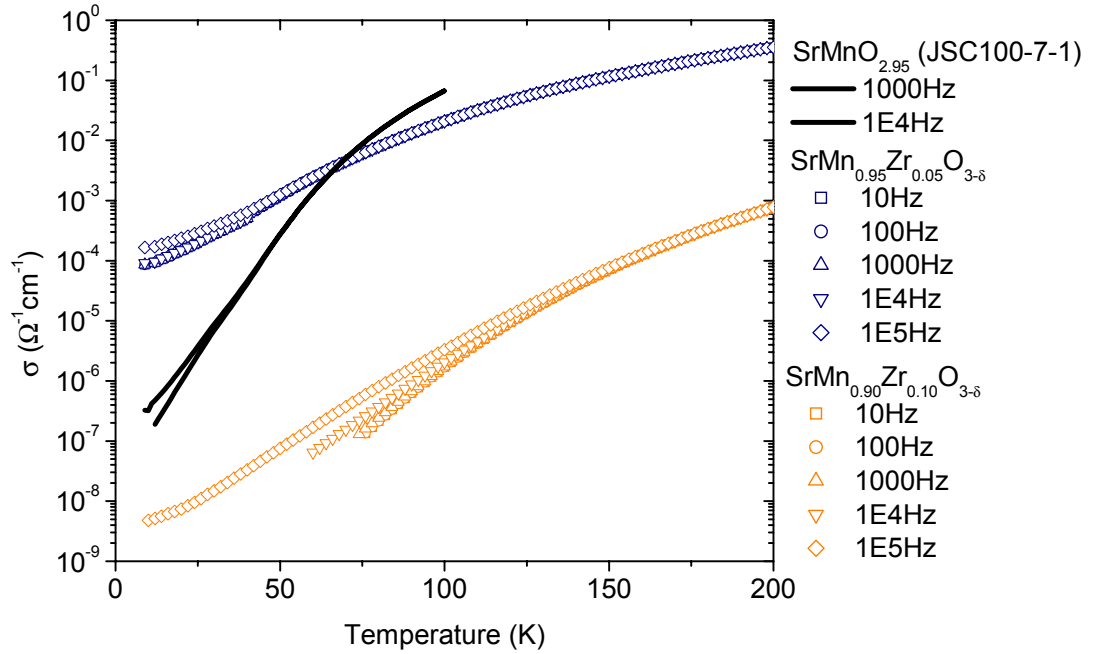


Figure 7.16: Comparison of the AC-conductivity of  $\text{SrMnO}_{2.95}$  (JSC100-7-1),  $\text{SrMn}_{0.95}\text{Zr}_{0.05}\text{O}_{3-\delta}$  (SMZ005), and  $\text{SrMn}_{0.90}\text{Zr}_{0.10}\text{O}_{3-\delta}$  (SMZ010).

As expected, the conductivity decreased with increasing Zr-content. Furthermore, the Zr-doped samples reduced the conductivity more efficiently than the Ti-doped samples. At low temperatures, sample SMZ005 with a Zr-content of 5%, had a conductivity two orders-of-magnitude greater than JSC100-7-1, but SMZ010 with a Zr-content of 10%, had a conductivity two orders-of-magnitude less than JSC100-7-1. In the SMT samples, a Ti-content of 40% was needed to lower the conductivity of sample enough to be of the same order-of-magnitude as JSC100-7-1.

The larger conductivity of the SMZ005 sample prevented its dielectric relaxation from being observed within the measurement space; however, the less conductive SMZ010 sample had fully relaxed to its temperature-independent value of  $\epsilon_r = 10.3$  by  $T = 30$  K.

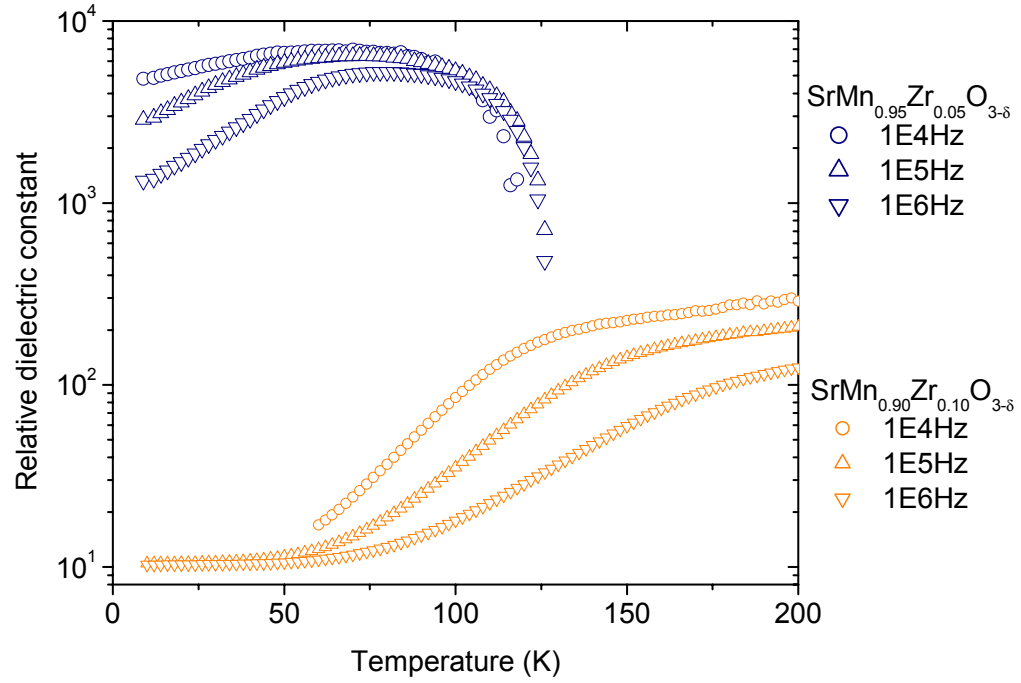


Figure 7.17: Comparison between the dielectric behaviors of  $\text{SrMn}_{0.95}\text{Zr}_{0.05}\text{O}_{3-\delta}$  (SMZ005)  $\text{SrMn}_{0.90}\text{Zr}_{0.10}\text{O}_{3-\delta}$  (SMZ010).

## 7.5 KRAMERS-KRONIG ANALYSIS OF $\text{SRMNO}_{3-\delta}$

In an article that focuses on the possibility of a low-temperature structural transition in the hexagonal-polytype phase of  $\text{SrMnO}_3$ , Sacchetti *et al.* measure the infra-red reflectivity of both the hexagonal-polytype and cubic perovskite phases of  $\text{SrMnO}_3$  (Sacchetti *et al.* 2005). Sacchetti *et al.* performed a Kramers-Kronig analysis on the infra-red reflectivity data and plotted the optical conductivity in addition to the reflectivity.

As mentioned in Chapter 4, the conductivity is proportional to the product of the imaginary part of the dielectric constant and the frequency (Equation 4.13); furthermore the imaginary part of the dielectric constant can be transformed to the real part of the dielectric constant via the Kramers-Kronig equations (Equations 4.10b, 4.11). Therefore, it is possible to determine the real part of the dielectric constant from the optical conductivity.

The optical conductivity data of Sacchetti *et al.* was converted to the imaginary part of the dielectric constant with Equation 4.13 and then the imaginary part of the dielectric constant was fit with Equation 4.19b; the parameters that resulted from the fit were then used in Equation 4.19a to calculate the real part of the dielectric constant. The imaginary part of the dielectric constant data taken from Sacchetti *et al.* (Sacchetti *et al.* 2005), the fit of the imaginary part of the dielectric constant, and the corresponding real part of the dielectric constant are plotted in Figure 7.18.

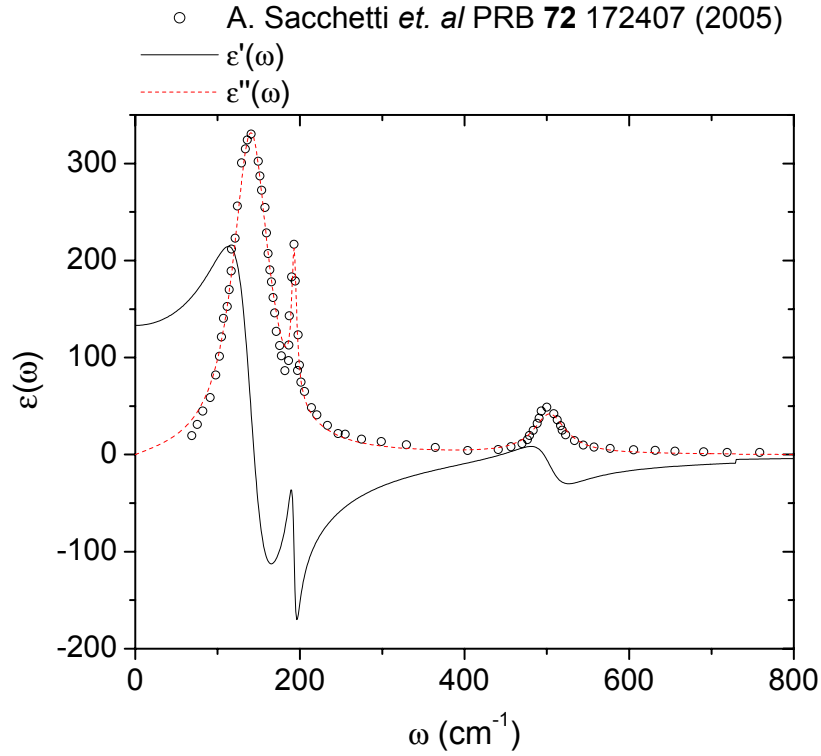


Figure 7.18: Infra-red imaginary part of the dielectric constant from Sacchetti *et al.* (Sacchetti *et al.* 2005) (open symbols), fitting of the imaginary dielectric constant with Equation 4.19b (dashed line), and corresponding plot of the real part of dielectric constant (solid line ) from Equation 4.19a.

The low-frequency value of the real part of the dielectric constant in Figure 7.18 is  $\epsilon_r = 133$ , which is very close to the value of  $\epsilon_r = 111$  measured for  $\text{SrMnO}_{2.95}$ . Since the value determined from infra-red reflectivity is the ionic polarization contribution to the dielectric constant, the agreement between the two values confirms that the value of  $\epsilon_r = 111$  measured for  $\text{SrMnO}_{2.95}$  is the high-frequency dielectric constant due to the ionic polarization. There are a couple of reasons why the value measured for  $\text{SrMnO}_{2.95}$  is less than the value determined from the reflectivity data of Sacchetti *et al.*: first, the high frequency error discussed in Chapter 4 suggested that the high-frequency dielectric data

underestimated the dielectric constant; secondly, it is likely that the sample measure for reflectivity was oxidized to have a larger  $\delta$  than 2.95 that increased the tensile strain on the (Mn – O) bond and increased the dielectric constant to  $\epsilon_r = 133$ .

## 7.6 DISCUSSION

Devising doping schemes to make  $\text{SrMnO}_{3-\delta}$  more insulating while not interfering with the dielectric behavior presents several electronic and structural challenges. Adding oxygen vacancies can make the  $\text{SrMnO}_{3-\delta}$  more insulating if the vacancies are ordered; however, if the vacancies are randomly distributed, increasing the number of oxygen vacancies can make the sample more conducting. The ordered and disordered phases segregate and their dielectric behavior is different, making physical interpretation more complex. Substitution of cations that trap electrons by chemically oxidizing the  $\text{Mn}^{3+}$  cation next to an oxygen vacancy to  $\text{Mn}^{4+}$  is not possible because  $\text{Mn}^{4+}$  does not tolerate 5-fold coordination. Substituting cations with a 4+ valance is possible, but if the 4+ randomizes the oxygen vacancies, as was the case for  $\text{Ti}^{4+}$ , then the doping increases the conductivity. The structural challenge of doping is that substituting a cation that is larger decreases the tolerance factor, which makes the sample easier to oxidize and observe the dielectric relaxation, but it sacrifices the tensile strain on the (Mn – O) bond that is responsible for a larger dielectric response. The interplay between the tolerance factor and dielectric response in doped  $\text{SrMnO}_{3-\delta}$  is displayed in Figure 7.19.

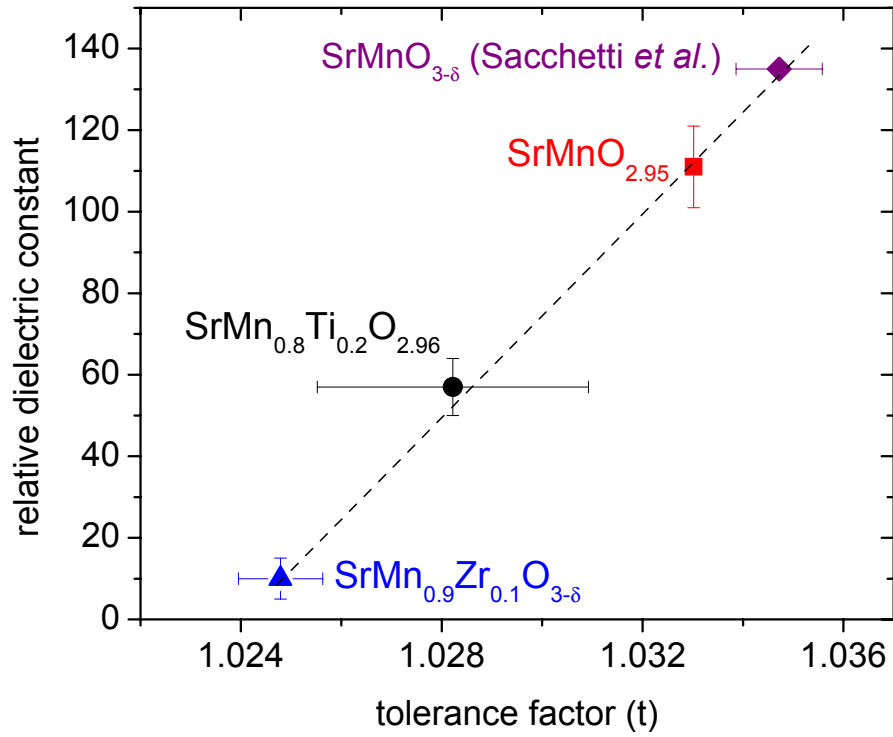


Figure 7.19: The relationship between the tolerance factor and the relative dielectric constant for doped  $\text{SrMn}_{1-x}\text{B}_x\text{O}_{3-\delta}$  for ( $\text{B}_x = \text{Ti}_{0.2}$  and  $\text{Zr}_{0.1}$ ); the tolerance-factor error of  $\text{SrMn}_{0.8}\text{Ti}_{0.2}\text{O}_{2.98}$  represents uncertainty in the distribution of  $\text{Ti}^{4+}$  on 5-fold and 6-fold coordinated sites and the tolerance-factor error of  $\text{SrMn}_{0.9}\text{Zr}_{0.1}\text{O}_{3-\delta}$  and  $\text{SrMnO}_{3-\delta}$  represents the uncertainty in  $\delta$ , assuming  $\delta \approx 0.00 \pm 0.02$ .

Where the tolerance factor is larger than 1, decreasing the tensile stress on the B – O – B array decreases the polarizability of the array and thus the dielectric constant decreases as well. Applying that same principle, decreasing the tensile strain on the A – O – A array when the tolerance factor is less than 1 must decrease the polarizability. This decrease in the tensile strain of the A – O – A network of the orthorhombic  $\text{Sr}_x\text{Ca}_{1-x}\text{MnO}_3$

samples is why the dielectric constant decreases from  $\epsilon_r = 50$  for  $\text{CaMnO}_3$  to  $\epsilon_r = 35$  for  $\text{Ca}_{0.8}\text{Sr}_{0.2}\text{MnO}_3$ .

Since the  $\epsilon_r = 111$  measured for  $\text{SrMnO}_{2.95}$  agrees with the value determined from the infra-red reflectivity data of Sacchetti *et al.*,  $\epsilon_r = 111$  is the dielectric constant due to the ionic polarization of the  $\text{Mn}^{4+}$  - O network in  $\text{SrMnO}_{2.95}$  and the decrease in the tolerance factor generally explains the decrease in  $\epsilon_r$  as  $\text{SrMn}_{1-x}\text{B}_x\text{O}_{3-\delta}$  is doped with larger B-cations (*i.e.*  $\text{Ti}^{4+}$  and  $\text{Zr}^{4+}$ ). However, the increase in dielectric constant from  $\epsilon_r = 57$  for  $\text{SrMn}_{0.8}\text{Ti}_{0.2}\text{MnO}_{2.98}$  to  $\epsilon_r = 93$  for  $\text{SrMn}_{0.6}\text{Ti}_{0.4}\text{MnO}_{2.98}$  suggests that it is the presence of the  $\text{Ti}^{4+}$  that increases the dielectric constant. Furthermore, it is certain that Zr doping decreases the tolerance factor, but the tolerance factor should still be greater than 1 for 10% Zr-doping and the  $(\text{Mn}^{4+} - \text{O})$  bonds should still be under tension. However, 10% Zr-doping lowered the dielectric constant below the value of  $\epsilon_r = 35$  measured for the  $\text{Sr}_x\text{Ca}_{1-x}\text{MnO}_3$   $0.2 \leq x \leq 0.5$  samples, where the tolerance factor is slightly less than one and the  $\text{Mn}^{4+} - \text{O}$  array is not under tension. Based on the results of the Ti and Zr-doping experiments, the lattice strain associated with having a  $t > 1$  is not the only mechanism affecting the dielectric behavior.



## Chapter 8: $\text{SrMn}_{1-x}\text{Ti}_x\text{O}_{3-\delta}$

In Chapter 7, Ti was substituted for Mn to illuminate the dielectric behavior of the Mn-rich portion of the phase diagram. Before beginning the synthesis of the  $\text{SrMn}_{1-x}\text{Ti}_x\text{O}_{3-\delta}$  (SMT) samples, a literature search revealed that the Ti-rich portion of the phase diagram has been investigated but the minimum amount of Ti content of previous synthesized samples was 85% (Tkach et al. 2006). In this chapter, the rest of the dielectric phase diagram is completed. The chapter begins with a review of the connection between the electronic, vibration, structural, and dielectric character for  $\text{ATiO}_3$  ( $A = \text{Ca}, \text{Sr}, \text{Ba}$ ) to better understand the parent compound  $\text{SrTiO}_3$ ; then the experimental results for the SMT phases are discussed.

### 8.1 $\text{ATiO}_3$ ( $A = \text{CA}, \text{SR}, \text{AND BA}$ )

The dielectric behavior of the perovskite  $\text{ATiO}_3$  samples all show a Curie-Weiss temperature dependence above a temperature  $T^*$  (Lemanov et al. 2005; Neville et al. 1972; Tkach et al. 2005):

$$\epsilon(T) = \frac{C}{T - T^*} + \epsilon_{\infty} \quad (8.1)$$

Where  $C$  and  $T^*$  are fitting parameters and  $\epsilon_{\infty}$  is the dielectric constant at frequencies greater than the maximum ionic vibration.

Increasing the tolerance factor with increasing larger effective A-site ionic radius from  $\text{Ca}^{2+}$  (1.35 Å), to  $\text{Sr}^{2+}$  (1.44 Å), to  $\text{Ba}^{2+}$  (1.60 Å) places increasing tensile stress on the Ti – O array and increases the dielectric response; as a result, both the parameters  $C$  and  $T^*$  increase from Ca to Sr to Ba. In Figure 8.1, the inverse dielectric constant is plotted versus temperature to give a linear relationship and show the systematic change in  $C$  and  $T^*$ .

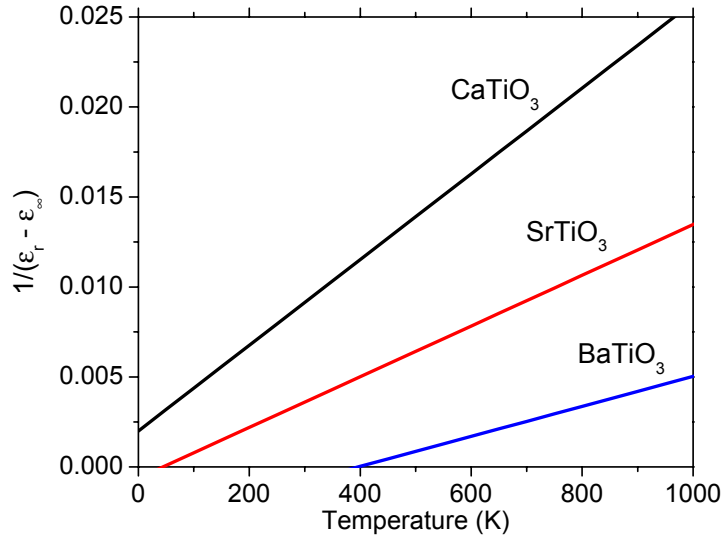


Figure 8.1: The Curie-Weiss temperature dependence of the dielectric constant of  $\text{CaTiO}_3$ ,  $\text{SrTiO}_3$ , and  $\text{BaTiO}_3$  (Rupprecht and Bell 1964).

The Curie-Weiss temperature dependence of the dielectric constant of  $\text{ATiO}_3$  is correlated with the temperature dependence of the “soft mode”. The soft mode (symmetry label  $F_{1u}$ ) develops in the titanates because of an instability in the crystal structure created by Ti-3d / O-2p hybridization (Cohen and Krakauer 1992). As the temperature decreases, the soft-mode’s oscillator strength increases, damping decreases, and frequency decreases (Servoin et al. 1980).

For  $\text{BaTiO}_3$  samples, a ferroelectric, first-order transition occurs where the  $F_{1u}$  soft-mode is unable to restore displaced Ti-ions to the center of symmetry (Cochran 1960).

The  $F_{1u}$  soft-mode in  $\text{SrTiO}_3$  cannot trigger the ferroelectric transition before the strain associated with the decreasing tolerance factor splits the triply-degenerate Raman-active bending mode (symmetry label ( $F_{2u}$ )) into a doublet (symmetry labels  $A_{1g}$  and  $E_g$ ,

respectively). The asymmetric energy of the bending-modes coincides with cooperative rotations of the oxygen octahedra and the lowering of the crystal symmetry from cubic ( $Pm\bar{3}m$ ) to tetragonal ( $I4/mcm$ ), a second-order transition. The  $F_{1u}$  soft-mode continues to increase the dielectric constant but the ferroelectric transition is suppressed by quantum fluctuations and the dielectric constant becomes temperature independent down to  $T = 0$  K (Barrett 1952; Muller and Burkard 1979; Zhong and Vanderbilt 1996).

In  $\text{CaTiO}_3$ , multiple second order phase transitions occur above room temperature to change the crystal symmetry on cooling from cubic  $Pm\bar{3}m$  to tetragonal  $I4/mcm$  to orthorhombic  $Cmcm$  and finally to orthorhombic  $Pbnm$  (Ball et al. 1998). As with  $\text{SrTiO}_3$ , the  $F_{1u}$  soft mode increases the dielectric constant through the structural transitions until quantum fluctuations suppress the dielectric constant to a temperature-independent value as temperatures approach 0 K (Lemanov et al. 1999).

The study of the infra-red and Raman multiple temperature spectra of cubic  $\text{SrMnO}_3$  by Sacchetti *et al.* revealed a “mode-hardening” of one of the optically active modes but no “soft-mode” (Sacchetti et al. 2005). This direct evidence of the absence of the soft-mode adds more support of the theory that it is the  $\text{Ti-d}^0$  electronic configuration, with its ability to hybridize and  $\pi$ -bond with O-2p orbitals, that is the origin of the crystal-instability and soft-mode behavior (Cohen and Krakauer 1992). Since it is expected that the soft mode is hardened by Mn-doping, “How much Mn-doping does it take to quench the soft mode?”

Measuring the temperature dependence of the dielectric constant offers an indirect route to observe the quenching of the soft-mode. This chapter investigates the unknown portion of the phase diagram and records the evolution of dielectric constant as the soft mode is introduced with increasing Ti content in  $\text{SrMn}_{1-x}\text{Ti}_x\text{O}_{3-\delta}$ .

## 8.2 SYNTHESIS

The synthesis procedure was the same for the rest of the SMT series as it was for the Mn-rich portion of the series described in Chapter 7. X-ray diffraction performed on the samples after oxygen annealing revealed that the samples are indeed single-phase with space group  $Pm\bar{3}m$ ; Figure 8.2 shows that the lattice constant increases linearly from the value of 3.8055 Å for  $\text{SrMnO}_{3-\delta}$  to 3.905 for  $\text{SrTiO}_3$ .

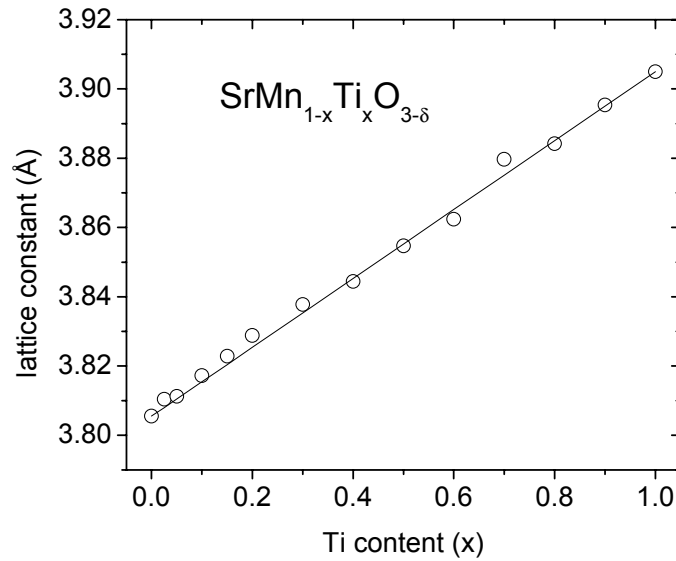


Figure 8.2: The change in the lattice constant with  $x$  for the series  $\text{SrTi}_x\text{Mn}_{1-x}\text{O}_{3-\delta}$ ; the solid line represents the linearly interpolated values calculated from the parent compounds  $\text{SrMnO}_3$  and  $\text{SrTiO}_3$ .

As was discussed in Chapter 7, the oxidation state of the samples could only be determined by iodimetric titration for  $x \leq 0.2$  because  $\text{Ti}^{4+}$  is insoluble in hydrochloric acid and cannot be reduced to a lower oxidation state with iodine. However, it is possible to measure the thermoelectric power of the series up to  $x = 0.6$ ; comparing the high-temperature limit of the thermoelectric power between the samples gives a relative, qualitative indication of the oxygen stoichiometry. The  $\alpha(T)$  curves are displayed in

Figure 8.3; samples with  $x > 0.6$  were too resistive at room temperature to attempt an accurate thermoelectric-power measurement.

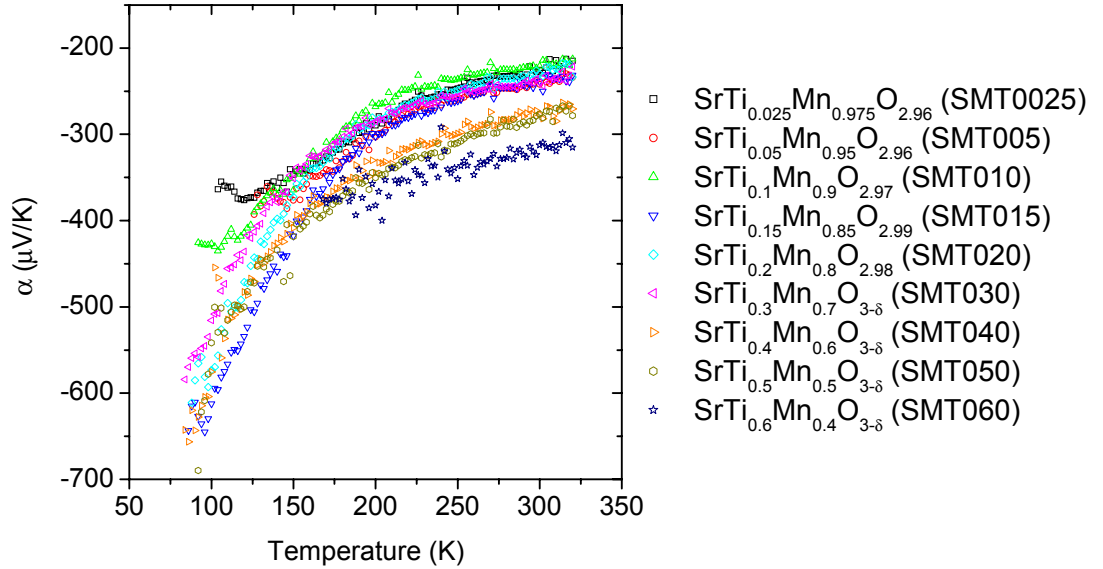


Figure 8.3: Thermoelectric power temperature dependencies for  $\text{SrMn}_{1-x}\text{Ti}_x\text{O}_{3-\delta}$  ( $0.025 \leq x \leq 0.6$ ).

The  $\alpha(T)$  curves shows groupings of high-temperature limits between  $-200 \mu\text{V/K}$  to  $-250 \mu\text{V/K}$  for samples with  $x = 0.025$  to  $0.3$ ,  $-250 \mu\text{V/K}$  to  $-300 \mu\text{V/K}$  for  $x = 0.4$  and  $0.5$ , and  $x = 0.6$  has a high-temperature limit with a magnitude greater than  $-300 \mu\text{V/K}$ . The similarity of the temperature dependencies of the different  $\alpha(T)$  traces gives confidence that the oxygen stoichiometry does not change much between the samples that were titrated for oxygen content and the samples that were not. The systematic increase in the high-temperature limit of  $\alpha(T)$  is due to either the increased oxygen stoichiometry of the samples or the decrease in possible hopping sites due to Ti substitution.

### 8.3 ADMITTANCE

The real and imaginary parts of the admittance, the AC-conductivity and dielectric constant were measured on SMT samples with  $x = 0.025, 0.005, 0.01, 0.015, 0.2, 0.3, 0.4, 0.5, 0.6, 0.7, 0.8, 0.9$ . The AC-conductivity of the samples decreased with increasing Ti content; Figure 8.4 displays the AC-conductivity for the samples with fractions of Ti content that are multiples of a tenth of a formula unit.

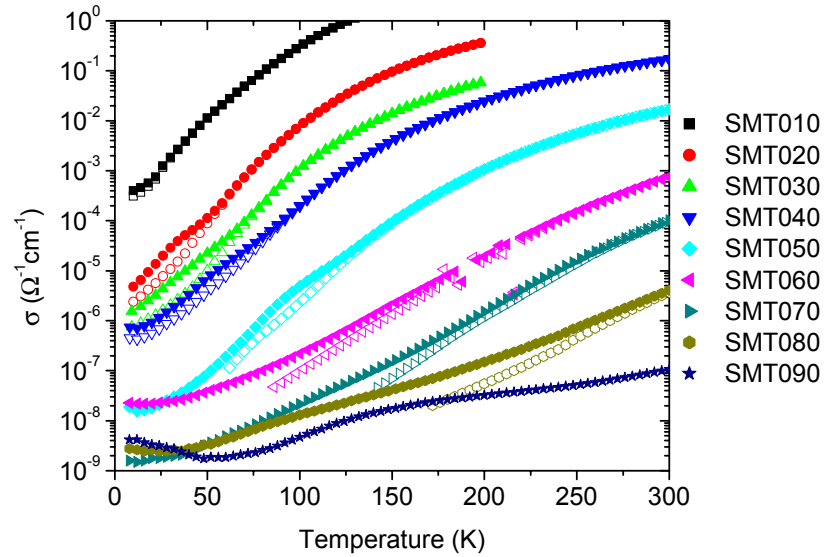


Figure 8.4: AC-conductivity temperature dependencies of  $\text{SrMn}_{1-x}\text{Ti}_x\text{O}_{3-\delta}$  for  $x = 0.1$  to  $0.9$ ; open symbols are for  $\nu = 10^3$  Hz and closed symbols for  $\nu = 10^4$  Hz.

It is expected that the conductivity will decrease with increasing Ti content since  $\text{SrTiO}_3$  is an insulator with a 3.2 eV bandgap and  $\text{SrMnO}_{3-\delta}$  is semiconducting with a bandgap on the order of a few 10s of meV.

Samples with  $x < 0.2$  were too conducting to observe dielectric relaxations; samples  $x = 0.2, 0.3$ , and  $0.4$  were close to a completed dielectric relaxation, but required curve fitting and extrapolation to determine the dielectric constant (Chapter 7). Samples

with  $x \geq 0.5$  all had well-converged dielectric relaxations as the temperature approached 0 K and the value of the dielectric constant at lowest temperature was taken to be the intrinsic dielectric constant due to the ionic polarization. Figure 8.5 shows the temperature dependence for  $x = 0.6$  to 0.9.

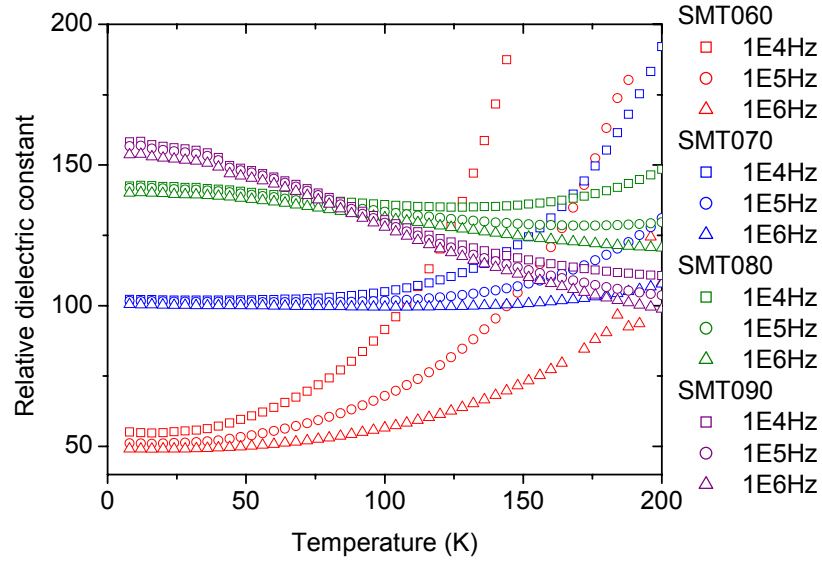


Figure 8.5: Temperature-dependent dielectric relaxations for SrMn<sub>1-x</sub>Ti<sub>x</sub>O<sub>3-δ</sub> (x = 0.6, 0.7, 0.8, 0.9).

The dielectric relaxations of the SMT samples from  $x = 0.6$  to 0.9 exhibit a systematic increase in the low-temperature limit of the dielectric constant. For samples  $x = 0.8$  and 0.9 there is a clear increase of the dielectric constant with temperature and a close inspection of  $x = 0.7$  reveals that there is a subtle increase in the dielectric constant with temperature. The soft mode responsible for the dielectric behavior of SrTiO<sub>3</sub> is clearly active in increasing the dielectric constant with temperature for SMT samples with  $x > 0.6$ .

## 8.4 DISCUSSION

The entire series of  $\text{SrMn}_{1-x}\text{Ti}_x\text{O}_3$  was synthesized to investigate the progression of the dielectric behavior as the amount of Ti content is increased from  $\text{SrMnO}_{3-\delta}$ , which has  $d^3 \text{Mn}^{4+}$  cations and no soft mode, to  $\text{SrTiO}_3$ , which has  $d^0 \text{Ti}^{4+}$  cations and an active soft mode. For samples with a Ti content  $0 < x < 0.2$ , the conductivity was too large to observe the dielectric relaxations; however, the value of  $\epsilon_r = 111$  measured for  $\text{SrMnO}_{2.95}$  and the value of  $\epsilon_r = 57$  measured for  $\text{SrMn}_{0.8}\text{Ti}_{0.2}\text{O}_{2.98}$  implies that the dielectric constant must decrease over this interval, and this decrease can be attributed to the decreasing tensile strain on the  $\text{Mn}^{4+} - \text{O}$  array as the tolerance factor decreases. As the Ti content is increased from  $x = 0.2$  to  $0.4$ , the dielectric behavior increases but then decreases from  $x = 0.4$  to  $0.6$ ; this hump in the dielectric constant cannot be explained in terms of the change in the tolerance factor, which is decreasing as  $x$  increases; the hump suggests that there are two interactions that compete to enhance or diminish the dielectric response.

Figure 8.6a, b show the results of two calculations that shed some light on the increase in the high-frequency dielectric constant from  $x = 0.2$  to  $0.4$  and the decrease from  $0.4$  to  $0.6$ . Figure 8.6a displays the probability of a randomly distributed Ti cation having “n” number of randomly distributed Ti cation near neighbors. For  $0.2 \leq x \leq 0.4$ , there are significant increases in the probabilities that a Ti cation has 2, 3, and 4 Ti near neighbors. On the other hand, Figure 8.7b shows the decrease in the estimated average (Mn – O) bond with increasing  $x$ ; it is worthy of note that the transition in the character of the strain on the (Mn – O) bond from tension to compression occurs for  $x \approx 0.4$ .



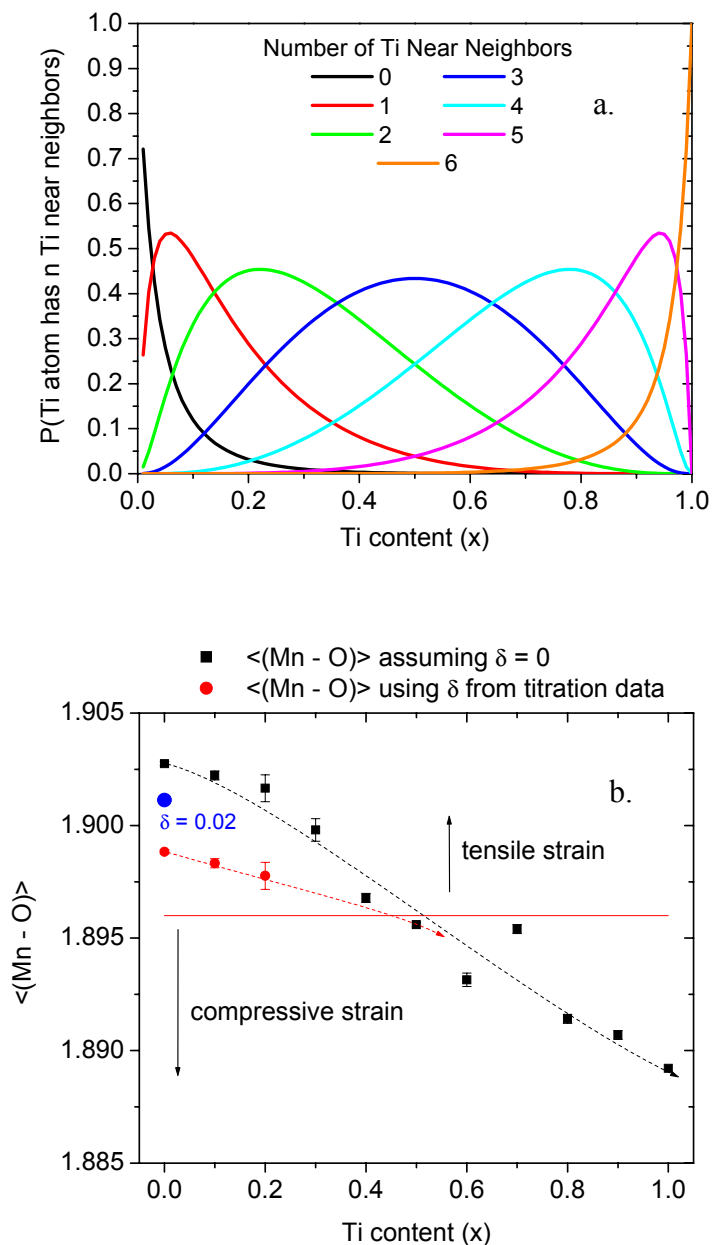


Figure 8.6: (a) Probability of a randomly distributed Ti cation having “n” number of randomly distributed Ti near neighbors; (b) the average (Mn – O) bond length vs.  $x$  in the  $\text{SrMn}_{1-x}\text{Ti}_x\text{O}_{3-\delta}$  system calculated from the lattice constant determined from room-temperature X-ray diffraction and assuming a constant ratio of (Ti – O) to (Mn – O) bond lengths as determined from the tabulated room-temperature equilibrium values.

The significant increase in the probability of Ti – Ti neighbors in the calculation shown in Figure 8.6a suggests that it is the increasing number of cooperative Ti displacements that increase the high-frequency dielectric constant; however, the (Mn – O) bond can no longer release its tensile strain to allow for the (Ti – O) bond length to be close to its equilibrium bond length where the (Mn – O) bond is placed under compression, and therefore the (Ti – O) bond is also placed under compression and its dielectric behavior is suppressed.

For samples with a Ti content greater than  $x = 0.6$ , the dielectric constant increases with decreasing temperature, which is an indication that the soft-mode is active in this portion of the phase diagram and the increasing Ti content increases the collective soft-mode dielectric behavior; the dielectric phase diagram for the  $\text{SrMn}_{1-x}\text{Ti}_x\text{O}_3$  series is shown in Figure 8.7.

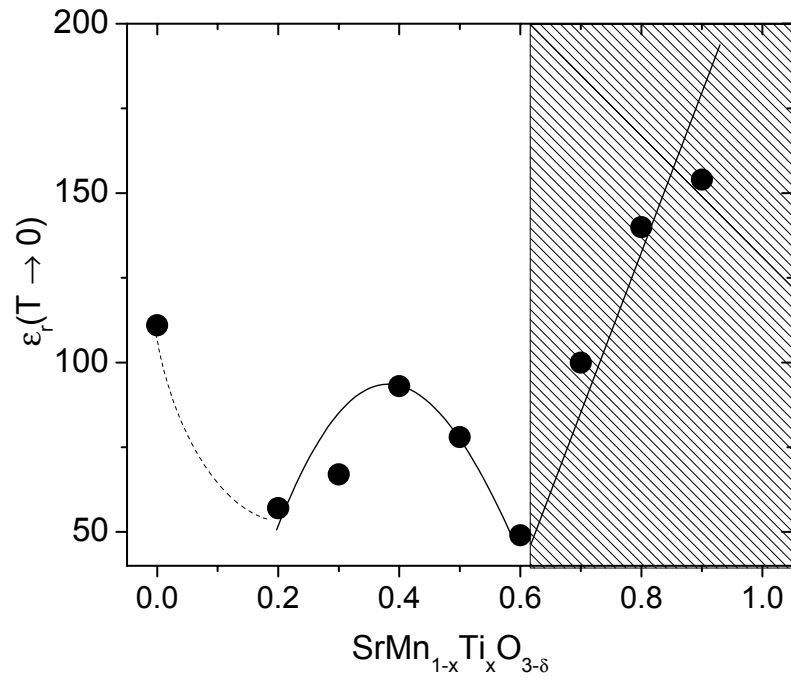


Figure 8.7: Dielectric phase diagram for the series  $\text{SrMn}_{1-x}\text{Ti}_x\text{O}_{3-\delta}$ ; the shaded region represents samples where the soft-mode is actively increasing the dielectric constant as the temperature decreases.

## Chapter 9: Conclusion

The work presented in this dissertation contained two primary investigations into the dielectric properties of non- $d^0$  perovskite-related manganese oxides: the first investigation probed the unique multiferroic properties of the hexagonal-perovskite series  $\text{RMn}_{1-x}\text{Ga}_x\text{O}_3$  ( $\text{R} = \text{Y}, \text{Ho}$ ) and the second explored the importance of lattice strain ( $t > 1$ ) and the  $d^n$  character of the transition-metal cation on the dielectric properties of the perovskite series  $\text{Sr}_y\text{Ca}_{1-y}\text{Mn}_{1-x}\text{B}_x\text{O}_{3-\delta}$  ( $\text{B} = \text{Ti}, \text{Zr}$ ). In both of these systems, the parent phase was systematically doped to observe systematic changes in the physical properties. The systematic changes in the physical properties allowed qualitative arguments to be made about the nature of the dominant physical processes and competing interactions.

### 9.1 MULTIFERROIC HEXAGONAL PEROVSKITES ( $\text{RMnO}_3$ )

The series of hexagonal perovskites ( $\text{RMnO}_3$ ) are ferrielectric and anti-ferromagnetic. Changing the R site from non-magnetic  $4d^0$  Y to magnetic  $4f^{10}$  Ho led to strong magnetic-phase competition in  $\text{HoMnO}_3$ . The magnetic-phase competition resulted in two spin-rotation transitions that coincided with peaks in the dielectric constant. Doping the Mn-site with Ga increased the  $c$  lattice constant and diluted the magnetic interactions in the  $ab$  plane; doping had the following effects: the ferrielectric transition temperature ( $T_C$ ) increased, the antiferromagnetic transition temperature ( $T_N$ ) decreased, the first spin-rotation temperature ( $T_{\text{SR}}$ ) increased, and the second spin-rotation temperature ( $T_2$ ) decreased. The following points highlight the important conclusions that can be made from this investigation:

1. Observation of a decrease of the thermal contraction below  $T_C$  provided additional evidence that the ferrielectric transition occurs at a temperature  $T_C < T_t$  where cooperative displacements of the R – O chains compensate the cooperative tilting of the trigonal-bipyramids that drove the *c*-axis thermal contraction
2. Doping with the larger  $Ga^{3+}$  ion increases the cooperative tilting of the trigonal-bipyramids and ferrielectric displacement of the R – O chains, which increases the *c*-axis lattice constant.
3. The increases of  $T_C$  and  $T_{SR}$  with Ga doping correlate a critical tilting of the trigonal-bipyramids with the ferrielectric and multiferroic transitions.
4. The decrease of  $T_2$  with increasing Ga doping highlights the importance of the Ho – O – Mn magnetic exchange in perturbing the spin-frustrated Mn – O planes and triggering the second spin-rotation transition.

Changing the multiferroic properties with chemical doping opens the door for more doping experiments. It should be possible to dope the R-site with small amounts of lanthanide ions that are slightly too large to form naturally in the hexagonal phase (e.g. Dy and Tb); this would have the effect of changing the average  $R^{3+}$  cation size, adding a variance to the (R – O) bond and changing the R – O – Mn exchange. Doping the Mn-site with Al or In offers opportunities to again change the *c*-axis with smaller and larger cations than Ga while continuing to dilute the magnetic interactions. The magnetic interactions can be perturbed in another way by doping the Mn-site with other transition metals that will tolerate the 5-fold coordination.

## 9.2 MANGANESE PEROVSKITES WITH STRESSED BONDS (AMnO<sub>3</sub>)

The goal of this investigation of perovskite AMnO<sub>3</sub> was to compare the dielectric properties of the network of d<sup>3</sup> Mn<sup>4+</sup> cations with isostructural ATiO<sub>3</sub>, which has d<sup>0</sup> Ti<sup>4+</sup> cations. In the perovskite titanates, the dielectric constant increases as the A-cation radius increases – opening the question as to whether the dielectric constant also increases with increasing A-cation radius in the perovskite manganites. In addition to the increase in dielectric constant with increasing A-cation radius, the perovskite titanates and other d<sup>0</sup> perovskites have a soft mode that increases the dielectric constant with decreasing temperature. Theoretical investigations have established the importance of transition-metal-cation d<sup>0</sup> – oxygen 2p  $\pi$ -bonding for creating the lattice instability that leads to the soft mode; the dielectric experiments on the d<sup>3</sup> perovskite manganites and mixed d<sup>0</sup>/d<sup>3</sup> character of the series SrMn<sub>1-x</sub>Ti<sub>x</sub>O<sub>3- $\delta$</sub>  put these theories to the test.

Throughout this investigation the tolerance factor  $t$  was referenced as an important parameter of the perovskite structure. Where  $t < 1$ , as is the case for CaBO<sub>3</sub> (B = Mn, Ti), the (A – O) bonds are under tensile stress and the (B – O) bonds are under compressive stress; where  $t > 1$ , as is the case for SrMnO<sub>3</sub> and high-temperature SrTiO<sub>3</sub>, the opposite is true.

The small band gap of the AMnO<sub>3</sub> perovskites and the chemical activity of the Mn<sup>4+</sup> cation were hurdles to measuring the dielectric behavior of Sr<sub>y</sub>Ca<sub>1-y</sub>MnO<sub>3- $\delta$</sub>  for  $y \geq 0.5$ . The compositions with  $y \geq 0.5$  required a special two-step synthesis technique to obtain single-phase perovskite samples; after the second-step oxygen anneal, the samples became too conducting to observe the dielectric relaxation to the high-frequency value representing the ionic contribution. One sample, SrMnO<sub>2.95</sub>, was resistive enough to allow the dielectric constant to be extrapolated to a high-frequency value  $\epsilon_{\infty} \cong 111$ . This value of  $\epsilon_{\infty} \cong 111$  was confirmed as the high-frequency dielectric constant due to the

ionic polarization by converting the infra-red optical conductivity data of Sacchetti *et al.* to the real part of the dielectric constant (Sacchetti et al. 2005).

To buttress the extrapolated high-frequency dielectric constant of  $\text{SrMnO}_{2.95}$  with supporting evidence, a doping scheme was devised to decrease the sample conductivity at the expense of some of the tensile stress on the (Mn – O) bond. The effect of dilute Ti-doping was the opposite of the intended effect; it increased the conductivity. To observe the dielectric relaxations, it was necessary to dope the B-site with a mole fraction of Ti greater than 20%. The addition of the larger  $\text{Ti}^{4+}$  cation decreased the tolerance factor, and the high-frequency dielectric constant decreased to  $\epsilon_{\infty} \cong 57$ . However, increasing the Ti doping from 20% to 30% and 40% increased the dielectric constant; this increase in  $\epsilon_{\infty}$  proves that the dielectric results of the Mn-rich side of the series  $\text{SrMn}_{1-x}\text{Ti}_x\text{O}_{3-\delta}$  cannot be explained in terms of the tolerance factor alone.

Dilute Ti doping increased the conductivity in comparison to the  $\text{SrMnO}_{2.95}$  sample because the Ti doping was able to substitute onto 5-fold coordinated sites and create  $\text{Mn}^{3+}$  cations on 6-fold coordinated sites; having the electron located at 6-fold coordinated decreased the electronic trapping energy.  $\text{Zr}^{4+}$  cations are not able to substitute onto a 5-fold coordinated site. As a result, Zr doping was more efficient at decreasing the conductivity than the Ti-doping; a Zr mole fraction of only 10% was needed to observe the dielectric relaxation. The drawback of the significantly larger ionic radius was that it lowered the tolerance factor further and dramatically decreased the high-frequency dielectric constant to an  $\epsilon_{\infty} \cong 10$ . This value for the high-frequency dielectric constant is less than the value of  $\epsilon_{\infty} \cong 35$  measured for  $t \leq 1$  in  $\text{Sr}_x\text{Ca}_{1-x}\text{MnO}_3$   $0.2 \leq x \leq 0.5$ . Since  $t > 1$  for  $\text{SrMn}_{0.9}\text{Zr}_{0.1}\text{O}_{3-\delta}$ , the tolerance factor alone cannot explain the decrease in  $\epsilon_{\infty}$ ; the dielectric constant must also decrease with increasing variance  $\sigma_B^2$  of the (B – O) bond length.

In addition to my stretching the (B – O) bond, the effect of the  $d^n$  character on the dielectric behavior was investigated in the series  $\text{SrMn}_{1-x}\text{Ti}_x\text{O}_{3-\delta}$ . The soft-mode dielectric behavior of the parent compound  $\text{SrTiO}_3$  ( $d^0 \text{ Ti}^{4+}$  cations) has been well-characterized in the literature, whereas the IR-spectroscopy experiments of Sacchetti *et al.* and the dielectric measurements of this work show that there is no soft-mode dielectric behavior in  $\text{SrMnO}_3$  ( $d^3 \text{ Mn}^{4+}$  cations). The difference in the dielectric behavior of the end members allows for the transition from non-soft-mode behavior to soft-mode behavior to be observed in this series. As the amount of Ti content was increased from 20% to 60%, there was a hump in  $\epsilon_\infty$  followed by an increase in  $\epsilon_\infty$  as the Ti content increased from 60% to 100%. Samples with Ti content greater than 60% exhibited the temperature-dependent dielectric behavior that is characteristic of the soft mode. However, the hump in the  $\epsilon_\infty$  phase diagram from 20% to 60% cannot be explained by the stress on the (B – O) bond; the increase in  $\epsilon_\infty$  from 20% to 40% is due to the increasing  $d^0 \text{ Ti}$  content whereas the decrease in  $\epsilon_\infty$  is correlated with the loss of tensile stress on the (Mn – O) bond leading to compression of the (Ti – O) bond.



The primary conclusions of this investigation on the perovskite manganese oxides with stretched (Mn – O) bonds are the following:

1. In the perovskite structure, the dielectric properties are dominated by the A – O polarization where  $t < 1$  and by the B – O polarization where  $t > 1$
2. Increasing tensile stress on the dominant ionic-polarization network increases its polarizability; also, decreasing the tensile stress or increasing the compressive stress dampens the polarizability of the ionic network
3. Increasing the bond-length variance  $\sigma^2$  of the dominant polarization network also dampens its cooperative polarizability
4. Adding  $d^3 \text{ Mn}^{4+}$  to  $\text{SrTiO}_3$  diminishes the cooperative dynamic  $\text{Ti}^{4+}$  displacements, which dampens the soft mode and leads to a transition to non-soft-mode dielectric behavior

A literature search on the relationship of the tolerance factor and dielectric properties found the first conclusion mentioned in several papers investigating  $d^0$  perovskite oxides for dielectric resonators (Petzelt et al. 1992; Shivasubramanian et al. 1997; Venkatesh and Murthy 1999; Zurmuhlen et al. 1995). Our work represents an experimental generalization of the first conclusion to include non- $d^0$  perovskite oxides.

When applied to the dielectric phase diagram of  $\text{Sr}_{1-x}\text{Ca}_x\text{MnO}_3$ , the first conclusion adequately explains the decrease in  $\epsilon_\infty$  as the Sr content is increased from  $x = 0$  to 0.2; the decrease in  $\epsilon_\infty$  was previously believed to be caused by some oxide-ion vacancies (Cohn et al. 2004). The tensile stress also explains the increase in the dielectric constant on the Sr-rich side of the phase diagram from  $\epsilon_\infty \cong 35$  for  $\text{Sr}_{0.5}\text{Ca}_{0.5}\text{MnO}_3$  to  $\epsilon_\infty \cong 111$  for  $\text{SrMnO}_{2.95}$ .

The investigation of the  $\text{SrMn}_{1-x}\text{Ti}_x\text{O}_3$  series is also significant because it is an experimental demonstration of the importance of “ $d^0$ -ness” to foster the soft-mode dielectric behavior; the importance of “ $d^0$ -ness” has already been established theoretically (Cohen and Krakauer 1992). It is also an experimental testament of the impossibility of obtaining a multiferroic phenomenon with a single cation array that has been pointed out in the analytical calculations of Hill and Filippetti (Hill 2000; Hill and Filippetti 2002), since classical electric ordering requires a  $d^0$  electronic configuration for a soft-mode ferroelectric transition and magnetic ordering requires non- $d^0$  configurations. The demonstrated exception is the electric polarization produced by spiral spin structures (Katsura et al. 2005) and observed in  $\text{TbMnO}_3$  (Kenzelmann et al. 2005). Another possible exception might be a  $d^1$  system where the two empty  $t_{2g}$ -orbitals are available for  $\pi$ -bonding and the single d-electron is available for antiferromagnetic and weak ferromagnetic exchange interactions.

Additional doping experiments can add to our investigations of the non- $d^0$  perovskites. For instance, substitution of  $\text{Ge}^{4+}$  for  $\text{Mn}^{4+}$  in  $\text{SrMnO}_3$  would increase the tolerance factor as well as the B – O bond-length variance; increasing the tolerance and bond-length variance would shed more light on the role those two effects have on the high-frequency dielectric constant. Our dielectric investigations of the perovskite manganites opens the door to investigate the dielectric behavior of other non- $d^0$  perovskites as the tolerance factor is varied from  $t < 1$  to  $t > 1$ .

The investigations of this dissertation fill gaps in the scientific literature on the dielectric behavior of non- $d^0$  perovskite-related transition-metal oxides. Hopefully this knowledge will lead to further investigations that will produce the following results: a better understanding of complex multiferroic phenomena and efficient design of magnetoelectric materials for *Spintronics* applications.

## References

- Abrahams, S. (2001). "Ferroelectricity and structure in the YMnO<sub>3</sub> family." *Acta Crystallographica Section B*, 57(4), 485-490.
- Ahn, K. H., and Millis, A. J. (2000). "Effects of magnetic ordering on the anisotropy and temperature dependence of the optical conductivity in LaMnO<sub>3</sub>: A tight-binding approach." *Physical Review B*, 61(20), 13545 - 13559.
- Aiken, J. G., and Jordan, A. G. (1968). "Electrical transport properties of single crystal nickel oxide." *Journal of Physics and Chemistry of Solids*, 29(12), 2153-2167.
- Azzoni, C. B., Mozzati, M. C., Paleari, A., Massarotti, V., Bini, M., and Capsoni, D. (2000). "Magnetic evidence of different environments of manganese ions in Mn-substituted strontium titanate." *Solid State Communications*, 114(12), 617-622.
- Ball, C. J., Begg, B. D., Cookson, D. J., Thorogood, G. J., and Vance, E. R. (1998). "Structures in the System CaTiO<sub>3</sub>/SrTiO<sub>3</sub>." *Journal of Solid State Chemistry*, 139(2), 238-247.
- Barrett, J. H. (1952). "Dielectric Constant in Perovskite Type Crystals." *Physical Review*, 86(1), 118 LP - 120.
- Barsoukov, E., and Macdonald, J. R. (2005). "Impedance Spectroscopy: Theory, Experiment, and Applications." John Wiley & Sons, Hoboken, New Jersey.
- Bednorz, J. G., and Muller, K. A. (1986). "Possible high T<sub>c</sub> superconductivity in the Ba-La-Cu-O system." *Zeitschrift fur Physik B Condensed Matter*, 64(2), 189-193.
- Bednorz, J. G., and Muller, K. A. (1988). "Perovskite-type oxides: the new approach to high-T<sub>c</sub> superconductivity." *Reviews of Modern Physics*, 60(3), 585 - 600.
- Binek, C., and Doudin, B. (2005). "Magnetoelectronics with magnetoelectrics." *Journal of Physics: Condensed Matter*, 17(2), L39.
- Blasco, J., Sanchez, M. C., Perez-Cacho, J., Garcia, J., Subias, G., and Campo, J. (2002). "Synthesis and structural study of LaNi<sub>1-x</sub>Mn<sub>x</sub>O<sub>3</sub>+ $\delta$  perovskites." *Journal of Physics and Chemistry of Solids*, 63(5), 781-792.
- Brinks, H. W., Rodriguez-Carvajal, J., Fjellvag, H., Kjekshus, A., and Hauback, B. C. (2001). "Crystal and magnetic structure of orthorhombic HoMnO<sub>3</sub>." *Physical Review B*, 63(9), 094411.
- Caignaert, V., Nguyen, N., Hervieu, M., and Raveau, B. (1985). "Sr<sub>2</sub>Mn<sub>2</sub>O<sub>5</sub>, an oxygen-defect perovskite with Mn(III) in square pyramidal coordination." *Materials Research Bulletin*, 20(5), 479-484.
- Chiang, C. C. K., and Poeppelmeier, K. R. (1991). "Structural investigation of oxygen-deficient perovskite CaMnO<sub>2.75</sub>." *Materials Letters*, 12(1-2), 102-108.
- Chmaissem, O., Dabrowski, B., Kolesnik, S., Mais, J., Brown, D. E., Kruk, R., Prior, P., Pyles, B., and Jorgensen, J. D. (2001). "Relationship between structural parameters and the Neel temperature in Sr<sub>1-x</sub>Ca<sub>x</sub>MnO<sub>3</sub> (0 ≤ x ≤ 1) and Sr<sub>1-y</sub>BayMnO<sub>3</sub> (y ≤ 0.2)." *Physical Review B*, 64, 134412.
- Cochran, W. (1960). "Crystal stability and the theory of ferroelectricity." *Advances In Physics*, 9(36), 387-423.

- Cohen, R. E., and Krakauer, H. (1992). "Electronic-Structure Studies of the Differences in Ferroelectric Behavior of BaTiO<sub>3</sub> and PbTiO<sub>3</sub>." *Ferroelectrics*, 136(1-4), 65-83.
- Cohn, J. L., Peterca, M., and Neumeier, J. J. (2004). "Low-temperature permittivity of insulating perovskite manganites." *Physical Review B*, 70(21), 214433-6.
- Cusack, N., and Kendall, P. (1958). "The Absolute Scale of Thermoelectric Power at High Temperature." *Proceedings of the Physical Society*, 72(5), 898-901.
- Dabrowski, B., Chmaissem, O., Mais, J., Kolesnik, S., Jorgensen, J. D., and Short, S. (2003). "Tolerance factor rules for Sr(1-x-y)Ca(x)Ba(y)MnO(3) perovskites." *Journal of Solid State Chemistry*, 170(1), 154-164.
- Datta, S., and Das, B. (1990). "Electronic analog of the electro-optic modulator." *Applied Physics Letters*, 56(7), 665-667.
- dela Cruz, C., Yen, F., Lorenz, B., Wang, Y. Q., Sun, Y. Y., Gospodinov, M. M., and Chu, C. W. (2005). "Strong spin-lattice coupling in multiferroic HoMnO<sub>3</sub>: Thermal expansion anomalies and pressure effect." *Physical Review B*, 71(6).
- Eerenstein, W., Mathur, N. D., and Scott, J. F. (2006). "Multiferroic and magnetoelectric materials." *Nature*, 442(7104), 759-765.
- Fiebig, M., Degenhardt, C., and Pisarev, R. V. (2002). "Magnetic phase diagram of HoMnO<sub>3</sub>." *J. Appl. Phys.*, 91(10), 8867-8869.
- Fiebig, M., Frohlich, D., Kohn, K., Leute, S., Lottermoser, T., Pavlov, V. V., and Pisarev, R. V. (2000). "Determination of the Magnetic Symmetry of Hexagonal Manganites by Second Harmonic Generation." *Physical Review Letters*, 84(24), 5620 - 5623.
- Fiebig, M., Lottermoser, T., and Pisarev, R. V. (2003). "Spin-rotation phenomena and magnetic phase diagrams of hexagonal RMnO<sub>3</sub>." *Journal of Applied Physics*, 93(10), 8194-8196.
- Garcia-Jaca, J., Mesa, J. L., Insausti, M., Larramendi, J. I. R., Arriortua, M. I., and Rojo, T. (1999). "Synthesis, crystal structure, stoichiometry and magnetic properties of (Ca<sub>1-x</sub>Sr<sub>x</sub>)VO<sub>3</sub>." *Materials Research Bulletin*, 34(2), 289-301.
- Geller, S., Jeffries, J. B., and Curlander, P. J. (1975). "The crystal structure of a new high-temperature modification of YGaO<sub>3</sub>." *Acta Crystallographica Section B*, 31(12), 2770-2774.
- Golin, S. (1963). "Polarization Conductivity in p-Type Germanium." *Physical Review*, 132(1), 178 - 188.
- Goodenough, J. B. (2003). "Rare Earth - Manganese Perovskites." Handbook on the Physics and Chemistry of Rare Earths, Vol. 33, K. A. Gschneidner and L. Eyring, eds., Elsevier Science, 249-351.
- Harrison, W. A. (2004). *Elementary Electronic Structure*, World Scientific Publishing Co. Pte. Ltd., Toh Tuck Link, Singapore.
- Hill, N. A. (2000). "Why are there so few magnetic ferroelectrics?" *Journal of Physical Chemistry*, 104, 6694-6707.
- Hill, N. A., and Filippetti, A. (2002). "Why are there any magnetic ferroelectrics?" *Journal of Magnetism and Magnetic Materials*, 242-245, 976-979.

- Hill, N. A., and Rabe, K. M. (1999). "First-principles investigation of ferromagnetism and ferroelectricity in bismuth manganite." *Physical Review B*, 59(13), 8759 - 8769.
- Ismailzade, I. G., and Kizhaev, S. A. (1965). "Determination of the Curie Point of the Ferroelectrics YMnO<sub>3</sub> and YbMnO<sub>3</sub>." *Soviet Physics - Solid State*, 7(1), 236-238.
- Jin, S., Tiefel, T. H., McCormack, M., Fastnacht, R. A., Ramesh, R., and Chen, L. H. (1994). "Thousandfold Change in Resistivity in Magnetoresistive La-Ca-Mn-O Films." *Science*, 264(5157), 413-415.
- Jonscher, A. K. (1977). "Universal Dielectric Response." *Nature*, 267(5613), 673-679.
- Kabashima, S., and Kawakubo, T. (1968). "High Frequency Conductivity of NiO." *Journal of the Physical Society of Japan*, 24(3), 493 - 497.
- Kao, K. C. (2004). *Dielectric phenomena in solids: with emphasis on physical concepts of electronic processes*, Elsevier, San Diego.
- Katsufuji, T., Mori, S., Masaki, M., Moritomo, Y., Yamamoto, N., and Takagi, H. (2001). "Dielectric and magnetic anomalies and spin frustration in hexagonal RMnO<sub>3</sub> (R=Y, Yb, and Lu)." *Physical Review B*, 64(10), 104419.
- Katsura, H., Nagaosa, N., and Balatsky, A. V. (2005). "Spin Current and Magnetoelectric Effect in Noncollinear Magnets." *Physical Review Letters*, 95(5), 057205-4.
- Kennedy, B. J., Howard, C. J., Thorogood, G. J., and Hester, J. R. (2001). "The Influence of Composition and Temperature on the Phases in Sr<sub>1-x</sub>BaxZrO<sub>3</sub> Perovskites: A High-Resolution Powder Diffraction Study." *Journal of Solid State Chemistry*, 161(1), 106-112.
- Kenzelmann, M., Harris, A. B., Jonas, S., Broholm, C., Schefer, J., Kim, S. B., Zhang, C. L., Cheong, S.-W., Vajk, O. P., and Lynn, J. W. (2005). "Magnetic Inversion Symmetry Breaking and Ferroelectricity in TbMnO<sub>3</sub>." *Physical Review Letters*, 95(8), 087206-4.
- Kimura, T., Goto, T., Shintani, H., Ishizaka, K., Arima, T., and Tokura, Y. (2003a). "Magnetic control of ferroelectric polarization." *Nature*, 426(6962), 55-58.
- Kimura, T., Kawamoto, S., Yamada, I., Azuma, M., Takano, M., and Tokura, Y. (2003b). "Magnetocapacitance effect in multiferroic BiMnO<sub>3</sub>." *Physical Review B*, 67(18), 180401-4.
- Lee, K. J., and Iguchi, E. (1995). "Electronic Properties of SrMnO<sub>3-x</sub>." *Journal of Solid State Chemistry*, 114, 242-248.
- Lee, S., Pirogov, A., Han, J. H., Park, J. G., Hoshikawa, A., and Kamiyama, T. (2005). "Direct observation of a coupling between spin, lattice and electric dipole moment in multiferroic YMnO<sub>3</sub>." *Physical Review B*, 71(18).
- Lemanov, V. V., Sotnikov, A. V., Smirnova, E. P., and Weihnacht, M. (2005). "Dielectric relaxation in doped SrTiO<sub>3</sub>: Transition from classical thermal activation to quantum tunnelling." *Journal of Applied Physics*, 98(5), 056102-3.
- Lemanov, V. V., Sotnikov, A. V., Smirnova, E. P., Weihnacht, M., and Kunze, R. (1999). "Perovskite CaTiO<sub>3</sub> as an incipient ferroelectric." *Solid State Communications*, 110(11), 611-614.
- Levin, I., Amos, T. G., Bell, S. M., Farber, L., Vanderah, T. A., Roth, R. S., and Toby, B. H. (2003). "Phase equilibria, crystal structures, and dielectric anomaly in the BaZrO<sub>3</sub>-CaZrO<sub>3</sub> system." *Journal of Solid State Chemistry*, 175(2), 170-181.

- Litvinchuk, A. P., Iliev, M. N., Popov, V. N., and Gospodinov, M. M. (2004). "Raman and infrared-active phonons in hexagonal HoMnO<sub>3</sub> single crystals: magnetic ordering effects." *Journal of Physics: Condensed Matter*, 16(6), 809.
- Lonkai, T., Hohlwein, D., Ihringer, J., and Prandl, W. (2002). "The magnetic structures of YMnO<sub>3</sub>-delta and HoMnO<sub>3</sub>." *Applied Physics a-Materials Science & Processing*, 74, S843-S845.
- Lorenz, B., Litvinchuk, A. P., Gospodinov, M. M., and Chu, C. W. (2004). "Field-induced reentrant novel phase and a ferroelectric-magnetic order coupling in HoMnO<sub>3</sub>." *Physical Review Letters*, 92(8).
- Lukaszewicz, K., and Karut-Kalicinska, J. (1974). "X-ray Investigations of the Crystal Structure and Phase Transitions of YMnO<sub>3</sub>." *Ferroelectrics*, 7, 81-82.
- Lunkenheimer, P., Bobnar, V., Pronin, A. V., Ritus, A. I., Volkov, A. A., and Loidl, A. (2002). "Origin of apparent colossal dielectric constants." *Physical Review B*, 66(5), 052105.
- Maignan, A., Hebert, S., Pi, L., Pelloquin, D., Martin, C., Michel, C., Hervieu, M., and Raveau, B. (2002). "Perovskite manganites and layered cobaltites: potential materials for thermoelectric applications." *Crystal Engineering Crystal Chemistry of Functional Materials II, Proceedings of Symposium L, E-MRS Spring Meeting, June 18-21, 2002*, 5(3-4), 365-382.
- Marder, M. P. (2000). *Condensed Matter Physics*, John Wiley and Sons, Inc., New York.
- Mori, M. (2004). "Effect of B-site doing on thermal cycle shrinkage for La<sub>0.8</sub>Sr<sub>0.2</sub>Mn<sub>1-x</sub>MxO<sub>3</sub>+[delta] perovskites (M=Mg, Al, Ti, Mn, Fe, Co, Ni; 0<math>x\leq 0.1</math>)." *Solid State Ionics Dokiya Memorial Special Issue*, 174(1-4), 1-8.
- Muller, K. A., and Burkard, H. (1979). "SrTiO<sub>3</sub>: An intrinsic quantum paraelectric below 4 K." *Physical Review B*, 19(7), 3593 LP - 3602.
- Munoz, A., Alonso, J. A., Martinez-Lope, M. J., Casais, M. T., Martinez, J. L., and Fernandez-Diaz, M. T. (2000). "Magnetic structure of hexagonal RMnO<sub>3</sub> (R=Y, Sc): Thermal evolution from neutron powder diffraction data." *Physical Review B*, 62(14), 9498 - 9510.
- Munoz, A., Alonso, J. A., Martinez-Lope, M. J., Casais, M. T., Martinez, J. L., and Fernandez-Diaz, M. T. (2001). "Evolution of the Magnetic Structure of Hexagonal HoMnO<sub>3</sub> from Neutron Powder Diffraction Data." *Chem. Mater.*, 13(5), 1497-1505.
- Negas, T., and Roth, R. S. (1970). "The system SrMnO<sub>3</sub>-x." *Journal of Solid State Chemistry*, 1(3-4), 409-418.
- Neumeier, J. J. (2005). "Question regarding PRB 70 214433 (2004)." J. Denyszyn, ed.
- Neville, R. C., Hoeneisen, B., and Mead, C. A. (1972). "Permittivity of Strontium Titanate." *Journal of Applied Physics*, 43(5), 2124-2131.
- Norton, D. P., Theodoropoulou, N. A., Hebard, A. F., Budai, J. D., Boatner, L. A., Pearton, S. J., and Wilson, R. G. (2003). "Properties of Mn-Implanted BaTiO<sub>3</sub>, SrTiO<sub>3</sub>, and KTaO<sub>3</sub>." *Electrochemical and Solid-State Letters*, 6(2), G19-G21.
- Pearton, S. J., Heo, W. H., Ivill, M., Norton, D. P., and Steiner, T. (2004). "Dilute magnetic semiconducting oxides." *Semiconductor Science and Technology*, 19(10), R59.

- Petzelt, J., Zurmuhlen, R., Bell, A., Kamba, S., Kozlov, G. V., Volkov, A. A., and Setter, N. (1992). "Dielectric-Spectroscopy of Some  $\text{Ba}(\text{B}'^{1/2}\text{b}^{1/2})\text{O}_3$  Complex Perovskites in the 10(11)-10(14)Hz Range." *Ferroelectrics*, 133(1-4), 205-210.
- Poepfelmeier, K. R., Leonowicz, M. E., and Longo, J. M. (1982). " $\text{CaMnO}_{2.5}$  and  $\text{Ca}_2\text{MnO}_{3.5}$ : New oxygen-defect perovskite-type oxides." *Journal of Solid State Chemistry*, 44(1), 89-98.
- Pollak, M., and Geballe, T. H. (1961). "Low-Frequency Conductivity Due to Hopping Processes in Silicon." *Physical Review*, 122(6), 1742 - 1753.
- Polnus, M. A. (1978). *Applied Electromagnetics*, McGraw-Hill, Inc., New York.
- Prellier, W., Fouchet, A., and Mercey, B. (2003). "Oxide-diluted magnetic semiconductors: a review of the experimental status." *Journal of Physics: Condensed Matter*, 15(37), R1583.
- Qin, S., Becerro, A. I., Seifert, F., Gottsmann, J., and Jiang, J. (2000). "Phase transitions in  $\text{Ca}_{1-x}\text{Sr}_x\text{TiO}_3$  perovskites: effects of composition and temperature." *Journal of Materials Chemistry*, 10, 1609-1615.
- Reller, A., Jefferson, D. A., Thomas, J. M., and Uppal, M. K. (1983). "Oxygen Vacancy Ordering in a Selective Oxidation Catalyst:  $\text{CaMnO}_{2.8}$ ." *Journal of Physical Chemistry*, 87, 913-914.
- Rupprecht, G., and Bell, R. O. (1964). "Dielectric Constant in Paraelectric Perovskites." *Physical Review*, 135(3A), A748 - A752.
- Sacchetti, A., Baldini, M., Crispoldi, F., Postorino, P., Dore, P., Nucara, A., Martin, C., and Maignan, A. (2005). "Temperature dependence of the optical phonons in  $\text{SrMnO}_3$  manganite: Evidence of a low-temperature structural transition in the hexagonal compound." *Physical Review B*, 72(17), 172407.
- Sanchez, M. C., Garcia, J., Blasco, J., Subias, G., and Perez-Cacho, J. (2002). "Local electronic and geometrical structure of  $\text{LaNi}_{1-x}\text{Mn}_x\text{O}_{3+\delta}$  perovskites determined by x-ray-absorption spectroscopy." *Physical Review B*, 65(14), 144409.
- Seehra, M. S., and Helmick, R. E. (1981). "Dielectric anomaly in  $\text{MnO}$  near the magnetic phase transition." *Physical Review B*, 24(9), 5098 - 5102.
- Servoin, J. L., Luspain, Y., and Gervais, F. (1980). "Infrared dispersion in  $\text{SrTiO}_3$  at high temperature." *Physical Review B*, 22(11), 5501 LP - 5506.
- Shannon, R. D., and Prewitt, C. T. (1969). "Effective ionic radii in oxides and fluorides." *Acta Crystallographica Section B*, 25(5), 925-946.
- Sharma, P. A., Ahn, J. S., Hur, N., Park, S., Kim, S. B., Lee, S., Park, J.-G., Guha, S., and Cheong, S.-W. (2004). "Thermal Conductivity of Geometrically Frustrated, Ferroelectric  $\text{YMnO}_3$ : Extraordinary Spin-Phonon Interactions." *Physical Review Letters*, 93(17), 177202-4.
- Shivasubramanian, V., Murthy, V. R. K., and Viswanathan, B. (1997). "Microwave dielectric properties of certain simple alkaline earth perovskite compounds as a function of tolerance factor." *Japanese Journal of Applied Physics*, 36, 194-197.
- Snowden, D. P., and Saltsburg, H. (1965). "Hopping Conduction in  $\text{NiO}$ ." *Physical Review Letters*, 14(13), 497 - 499.

- Sugie, H., Iwata, N., and Kohn, K. (2002). "Magnetic ordering of rare earth ions and magnetic-electric interaction of hexagonal RMnO<sub>3</sub> (R=Ho, Er, Yb or Lu)." *Journal of the Physical Society of Japan*, 71(6), 1558-1564.
- Tichy, R. S., and Goodenough, J. B. (2002). "Oxygen permeation in cubic SrMnO<sub>3</sub>-[delta]." *Solid State Sciences*, 4(5), 661-664.
- Tkach, A., Vilarinho, P. M., and Kholkin, A. L. (2005). "Structure-microstructure-dielectric tunability relationship in Mn-doped strontium titanate ceramics." *Acta Materialia*, 53(19), 5061-5069.
- Tkach, A., Vilarinho, P. M., Kholkin, A. L., Pashkin, A., Veljko, S., and Petzelt, J. (2006). "Broad-band dielectric spectroscopy analysis of relaxational dynamics in Mn-doped SrTiO<sub>3</sub> ceramics." *Physical Review B*, 73(10), 104113-7.
- Vajk, O. P., Kenzelmann, M., Lynn, J. W., Kim, S. B., and Cheong, S.-W. (2005). "Magnetic Order and Spin Dynamics in Ferroelectric HoMnO<sub>3</sub>." *Physical Review Letters*, 94(8), 087601-4.
- Van Aken, B. B., Meetsma, A., and Palstra, T. T. M. (2001a). "Hexagonal ErMnO<sub>3</sub>." *Acta Crystallographica Section E-Structure Reports Online*, 57, I38-I40.
- Van Aken, B. B., Meetsma, A., and Palstra, T. T. M. (2001b). "Hexagonal LuMnO<sub>3</sub> revisited." *Acta Crystallographica Section E-Structure Reports Online*, 57, I101-I103.
- Van Aken, B. B., Meetsma, A., and Palstra, T. T. M. (2001c). "Hexagonal YbMnO<sub>3</sub> revisited." *Acta Crystallographica Section E-Structure Reports Online*, 57, I87-I89.
- Van Aken, B. B., and Palstra, T. T. M. (2004). "Influence of magnetic on ferroelectric ordering in LuMnO<sub>3</sub>." *Physical Review B*, 69(13), 134113-6.
- Van Aken, B. B., Palstra, T. T. M., Filippetti, A., and Spaldin, N. A. (2004). "The origin of ferroelectricity in magnetoelectric YMnO<sub>3</sub>." *Nature Materials*, 3(3), 164-170.
- Venkatesh, J., and Murthy, V. R. K. (1999). "Microwave dielectric properties of (Ba, Sr)(Zn<sub>1/3</sub>Ta<sub>2/3</sub>)O<sub>3</sub> dielectric resonators." *Materials Chemistry and Physics*, 58(3), 276-279.
- von Hippel, A. (1950). "Ferroelectricity, Domain Structure, and Phase Transitions of Barium Titanate." *Reviews of Modern Physics*, 22(3), 221 - 237.
- Yen, F., dela Cruz, C. R., Lorenz, B., Sun, Y. Y., Wang, Y. Q., Gospodinov, M. M., and Chu, C. W. (2005). "Low-temperature dielectric anomalies in HoMnO<sub>3</sub>: The complex phase diagram." *Physical Review B*, 71(18), 180407-4.
- Zhong, W., and Vanderbilt, D. (1996). "Effect of quantum fluctuations on structural phase transitions in SrTiO<sub>3</sub> and BaTiO<sub>3</sub>." *Physical Review B*, 53(9), 5047 LP - 5050.
- Zhou, H. D., Denyszyn, J. C., and Goodenough, J. B. (2005). "Effect of Ga doping on the multiferroic properties of RMn<sub>1-x</sub>Ga<sub>x</sub>O<sub>3</sub> (R = Ho, Y)." *Physical Review B*, 72(22), 224401-5.
- Zhou, H. D., Janik, J. A., Vogt, B. W., Jo, Y. J., Balicas, L., Case, M. J., Wiebe, C. R., Denyszyn, J. C., Goodenough, J. B., and Cheng, J. G. (2006a). "Specific heat of geometrically frustrated and multiferroic RMn<sub>1-x</sub>Ga<sub>x</sub>O<sub>3</sub>." *submitted to Physical Review B*.



- Zhou, J.-S., Goodenough, J. B., Gallardo-Amores, J. M., Moran, E., Alario-Franco, M. A., and Caudillo, R. (2006b). "Hexagonal versus perovskite phase of manganite  $\text{RMnO}_3$  ( $R = \text{Y, Ho, Er, Tm, Yb, Lu}$ )."  
*Physical Review B*, 74(1), 014422-7.
- Zurmuhlen, R., Petzelt, J., Kamba, S., Voitsekhovskii, V. V., Colla, E., and Setter, N. (1995). "Dielectric-Spectroscopy of  $\text{Ba}(\text{B}'\text{b}-1/2)(1/2)\text{O}_3$  Complex Perovskite Ceramics - Correlations between Ionic Parameters and Microwave Dielectric-Properties .1. Infrared Reflectivity Study ( $10^{12}$ - $10^{14}$  Hz)."  
*Journal of Applied Physics*, 77(10), 5341-5350.

## Vita

Jonathan Charles Denyszyn was born in Durham, North Carolina on July 8<sup>th</sup>, 1977 to Patricia and Robert Denyszyn. The Denyszyn family left North Carolina when Jonathan was six-months old and moved to Bucks County, Pennsylvania where Jonathan attended Gayman Elementary School and later Holicong Middle School. In 1991, the Denyszyns relocated to League City, Texas where Jonathan attended Clear Creek High School. Jonathan graduated from Clear Creek High School in the spring of 1995; in the fall of 1995, Jonathan began his career at The University of Texas at Austin as a freshman Electrical Engineering student.

After graduating from The University in December of 1999, Jonathan traveled to Sacramento, California and worked a spring internship in *Intel's* Flash Products Division. Jonathan returned to Austin in the summer of 2000 and worked another internship in *Motorola's* MOS-13 fabrication facility. In the fall of 2000, Jonathan began his graduate career at The University of Texas at Austin and conducted research under the supervision of Dr. Russell Dupuis; Jonathan received his Master's degree in Electrical Engineering in May 2002. In January 2003, Jonathan began his doctoral research under the supervision of Dr. John B. Goodenough and Dr. Jianshi Zhou.

Upon successful completion of the requirements for a Ph.D. degree, Jonathan will begin working as a product development engineer for *Advanced Micro Devices*.

Permanent address: 6910 Hart Lane Apt. 706, Austin, Texas 78731

This dissertation was typed by the author.